THÈSE

En vue de l'obtention du

DOCTORAT DE L'UNIVERSITÉ DE TOULOUSE

Délivré par :

Institut National Polytechnique de Toulouse (INP Toulouse)

Discipline ou spécialité :

Dynamique des fluides

Présentée et soutenue par :

M. THOMAS ABADIE

le jeudi 14 novembre 2013

Titre :

HYDRODYNAMICS OF GAS-LIQUID TAYLOR FLOW IN MICROCHANNELS.

Ecole doctorale :

Mécanique, Energétique, Génie civil, Procédés (MEGeP)

Unité de recherche :

Institut de Mécanique des Fluides de Toulouse (I.M.F.T.)

Directeur(s) de Thèse :

M. DOMINIQUE LEGENDRE

MME JOELLE AUBIN

Rapporteurs :

M. DAVID FLETCHER, UNIVERSITY OF SYDNEY

M. STEPHANE POPINET, UNIVERSITE PIERRE ET MARIE CURIE

Membre(s) du jury :

M. CHRISTOPHE CLANET, ECOLE POLYTECHNIQUE, Président

M. DOMINIQUE LEGENDRE, INP TOULOUSE, Membre

Mme CATHERINE XUEREB, INP TOULOUSE, Membre

Mme JOELLE AUBIN, INP TOULOUSE, Membre

M. YVES GONTHIER, UNIVERSITE DE SAVOIE CHAMBERY-ANNECY, Membre

Abstract

This thesis focuses on the hydrodynamics of gas-liquid Taylor flow (or slug flow) in microchannels. These flows, which are generally dominated by surface tension forces, have been investigated in rectangular channels of various cross-sectional aspect ratios by means of both experimental visualizations and numerical simulations. The first experimental part aims at characterizing the bubble generation process (bubble length and frequency of break-up) depending on the operating conditions, the fluid properties, as well as the junction where both fluids merge. Numerical simulations of fully developed Taylor flow have been carried out with the *JADIM* code. The computation of such surface tension dominated flows requires an accurate calculation of the surface tension force. Some limitations of the Volume of Fluid method have been highlighted and a Level Set method has been developed in order to improve the calculation of capillary effects. Both methods have been compared in detail in terms of spurious currents. 3D numerical simulations have been performed and the influence of the capillary number, as well as the effects of geometry have been highlighted. Inertial effects have been taken into account and their influence on the pressure drop has been shown to be non-negligible. Mixing in the liquid slug has also been studied.

Résumé

Cette thèse porte sur l étude des écoulements de Taylor (ou poche/bouchon) gaz-liquide en microcanal. Ces écoulements où les effets de tension de surface sont prépondérants ont été étudiées expérimentalement et numériquement pour des géométries rectangulaires avec divers rapports d aspects. Une première partie expérimentale a consisté à caractériser la formation de bulles (taille, fréquence) en fonction des conditions opératoires, des propriétés des fluides (notamment à travers le nombre capillaire) et du mode de mise en contact des fluides. La dynamique de l écoulement établi a par la suite été étudiée à l aide du code *JADIM*. La simulation de ces écoulements dominés par la tension de surface a nécessité de lever les limitations liées à la prise en compte de la force capillaire. En effet des courants parasites numériques sont créés à proximité de l interface lors de la simulation d écoulements capillaires. Une méthode Level Set a été implémentée et comparée à la méthode Volume of Fluid d origine en termes de courants parasites. Des simulations numériques 3D ont permis l étude des effets du nombre capillaire et de la géométrie sur la dynamique des bulles de Taylor (vitesse, pression et formes de bulles). Les effets inertiels souvent négligés ont été considérés et leur influence, notamment sur les sauts de pression à l interface, a été mise en évidence. Le mélange dans le bouchon liquide a également été étudié.

Remerciements

Je remercie Christophe Clanet pour avoir accepté de présider mon jury de soutenance, Catherine Xuereb et Yves Gonthier pour avoir accepté de faire partie de ce jury et tout particulièrement Stéphane Popinet et David Fletcher pour le temps consacré à la lecture de ce manuscrit et leurs commentaires constructifs en tant que rapporteurs.

Je suis reconnaissant envers le personnel de l ENSEEIHT qui m a permis de faire des vacations dans le département HMF, notamment les directeurs successifs du département (Wladimir Bergez et Denis Dartus), ainsi que Alexei Stoukov, Gérald Debenest, Veronique Roig et Philippe Fernandez pour leur aide lors des TD/TP et bien sûr Maryse André.

Je remercie également le LGC et l IMFT pour leur accueil et le cadre de travail proposé, notamment grâce aux différents services. Je pense particulièrement à Marie-Hélène pour son aide pour les démarches administratives, très abstraites à mes yeux, et toujours dans la bonne humeur. Je remercie le service Cosinus et notamment Annaïg pour son aide précieuse et très efficace sur *JADIM*. J en profite également pour remercier, en plus de mes collègues de bureau dont le tour viendra, Thomas B., disponible pour les diverses questions VOF, ainsi que Franck pour les questionnements numériques communs... Je pense également à Alain Pontier pour le suivi sur la partie expérimentale, ainsi que Vincent, Gilles et Alain pour la construction des canaux.

Je tiens à remercier chaleureusement mes directeurs de thèse qui m ont donné l opportunité de faire cette thèse à la suite du stage de Master. Je remercie Joëlle et Dominique (malgré des défaites parfois cruelles lors des tournois de pétanque et ping-pong...) pour m avoir permis de travailler avec autonomie, prendre des initiatives, tout en étant disponible et en me guidant de façon toujours pertinente. Je leur suis très reconnaissant pour leur soutien et leur (grande) patience lors de la rédaction et pendant que je fouinais dans le code. Grâce à leurs compétences scientifiques et leurs qualités humaines, leur encadrement/accompagnement a grandement contribué au fait que j ai particulièrement apprécié ces trois années de thèse.

Je remercie également tous les membres permanents du groupe Interface pour l ambiance générale qui règne dans le groupe via les discussions scientifiques ou plus légères au cours des pauses. Merci à Greg pour ses nombreuses blagues et faits divers originaux; René, alias "Mantequilla" et partenaire officiel lors des tournois, pour les spécialités mexicaines et sa gentillesse; Marie, Elise et Audrey pour les bons moments passés au laboratoire et à l extérieur, leur soutien pendant la rédaction et leur générosité (notamment lors des repas où elles avaient pitié de moi avec le fameux sandwich rosette de la machine...).

Je suis également reconnaissant envers l IMFT pour sa proximité avec les installations sportives de Nakache dont on a pleinement profité. Je remercie donc les sportifs : à commencer par Yohann, qui pratique à peu près tous les sports du monde; Nicolas et Romain entre autres pour les nombreuses pétanques (et ce qui va avec...); les joueurs de tennis Sébastien C. (très patient pendant ma petite demi-heure de chauffe...) et Jean-Lou; sans oublier les footeux les plus assidus, Michael (et ses tentatives de volées acrobatiques), Mathieu, René, Jérôme ainsi que Greg, Max, Ruddy, Joël, Mithlesh, Sergio, Thomas B., Hervé, Luigi, etc. Je pense également aux thésards, stagiaires et post-doctorants que j ai croisés au cours de ces 3 années de thèse et qui participent à

l ambiance conviviale et très agréable qui règne dans le groupe et le laboratoire : Lucia, Yuri, Emmanuella, Erik, Auriane, Nicolas, Carlos, Manel, Cédric, Benjamin, Martin, Christophe, Hervé M., Laurence, Marco, Antoine, Bryan, ... Je remercie également les doctorants du LGC, Alex, Miruna, Tanya, Emeline, Félicie qui m ont accueilli lors de mes visites pour les campagnes expérimentales.

Enfin, un immense merci aux collègues de bureau pour avoir supporté la déco TFC. Je remercie Jean-François, malgré une rivalité entre nous au ping-pong, pour sa bonne humeur et ses "blagues". Et bien entendu, les meilleures pour la fin, Mélanie et Agathe qui m ont accueilli dans le bureau. Merci d une part pour leur aide *JADIM* pour le côté travail, mais aussi (et surtout) pour l ambiance dans le bureau au quotidien, leur gentillesse, les discussions scientifiques et (beaucoup) moins sérieuses, les apéros et les ascenseurs émotionnels (parfois surprenants) de Mélanie. En résumé, plein de bons moments partagés, merci !

Enfin, je remercie ma famille pour leur soutien pendant ces trois années et mes amis qui m ont permis de penser à autre chose en dehors du laboratoire et sortir de ce monde de petites bulles.

Contents

Introduction

General context

The interest of the process industries in microreaction technology for process intensification has become increasingly important over recent years. Microreaction technology involves the use of small-scale structured devices that have characteristic dimensions of the order of several hundreds of microns to $1-2$ millimeters for performing diverse operations (*e.g.* mixing, separation, reaction, mass and heat transfer) in the chemical and related industries. Due to the small-scale characteristic dimensions of microreaction technology, extremely high surface to volume ratios are attained when compared with conventional equipment, allowing the intensification of heat and mass transfer and tight control of the temperature within the reactor.

The positive consequences of such intensification and control are a decrease in the risk of runaway reactions, reactor explosion as well as a decrease in energy consumption since less cooling (or heating) is required. The use of microstructured devices also provides the opportunity to carry out reactions in more concentrated conditions, which not only reduces the reaction time and the amount of solvent used but also increases the selectivity of reactions which means that separation steps to recover main products can essentially be eliminated.

Amongst the different process applications, microreactors are particularly interesting for fast and highly exothermic and/or mass transfer limited gas-liquid reactions since heat and mass transfer are remarkably intensified. Several research studies have demonstrated that gas-liquid microreactors have unique advantages for various and some typically dangerous gas-liquid reaction systems, such as gas absorption (Yue et al. [2007]), direct fluorination (Chambers et al. [2005]), three-phase hydrogenation reactions (Kobayashi et al. [2004]) and photochemical gas-liquid reactions (Ehrich et al. [2002]). Although microreaction technology is already implemented in industry (Aubin et al. [2010]), the engineering methodologies and rules for the design and integration of microreactors, as well as how they should be operated, are still not clearly defined. The development of such methodologies and rules requires fundamental understanding of the physical phenomena that control the process operation and the specificities of equipment design.

This work is part of the project MIGALI (Microreactors for Intensifying Gas-Liquid Transport Phenomena), funded by the french National Research Agency (ANR MIGALI-no ANR-09-BLANC-0381-01,2010-2013). This project is an international project which involves three French laboratories and three Chinese laboratories:

- Laboratoire de Génie Chimique (LGC),
- Laboratoire Optimisation de la Conception en Ingénierie de l Environnement (LOCIE),
- Institut de Mécanique des Fluides de Toulouse (IMFT),

- Microchemical Group, Dalian Institute of Chemical Physics (DICP), Chinese Academy of Sciences,
- State Key Laboratory of Chemical Engineering, Tianjin University (TU),
- State Key Laboratory of Chemical Engineering, East China University of Science and Technology (ECUST).

This project aims at gaining fundamental knowledge on the intensification of hydrodynamics and mass transfer of gas-liquid processes and the dependency of these phenomena on both the operating conditions and the geometrical characteristics of equipment.

Introduction to Taylor flow in microchannel

This part aims at introducing the characteristics of gas-liquid Taylor flow in microchannels. The literature review relative to each aspect of this work will be presented as an introduction at the beginning of each chapter. Gas-liquid flows in channels are encountered in many industrial applications, from small scale processes where capillary forces are generally dominant (*e.g.* chemical microreactors for process engineering, fuel cells, cooling microsystems, coating) to larger scale processes where inertial and gravitational effects play a non-negligible role (*e.g.* petroleum engineering). In this work, we focus on microscale flows where, as it will be detailed in chapter 1, gravitational effects can be considered as negligible.

Gas-liquid flows in microchannels can be found in different flow regimes. Indeed, the topology of the interface depends on the fluid properties, the operating conditions as well as the geometry of the channel. Much work has been dedicated to the development of flow pattern maps which define the transition between the following regimes:

- bubbly flow, characterized by a number of tiny bubbles, smaller than the channel diameter;
- slug or Taylor flow, characterized by bubbles that are longer than the characteristic dimension of the channel and separated from the walls by a thin liquid film;
- annular flow, characterized by a continuous core of gas surrounded by a thin liquid film;
- churn flow, which is between annular and bubbly flow, where the gas core breaks into tiny bubbles.

In microchannels, the transition between flow regimes have been identified in the literature and a number of flow pattern maps are available. Flow pattern maps are generally based on the superficial gas and liquid velocities (Triplett et al. [1999], Waelchli and Von Rohr [2006], Zhang et al. [2011]) as it is shown in figure 1. However, these maps based on the superficial velocities are only valid for one given pair of fluids. Akbar et al. [2003] generalized these flow pattern maps by gathering data obtained with different liquids and identified the Weber number as the dimensionless number that governs the transition between the different regimes in microchannels.

As shown in figure 1, slug flow is generated for a wide range of gas and liquid velocities and the objective of this work is to focus on this flow regime. This gas-liquid dispersion is very regular, leading to a flow with homogeneous bubble break-up frequencies, volumes, and velocities.

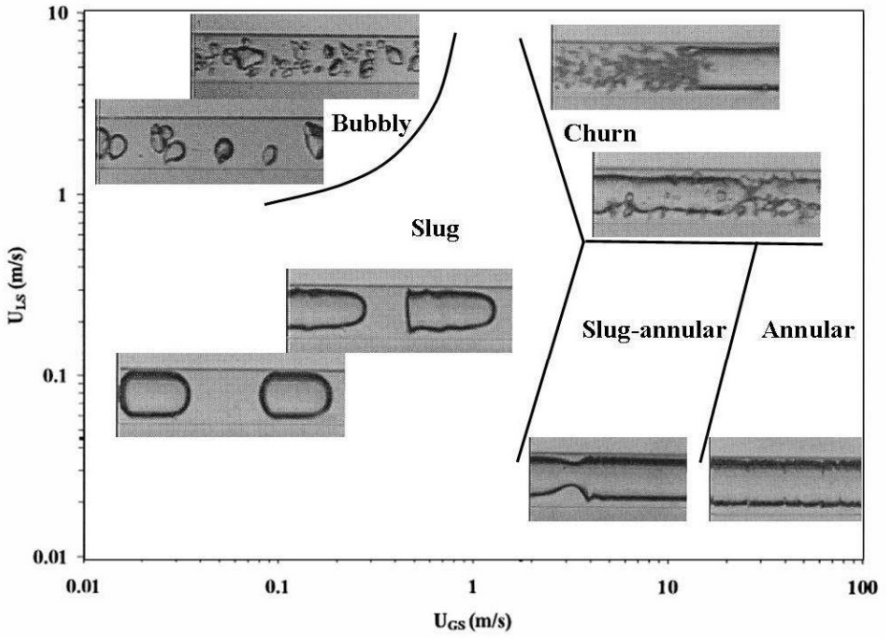

Figure 1: Typical flow pattern map for gas-liquid flow in microchannels (adapted by Volkel [2009] from Triplett et al. [1999]).

The Taylor flow structure presents many advantages for engineering processes. In addition to the high interfacial areas and the high regularity of the flow, the residence time in gas-liquid Taylor flow is well characterized as it is directly related to the velocity of the bubble since the flow is unidirectional. The bubble velocity therefore governs the residence time but also the flow pattern in the liquid slug. Indeed, the bubble velocity is generally greater than the average two-phase velocity U_{TP} and lower than the maximum velocity on the centerline. Thus, in the frame of reference moving with the bubble, at the center of the channel, fluid particles flow from the nose of a bubble towards the previous bubble in the bubble train while fluid particles close to the wall flow in the other direction. This slip velocity between the bubble and the mean flow generates a flow recirculation, which is of main interest in mixing and reaction applications. In addition, this recirculation motion in the liquid slugs occupies a major part of the channel cross-section, thereby reducing communication between slugs and increasing plug flow since radial mixing is enhanced by this recirculation motion (Thulasidas et al. [1997]).

The dynamics of fully-developed Taylor flow at low Reynolds number in microchannels is well characterized (Bretherton [1961], Aussillous and Quéré [2000]) but less attention has been paid to polygonal capillaries and in particular square and rectangular geometries (Wong et al. [1995a,b], De Lozar et al. [2008]). These geometries are particularly interesting in microreaction technologies and especially for micro reactor-heat exchangers since the exchange surface between reaction plates and cooling plates is enhanced. Although the use of rectangular microchannels of high aspect ratio appear to be interesting from a heat control point of view, the cost in terms of the energy needed to drive such flows (*i.e.* pressure drop) and its performance in terms of mixing and mass transfer need to be estimated. One objective of this study is to consider the effects of geometry on Taylor flow.

In flows dominated by surface tension in microchannels, the confinement is crucial and plays a major role in both the dynamics of the fully developed flow and in the

gas bubble dispersion. Depending on the microchannel geometry and the operating conditions, the bubble volume and length vary. Indeed, the distribution size will be mainly governed by the size of the equipment and the flow rates of each phase (Garstecki et al. [2006]). In addition, the mechanism of bubble break-up in microfluidics devices like T-shaped junctions (Garstecki et al. [2006]) or cross-junctions (Cubaud et al. [2005]) have been introduced. However, the role of the channel geometry and the effects of fluid properties are not clear.

This motivates the first part of this work where the bubble dispersion process has been characterized in a cross-junction by means of experimental visualizations (figure 2(a)). The results and mechanism of break-up have then been compared to other geometries (different T-shaped junctions illustrated in figures 2(b) and (c)).

(a) cross-junction (b) side-T junction (c) T-junction

Figure 2: Illustration of the junctions studied.

General notation used in this work

The general notations used throughout this study are illustrated in figure 3.

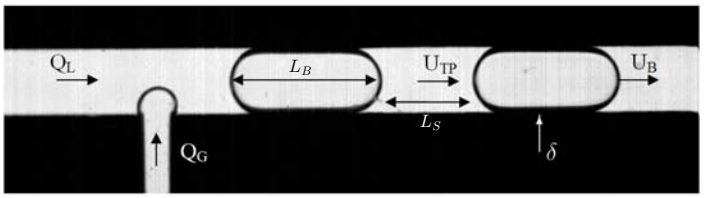

Figure 3: Contacting section: bubble formation. The notation used is: $Q_{G,L}$ for gas and liquid flow rates, $L_{B,S}$ for bubble and slug lengths, δ the liquid film thickness, U_B the bubble velocity and U_{TP} the superficial two-phase velocity. A_{ch} is the cross-sectional area.

The phase distribution in the microchannel is described using the flow rate ratio or equivalently the velocity ratio. The superficial velociy of each phase is:

$$U_{G,L} = \frac{Q_{G,L}}{A_{ch}} \tag{1}$$

where A_{ch} is the cross-sectional area of the microchannel and $Q_{G,L}$ are the gas and liquid volumetric flow rates. Thus, according to the volume balance between the two inlets and an outlet placed in a slug, the averaged velocity in this slug, called two-phase velocity U_{TP}, is expressed as:

$$U_{TP} = \frac{Q_L + Q_G}{A_{ch}} = U_L + U_G \tag{2}$$

Some dimensionless groups are introduced to characterize the flow. The Bond number compares the gravitational and capillary effects:

$$Bo = \frac{(\rho_L - \rho_G)\, D_h^2\, g}{\sigma} \tag{3}$$

where D_h is the hydraulic diameter, σ is the surface tension, ρ_L and ρ_G are the liquid and gas densities. In microchannels, the Bond number is generally low and capillary forces dominate gravitational forces.

The pioneering works of Taylor [1961] and Bretherton [1961] identified the bubble capillary number Ca_B as the dimensionless number that characterizes the dynamics of the flow:

$$Ca_B = \frac{\mu_L\, U_B}{\sigma} \tag{4}$$

where μ_L is the liquid dynamic viscosity and U_B is the bubble velocity.

The effects of inertia are considered in this study through the dimensionless Reynolds number, which compares inertial and viscous forces:

$$Re_B = \frac{\rho_L\, U_B\, D_h}{\mu_L} \tag{5}$$

Two other dimensionless numbers which can be written as a combination of the Reynolds and capillary numbers will be mentioned: the Weber number We_B which compares inertial and capillary effects and the Laplace number La which depends on the fluid properties and the geometry only:

$$We_B = Re_B \times Ca_B = \frac{\rho_L\, U_B^2\, D_h}{\sigma} \tag{6}$$

$$La = \frac{Re_B}{Ca_B} = \frac{\rho_L\, \sigma\, D_h}{\mu_L^2} \tag{7}$$

Structure of the manuscript

The observations on the advantages of Taylor (or slug) flow in microreaction technology motivate our work with the following objectives:

- understanding the effects of geometry and fluid properties on the gas bubble dispersion in the Taylor flow regime;
- characterizing the hydrodynamics of Taylor flow in rectangular microchannels, *i.e.* the pressure drop and the bubble velocity that controls the residence time and the flow structure in the liquid slug;
- investigating mixing and mass transfer in rectangular microchannels.

This study is based on both experiments and numerical simulations. The experiments have been performed at LGC while the numerical simulations have been carried out with the *JADIM* code developed at IMFT. This work is structured around seven chapters.

The first chapter is dedicated to the presentation of the experimental set-up. The description of the experimental apparatus includes the design of the microchannel, the flow control equipment, as well as the operating conditions that have been covered. The imaging methods are described and validated with a reference sequence.

The chapters 2, 3 and 4 aim at presenting the numerical method, the developments made during this study and its validations. More specifically, chapter 2 briefly reviews the numerical methods for the numerical simulation of two-phase flows. The *JADIM* code based on a Volume of Fluid (VOF) method to capture the interface is then described before our developments. Special care is taken to describe the calculation of the surface tension force and the transport of the scalar function that defines the interface. The limitations of the VOF method to deal with the simulation of gas-liquid Taylor when the capillary forces are dominant lead us to implement another method for considering the interface transport. The Level Set method is presented and validated in chapter 3.

Chapter 4 is dedicated to the study of spurious currents arising in numerical simulations which involve capillary effects. Such parasitic flows develop when the capillary number is decreased. The comparison of the previous VOF formulation and the LS method implemented is the topic of this chapter which is the subject of a paper that has been submitted to *Computers and Fluids* in August 2013. A detailed analysis of the spurious currents generated in various test cases is given and the interest of the method for the application to the simulation of Taylor flow is highlighted at the end of this chapter.

The next chapters concern more specifically the physical results concerning Taylor bubble flows obtained in this thesis. Chapter 5 investigates the role of the channel geometry and the fluid properties on the generation of slug flow. The bubble lengths and frequencies of generation are analyzed through experimental visualizations. This chapter follows the work carried out during my master thesis that has been published in *Micro uidics and Nano uidics* (Abadie et al. [2012], appendix C).

Chapter 6 focuses on the dynamics of fully-developed Taylor flow. 3D numerical simulations of Taylor bubbles have been performed. The dynamics of the Taylor bubble in terms of velocity and pressure drop are studied and the bubble velocities obtained in the numerical simulations are compared with the experimental data. The chapter comprises two main parts: first, the results at low Reynolds number and then the effects of inertia are presented.

Chapter 7 concerns the charactistic times and volumes of mixing in the slug between two consecutive bubbles. This chapter has been published in *Chemical Engineering Research and Design* in 2013 (Abadie et al. [2013]). The effects of the rectangular geometry on the mixing in the liquid slug are studied. The results are based on both numerical simulations and the theoretical velocity profile of single-phase flows that approximates infinite slug lengths.

Finally, a conclusion presents the main results of this work and outlines some challenging perspectives such as the simulation of mass transfer from Taylor bubbles to the liquid slug.

Chapter 1

Experimental apparatus and imaging methods

Contents

1.1 Experimental apparatus

The experimental apparatus detailed in this section and illustrated in figures 1.1-1.2 allows gas-liquid flows to be generated and the bubble dispersion to be studied in terms of frequency, volume and length, as well as velocity. The experimental rig comprises:

- the microchannel,
- the feeding equipment to provide controlled gas and liquid flow rates,
- the digital imaging equipment.

The experiments are based on shadow-casting, which allows detection of the interface of the bubbles on every image due to the change in the optical light path where the interface is curved. The flow characteristics, which include bubble size, break-up frequency and velocity are then extracted using an image processing software.

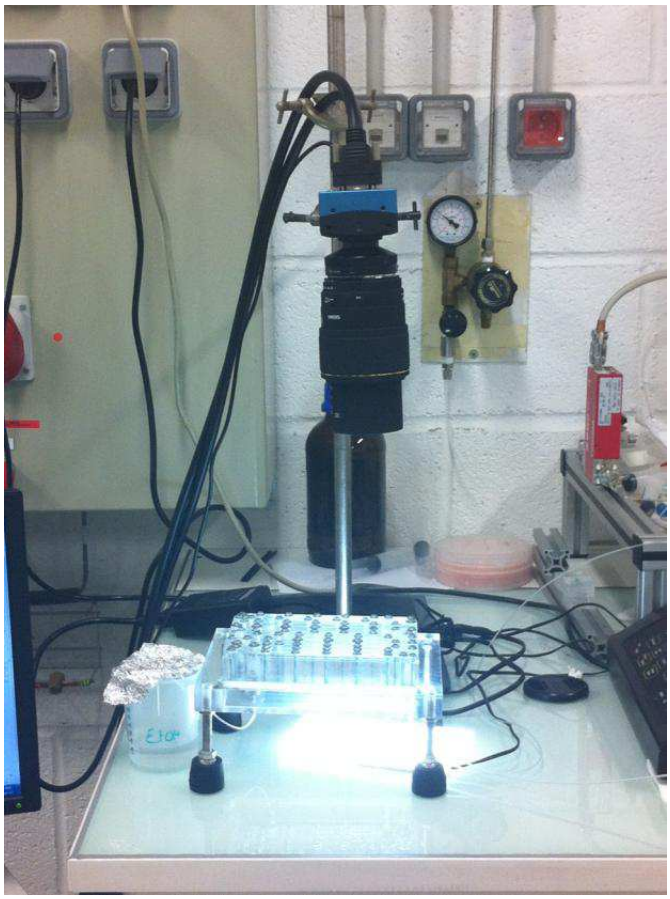

Figure 1.1: Experimental apparatus - the microchannel is horizontal and the image sequences are taken with a digital camera placed above.

1.1.1 Microchannel design

Materials

The channels used to study the bubble generation and velocity are square and rectangular microchannels milled in Polymethyl Methacrylate (PMMA) with a micro-milling machine at the mechanical workshop at INP Toulouse. This milled microchannel plate is covered with another plate of PMMA as seen in figure 1.3, which is an

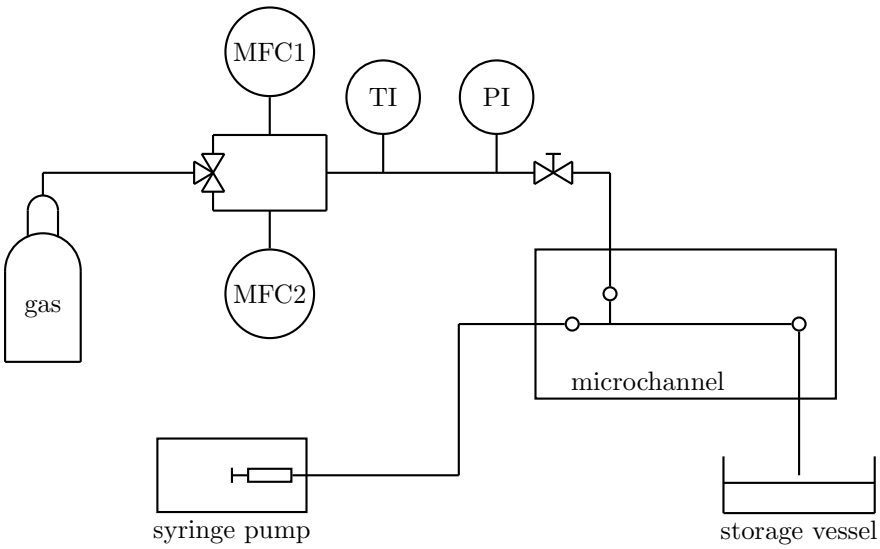

Figure 1.2: General illustration of the experimental set-up (MFC: mass flow controllers (MFC1: flow rates $0-1$ SCCM and MFC2: flow rates $1-20$ SCCM) ; PI: pressure indicator ; TI: temperature indicator).

image of the cross-section of a channel obtained with a scanning electron microscope. PMMA presents the advantages of being transparent for visualization experiments.

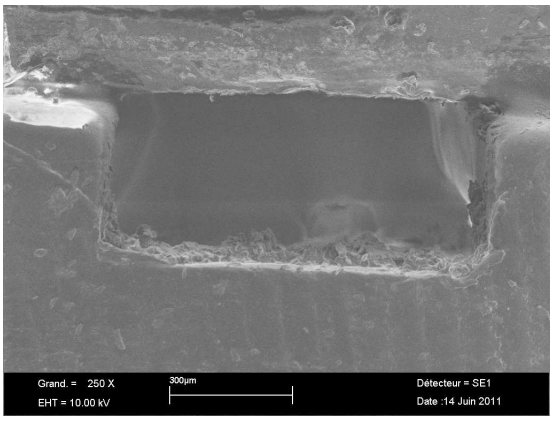

Figure 1.3: Cross-sectional shape of a channel obtained with a scanning electron microscope. The aspect ratio is α= 2.5 ($w = 1000\mu m$ and $h = 400\mu m$).

Channel dimensions

The channel aspect ratio affects both the hydrodynamics of the fully-developed Taylor flow and the bubble generation mechanism. To study the effects of the cross-sectional geometry of the channel, three moderate aspect ratios have been tested $\alpha = [1\,;\,2.5\,;\,4]$. The dimensions of the channels have been chosen in agreement with

previous experiments conducted in the group and detailed in Volkel [2009], Abadie et al. [2012] and Zaloha et al. [2012]. The hydraulic diameter has been kept constant around $550\mu m$ and the characteristics of the three geometries are given in table 1.1.

aspect ratio	width (μm)	depth (μm)	hydraulic diameter (μm)
1	550	550	550
2.5	1000	400	571
4	1400	350	560

Table 1.1: Dimensions of the three microchannels used.

Since the depth of the microchannels varied from $350\mu m$ to $550\mu m$, even a default of a few micrometers would be non-negligible, therefore special care was taken to perfect the surface and flatness of both plates using diamond polishing.

In addition to the importance of the flatness relative to the depth of the channel, it is absolutely necessary to obtain flat plates to avoid leakage between the milled and cover plates. Bonding tests were performed using chloroform as a solvent but although this method can be used easily with straight channels or short channels, the difficulty increases in complex geometries as it is the case in the channels used, which are $30cm$ long and present 2 curved bends. Since the flatness of the channels was carefully ensured, leaks have been prevented by using a number of screws every 1 or 2 centimeters. A drawback of this solution could have been the bending of the PMMA plates but it will be seen in section 1.3.3 that the cross-sectional area does not change along the microchannel since the bubble sizes and velocities are constant. A view of the final microchannel focused on the contacting geometry is shown in figure 1.4.

Figure 1.4: Top view of the microchannel.

Contacting geometries

The geometry of the channel at the gas-liquid contacting point is of main importance in the bubble formation step. Indeed, it has been observed that bubble volumes and break-up frequencies in microchannels where capillary effects are dominant are mainly

governed by the geometrical characteristics of the channel (*i.e.* width w, channel aspect ratio α, gas to liquid inlet width ratio $w_{in,g}/w$) and the operating conditions (gas to liquid volumetric flow rates ratio Q_G/Q_L). In the literature, geometrical models for predicting bubble size are commonly encountered (Garstecki et al. [2006], Van Steijn et al. [2007, 2010], Volkel [2009], Abadie et al. [2012]).

To study the effects of the contacting geometry on the bubble generation mechanism, three channels with different contacting modes are considered:

- a side-entering T-junction (figure 1.5(a)), *i.e.* the two fluids merge at a right angle. The liquid is flowing in the main channel while the gas is supplied by the orthogonal channel, which is narrower than the main inlet ($w_{g,in} = w/2$),
- a T-junction (figure 1.5(b)), *i.e.* the two fluids merge frontally. The liquid and gas are flowing in channels that are both orthogonal to the main channel and both inlets have the same width as the main channel,
- a cross-junction (figure 1.5(c)), *i.e.* the two fluids merge in a cross where the gas is flowing in the main channel and the liquid is supplied with two orthogonal channels, with the same width as the main channel, to squeeze the bubbles.

1.1.2 Flow control

The schematic diagram of the full experimental set-up is given in figure 1.2. Air is supplied from a pressurized vessel and controlled by two distinct mass-flow controllers depending on the flow rate:

- one to cover low flow rates with a good accuracy ($0-1SCCM$): *HORIBA SEC-7320*, which allows flow rates ranging from 0.00 to $1.00\,mL/min$ under atmospheric pressure with a minimum regulation of $0.02\,mL/min$,
- one to cover higher flow rates ($1-20SCCM$): *HORIBA SEC-Z500*, which allows flow rates ranging from 0.0 to $20.0\,mL/min$ under atmospheric pressure with a minimum regulation of $0.2\,mL/min$.

Concerning the liquid, the flow control equipment is a syringe pump (*HARVARD Apparatus PHD 2000*) on which two plastic syringes are placed. Two different sizes of syringes have been used: syringes containing $20mL$ of liquid with an inner diameter of $20.05mm$ have been used for the lower liquid flow rates (up to $1.6mL/min$) and syringes of diameter $26.594mm$ containing $60mL$ for higher liquid flow rates. With the smaller syringes, the pump can supply flow rates ranging from $0.0500\mu L/min$ to $50.000\,mL/min$. Although the maximum flow rate available was not reached with these syringes, the time needed to empty the syringes was too short with flow rates greater than $1.6mL/min$ when compared with the time needed for the flow to develop and the sequence to be recorded. Therefore syringes with a bigger diameter were used for liquid flow rates between $2.4mL/min$ and $12.8mL/min$. The maximum flow rate available with these syringes is about $130.000mL/min$.

All the experiments were conducted at room temperature and ambient pressure at the outlet. For each experiment, the temperature of the gas and liquid phases was measured by thermocouples just before the two fluids were contacted. The pressure in the gas phase was also measured before the contacting section so that the mass flow rates could be converted to volumetric flow rates. The pressure measurements are detailed in section 1.1.4.

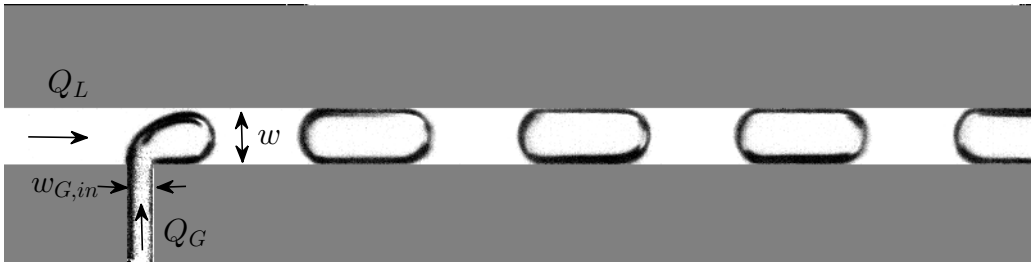

(a) side T-junction

(b) T-junction

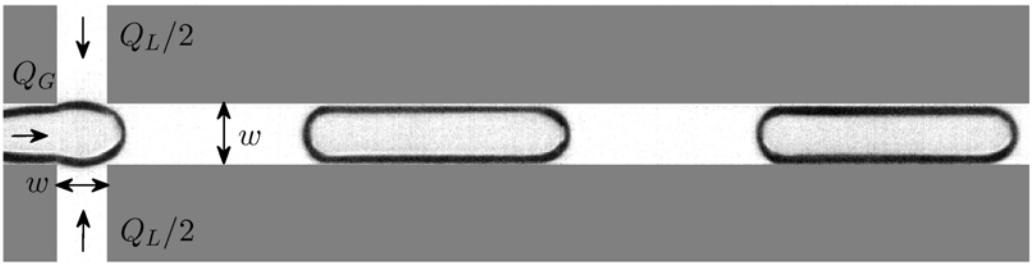

(c) cross-junction

Figure 1.5: Illustration of the three contacting sections studied: (a) side T-junction; (b) T-junction; (c) cross-junction.

1.1.3 Fluid properties and Operating conditions

The initial fluid system is an ethanol-air system, which allows a regular and relatively easy bubble formation (Volkel [2009], Abadie et al. [2012]). In these surface tension dominated flows, the capillary number has been shown, both experimentally and theoretically (Taylor [1961], Bretherton [1961]), to be well adapted for the characterization of bubble shapes and velocities. The effects of fluid properties are often neglected in models that take into account the geometry of the channel and the contacting section, as well as the ratio of gas to liquid flow rates. However, it has also been observed in other studies that the fluid properties can have a non-negligible role in the bubble break-up (Christopher et al. [2008], Fu et al. [2010a], Abadie et al. [2012]).

For this purpose, solutions of ethanol and glycerol have been used to vary the density and particularly the viscosity and the surface tension. The properties of the fluids used have been measured and are reported in table 1.2. The percentages indicated for ethanol/glycerol solutions are volume ratios.

fluid	ρ_L (kg/m^3)	μ_L $(Pa \cdot s)$	σ (N/m)	La $(-)$	Bo $(-)$
air	1.204	1.815×10^{-5}	–	–	–
ethanol (EtOH)	789	1.37×10^{-3}	0.0227	5440	0.111
glycerol 15% in EtOH	882	3.3×10^{-3}	0.0247	1130	0.114
glycerol 30% in EtOH	957.3	8.08×10^{-3}	0.0267	223	0.114
glycerol 60% in EtOH	1065.6	23.59×10^{-3}	0.0304	33	0.102

Table 1.2: Fluid properties (under room temperature $T = 22 - 23\,°C$). The Laplace and Bond numbers (La and Bo) are calculated using $D_H = 570\mu m$.

It is important to note that the Bond numbers obtained with these fluid properties and this microchannel hydraulic diameter are of the order of $Bo \sim 0.1$, which suggests that the effects of the acceleration due to gravity are negligible when compared with capillary effects. It is then consistent to assume that the shape of the bubble is governed by capillary effects and remains symmetrical throughout the depth of the channel.

fluid	Q_L (mL/min)	Re_L	Ca_L	We_L
air-EtOH	0.2 - 12.8	3.62 - 231	6.65×10^{-4} - 4.26×10^{-2}	2.41×10^{-3} - 9.87
air-glycerol (15% in EtOH)	0.2 - 12.8	1.66 - 106	1.47×10^{-3} - 9.42×10^{-2}	2.45×10^{-3} - 10.0
air-glycerol (30% in EtOH)	0.2 - 6.4	0.746 - 23.88	3.34×10^{-3} - 1.07×10^{-1}	2.49×10^{-3} - 2.56
air-glycerol (60% in EtOH)	0.1 - 1.6	0.142 - 2.27	4.28×10^{-3} - 6.84×10^{-2}	6.08×10^{-4} - 0.155

Table 1.3: Velocities and dimensionless numbers in the square microchannel ($550 \times 550\ \mu m^2$).

According to these fluid properties and to the available gas and liquid flow rates, the ranges of dimensionless numbers for the experiments are summarized in table 1.3 and the Reynolds and capillary numbers are illustrated in figure 1.6. The values of the capillary number (viscosity/capillarity) are very low, thereby indicating that capillary effects overcome viscous effects. In such conditions, the shape of the bubble is mainly governed by capillary effects which prevent bubble deformation. However, capillary numbers of the order of $Ca_L \sim 0.1$ are reached when the liquid velocity is increased and above this value the bubble is deformed. In addition, the values of the Reynolds and Weber number indicate that for ethanol, glycerol 15% and glycerol 30% in ethanol at high velocity, the inertial effects are non-negligible although they are often neglected in microchannels. These inertial effects are even stronger than the viscous effects and the capillary forces in these cases, threreby modifying the shape of the bubbles, their velocities and the pressure drops across the bubbles.

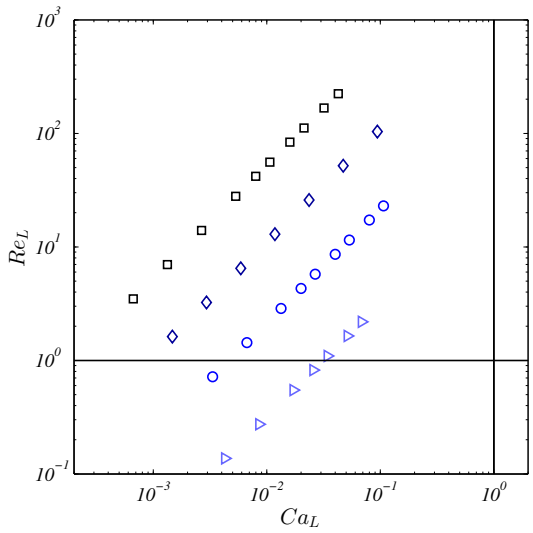

Figure 1.6: Summary of the experiments performed in a square channel where the fluids merge at a cross-junction in terms of Reynolds and capillary numbers.
Legend: (□) $La = 5440$; (◇) $La = 1130$; (○) $La = 223$; (▷) $La = 33$.

1.1.4 Pressure measurements

In microscale devices, the pressure drop is enhanced when compared with bigger channels as it is inversely proportional to the hydraulic diameter. The upstream pressure also increases when viscous liquids are used and when the mean velocity in the channel is increased. The gas flow rate delivered is a mass flow rate and a digital manometer (*KELLER LEO 2*) has therefore been placed between the gas inlet channel and the mass flow controller in order to measure the upstream pressure, *i.e.* the pressure at the gas inlet. Knowledge of the pressure together with the ideal gas law allows the mass flow rate to be converted into a volumetric flow rate at the gas inlet:

$$Q_G = \frac{Q_G^m}{\rho_G/\rho_{G,atm}} = \frac{Q_G^m\, P_{atm}}{P_{manometer}}, \tag{1.1}$$

where Q_G^m is the mass flow rate scaled by the density of the air under atmospheric pressure. Indeed, the volumetric flow rate is needed to characterize the flow parameters such as the bubble volume as it is equal to the bubble formation time multiplied by the volumetric gas flow rate. The mean velocity in the channel is also related to the volumetric flow rates and will be used to study the slip velocity between the bubble and the mean flow. From the channel length and the fluid properties, the single-phase pressure drop across the channel has been evaluated to estimate the accuracy and the pressure range that the manometer needed to cover. This manometer can measure pressures ranging from 0 to 5 bars while in the experiments, the maximum pressure measured was 2.3 bars.

Figure 1.7 shows the upstream pressures measured as a function of the gas mass flow rate. Two extreme cases are shown for a square channel and a cross-junction:

- With ethanol (low viscosity) flowing at a low velocity, the measured pressure is close to atmospheric pressure and the conversion factor between mass and volumetric flow rates is close to 1. The upstream pressure increases with both

the liquid and gas flow rates as the pressure drop increases. However, it is not greater than 1.5 bar with ethanol.

- With glycerol 60% in ethanol, the same trends as above are observed but they are enhanced due to the higher viscosity and the upstream pressure can reach up to 2.3 bars.

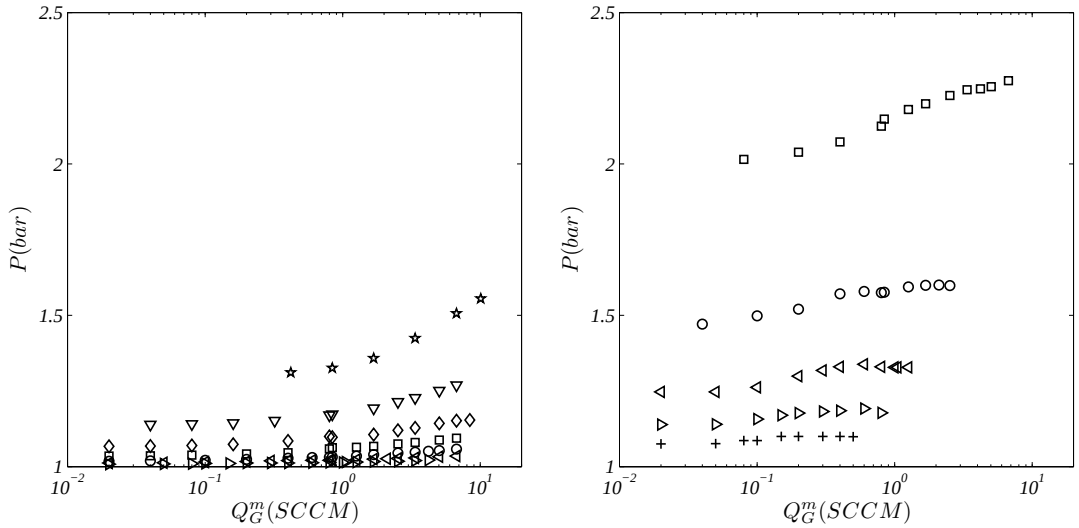

(a) Ethanol ($La = 5440$)

(b) Glycerol 60% in ethanol ($La = 33$)

Figure 1.7: Evolution of the upstream pressure as a function of the gas mass flow rate in the square microchannel with a cross-junction: (a) ethanol; (b) glycerol 60% in ethanol.
Legend: (+) $Q_L = 0.1\,mL/min$; ($\triangleright$) $Q_L = 0.2\,mL/min$; ($\triangleleft$) $Q_L = 0.4\,mL/min$; ($\circ$) $Q_L = 0.8\,mL/min$; ($\square$) $Q_L = 1.6\,mL/min$; ($\diamond$) $Q_L = 3.2\,mL/min$; ($\triangledown$) $Q_L = 6.4\,mL/min$; ($\star$) $Q_L = 12.8\,mL/min$.

Figure 1.8 shows the volumetric gas flow rate as a function of the mass flow rate in these cases. Indeed, the scale factor between the mass flow rate and the volumetric flow rate is greater in experiments where glycerol is used because of the increased pressure drop due to the fact that the viscosity of glycerol is greater than the viscosity of ethanol.

1.2 Flow visualization

The visualisation equipment and its position with respect to the microchannel is represented schematically in figure 1.9. Flow visualisation was conducted with a high-speed camera (*Mikrotron EoSens MC-1362*), which allows a maximum frame rate of $506fps$ (frames per second) at full resolution (1280 pix $\times$ 1024 pix). Since the flow studied here is unidirectional, the full resolution was not necessary and the region of interest was reduced to a window of 1280 pix $\times$ 200 pix. In addition, this use of reduced resolution allows the maximum frame rate available to be increased. Sequences of 1024 images were therefore recorded with a maximum frame rate of $2500fps$. The camera was placed at a distance of $35cm$ from the channel and the lens (*Sigma DG macro 105 mm*) was placed at a distance of $17cm$. The physical region of interest is $28.2mm \times 4.4mm$. This means that 1 pixel is $22\mu m \times 22\mu m$ in size.

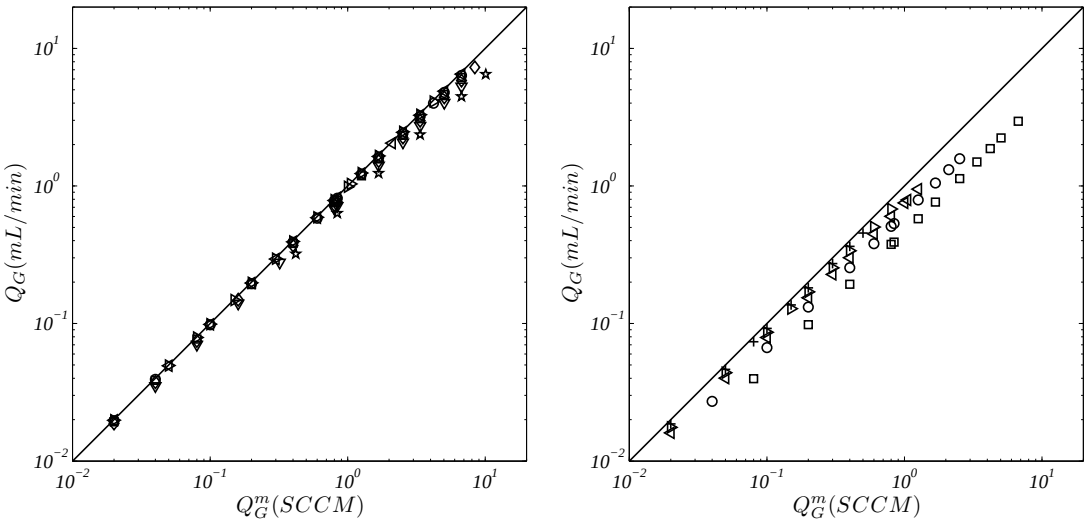

(a) Ethanol ($La = 5440$)

(b) Glycerol 60% in ethanol ($La = 33$)

Figure 1.8: Evolution of the gas volumetric flow rate as a function of the gas mass flow rate in the square microchannel with a cross-junction: (a) ethanol; (b) glycerol 60% in ethanol.
Legend: $(-)$ parity line, $(+)$ $Q_L = 0.1\,mL/min$; $(\triangleright)$ $Q_L = 0.2\,mL/min$; $(\triangleleft)$ $Q_L = 0.4\,mL/min$; $(\circ)$ $Q_L = 0.8\,mL/min$; $(\square)$ $Q_L = 1.6\,mL/min$; $(\diamond)$ $Q_L = 3.2\,mL/min$; $(\triangledown)$ $Q_L = 6.4\,mL/min$; $(\star)$ $Q_L = 12.8\,mL/min$.

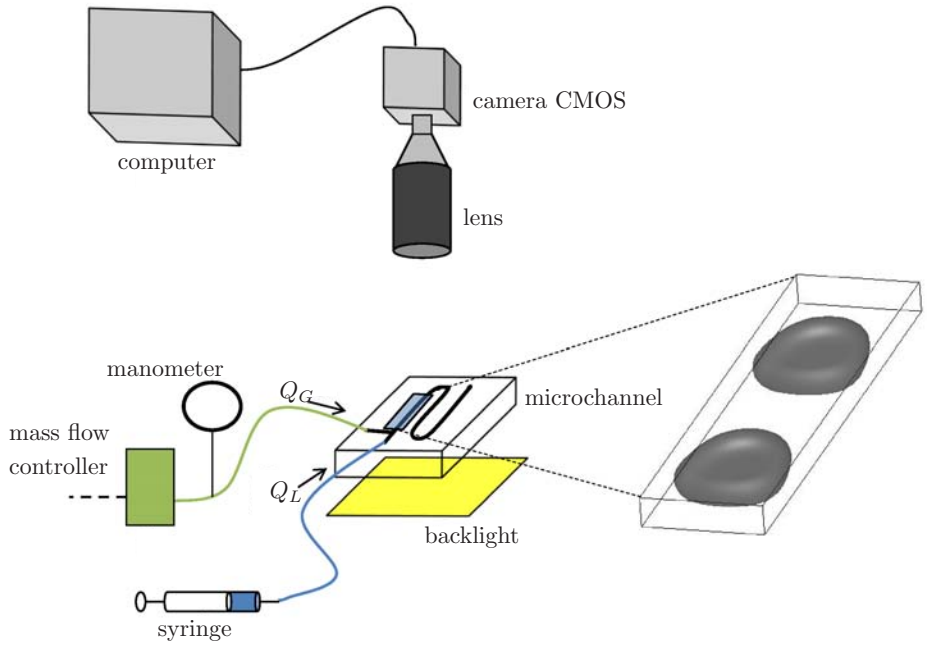

Figure 1.9: Schematic representation of the image processing equipment and its integration in the experimental set-up.

The shutter time has been set according to two criteria:

- firstly, it must be short enough to visualize a sharp gas-liquid interface. If the bubble moves more than a few pixels whilst the shutter is open, the interface is diffuse on the images and it becomes difficult to accurately detect the position of the bubble caps and thus the bubble lengths,

- secondly, it must be chosen such that enough light is provided during the exposure time.

A backlight (*Rosco LitePad*) that is made of a LED panel of dimensions $76.2 \times 152.4\ mm^2$ and of intensity $0.5A$ is placed underneath the channel. This backlight is used to provide enough light throughout the exposure time, which has been set to $t_{shutter} = 100\,\mu s$ in the experiments so that bubbles do not cross more than 2 pixels during this period. In extreme cases, which only concern two sets of experiments out of approximately 40 in each geometry, the bubbles may cross up to 5 pixels during the exposure time.

Image sequences were recorded in order to get a representative sample of bubbles passing through the observation window and to identify the existence of unsteady flow, which is mainly characterized by a significant deviation in the bubble lengths. Bubble and slug lengths were evaluated with image processing software that is detailed in the next section 1.3. Every bubble that enters the observation window is analysed and the final lengths are an average of approximately 100 bubbles. The frame rate was adjusted in each experiment in order to record around 100 different bubbles in the sequence of 1024 images. In these sequences, the bubble generation process was recorded in only about 10 frames. In order to gain insight on the mechanism of bubble formation and record the different steps of the bubble break-up process with better accuracy, the frame rate was therefore increased in some experiments. The bubble velocities were evaluated by determining the time required for gas-liquid interface to travel between the entrance and the exit of the observation window and averaged arithmetically for approximately 100 bubbles.

The equipment and settings used for the sequence acquisition are summarized in table 1.4.

camera	*Mikrotron EoSens MC-1362*
lens	*Sigma DG macro 105 mm*
working distance	$17cm$
resolution	$1280pix \times 200pix$
field dimensions	$27.92mm \times 4.36mm$
definition	$45.84pix/mm$
frame rate $(-)$	$10 - 2500fps$ $\sim 10 \times f_B$
shutter time	$100\mu s$
opening	$f/2.8$
backlight dimension	$76.2 \times 152.4mm^2$
backlight intensity	$0.5A$

Table 1.4: Camera, lens and backlight settings used for the shadow-casting visualisations.

1.3 Image processing

The aim of the experiments based on shadow-casting is to characterize the bubble and slug sizes, the bubble break-up frequencies and the bubble velocities under different operating conditions. For this purpose, the processing of the image sequences is performed with the commercial software *MATLAB*. The image processing comprises two main steps:

- the bubble detection that allows to determine its shape, size and position,
- the tracking of the bubbles in order to evaluate their velocities.

These are described in sections 1.3.1 and 1.3.2.

1.3.1 Bubble detection

The sequences recorded with the camera comprise 1024 images with a resolution 1280×200 pixels. The images are encoded on 16 bits in gray levels and are saved with a TIFF format. An image processing software using *MATLAB* functions has been implemented to detect the interface of the bubbles and track them during the sequence. Figure 1.10 shows the main steps of in the image processing routine:

- (a)-(b): raw images are normalized with a reference image of the background without bubbles to remove noise, the contrast is enhanced and a filtering procedure is applied to smooth the contours,
- (b)-(c): the gray level gradient intensity is calculated after filling the objects so that the magnitude of the gradient is maximum at the outer front of the interface,
- (c)-(d): a threshold on the gradient intensity is used to detect interfacial pixels and the objects detected are then filled in order to determine the cross-sectional area of the bubble.

In addition, it is generally not too difficult to identify the bubbles. Three criteria are set to remove noisy objects:

- the position of the bubbles: the vertical coordinate of the center of mass can be restricted to a region of a few pixels around the centerline,
- the bubble size: this work focuses on Taylor bubbles whose sizes are generally greater than the channel width,
- the orientation of the bubbles: they are generally confined such that the major axis of the bubbles are oriented horizontally.

These criteria allow identification of whether the objects detected in the first step of the image processing routine are noisy objects or actual bubbles. It should be mentioned that the threshold of the criteria were adapted when dealing with slug flow where small bubbles were generated.

From the final binary images (figure 1.10(d)), it is possible to extract the characteristics of each bubble: the position, the shape, the orientation, the length and the area which are processed to identify the bubbles and track them.

Figure 1.11 shows the variations in size of 7 different bubbles along the length of the observation window. Only 7 bubbles are shown but the lengths of the 200 bubbles

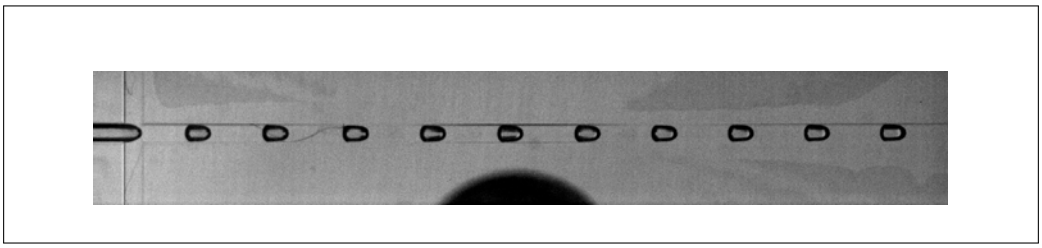

(a) Raw image

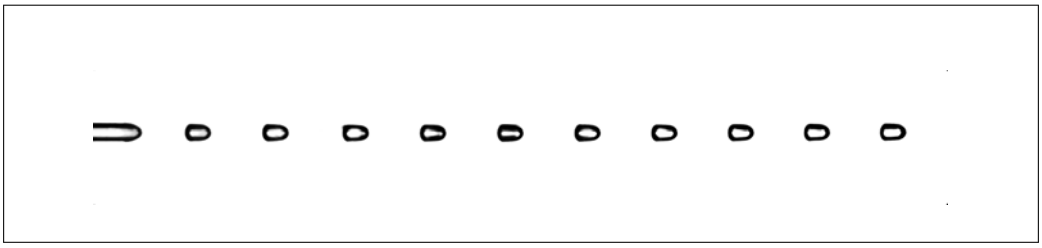

(b) Normalized image with contrast enhancement

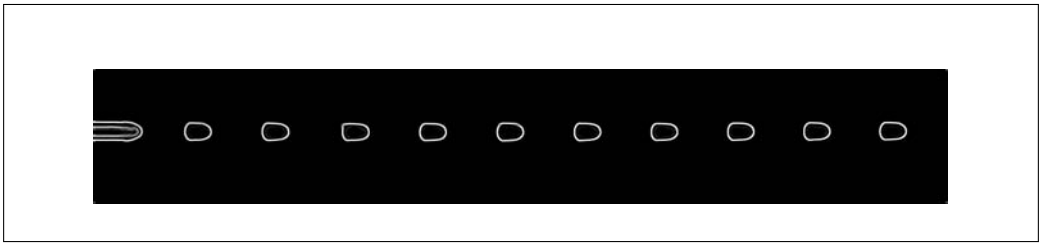

(c) Gradient intensity

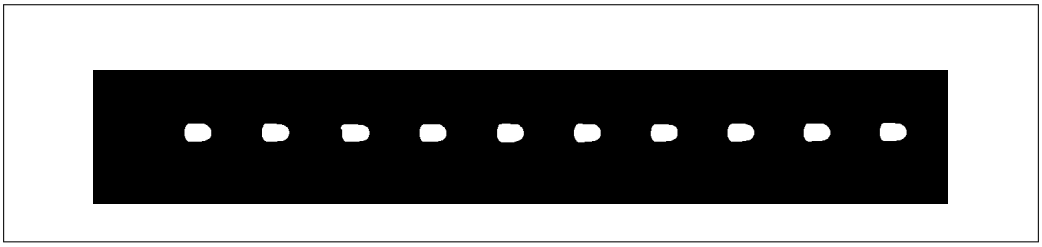

(d) Bubbles detected (binary images)

Figure 1.10: Illustration of the main steps in the processing of raw images to binary images with the detected bubbles
Operating conditions : glycerol 60% (vol.) in ethanol and air in a square microchannel with a cross-junction ($Q_L = 0.8mL/min$ and $Q_G = 0.4mL/min$).

of the sequence were estimated within the same range. The detection of the bubbles is very efficient and it is seen in figure 1.11 that along the channel, the bubble length varies between $0.85^{\pm}0.02mm$, which corresponds to fluctutations of $^{\pm}1$ pixel. This also shows that the depth of the channel is constant since there is no elongation or compression of the bubble that would result from the convergence or divergence of the channel cross-section.

1.3.2 Bubble velocity

The tracking of the bubbles is made easier by the characteristics of the flow, which is unidirectional. In addition, as previously detailed in section 1.2, the frame rate has been set so that approximately 10 frames are recorded during the time needed for a

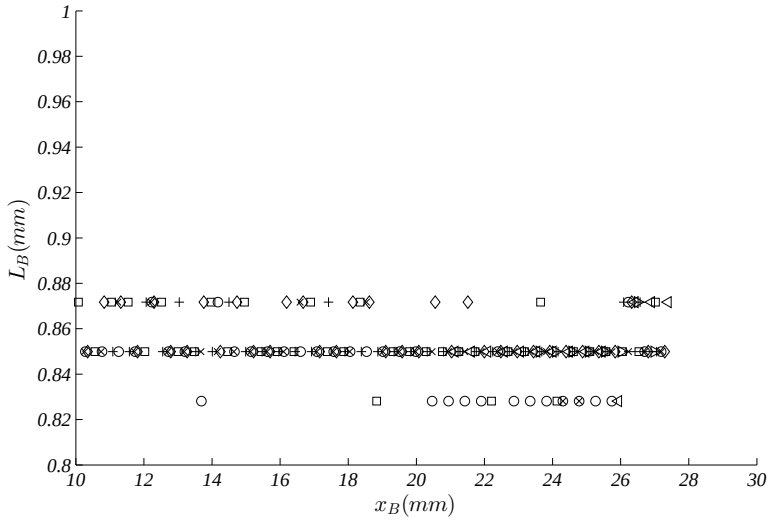

Figure 1.11: Bubble lengths $L_B(mm)$ as a function of their position along the channel. Each symbol ($\bigcirc$,$\square$,$\Diamond$,$\triangleright$,$\triangleleft$,+,$\times$) represents a different bubble. Operating conditions: glycerol 60% (vol.) in ethanol and air in a square microchannel with a cross-junction ($Q_L = 0.8mL/min$ and $Q_G = 0.4mL/min$).

bubble to detach from the contacting section. In other words, the frame rate is about ten times the frequency of break-up. This means that between two consecutive frames, a bubble will move from approximately one tenth of the distance that separates two bubbles which renders the tracking straightforward. Indeed, a bubble at a position x_B^t will be identified in the next frame as the nearest one within the range of bubbles whose positions x_B^{t+dt} are greater than x_B^t. The tracking of the bubbles is shown in figure 1.12 where each bubble is assigned a different color with respect to the assigned number.

Figure 1.13 shows the position of bubbles as a function of the time. Each diagonal set of points corresponds to a different bubble. The bubble velocity can be calculated at each position by differenciating the positions between two consecutive time steps. However, as the bubble position evolves linearly with time since the bubble velocity is very regular, the velocity is deduced by fitting each set of points with a first order polynomial as it is shown in figure 1.13. In addition, it has been said that Taylor flow allows the generation of regular bubbles with uniform velocities. It is seen in figure 1.13 that the set of points are parallel, which means that all the bubbles move with the same velocity.

1.3.3 Flow regularity

The regularity of the Taylor bubble flow is illustrated in figure 1.14, which presents the length of each bubble thoughout a sequence that comprises approximately 200 bubbles in glycerol 60% (vol.) in ethanol flowing in a square microchannel. Gas and liquid flow rates are $Q_L = 0.8mL/min$ and $Q_G = 0.4mL/min$, respectively, and they merge in a cross-junction. It is seen that the bubble lengths lie within less than 5% for the entire sequence.

Similar results are found for the velocity where fluctutations of about 2% are observed. This confirms the high regularity of Taylor flows and the flatness of the channels.

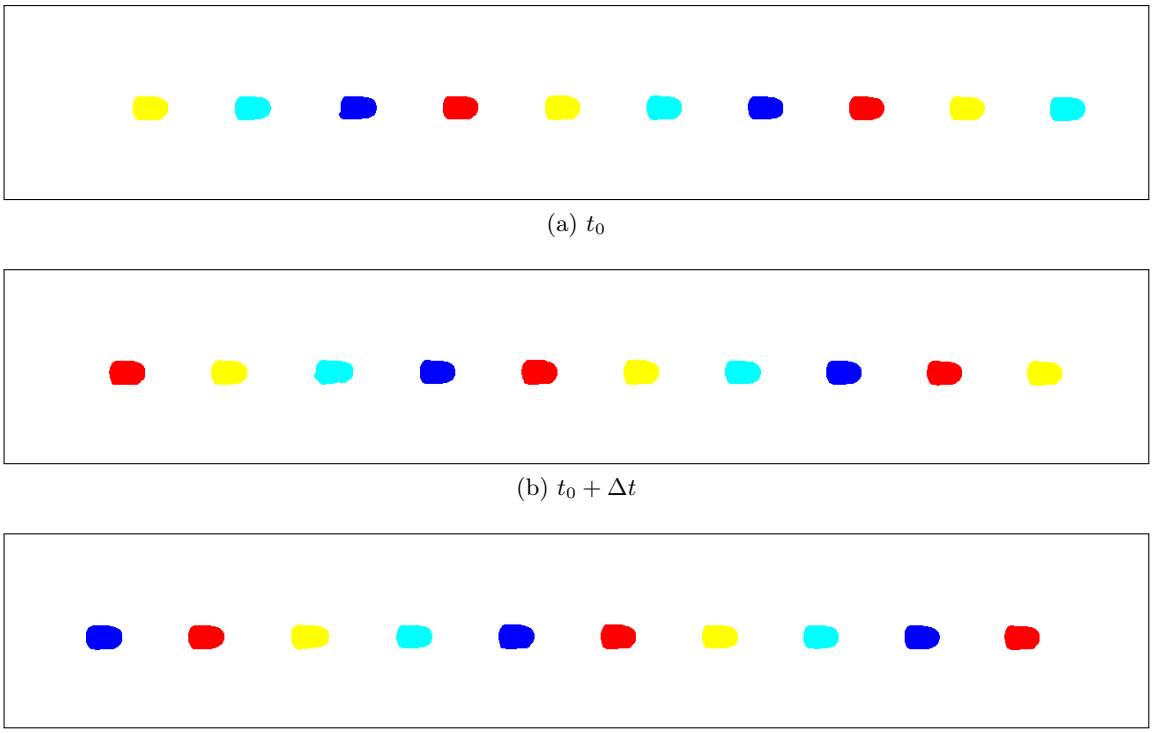

(a) t_0

(b) $t_0 + \Delta t$

(c) $t_0 + 2\Delta t$

Figure 1.12: Position of the color-coded bubbles with respect to the assigned bubble number at different times.
Operating conditions: glycerol 60% (vol.) in ethanol in a square microchannel with a cross-junction ($Q_L = 0.8mL/min$ and $Q_G = 0.4mL/min$).

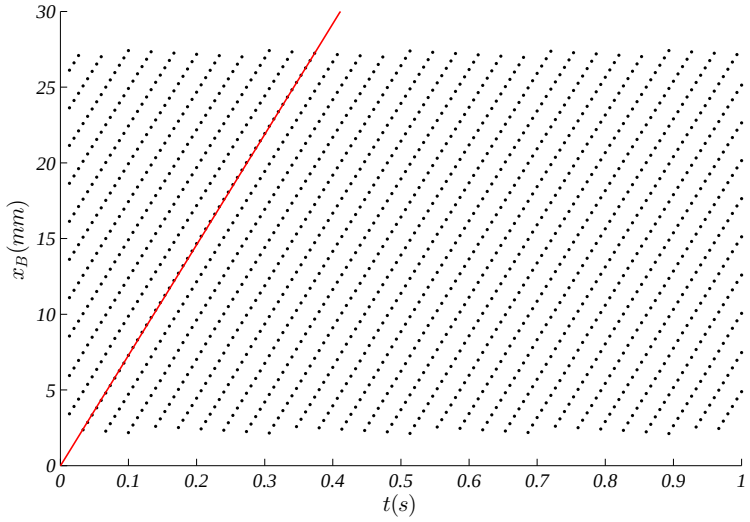

Figure 1.13: Position of the center of mass of each bubble as a function of the time.
Operating conditions: glycerol 60% (vol.) in ethanol and air in the square microchannel with a cross-junction ($Q_L = 0.8mL/min$ and $Q_G = 0.4mL/min$). Legend: (·) experimental data; (red line) example of experimental fit.

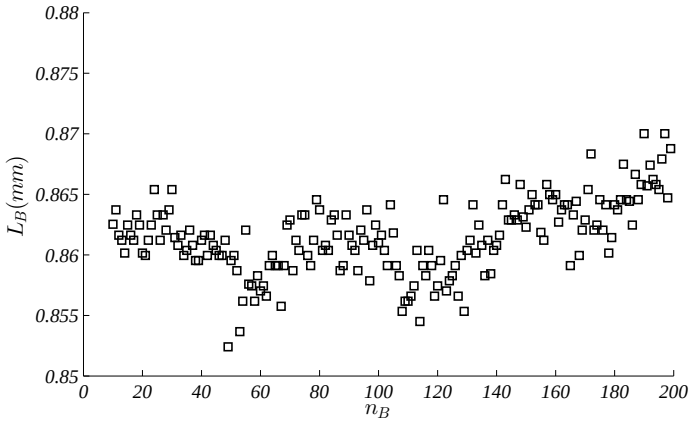

Figure 1.14: Bubble lengths $L_B(mm)$ as a function of their assigned bubble number. Operating conditions: glycerol 60% (vol.) in ethanol and air in a square microchannel with a cross-junction ($Q_L = 0.8mL/min$ and $Q_G = 0.4mL/min$).

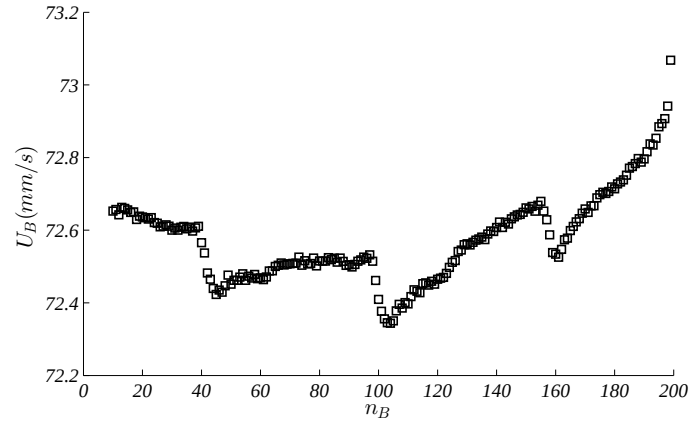

Figure 1.15: Bubble velocities $U_B(mm)$ as a function of their index.
Operating conditions: glycerol 60% (vol.) in ethanol and air in a square microchannel with a cross-junction ($Q_L = 0.8mL/min$ and $Q_G = 0.4mL/min$).

1.4 Summary

Microchannels have been designed to study gas-liquid dispersion through experimental visualizations. Special care has been taken to ensure the flatness of the PMMA plates as well as the uniformity of the cross-section along the channel. The regularity of bubble length and velocity throughout a sequence confirms that the flow control equipment delivers continuous flow rates. The image proccessing software allows to detect bubbles with a good accuracy. Indeed, the bubble lengths are captured with an error of approximately $^{\pm}1$ pixel.

Chapter 2

Numerical code *JADIM-VOF*

Contents

2.1 Numerical techniques for multiphase flows with deformable interface

Numerical simulations of industrial processes, as well as fundamental problems often involve two immiscible fluids. While numerical simulations of two-phase flows were possible 20 years ago, a number of computational methods have been developed over the past decade to improve the computation of multiphase flows. The numerical methods to simulate multiphase flows can be classified into two main groups : the "Lagrangian" methods and the "Eulerian" methods. This chapter briefly presents the different numerical techniques to simulate multiphase flows. The *JADIM* code that is developed at IMFT is then presented and the methods developed during this study will be given in chapter 3.

2.1.1 Lagrangian methods

Moving grids

Within lagrangian methods, the interface can be tracked explicitly and used as a boundary of the moving mesh. It has been used for example to simulate bubble oscillations with the *JADIM* code by Blanco [1995] (figure 2.1(a)). Although these methods are very accurate since there is no approximation of the interface shape and filtering of capillary forces, they suffer from two main drawbacks: the flow in the gas phase is not simulated and thereby limiting these methods to cases where the gas phase has no effect on the interface shape and as the interface moves. In addition, the computational domain needs to remeshed at every time step, which is computationally very expensive.

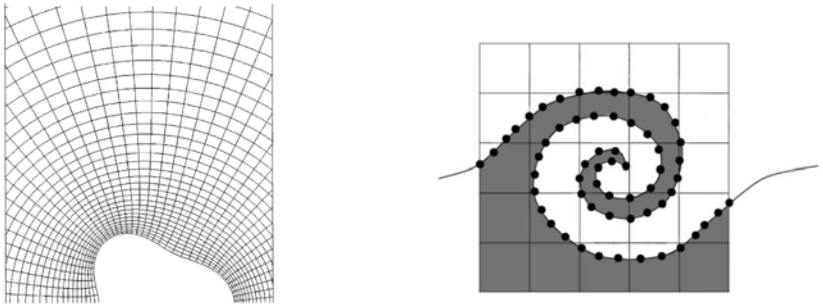

(a) (b)

Figure 2.1: Examples of lagrangian computational methods: (a) moving grid from Blanco [1995] and (b) schematic illustration of front-tracking technique (image from Scadovelli and Zaleski [1999]).

Marker and cell (MAC)

Another approach based on a lagrangian representation of the multiphase flow is to track the interface using lagrangian markers. In Harlow and Welch [1965], the localization of the interface was deduced from volume markers that were placed in one phase. However, the accurate location of the interface is not explicit and requires many markers to be precise, which is also computationally expensive. More recently, Enright et al. [2002] used volume markers coupled to a Level Set function to combine the accurate representation of the interface provided by the Level Set function and the

good representation of the interface in under-resolved regions thanks to the lagrangian particles. This hybrid method allows to decrease volume conservation errors which are inherent to Level Set methods in such under-resolved regions.

Front-tracking

To reduce the computational time required by volume markers, surface markers were introduced by Unverdi and Tryggvason [1992] (a schematic illustration is given in figure 2.1(b)). In addition, the interface is explicitly tracked and the calculation of geometrical properties (the normal of the interface and the curvature) exhibits a high accuracy. Accurate numerical simulations of bubble free rise, bubble coalescence and collision were performed. However, the implementation of such methods in 3D is not straightforward and specific algorithms are required to deal with the distribution of markers, as well as changes in topology. Popinet and Zaleski [1999] also used a front-tracking method for the simulation of surface tension dominated flows, they showed that the front-tracking method coupled to a pressure correction to take into account the capillary pressure jump at the interface, allowed to give an accurate representation of the interface and the surface tension contribution. More recently, improvements have been made using front-tracking without connectivity (Torres and Brackbill [2000], Shin and Juric [2002]).

2.1.2 Eulerian methods

The second group uses an implicit representation of the phases in each cell with an additional scalar field. The most common approaches are the Volume of Fluid (VOF) methods (Hirt and Nichols [1981], Lafaurie et al. [1994], Bonometti and Magnaudet [2007], Dupont and Legendre [2010]) and the Level Set (LS) methods (Sussman et al. [1994, 1997], Herrman [2008], Tanguy and Berlemont [2005]). VOF methods are generally well adapted to conserve the mass of the phases and appear to be a natural choice in a finite volume framework, while LS methods are known to allow better computation of the geometrical properties of the interface. Eulerian methods have been shown to be well adapted to deal with various configurations, including single bubble rising in a liquid (Bonometti and Magnaudet [2007]), jet or drop breakup (Popinet [2009], Renardy and Renardy [2002]), coalescence (Tanguy and Berlemont [2005]), atomization with a number of inclusions of different sizes (Fuster et al. [2009]), drop spreading (Legendre and Maglio [2013]).

Within this Eulerian representation of two-phase flow, great effort has been dedicated to two main features: the transport of the interface and the consideration of capillary forces.

Volume of Fluid (VOF)

The VOF method is based on an indicator function that is $\chi(\mathbf{x}, t) = 1$ in one fluid and $\chi(\mathbf{x}, t) = 0$ in the other. In each computational cell, a volume fraction of one phase can then be deduced by intergrating this indicator function in the cell:

$$C = \int_V \chi(\mathbf{x}, t) dV \ .$$

Thus, the volume fraction is $C = 1$ in cells filled with fluid 1, $C = 0$ in cells filled with fluid 2 and it takes intermediate values in cells that are cut by the interface. A representation of the volume fraction in a computational domain is given in figure 2.2.

The position of each phase is then available through their volume fraction in each cell. An additional advection equation needs to be solved at each time step in order

to determine the position of the interface. In a finite volume framework, the VOF formulation appears to be a natural choice and the use of a conservative scheme allows the mass conservation of each fluid. Different approaches have been developed for the interface transport: VOF with geometrical reconstruction of the interface and VOF without reconstruction.

VOF with interface reconstruction - Piecewise Linear Interface Calculation (PLIC)

The transport equation can be solved after a reconstruction step where the interface is approximated in each cell as a segment in 2D or a plane in 3D. Several reconstruction techniques have been developed (see Scadovelli and Zaleski [1999], Rudman [1997] for more details) and the most common approach is the PLIC method (Lafaurie et al. [1994], Gueyffier et al. [1999], Lopez and Hernandez [2008]). The segments or planes are evaluated from the normal to the interface and the volume fraction in each cell. Once reconstructed, the interface is advected either by calculating the volume advected or by transporting the extremities of the segment in a lagrangian way. This method is very efficient for keeping a sharp interface and for conserving the mass. However, the reconstruction step is not straightforward in three dimensions. Indeed, many logical tests are required to cover the wide range of possible geometrical configurations which depend on the normal to the interface and the volume fraction.

It is interesting to mention the reconstruction method proposed by Renardy and Renardy [2002] who obtained nice results about spurious currents. A Parabolic Reconstruction of Surface Tension force (PROST), which is based on a quadratic representation of the interface, was proposed together with an optimal fit for the interface curvature whose computational cost is very expensive.

VOF without reconstruction

Another class of methods consists in solving the hyperbolic equation in an implicit way thanks to adapted schemes. The most common schemes used are Flux Corrected Transport schemes (Zalesak [1979]), Total Variational Diminishing schemes, and Weighted Essentially Non Oscillatory schemes. However, while these schemes can conserve the mass of the fluids, if well implemented, and avoid dispersion by keeping the volume fraction between $0 < C < 1$, the diffusion of the interface over a numerical thickness of a few cells remains difficult to control despite recent improvements (Bonometti and Magnaudet [2007]).

Whatever the VOF method used, the sharp variations of the volume fraction induce major difficulties for calculating its gradients and the geometrical properties of the interface.

Level Set (LS)

Due to the difficulty to keep a sharp interface in VOF methods and the inaccuracies in the geometrical description of the interface, Level Set methods that are based on a continuous distance function to the interface have been developed. The Level Set function ϕ is negative in one fluid and positive in the other, while the interface is located with the iso-value $\phi = 0$. The use of a scalar field that varies smoothly allows an accurate calculation of its gradients. In addition, the Level Set function is corrected at each time step so that it is as close as possible to a distance function with the magnitude of the gradient being equal to 1. However, the Level Set methods are known to suffer from mass conservation problems.

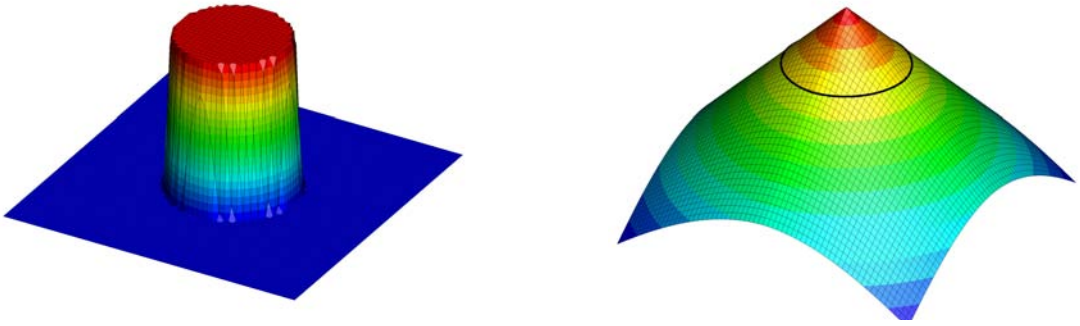

(a) Volume of Fluid (b) Level Set

Figure 2.2: Illustration of (a) the volume fraction field in a VOF framework (b) the distance function in a LS framework.

Other methods

Other methods can be found in the literature such as Lattice-Boltzmann methods and Phase-Field methods (Jacqmin [1999], Jamet et al. [2002]). All the methods presented have their own advantages and drawbacks. To overcome the limitations, a number of methods have considered coupling two of these methods. We can cite in particular the coupling between Level Set and VOF CLSVOF (Sussman and Puckett [2000]), and the coupling between Level Set and Lagrangian techniques (Enright et al. [2002]).

2.2 The *JADIM* code - VOF version

2.2.1 One fluid formulation

The numerical code used for this study is the *JADIM* code, which has been developed at IMFT. Computational methods have been implemented to simulate dispersed two-phase flows, including lagrangian particles (Climent [1996]), hydrodynamics and transfer phenomena around spherical bubbles (Legendre [1996]) and deformable interfaces with a VOF technique (Benkenida [1999]). These methods, and in particular the VOF module for computing moving interfaces on a fixed grid, have been validated and used to simulate various multiphase flows systems Benkenida [1999], Bonometti and Magnaudet [2007], Dupont and Legendre [2010], Legendre and Maglio [2013], Abadie et al. [2012]. The interface is captured by an Eulerian description of each phase on a fixed grid with variable density and viscosity. Under the assumptions that (i) the fluids are Newtonian and incompressible, (ii) there is no mass transfer at the interface, (iii) the flow is isothermal and (iv) the surface tension is constant, the fluid flow can be described by the classical one fluid formulation of the Navier-Stokes equations:

$$\nabla \cdot \mathbf{U} = 0 \tag{2.1}$$

$$\frac{\partial \mathbf{U}}{\partial t} + (\mathbf{U} \cdot \nabla)\,\mathbf{U} = -\frac{1}{\rho}\nabla P + \frac{1}{\rho}\nabla \cdot \mathbf{\Sigma} + \mathbf{g} + \mathbf{F}_{\sigma,\mathbf{s}} \tag{2.2}$$

where $\mathbf{\Sigma}$ is the viscous stress tensor, $\mathbf{g}$ is the acceleration due to gravity, and ρ and μ are the local density and dynamic viscosity, respectively. $\mathbf{F}_{\sigma,\mathbf{s}}$ is the capillary contribution and its calculation is described in section 2.2.2. The accurate representation of

capillary effects is of major importance in the numerical simulations of Taylor flow in microchannels that are dominated by surface tension effects.

ρ and μ are the local density and dynamic viscosity, which are deduced from the volume fraction C of one phase by a linear interpolation:

$$\rho = C\,\rho_1 + (1 - C)\,\rho_2 \tag{2.3}$$
$$\mu = C\,\mu_1 + (1 - C)\,\mu_2 \tag{2.4}$$

where the volume fraction is $C = 1$ (resp. $C = 0$) in cells filled with fluid 1 (resp. fluid 2) and $0 < C < 1$ in cells cut by the interface. The density is effectively an extensive property so that equation 2.3 can be applied. However, this is not the case of the viscosity and another model that consists in using an harmonic interpolation instead of a linear interpolation to ensure the continuity of the shear stresses at the interface is discussed in Bonometti [2005]. In the cases studied in the following, no differences have been observed and equation 2.4 has been used.

An additional transport equation for the volume fraction is solved to capture the interface between the two phases:

$$\frac{\partial C}{\partial t} + \mathbf{U} \cdot \nabla C = 0 \tag{2.5}$$

2.2.2 Spatial discretization

Equations 2.1, 2.2 and 2.5 are discretized on a staggered grid using a finite volume method, spatial derivatives being approximated using second-order centered schemes (Magnaudet et al. [1995]). Each variable has its own control volume of integration. The positions and the control volumes are illustrated in figure 2.3 in 2D. The extension to the third dimension is straightforward.

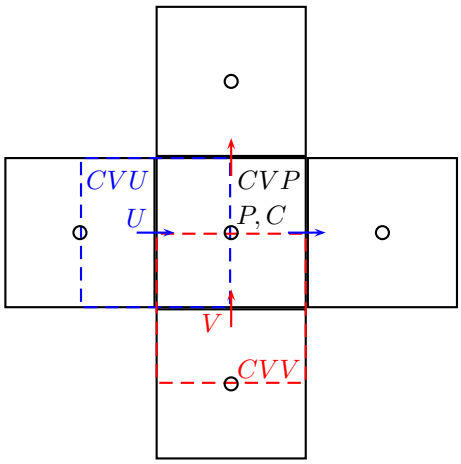

Figure 2.3: Staggered grid in 2D with the positions of the pressure P, the volume fraction C, and the velocity variables U and V on the west and south faces of the cell. The corresponding control volumes are denoted CVP , CVU and CVV.

Surface tension force - VOF Classic Continuum Surface Force

The one-fluid formulation of the Navier-Stokes equations involve an additional source term when compared with single-phase equations, that corresponds to the capillary force at the interface:

$$\mathbf{F}_{\sigma,\mathbf{s}} = -\sigma/\rho\,(\nabla\cdot\mathbf{n})\;\mathbf{n}\delta_I \tag{2.6}$$

where σ is the surface tension, $\mathbf{n}$ the normal to the interface and δ_I is the dirac distribution localizing the interface. The numerical method used to solve the interfacial force is the Continuum Surface Force (CSF) proposed by Brackbill et al. [1992]. From an Eulerian representation involving a scalar function, the geometrical properties of the interface can be calculated from the successive derivatives of the scalar function.

$$\mathbf{n}\,\delta_I = \nabla C \tag{2.7}$$

$$\kappa = \nabla\cdot\left(\frac{\nabla C}{||\nabla C||}\right) \tag{2.8}$$

The surface force $\mathbf{F}_{\sigma,\mathbf{s}}$ is then transformed into a volume force $\mathbf{F}_{\sigma,\mathbf{v}}$ by distributing its effects over grid points in the vicinity of the interface in a region that is a few cells thick through a non-zero gradient of the volume fraction:

$$\mathbf{F}_{\sigma,\mathbf{v}} = -\frac{\sigma}{\rho}\nabla\cdot\left(\frac{\nabla C}{||\nabla C||}\right)\nabla C. \tag{2.9}$$

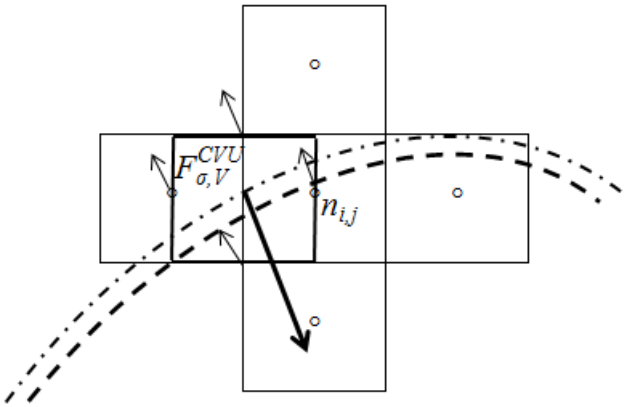

Figure 2.4: Schematic representation of the capillary force with a Continuum Surface Force model on staggered grids.

In *JADIM*, the curvature is calculated at the center of the staggered control volume as illustrated in figure 2.4 and the divergence of the unit normal to the interface is calculated in a conservative way Benkenida [1999]:

$$\mathbf{F}_{\sigma,\mathbf{v}} = \frac{-\sigma}{\overline{\rho}V}\int_V \nabla\cdot\left(\frac{\nabla C}{\|\nabla C\|}\right)\nabla C dV \tag{2.10}$$

$$\approx \frac{-\sigma}{\overline{\rho}V}\overline{\nabla C}\int_V \nabla\cdot\left(\frac{\nabla C}{\|\nabla C\|}\right)dV \tag{2.11}$$

$$= \frac{-\sigma}{\overline{\rho}V}\overline{\nabla C}\int_{\partial S}\left(\frac{\nabla C}{\|\nabla C\|}\right)\cdot\mathbf{n_{cell}}dS \tag{2.12}$$

where $\overline{\nabla C}$ is the average value of ∇C in the staggered control volume and $\overline{\rho} = (\rho_1 + \rho_2)/2$ is the mean density since it has been shown to decrease the intensity of spurious currents (Brackbill et al. [1992]).

Since the volume fraction varies from 0 to 1 over a thickness of 2 to 3 cells, it has been shown that a smoothing procedure allows a decrease in the errors due to the discretization of the gradient and divergence operators (Dupont and Legendre [2010]). For a 2D geometry $\widehat{C}$ is the smoothed volume fraction as proposed by Brackbill et al. [1992] to decrease these unphysical spurious currents :

$$\widehat{C}^k_{i,j} = \frac{3}{4}\widehat{C}^{k-1}_{i,j} + \frac{1}{16}\left(\widehat{C}^{k-1}_{i+1,j} + \widehat{C}^{k-1}_{i-1,j} + \widehat{C}^{k-1}_{i,j+1} + \widehat{C}^{k-1}_{i,j-1}\right) \tag{2.13}$$

where k is the number of iterations used to smooth the volume fraction. The smoothing of the volume fraction for the calculation of the curvature and the localization of the interface can be uncoupled. Indeed, the smoothing of volume fraction allows minimization of the variations in the curvature of the interface, used to calculate the capillary pressure jump while it is better to keep a sharp capillary force. In chapter 4, the smoothing step involves 12 and 6 iterations to calculate the curvature and the normal (localization and orientation of the force), respectively, as recommended in (Dupont and Legendre [2010]). In chapter 6, the smoothing step has been reduced to 8 and 4 iterations to avoid spreading of the capillary force throughout the liquid film.

2.2.3 Temporal discretization

The time scheme used to compute the advective terms in the Navier-Stokes equations is a third-order Runge-Kutta type scheme, while viscous stresses are solved using a semi-implicit Crank-Nicolson method. The incompressibility is ensured with a projection method, which consists in splitting the velocity field into two contributions: a rotational one, which gives a predicted velocity field calculated semi-implicitly, and a potential one, obtained from a pressure correction solution of a pseudo-Poisson equation, whose divergence is zero. Since the viscosity contribution is calculated implicitly, the constraining criterium on the time step due to viscosity is avoided. The capillary force introduces an additional time step constraint that is based on an advective time step where the velocity would be the maximum veloctiy of a capillary wave (Brackbill et al. [1992]). The time step criteria are summarized in table 2.1. In capillary dominated flows, as mostly considered in this study, the limiting time step is given by the capillarity criteria.

gravitational effects	$\Delta t < \sqrt{\frac{\Delta x}{g}} \to +\infty$
advection	$\Delta t < \sqrt{3}\,\frac{\Delta x}{U}$
viscosity	$\Delta t < \frac{\Delta x^2}{\nu} \to +\infty$ *(implicit)*
capillarity	$\Delta t < \sqrt{\frac{(\rho_1 + \rho_2)\,\Delta x^3}{8\,\sigma}}$

Table 2.1: Time step constraints

To sum-up, the main steps in the time advancement in the calculation of the velocity and pressure fields are:

1. update for the color function C: calculation of ρ^{n+1} and μ^{n+1} solving equation 2.5.

2. momentum semi-implicit resolution: a third order Runge-Kutta type scheme is used for the time advancement. Advective and body terms are calculated explicitly, while viscous terms are calculated using a semi-implicit Crank-Nicolson algorithm. This results in the calculation of the predicted velocity field $\mathbf{U}^*$ comprising the vorticity of $\mathbf{U^{n+1}}$.

3. capillary contribution: a second predicted velocity field $\mathbf{U}^{**}$ is computed from $\mathbf{U}^*$ and $\mathbf{F}_{\sigma,\mathbf{v}}$ (eq. 4.1) with C defined in equation 2.13.

4. projection step: pressure field P^{n+1} is computed solving a pseudo-Poisson equation from $\mathbf{U}^{**}$ and $\mathbf{U^{n+1}}$ is calculated (divergence free) with a projection method.

2.2.4 Volume fraction transport: the Flux Corrected Transport scheme

In the *JADIM* code, the location and thickness of the interface are both controlled by an accurate algorithm based on Flux-Corrected Transport (FCT) schemes (Zalesak [1979], Bonometti and Magnaudet [2007]). The transport equation 2.14 can be written as:

$$\frac{\partial C}{\partial t} + \nabla \cdot (C\mathbf{U}) = C \nabla \cdot \mathbf{U} \ . \tag{2.14}$$

While the incompressibility ensures $\nabla \cdot \mathbf{U} = 0$, the sheme is splitted direction by direction and the velocity field is not divergence free in each direction. Thus, as the volume fraction is not equal in every sub-step, the scheme is not explicitly conservative (Bonometti [2005]). In addition, due to the shear normal to the interface, a drawback of the methods without interface reconstruction is the non-physical spreading of the interface over a non negligible thickness of cells. To correct this excessive spreading of the interface, the velocity field is modified so that the volume fraction of all interfacial cells in the direction normal to the interface is advected with the velocity of the interface represented by the iso-contour $C = 0.5$. However, the modified velocity field is generally not divergence free and contributes to a gain or loss of mass of one of the phases. To solve this problem, an algorithm that redistributes mass in a global manner is used (Bonometti and Magnaudet [2007]) similarly to what can be done in LS methods by changing the contour representing the interface (Chang et al. [1996]). In the next chapter 3, this method is named VOF-FCT-0. It corresponds to the method developed in *JADIM* before this work.

Additional cut-off algorithm to the FCT scheme

While these modifications in the Flux Corrected Transport scheme significantly improve the interface transport (Bonometti and Magnaudet [2007]), the interface still spreads over more than 3 cells in certain cases, and notably for the simulation of Taylor bubbles. In addition, due to the slow establishment of the flow at Reynolds numbers of order of unity and also due to the constraint of stability induced by the capillary force (Brackbill et al. [1992]), these simulations promote this interface spreading since they often involve several hundreds thousands iterations. To avoid this unphysical spreading of the interface that leads to the diffuse variation of physical properties, as well as the pressure jump at the interface, a rough cut-off algorithm has been implemented and employed when necessary. This consists in imposing the volume fraction $C = 0$ (or $C = 1$) if the volume fraction takes an intermediate value and the interface does not cross the cell, thereby neglecting structures thinner than the dimension of the cell. This

results in local gains/losses of mass in the proximity of the interface and is therefore applied before the global redistribution of mass. The algorithm is given below in 2D and the extension in 3D is straightforward.

Cut-off algorithm
if $(0 < C_{i,j} < 1)$
if $\Big(C^-_{i-nc,j} > 0 \quad \& \quad C^-_{i+nc,j} > 0 \quad \& \quad C^-_{i,j-nc} > 0 \quad \& \quad C^-_{i,j+nc} > 0\Big)$
if $(C_{i,j} > 0.5) \quad C_{i,j} = 1$
if $(C_{i,j} < 0.5) \quad C_{i,j} = 0$

The notations used are $C^-_{i+k,j+l} = (C_{i,j} - 0.5) \times (C_{i+k,j+l} - 0.5)$ and nc is approximately half the permitted numerical thickness. In our cases, $nc = 1$ and 2 have been tested with the test presented in section 4.6. It has been found that the cut-off algorithm combined with the velocity extension and global mass redistribution do not significantly change the intensity of the spurious currents and the maximum velocity is slightly decreased with $nc = 2$. Thus, the FCT transport scheme with interface velocity extension, global mass redistribution and $nc = 2$ seems to be the best compromise between interface thickness and spurious currents.

In the following, this method is named VOF-FCT. The results obtained with this cut-off algorithm in the case of a disc in a rotating shear flow (Rider and Kothe [1998], Bonometti [2005], Tanguy [2004]) will be compared in the next chapter to the results obtained with the FCT scheme without this cut-off and finally with those obtained with the Level Set method.

2.3 Conclusion

The numerical schemes and methods available in the *JADIM* code before this work have been presented with a particular attention to the transport scheme and the balanced algorithm for the calculation of the surface tension force. Indeed, these two aspects of computation of multiphase flows will be a central part of the two next chapters. Although the described VOF method allows the simulation of various multiphase flow systems, we will show that it has some limitations. The implementation of a Level Set method is the topic of the next chapter 3 and the improved results brought by this method in the cases of interest for this study will be shown in the chapter 4.

Chapter 3

Implementation of a Level Set method *JADIM-LS*

Contents

3.1 Motivation

Taylor flow in microchannels is dominated by surface tension effects and therefore care needs to be taken in the calculation of the capillary force. Eulerian methods that are used to capture the interface are well-known to produce a non-physical vorticity in the vicinity of the interface and spurious currents develop. The intensity of these spurious currents can be prohibitive when dealing with surface tension driven flows. Within VOF formulations, the sharp variation of volume fraction across the interface does not allow the accurate calculation of the geometrical properties at the interface from the derivatives of the scalar field representing the interface. The Level Set method (Sussman et al. [1994], Chang et al. [1996]) involves a signed distance function instead of a volume fraction in each computational cell. This distance function allows the precise computation of geometrical properties (normal and curvature) of the interface. This precision is ensured by the smooth transition from one phase to the other and is enhanced when the Level Set function gradient magnitude is constant in the domain. An example of spurious currents in a VOF simulation of a static bubble is given in figure 3.1. The velocity should remain zero in the absence of gravity and the pressure in the bubble should obey the Laplace pressure jump. It is seen that spurious velocities are generated in the vicinity of the interface, while the Laplace pressure jump seems to be well estimated. This chapter present the Level Set method that has been implemented in *JADIM* during this work. We first describe the transport of the Level Set function and then, the calculation of the capillary force is given, with respect to the calculation of the capillary force in the VOF method presented in the previous chapter. The Level Set method has been developed in order to improve the calculation of flows at low capillary numbers. A detailed analysis of spurious currents will be provided in the next chapter which is dedicated to the evaluation of spurious currents and the comparison of different methods.

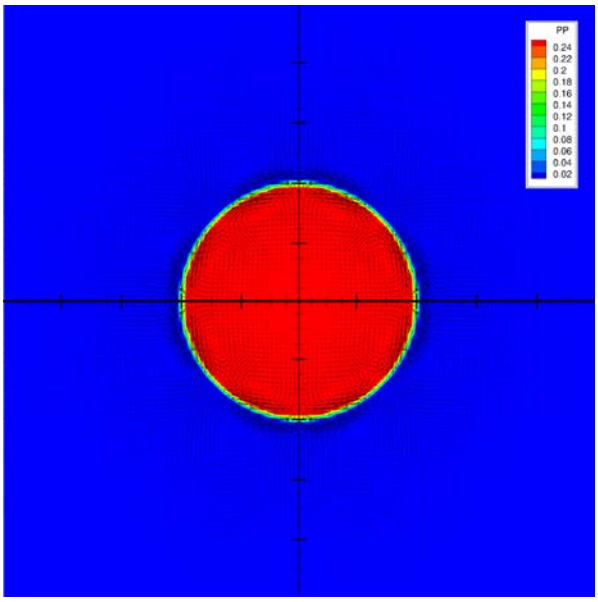

Figure 3.1: Spurious currents and pressure field in the case of a static bubble. The mesh resolution is $R_0/\Delta x = 12.8$, the bubble is placed at the center of the domain that is 2.5 times greater than the diameter of the bubble and no-slip boundary conditions are used. The Laplace number is $La = 12000$, the viscosities and densities of both phases are equal.

3.2 Advection of the Level Set function

3.2.1 Transport equation

The distance function obeys the same hyperbolic advection equation 2.5 as the VOF function, which can be written by replacing the volume fraction C by the distance function ϕ:

$$\frac{\partial \phi}{\partial t} + \mathbf{U} \cdot \nabla (\phi) = 0 \ . \tag{3.1}$$

In order to limit mass losses that are the major drawback of Level Set methods, the advective term is generally discretized with a high order scheme. The fifth order WENO scheme is widely used to solve the Level Set advection equation.

Using the fact that the velocity field is divergence free, equation 3.1 can be written as:

$$\frac{\partial \phi}{\partial t} + \nabla \cdot (\mathbf{U}\phi) = 0 \ . \tag{3.2}$$

In addition, using the conservative form of the transport equation, Couderc [2007] developed a conservative form of the fifth order WENO scheme following the idea of applying the coefficients of the WENO scheme on the Level Set function instead of on its gradients. This conservative formulation allows to take advantage of the finite volume by calculating fluxes crossing the faces of the control volume. Although the scheme is conservative, it should be kept in mind that it is the distance function that is conserved and not the volume fraction. Comparisons between different spatial and temporal discretization schemes can be found in Tanguy [2004] and for further details, the reader is referred to this work.

As the densities and viscosities of the fluids are calculated with the volume fraction of one phase as in the VOF formulation (equations 2.3 and 2.4), a volume fraction is approximated in each computational cell using a smooth Heaviside function as defined by equation 3.3.

$$C = H(\phi) = \begin{cases} 0 & \text{if } \phi < -\varepsilon \ , \\ 0.5\left(1 + \dfrac{\phi}{\varepsilon} + \dfrac{1}{\pi} sin\left(\dfrac{\pi\phi}{\varepsilon}\right)\right) & \text{if } |\phi| \leq \varepsilon \ , \\ 1 & \text{if } \phi > \varepsilon \ . \end{cases} \tag{3.3}$$

where $\varepsilon = \sqrt{2}\Delta x$ is half the numerical thickness of the interface.

Spatial discretization

Couderc [2007] and Tanguy [2004] have shown that the conservative fifth order WENO scheme (denoted WENO5c) generally performs better than the original WENO5 scheme and it notably allows better mass conservation after transport. This spatial scheme has then been chosen and the algorithm to calculate the fluxes is presented in this section for the x spatial direction with the indice i and the velocity u_i. The extension to the other directions is straightforward.

The discrete form of equation 3.2 is:

$$\left(\frac{\partial \phi}{\partial t}\right) + \frac{F_{i+\frac{1}{2}} - F_{i-\frac{1}{2}}}{\Delta x} = 0 \tag{3.4}$$

with F being the flux that crosses a face of the computational cell.

Using the upwind formulation, the flux across the cell can be written:

$$F_{i+\frac{1}{2}} = \begin{cases} u_{i+\frac{1}{2}} \overline{\phi}^{+}_{i-1} & \text{if } u_{i+\frac{1}{2}} > 0 \ , \\ u_{i+\frac{1}{2}} \overline{\phi}^{-}_{i} & \text{if } u_{i+\frac{1}{2}} < 0 \ . \end{cases} \tag{3.5}$$

By taking $\overline{\phi}^{+}_{i-1} = \phi_{i-1}$ and $\overline{\phi}^{-}_{i} = \phi_i$, a first order upwind scheme is recovered.

The high order WENO fluxes compute the values $\overline{\phi}^{\pm}_{i}$ as a weighting of the derivatives calculated with three stencils around the cell face of interest.

$$\overline{\phi}^{\pm}_{i} = \omega_0^{\pm} \, \phi_i^{\pm 0} \ + \ \omega_1^{\pm} \, \phi_i^{\pm 1} \ + \ \omega_2^{\pm} \, \phi_i^{\pm 2} \tag{3.6}$$

The $+$ or $-$ index refers to the preferred upwind direction to build the stencils on which the derivatives $\phi_i^{\pm 1,2,3}$ are calculated:

$$\begin{cases} \phi_{i+\frac{1}{2}}^{\pm 0} = & \frac{1}{3} r_1^{\pm} & - \frac{7}{6} r_2^{\pm} & + \frac{11}{6} r_3^{\pm} \\ \phi_{i+\frac{1}{2}}^{\pm 1} = & -\frac{1}{6} r_2^{\pm} & + \frac{5}{6} r_3^{\pm} & + \frac{1}{3} r_4^{\pm} \\ \phi_{i+\frac{1}{2}}^{\pm 2} = & \frac{1}{3} r_3^{\pm} & + \frac{5}{6} r_4^{\pm} & - \frac{1}{6} r_5^{\pm} \end{cases} \tag{3.7}$$

where $r^{\pm}$ are:

$$r_1^{-} = \overline{\phi}_{i-2} \quad , \quad r_2^{-} = \overline{\phi}_{i-1} \quad , \quad r_3^{-} = \overline{\phi}_{i} \quad , \quad r_4^{-} = \overline{\phi}_{i+1} \quad , \quad r_5^{-} = \overline{\phi}_{i+2} \tag{3.8}$$

$$r_1^{+} = \overline{\phi}_{i+3} \quad , \quad r_2^{+} = \overline{\phi}_{i+2} \quad , \quad r_3^{+} = \overline{\phi}_{i+1} \quad , \quad r_4^{+} = \overline{\phi}_{i} \quad , \quad r_5^{+} = \overline{\phi}_{i-1} \tag{3.9}$$

The weighting coefficients are calculated:

$$\begin{cases} \omega_0^{\pm} = & \dfrac{\alpha_0^{\pm}}{\alpha_0^{\pm} + \alpha_1^{\pm} + \alpha_2^{\pm}} \\ \omega_1^{\pm} = & \dfrac{\alpha_1^{\pm}}{\alpha_0^{\pm} + \alpha_1^{\pm} + \alpha_2^{\pm}} \\ \omega_2^{\pm} = & \dfrac{\alpha_2^{\pm}}{\alpha_0^{\pm} + \alpha_1^{\pm} + \alpha_2^{\pm}} \end{cases} \tag{3.10}$$

so that the sum $\omega_0^{\pm} + \omega_1^{\pm} + \omega_2^{\pm} = 1$ and with:

$$\begin{cases} \alpha_0^{\pm} = & \frac{1}{10} \left(\dfrac{1}{\epsilon + IS_0^{\pm}} \right)^2 \\ \alpha_1^{\pm} = & \frac{6}{10} \left(\dfrac{1}{\epsilon + IS_1^{\pm}} \right)^2 \\ \alpha_2^{\pm} = & \frac{3}{10} \left(\dfrac{1}{\epsilon + IS_2^{\pm}} \right)^2 . \end{cases} \tag{3.11}$$

In the simulations, ϵ is generally fixed at 10^{-6} to avoid dividing by zero. The $IS_{0,1,2}^{\pm}$

represent regularity indicators which are defined as:

$$\left\{\begin{array}{lll} IS_0^{\pm} &=& \frac{13}{12}\left(r_1^{\pm} - 2\,r_2^{\pm} + r_3^{\pm}\right)^2 + \frac{1}{4}\left(r_1^{\pm} - 4\,r_2^{\pm} + 3\,r_3^{\pm}\right)^2 \\ IS_1^{\pm} &=& \frac{13}{12}\left(r_2^{\pm} - 2\,r_3^{\pm} + r_4^{\pm}\right)^2 + \frac{1}{4}\left(r_2^{\pm} - r_4^{\pm}\right)^2 \\ IS_2^{\pm} &=& \frac{13}{12}\left(r_3^{\pm} - 2\,r_4^{\pm} + r_5^{\pm}\right)^2 + \frac{1}{4}\left(3\,r_3^{\pm} - 4\,r_4^{\pm} + r_5^{\pm}\right)^2 \end{array}\right. \tag{3.12}$$

Temporal discretization

Tanguy [2004] compared the efficiency of different time schemes and observed that an explicit Euler discretization is not sufficient and high order time schemes are required. The distance function ϕ is then advanced in time with a third order Runge-Kutta time scheme, which is written (with the notation $\frac{\partial \phi}{\partial t} = L(\phi)$):

$$\left\{\begin{array}{lll} \phi^1 = & \phi^n + & \Delta t\; L\left(\phi^n\right) \\ \phi^2 = & \frac{3}{4}\phi^n + & \frac{1}{4}\left(\phi^1 + \Delta t\; L\left(\phi^1\right)\right) \\ \phi^{n+1} = & \frac{1}{3}\phi^n + & \frac{2}{3}\left(\phi^2 + \Delta t\; L\left(\phi^2\right)\right) \end{array}\right. \tag{3.13}$$

3.2.2 Redistancing equation

Since the velocity normal to the interface is not constant, the distance function can be stretched or compressed when the Level Set function is transported. This results in a loss of accuracy when deriving the normal to the interface and the curvature. This is similar to the difficulty that arises within the VOF without reconstruction framework where the numerical thickness of the interface tends to be either sharpened or stretched during long simulations. Different methods are used in the literature to solve this problem either after the transport with a redistancing algorithm (Sussman et al. [1997]), the fast-marching method or directly in the advection step by extending the velocity field of the interface to the cells surrounding the surface. In *JADIM*, in order to keep the Level Set function as close as possible to a signed distance function, a redistancing procedure is applied using equation 3.14 (Sussman et al. [1997]):

$$\frac{\partial \widetilde{\phi}}{\partial \tau} + \mathrm{sgn}(\widetilde{\phi^0})\left(|\nabla \widetilde{\phi}| - 1\right) = 0\ , \tag{3.14}$$

where τ is a fictitious time used to reinitialize the Level Set function. ϕ is the temporary Level Set function during the iterative resolution of equation 3.14 with $\widetilde{\phi}^0 = \phi$ and $\widetilde{\phi}^{end} = \phi^{n+1}$. The sign function sgn is smoothed over the computational mesh:

$$\mathrm{sgn}\left(\widetilde{\phi}\right) = \left\{\begin{array}{ll} -1 & \text{if} \quad \phi < -\Delta x \\ \dfrac{\phi}{\sqrt{\phi^2 + \Delta x^2}} & \text{if} \quad |\phi| \leq \Delta x \\ 1 & \text{if} \quad \phi > \Delta x \end{array}\right. \tag{3.15}$$

Equation 3.14 can be written as:

$$\frac{\partial \widetilde{\phi}}{\partial \tau} + \left(\mathrm{sgn}\left(\phi\right)\frac{\nabla \widetilde{\phi}}{|\nabla \widetilde{\phi}|}\right) \cdot \nabla \widetilde{\phi} = \mathrm{sgn}(\phi) \tag{3.16}$$

This non-linear hyperbolic equation corresponds to the propagation of the characteristics from the iso-contour $\phi = 0$ in the direction normal to the interface with the speed

$\text{sgn}\left(\phi^0\right)\dfrac{\nabla\widetilde{\phi}}{|\nabla\widetilde{\phi}|}$. Thus, the points near the interface where the Level Set function needs to be as close as possible to a distance function will be reinitialized first. It should be mentioned that this redistancing equation converges towards the solution $|\nabla\widetilde{\phi}| = 1$ and the iso-contour $\phi = 0$ is supposed not to be moved.

The discrete form of equation 3.14 (in 2D) is:

$$\left(\frac{\partial\phi}{\partial t}\right) = \widehat{H}\left(D_x^+\phi_{i,j}\ ,\ D_x^-\phi_{i,j}\ ,\ D_y^+\phi_{i,j}\ ,\ D_y^-\phi_{i,j}\right) \tag{3.17}$$

where $\widehat{H}$ is the numerical Hamiltonian whose calculation is given in equation 3.21 and $D_x^+\phi_{i,j}$, $D_x^-\phi_{i,j}$, $D_y^+\phi_{i,j}$ and $D_y^-\phi_{i,j}$ are upwind and downwind spatial derivatives approximated with a WENO5 scheme whose algorithm is detailed below.

Spatial discretization

The algorithm for determining the high order spatial derivatives is given in one dimension for simplicity of the notations:

$$\begin{cases} \nu_k^- = \dfrac{\widetilde{\phi}_{i-2+k} - \widetilde{\phi}_{i-3+k}}{\Delta x} \\ \nu_k^+ = \dfrac{\widetilde{\phi}_{i+4-k} - \widetilde{\phi}_{i+3+k}}{\Delta x} \end{cases} \quad , \quad \text{with} \quad 1 < k < 5. \tag{3.18}$$

Similarly to the conservative WENO5 scheme, regularity indicators are introduced:

$$\begin{cases} IS_0^{\pm} = \dfrac{13}{12}\left(\nu_1^{\pm} - 2\,\nu_2^{\pm} + \nu_3^{\pm}\right)^2 + \dfrac{1}{4}\left(\nu_1^{\pm} - 4\,\nu_2^{\pm} + 3\,\nu_3^{\pm}\right)^2 \\ IS_1^{\pm} = \dfrac{13}{12}\left(\nu_2^{\pm} - 2\,\nu_3^{\pm} + \nu_4^{\pm}\right)^2 + \dfrac{1}{4}\left(\nu_2^{\pm} - \nu_4^{\pm}\right)^2 \\ IS_2^{\pm} = \dfrac{13}{12}\left(\nu_3^{\pm} - 2\,\nu_4^{\pm} + \nu_5^{\pm}\right)^2 + \dfrac{1}{4}\left(3\,\nu_3^{\pm} - 4\,\nu_4^{\pm} + \nu_5^{\pm}\right)^2 \end{cases} \tag{3.19}$$

The smoothness indicators $IS^{\pm}$ allow the weighting coefficients to be calculated with equations 3.10 and 3.11.

Finally, the spatial derivatives are written:

$$\begin{aligned} D_x^{\pm}\widetilde{\phi}_i &= \omega_0^{\pm}\left(\frac{\nu_1^{\pm}}{3} - \frac{7\nu_2^{\pm}}{6} + \frac{11\nu_3^{\pm}}{3}\right) \\ &+ \omega_1^{\pm}\left(-\frac{\nu_2^{\pm}}{6} - \frac{5\nu_3^{\pm}}{6} + \frac{\nu_4^{\pm}}{3}\right) \\ &+ \omega_2^{\pm}\left(\frac{\nu_3^{\pm}}{3} + \frac{5\nu_4^{\pm}}{6} - \frac{\nu_5^{\pm}}{6}\right) \end{aligned} \tag{3.20}$$

Once the upwind and downwind derivatives $D_{x,y}^{\pm}$ are known, the numerical Hamil-

tonian (equation 3.17) is calculated with a Godunov flux (Sussman et al. [1994]):

$$\widehat{H}\left(F_1,F_2,F_3,F_4\right)=\begin{cases}\operatorname{sgn}\left(\phi\right)\left(\sqrt{\max\left(\left(F_1\right)^-,\left(F_2\right)^+\right)^2+\max\left(\left(F_3\right)^-,\left(F_4\right)^+\right)^2}-1\right) & \\ \qquad\qquad\qquad\qquad\qquad\qquad\qquad\qquad \text{if} \quad \operatorname{sgn}(\phi)>0 & \\ \operatorname{sgn}\left(\phi\right)\left(\sqrt{\max\left(\left(F_1\right)^+,\left(F_2\right)^-\right)^2+\max\left(\left(F_3\right)^+,\left(F_4\right)^-\right)^2}-1\right) & \\ \qquad\qquad\qquad\qquad\qquad\qquad\qquad\qquad \text{if} \quad \operatorname{sgn}(\phi)<0 & \end{cases} \tag{3.21}$$

with F_k being the derivatives (for simplicity of notation) and the operators $()^+$ and $()^-$ are:

$$\begin{cases}\left(F_k\right)^-= & -\min\left(F_k,0\right)\\ \left(F_k\right)^+= & \max\left(F_k,0\right)\end{cases}, \quad \text{with} \quad 0<k<4. \tag{3.22}$$

Temporal discretization

The temporary Level Set function during the redistancing step is advanced in time with a third order Runge-Kutta scheme for the temporal discretization. Equation 3.16 indicates that the magnitude of the propagation speed of the characteristics is unity so the fictitious time step is chosen:

$$\Delta\tau=0.5\Delta x, \tag{3.23}$$

as recommended in Couderc [2007].

In addition, three iterations are generally enough to reinitialize the distance function (Tanguy [2004], Couderc [2007]).

3.2.3 Mass redistribution

The mass conservation is a major drawback of Level Set metods. Indeed, although the use of high order numerical schemes, as well as the use of a conservative WENO5 scheme in the transport equation have been shown to significantly improve the results, this remains a challenge within Level Set methods. A simple but efficient algorithm allows the mass to be conserved in a global manner by changing the contour representing the interface (Chang et al. [1996]). An iterative procedure is applied until the iso-contour around the interface that allows mass conservation to be respected within the specified criteria ($\Delta m/m_0 \leq 0.01\%$ in this work) is found. This is also what is done in the VOF method in *JADIM* (Bonometti [2005]). The efficiency of this algorithm is shown in section 3.2.4. However, this method conserves the mass in a global manner and the simulation of a number of bubbles would still need further improvements.

3.2.4 Validation test: rotation in a shear flow

This section aims at validating the whole transport algorithm. The advection test chosen is a disc in a rotating shear flow as described in Rider and Kothe [1998]. This is interesting as it is widely used and it has already been simulated with *JADIM* (Bonometti [2005]). The computational domain is a square of width 1 and a disc of radius $R_0 = 0.15$ is placed at the position $[x;y] = [0.5;0.75]$. The velocity field is imposed and the stream function of this flow is $\psi = \pi^{-1}\left(\sin(\pi x)\right)^2\left(\sin(\pi y)\right)^2$. The disc is stretched until the time $t = T = 1$ and the flow is then reversed until the disc comes back to its approximate initial position.

Redistancing

The necessity of using a redistancing step is shown in figure 3.2. It is seen that the Level Set function is not a distance function anymore without the redistancing step when a shear rate is exerted on the interface and the sharpness of the interface described by the smooth Heaviside function defined in equation 3.3 is not constant. In addition, it is also observed that the redistancing step is efficient and the iso-contours of the Level Set function are well redistributed.

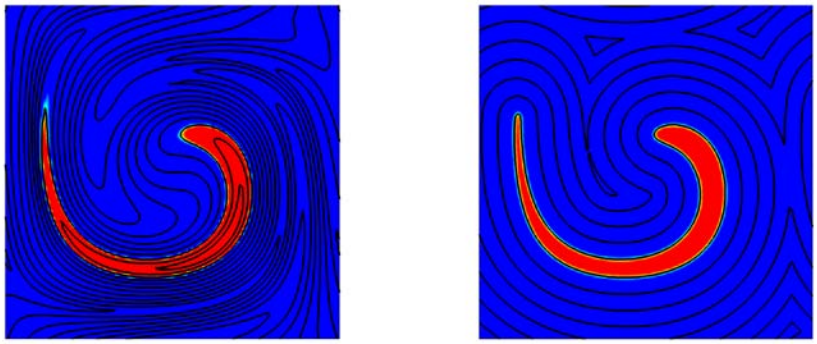

(a) without redistancing (b) with redistancing

Figure 3.2: Disc in rotating shear flow at time at its maximum stretching in this test case ($t = T = 1$) (a) without the redistancing algorithm ; (b) with the redistancing algorithm.

Mass conservation

The variation of mass during the simulation is shown in figure 3.3. It is seen that without the mass conservation, mass variations arise and can be reduced by increasing the mesh size (solid and dashed black lines). With the mass redistribution algorithm, the variations of mass remain within the allowed error ($^{\pm}0.01\%$) with both meshes. In addition, independently of the mesh used, the mass conservation step remains efficient (the solid and dashed blue lines cannot be distinguished). This is similar to the results obtained with the VOF-FCT-0 scheme with mass redistribution (red lines).

Comparison between VOF and LS

The transport schemes are compared in this section in the case of the rotating shear flow. The transport schemes compared are:

- VOF-FCT-0, which is the scheme that has been developed in Benkenida [1999] and significantly improved in Bonometti [2005];

- VOF-FCT, which corresponds to the previous scheme with the additional cut-off algorithm presented in section 2.2.4;

- LS, the Level Set method implemented which is mostly based on the works of Tanguy [2004], Couderc [2007].

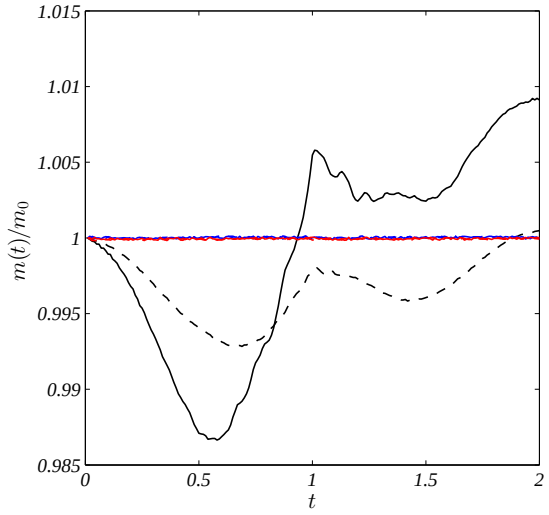

Figure 3.3: Mass variations.
Legend: (black) LS without mass correction ; (blue) LS with mass correction ; (red) VOF-FCT-0 ; (solid lines) mesh 64×64, *i.e.* $R_0/\Delta x = 9.6$; (dashed lines) mesh 128×128, *i.e.* $R_0/\Delta x = 19.2$.

We remind that the scope of this work is to find the best method for the capillary force in order to reduce spurious currents (see chapter 4). This section shows the validation of the transport scheme. Figure 3.4 shows the shape of the disc in the rotating shear flow for the three transport schemes with a resolution $R_0/\Delta x = 19.2$. Although the Level Set method consists in advecting a distance function, the results are shown in terms of volume fractions (estimated with equation 3.3), in order to compare the three methods with a unique scalar field.

It is seen that the position and the shape of the iso-contour representing the interface $C = 0.5$ are approximately the same with the three methods. However, the spreading of the interface over a few cells that is observed in the VOF-FCT-0 scheme is prevented with the cut-off algorithm (VOF-FCT), as well as with the LS method since the smooth Heaviside function forces the thickness of the interface to approximately 3 cells, as long as the Level Set function is close to a distance function. The results of the VOF-FCT and LS schemes are qualitatively similar.

Table 3.1 shows the error norms

$$E_1 = \frac{\sum |C_{i,j}^{2T} - C_{i,j}^{0}|}{\sum C_{i,j}^{0}} \quad \text{and} \quad E_2 = \frac{\sum |C_{i,j}^{2T} - C_{i,j}^{0}|}{2\pi R \Delta x} \ ,$$

where $C_{i,j}^{0}$ and $C_{i,j}^{2T}$ are the initial and final volume fraction fields, respectively. The error E_1 represents the relative area of the difference between the initial and final discs, while the error E_2 corresponds to the same difference in the areas but made dimensionless with interfacial area. This error norm appears to be relevant as the errors are mainly localized around the interfacial area. It is seen that at low resolution, the cut-off algorithm 2.2.4 improves the results when compared with the previous VOF-FCT-0 scheme. As the resolution is increased, it is also seen that the results are similar with and without the cut-off step since the volume fraction is not spread over enough

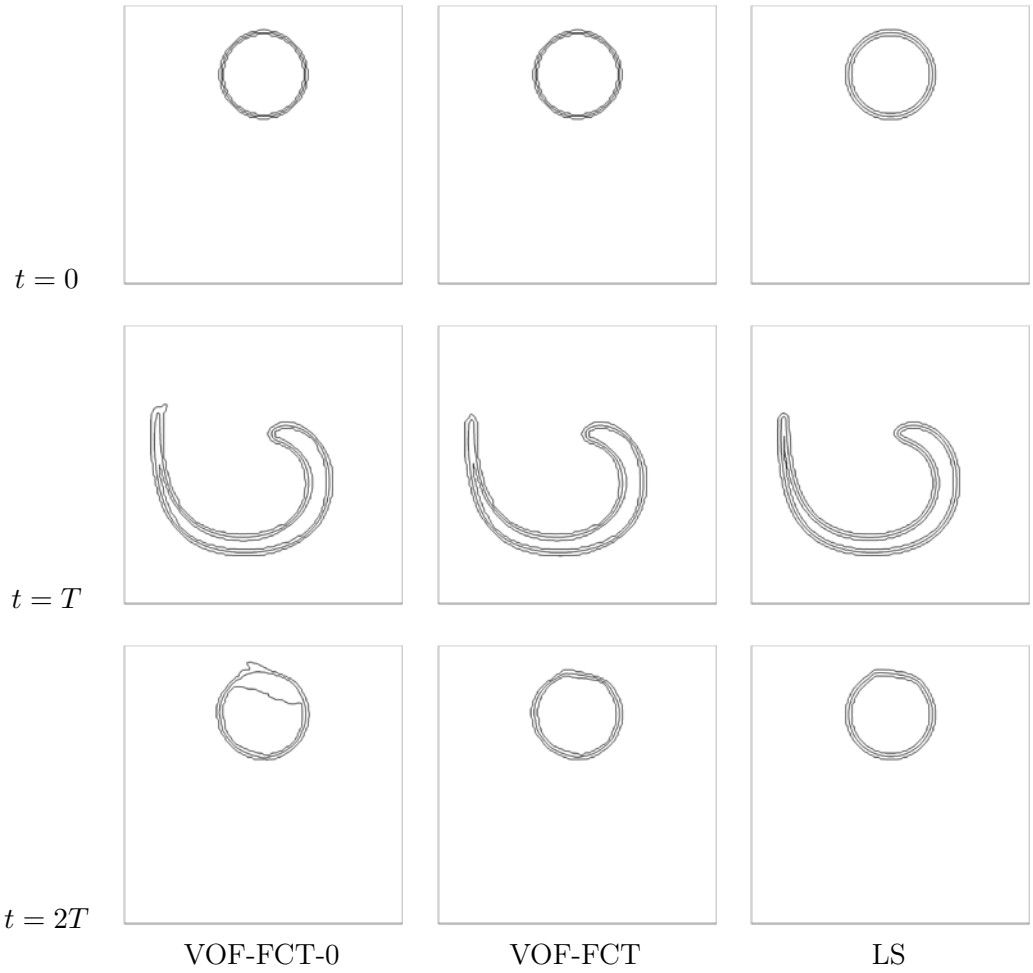

Figure 3.4: Disc in rotating shear flow. The lines represent the iso-contours [0.01 ; 0.5 ; 0.99].

cells to enter the cut-off algorithm. The FCT scheme with the cut-off algorithm has then been used in the following. Finally, the Level Set method shows better results for both error norms from low to high resolutions.

	VOF-FCT-0		VOF-FCT		LS	
$R_0/\Delta x$	E_1	E_2	E_1	E_2	E_1	E_2
9.6	0.1899	0.9116	0.1123	0.5392	0.0522	0.2509
19.2	0.0805	0.7728	0.0346	0.3324	0.0115	0.1104
38.4	0.0198	0.3795	0.0198	0.3795	0.0031	0.0603

Table 3.1: Error norms as a function of the spatial resolution for the 3 transport schemes considered.

3.3 LS Classic Continuum Surface Force (LS-CCSF)

The LS method has been validated in terms of the transport equation. Concerning its coupling with the Navier-Stokes equations, the capillary force is not calculated

exactly in the same way within VOF and LS methods, although the key idea remains the same, *i.e.* the spreading of the surface force on a region which is a few cells thick. In the LS-CCSF method, the same discretization as used in the VOF-CCSF method (equation 2.12) is employed:

$$\mathbf{F}_{\sigma,\mathbf{v}} = \frac{-\sigma}{\rho V}\overline{\nabla C}\int_{\partial S}\left(\frac{\nabla\phi}{\|\nabla\phi\|}\right)\cdot\mathbf{n_{cell}}dS \tag{3.24}$$

The delta dirac function can be approximated by the derivative of the smooth Heaviside function and applied directly, while the gradient of the level set function can be used for the curvature and the orientation of the force. Here, both the localization and the orientation are deduced from the volume fraction calculated with the Level Set function, *i.e.* $\mathbf{n}\delta_I = \overline{\nabla C}$. Indeed, this leads to a balanced surface force scheme since the volume fraction and the pressure gradients are discretized in the same way at the center of the staggered control volumes. Therefore, the main difference between the capillary force calculated in the VOF-FCT-CCSF and in the LS-CCSF method resides in the calculation of the curvature:

$$\kappa = \nabla\cdot\left(\frac{\nabla\phi}{|\nabla\phi|}\right) \tag{3.25}$$

Note also that the inverse of the density in the cell is used instead of the inverse of the mean density as it is the case in the VOF formulation (2.12). It was suggested that the use of the mean density reduces the spurious currents intensity within a VOF formulation (Brackbill et al. [1992]) but this has not been observed with the Level Set method and it appears more appropriate to discretize the capillary forces and pressure gradient in a consistent way.

3.4 Conclusion

A Level Set method has been implemented and validated through an academic test case. It has been shown that the results obtained in the case of a rotating shear flow are in good agreement and even improved when compared with those obtained with the VOF version of *JADIM*. The surface tension force is calculated following the same idea as in the balanced VOF-CSF formulation described in the previous chapter. The divergence theorem is used to evaluate the curvature at the center of the staggered control volumes and both the localization and the orientation of the surface tension force are calculated through the gradient of volume fraction in order to to keep a consistent discretization between the pressure gradient and the surface tension force. The coupling between the Level Set transport equation, the surface force calculation and the Navier-Stokes flow solver are discussed in the next chapter devoted to the characterization and the reduction of the spurious currents.

Chapter 4

Spurious currents

Contents

4.1 Introduction

When dealing with flows where capillary forces are preponderant, such as the simulation of Taylor flow (or slug flow) in microchannels, care needs to be taken in the computation of surface tension forces. This suggests that the normal to the interface and the curvature need to be accurately estimated. This capillary force located on the interface can be represented in a spatially filtered way using an interface thickness with the Continuum Surface Force method (Brackbill et al. [1992]) or in a sharp way using the location of the interface at a sub-cell level, *e.g.* Ghost Fluid Method (GFM) (Kang et al. [2000]), the Sharp Surface Force (SSF) (Francois et al. [2006]). Within implicit representations of the interface, many methods consider the successive derivatives of the scalar field representing the interface. More recently, Cummins et al. [2005] and Popinet [2009] have shown that the construction of height functions allows a better approximation of the interface curvature. Indeed, this method consists in finding the position of the interface with a good accuracy by adding successive volume fractions in a column of fluid (see section 4.3.2). Using this height function technique, Popinet [2009] achieved an exact numerical balance between surface tension forces and pressure jump with the elimination of spurious currents in the case of a static interface.

However, it was also shown that the coupling between transport schemes, surface tension force with Navier-Stokes equations and curvature estimation still needs improvements since the zero velocity field expected in the frame of reference moving with the bubble (like for the static case in Popinet [2009]) is not recovered when the interface is translated in a uniform flow. These observations motivated our work. Different numerical methods implemented in the same flow solver have been compared in terms of the magnitude of spurious currents and pressure jump evaluation on the basis of four test cases: the static bubble case for which a number of results are available in the literature; the translating bubble, which seems more related to physical flows; a bubble in a rotating flow; and the dynamics of Taylor bubble in a circular microchannel. The translating and rotating test cases have already been used to characterize transport schemes without solving the Navier-Stokes equations (Benkenida [1999]) but less attention has been paid to the study of spurious currents generated in these configurations, whereas these are mainly the consequence of errors in the advection step, as soon as the bubble is not static (Popinet [2009]). Due to the coupling between the errors in the bubble shape introduced in the advection step and the parasitic currents, which alter the theoretical velocity field close to the interface, the effects of fluid properties are considered by varying the Laplace number and the Weber number. The dynamics of Taylor bubbles in microchannels appear to be representative of the ability of a particular method to deal with spurious currents since these flows are dominated by surface tension (low capillary number and low Weber number) and approach stationary motion in the frame of reference moving with the bubble. As it will be shown, the development of spurious currents in such flows can promote the development of non-physical recirculation areas and consequently, erroneous slip velocity between the bubble velocity and mean velocity in the liquid slug which characterizes the drainage of such capillaries (Aussillous and Quéré [2000]), residence time and mixing characteristics (Abadie et al. [2013]), and ultimately heat and mass transfer processes.

4.2 Numerical schemes

4.2.1 Transport schemes

In this section, we briefly present the transport schemes that have been used to characterize the spurious currents in the different simulations carried out in this work.

Two different VOF schemes have been used :

- the VOF-FCT scheme that has been presented in chapter 2;
- a geometrical VOF-PLIC scheme in order to compare the effects of the scalar field transport and and in particular the sharpness of the interface on the spurious currents;
- the LS method described in chapter 3.

VOF-PLIC

The previous VOF-FCT without reconstruction scheme is considered diffusive since the interface is generally spread over a few cells thickness and therefore a geometrical 2-dimensional VOF-PLIC scheme based on the *VOF Tools* libraries developed by Lopez and Hernandez [2008] has been tested to compare the coupling of momentum equations with accurate surface tension schemes and transport equations within VOF formulations. The normals used to determine the linear reconstruction are calculated in the same way as those calculated for the surface tension force (see section 4.3). From the calculated normals and the given volume fraction, the interface is represented by a segment in each interfacial cell. The advection scheme is based on the same direction-split algorithm as the FCT scheme (Rudman [1998]). With staggered grids, the volume fraction enclosed in the volume advected by each velocity component is fluxed through the corresponding cell face. Note that a wide variety of PLIC schemes exist in the literature and the following observations, especially the rates of convergence, could be modified with another VOF geometrical scheme.

4.3 Surface tension force, origin of spurious currents

The calculation of the capillary force in both a VOF and a LS framework have been presented in the previous chapters. A brief summary of the methods used and variants of these methods are introduced in this section and the origin of spurious currents is discussed. These variants consist in calculating the curvature with a more accurate method (Height Functions) and another variant consists in imposing a sharp surface force instead of a continuous surface force (SSF).

The capillary force in the CSF model detailed in section 2.2.2 is written:

$$\mathbf{F}_{\sigma,\mathbf{v}} = -\frac{\sigma}{\rho}\kappa\nabla C. \tag{4.1}$$

where κ is the curvature of the interface and the localization of the interface is available through a non-zero gradient of the volume fraction.

The approaches considered in this work are mostly variants of the CSF method (Brackbill et al. [1992]) that differ in the way the curvature is discretized. The manner in which the capillary surface force is converted into a volume force and is spread over the finite volume mesh is not affected except in the SSF method. The CSF methods

based on the calculation of the curvature by means of the divergence of normal vectors or height functions are differenciated by calling them Classic Continuum Surface Force (CCSF) and Height Function Continuum Surface Force (HFCSF). The Sharp Surface Force (SSF) (Francois et al. [2006]), which roughly sets the pressure jump between cells that are cut by the interface, slightly differs from the Continuum Surface Force in that there is no discretization of a Delta Function to estimate the surface of the interface that cut the interface. The formulation of Sharp Surface Force (SSF), results in a sharp pressure jump like that obtained with the Ghost Fluid Method (Kang et al. [2000]) or the pressure correction proposed in (Popinet and Zaleski [1999]).

4.3.1 VOF Classic Continuum Surface Force (VOF-CCSF)

The VOF-CCSF method which has been developed in *JADIM* is based on the implicit representation of the interface that allow the calculation of the normal and the curvature from the successive derivatives of the scalar function representing te interface:

$$\delta_I \mathbf{n} = \nabla C \tag{4.2}$$

$$\kappa = \nabla \cdot \left(\frac{\nabla C}{||\nabla C||} \right) \tag{4.3}$$

The capillary force is given by (similar to 2.12):

$$\mathbf{F}_{\sigma,\mathbf{v}} = \frac{-\sigma}{\overline{\rho} V} \overline{\nabla C} \int_{\partial S} \left(\frac{\nabla C}{\|\nabla C\|} \right) \cdot \mathbf{n}_{\mathbf{cell}} dS \tag{4.4}$$

where $\overline{\nabla C}$ is the average value of ∇C in the staggered control volume and $\overline{\rho} = (\rho_1 + \rho_2)/2$ is the mean density since it has been shown to decrease the intensity of spurious currents (Brackbill et al. [1992]). A key point of this method is that the gradient of volume fraction in equation 4.4 is discretized in the same way as the pressure gradient in equation 2.2. This consistent discretization results in a balanced surface tension scheme (Renardy and Renardy [2002], Francois et al. [2006], Popinet [2009]) for iso-density flows whose benefit will be detailed in section 4.4.

4.3.2 VOF Height Function Continuum Surface Force (VOF-HFCSF)

The height function technique (Cummins et al. [2005], Popinet [2009]) allows the geometrical properties of the interface to be accurately calculated by summing the volume fractions of fluid columns. When the interface is well resolved, the use of height functions allows the position of the interface, described by a segment (in 2D) or a plane (in 3D), to be obtained. The stencils are oriented along the main component of the normal to the interface and they are adapted in every column until a cell of volume fraction of 0 is reached in the direction of negative gradient of volume fraction and a volume fraction of 1 in the positive direction (see figure 4.1.b). Once the position of the interface is evaluated, the curvature is calculated from the plane curve $y = f(x)$ via equation 4.5 :

$$\kappa = \frac{y''}{(1 + y'^2)^{3/2}} \ . \tag{4.5}$$

The surface tension force is therefore given by:

$$\mathbf{F}_{\sigma,\mathbf{v}} = \frac{-\sigma}{\rho V} \overline{\nabla C} \int_V \left(\frac{y''}{(1 + y'^2)^{3/2}} \nabla C \right) dV \tag{4.6}$$

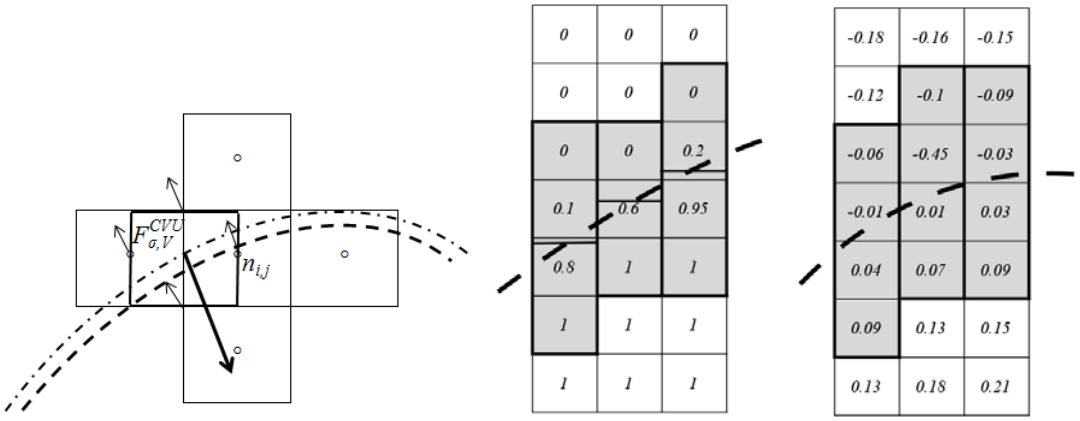

(a) (b) (c)

Figure 4.1: (a) Schematic representation of the capillary force with a Continuum Surface Force model on staggered grids. Adaptive stencil for the construction of height functions in (b) a Volume of Fluid formulation ; (c) a Level Set formulation. The dashed line represents the interface while the dash-dotted line represents the iso-contour where the curvature is calculated in the classic continuum surface force model.

In addition, the local density in the cell ρ is used in VOF-HFCSF instead of the mean density $\overline{\rho}$ as in VOF-CCSF (equation 4.4) in order to get a balanced-force algorithm whatever the density ratio, with a consistent discretization with the pressure gradient term where the local density is used.

4.3.3 LS Classic Continuum Surface Force (LS-CCSF)

In the LS-CCSF method, the same conservative discretization used in the VOF-CCSF method is employed.

$$\mathbf{F}_{\sigma,\mathbf{v}} = \frac{-\sigma}{\rho V}\overline{\nabla C}\int_{\partial S}\left(\frac{\nabla\phi}{\|\nabla\phi\|}\right)\cdot\mathbf{n_{cell}}dS \tag{4.7}$$

Note that, like in VOF-HFCSF, the local density in the cell ρ is used in LS-CCSF instead of the mean density $\overline{\rho}$ as in VOF-CCSF. The delta dirac function could be approximated by the derivative of the smooth Heaviside function and applied directly while the gradient of the Level Set function would be used for the curvature and the orientation of the force. Here, both the localization and the orientation are deduced from the volume fraction calculated with the Level Set function, *i.e.* $\mathbf{n}\delta_I = -\nabla C$, since natural equilibrium is reached with this formulation as soon as the curvature is constant along the interface and both the pressure and volume fraction gradients in equation 4.9 are discretized in the same way.

4.3.4 LS Height Function Continuum Surface Force (LS-HFCSF)

In a Level Set framework, the position of the interface can be found by linear interpolation or more accurately using quadratic interpolations with the four cells surrounding the interface (see figure 4.1.c). The procedure to locate the interface is the same as the one used by Min and Gibou [2007]. In order to improve the stability of the quadratic interpolations near discontinuities, a minmod operator was introduced

by Min and Gibou [2007] on the second derivatives of the Level Set function calculated on each side of the interface. The curvature and volume force are also calculated with equations 4.5 and 4.6 respectively.

4.3.5 LS Sharp Surface Force (LS-SSF)

In the Sharp Surface Force model (Francois et al. [2006]), the surface tension force is non zero only in the cells crossed by the interface; this is different to the CSF method, which imposes the Laplace pressure jump continuously along the interface. The curvature is calculated following the same procedure as the LS-CCSF method. For the horizontal direction, if the control volume centered on the x-component of the velocity is crossed by the interface, *i.e.* $\phi_{i-1} \times \phi_i < 0$, the surface tension force is:

$$F_{\sigma,v} = -(\sigma\kappa_I)/(\rho\Delta x), \tag{4.8}$$

where κ_I is the curvature interpolated on the interface $\kappa_I = \dfrac{|\phi_i|\kappa_{i-1} + |\phi_{i-1}|\kappa_i}{|\phi_i| + |\phi_{i-1}|}$.

4.4 Origin of spurious currents, vorticity source

In simple cases, such as a static or a translating bubble or drop, the momentum conservation equation reduces to:

$$0 = -\nabla P + \sigma\kappa\nabla C, \tag{4.9}$$

such that, when taking the curl of equation 4.9, the curvature should satisfy:

$$\nabla\kappa \times \nabla C = 0\ . \tag{4.10}$$

Spurious currents are generated when this condition is not satisfied. In the particular case of a surface with a constant curvature (*e.g.* a spherical bubble or drop), the flow will be curl free if the computed curvature is indeed constant. In addition, the elimination of spurious currents requires the use of balanced-force algorithms (Francois et al. [2006], Herrman [2008], Popinet [2009]) with consistent discretization of pressure and capillary forces to satisfy equation 4.9. Curvature gradients as sources of vorticity are identified when writing the vorticity equation from equation 2.2:

$$\frac{\partial\omega}{\partial t} + (\mathbf{U}\cdot\nabla)\,\omega + (\omega\cdot\nabla)\,\mathbf{U} = \frac{\mu}{\rho}\nabla^2\omega - \frac{\sigma}{\rho}\nabla\kappa\times\nabla C \tag{4.11}$$

From equation 4.11, it is seen that the surface tension force can contribute as a source term for vorticity production when condition 4.10 is not satisfied. Equation 4.11 also shows that a steady state can be reached for the spurious currents of magnitude U_σ. When viscous effects are dominant, the vorticity source term ($\sigma\nabla\kappa\times\nabla C \sim \sigma/D^3$) is balanced by the viscous term ($\mu\nabla^2\omega \sim \mu U_\sigma/D^3$):

$$U_{\sigma,visc} \sim \frac{\sigma}{\mu} \tag{4.12}$$

Thus, the intensity of spurious currents can be written using a characteristic capillary number ($Ca = \mu U_{\sigma,visc}/\sigma \sim c$ where c is a constant). This is consistent with previous works in which the magnitude of spurious currents was related empirically to σ/μ (Dupont and Legendre [2010], Herrman [2008], Renardy and Renardy [2002]).

When inertia is dominating, the source term is balanced by the inertial term ($\rho\,(\mathbf{U}\cdot\nabla)\,\omega \sim \rho U_\sigma^2/D^2$) resulting in the characteristic velocity:

$$U_{\sigma,in} = \sqrt{\frac{\sigma}{\rho D}}. \tag{4.13}$$

This is the characteristic velocity used in the inviscid problem (Popinet [2009]). These two characteristic velocities are closely related since

$$U_{\sigma,visc} = \sqrt{La}\, U_{\sigma,in} \tag{4.14}$$

where $La = \dfrac{\rho D \sigma}{\mu^2}$ is the Laplace number.

In this work, $U_{\sigma,visc}$ has been chosen to make the velocities dimensionless since the simulations have been performed at a finite Laplace number and it is consistent with a previous study with *JADIM* (Dupont and Legendre [2010]).

4.5 Static bubble

The first test case that we consider is the 2-dimensional static bubble (Popinet [2009]). A cylindrical interface is initialized in a continuous phase without gravity and both fluids have equal density and viscosity. The Laplace number is $La = 12000$. Only a quarter of the bubble of radius $R_0 = 0.4$, placed in the bottom left hand side of a square computational domain of length 1 is simulated. Symmetry boundary conditions are applied on the left and bottom boundaries while no-slip boundary conditions are applied on the top and right boundaries. The exact solution of the velocity field should remain zero in the whole domain and the pressure should obey the Laplace pressure jump at the interface.

The analysis of the intensity of spurious currents and pressure jumps is based on the following error norms:

- U_{max} is the maximum absolute velocity in the whole domain and $Ca_{max} = \mu U_{max}/\sigma$ is its dimensionless form used in the following,
- $|\nabla\kappa \times \nabla C|$ is the norm of the source term in equation 4.11 and will be used to characterize the vorticity production and the associated spurious currents,
- ΔP_{total} is the pressure jump between the average pressure in the bubble ($C \geq 0.5$) and the average pressure in the continuous phase ($C \leq 0.5$),
- ΔP_{max} is the pressure jump between the maximum and minimum pressure in the domain.

The numerical parameters considered correspond to those used by Popinet [2009] where after transient motion, the bubble shape reached a numerical equilibrium with a constant curvature estimated along the interface, leading to an exact balance between surface tension and pressure forces, and the elimination of spurious currents. The time is made dimensionless with the capillary time scale $T_\sigma = \sqrt{\dfrac{\rho D^3}{\sigma}}$.

The relevance of the space discretization between pressure gradient and surface tension force has firstly been tested by imposing the exact curvature in the whole domain for the calculation of $\mathbf{F}_{\sigma,\mathbf{v}}$. The maximum dimensionless velocity in the whole domain reached $Ca_{max} \simeq 5.08\times10^{-18}$ showing that equation 4.10 is satisfied to machine accuracy so that the source term in equation 4.11 is negligible and no spurious currents develop. Thus, the exact balance between the volume fraction and pressure gradients is verified and the spurious currents observed in the following can be attributed to the errors in the calculation of the curvature and more precisely, in the gradients of curvature along the interface due to the resolution of a curved interface on a cartesian grid.

Figure 4.2 shows the velocity field and the intensity of the source term in the vorticity equation for the different methods. It is clearly seen that the maximum intensities of velocity and the maximum intensities of the vorticity source are collocated.

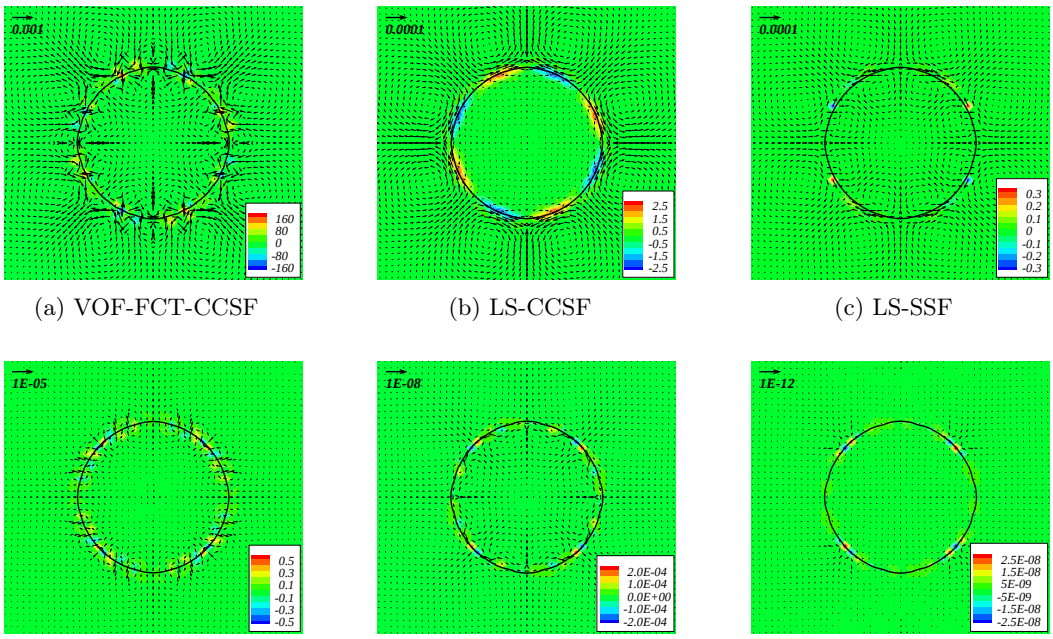

(a) VOF-FCT-CCSF (b) LS-CCSF (c) LS-SSF

(d) LS-HFCSF (e) VOF-FCT-HFCSF (f) VOF-PLIC-HFCSF

Figure 4.2: Intensity of the source term $|\nabla\kappa \times \nabla C|$ in the vorticity equation 4.11 and velocity field (by decreasing spurious currents from (a) to (f)) for $R_0/\Delta x = 12.8$ and $La = 12000$.

Figure 4.3 shows the evolution of the maximum intensity of the spurious currents with the different methods. Within a VOF framework, it is clearly seen that the height function curvature calculation allows the spurious currents to be decreased by approximately six orders of magnitude with the VOF-FCT-HFCSF method when compared with the standard curvature calculation (VOF-FCT-CCSF) and spurious velocities are close to machine accuracy with VOF-PLIC-HFCSF, as in Popinet [2009]. In addition to the accuracy obtained with the height function technique (Cummins et al. [2005], Popinet [2009]), the curvature calculated is that at the interface while the curvature estimated with CCSF methods is that at the center of the control volume as illustrated in figure 4.1. The error induced by the location of the curvature calculation promotes curvature gradients, which are source of vorticity in the vicinity of the interface (equation 4.11). As expected, the Classic Continuum Surface Force method gives better results when coupled to a distance function than a volume fraction. Within a LS framework, figure 4.3 shows that both continuous and sharp methods (LS-CCSF and LS-SSF) are close in terms of the intensity of spurious currents. These similarities in the results obtained with LS-CCSF and LS-SSF methods are consistent with the observations of Francois et al. [2006] who found similar spurious velocities with continuous and sharp surface tension models.

In a LS context, the height function curvature calculation improves the results by more than one order of magnitude. However, the exact balance between pressure and capillary forces that is achieved in a VOF framework, with or without reconstruction, is not obtained with the LS-HFCSF method. Interestingly, when the redistancing step in the LS transport scheme is skipped, the spurious currents are significantly decreased

and it is possible to obtain the exact equilibrium between pressure and capillary forces with both Sharp Surface Force (LS-SSF) and Height Function Continuum Surface Force (LS-HFCSF). Indeed, both methods estimate the curvature at the interpolated position of the interface and the interface oscillates around the position of numerical equilibrium while the velocities tend towards zero. This balance cannot be reached when the redistancing step is activated because the position of the interface (represented by the iso-contour $\phi = 0$) is slightly moved during the redistancing step (Min and Gibou [2007]), thereby maintaining the spurious currents. Spurious currents are mainly due to the redistancing step in LS methods when the curvature is calculated on the interface (LS-SSF and LS-HFCSF). Nevertheless, the redistancing equation will be solved in the following as it is necessary to maintain the level set function as a distance function.

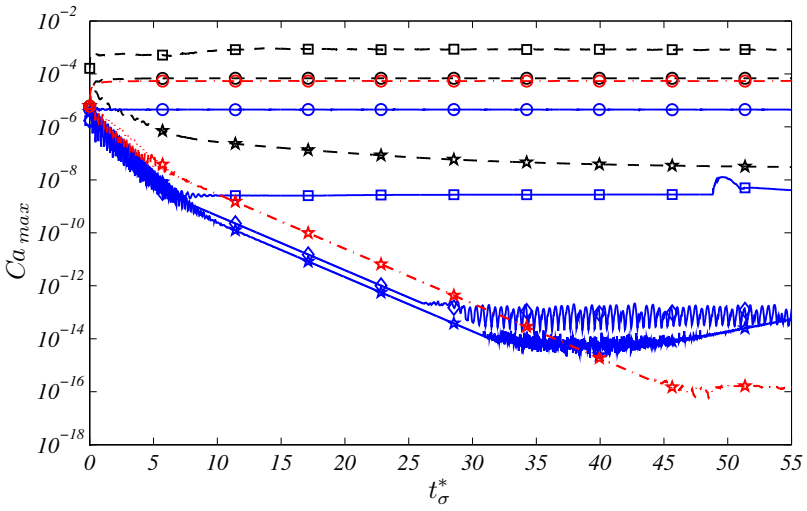

Figure 4.3: Evolution of the maximum intensity of the spurious currents in the computational domain over time. Legend : (–□–) VOF-FCT-CCSF ; (□) VOF-FCT-HFCSF ; (◇) VOF-PLIC-HFCSF ; (–○–) LS-CCSF ; (○) LS-HFCSF ; (○ ·) LS-SSF ; (–★–) LS-CCSF without redistancing ; (★) LS-HFCSF without redistancing ; (★ ·) LS-SSF without redistancing.

In addition, the temporal evolution of the intensity of vorticity source is reported in figure 4.4. A good correlation between this source term and the spurious velocities is observed. Indeed, the curvature gradients and therefore the vorticity source term almost vanish with the VOF-FCT-HFCSF method and are reduced to 10^{-12} with the VOF-PLIC-HFCSF. On the other hand, with the other methods, this vorticity source does not vanish and is balanced by viscous dissipation (see section 4.4). These trends are similar to those observed with the maximum intensity of spurious currents.

The balance between pressure jump and surface tension forces observed with both the VOF-FCT-HFCSF and VOF-PLIC-HFCSF methods has been verified for different Laplace numbers ranging from 120 to 12000 and different meshes involving between 10 and 50 cells per bubble radius. Convergence of the other methods with mesh refinement has been studied and is shown in figure 4.5. As mentioned in Dupont and Legendre [2010], the spurious currents obtained with the VOF-FCT-CCSF method do not decrease with grid refinement. Since the number of smoothing steps that spreads the interface on a given number of cells has been kept constant, the physical length of smoothing is smaller and the filter is less efficient when the grid spacing is decreased. Spurious currents with LS-CCSF, LS-SSF and LS-HFCSF decrease with a rate of convergence close to 2.

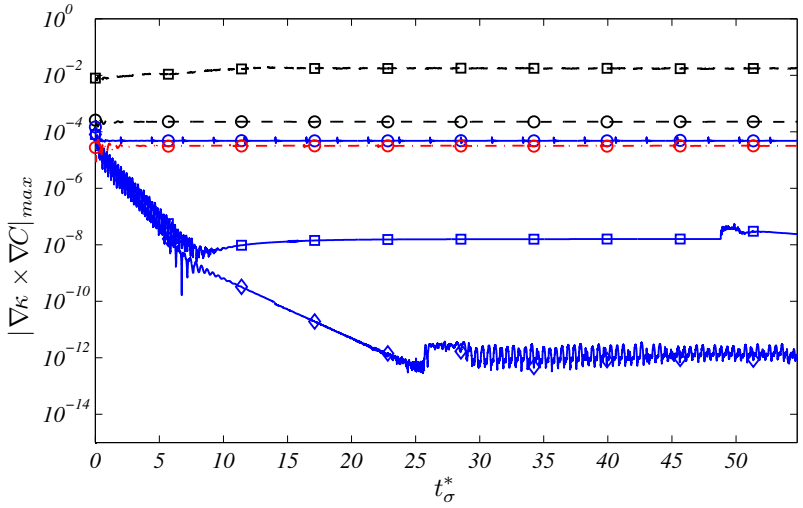

Figure 4.4: Evolution of the maximum intensity of the source term $|\nabla\kappa \times \nabla C|$ in the vorticity equation 4.11 over time.
Legend : (–□–) VOF-FCT-CCSF ; (□) VOF-FCT-HFCSF ; (◊) VOF-PLIC-HFCSF ; (–◯–) LS-CCSF ; (◯) LS-HFCSF ; (◯ ·) LS-SSF.

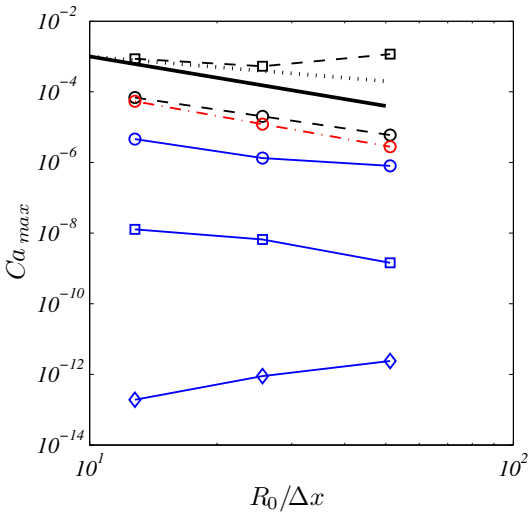

Figure 4.5: Convergence with spatial resolution of maximal spurious currents velocities.
Legend : (–□–) VOF-FCT-CCSF ; (□) VOF-FCT-HFCSF ; (◊) VOF-PLIC-HFCSF ; (–◯–) LS-CCSF ; (◯) LS-HFCSF ; (◯ ·) LS-SSF ; (• • •) $Ca_{max} \sim (R_0/\Delta x)^{-1}$; (—) $Ca_{max} \sim (R_0/\Delta x)^{-2}$.

4.6 Translating bubble

The second test case consists in a uniform flow field that translates the bubble as proposed in Popinet [2009]. This test allows the precision and robustness of the coupling between advection schemes, Navier-Stokes solver and capillary term calculation to be characterized. A uniform horizontal velocity U_0 is imposed in the whole domain with periodic boundary conditions on lateral sides and symmetry boundary conditions on the top and bottom. Both fluids have equal density and viscosity. The cylindrical bubble/droplet should move with the external flow at the same velocity U_0, the velocity field in the frame of reference moving with the bubble should ideally be zero and the pressure field should obey the Laplace pressure jump at the interface.

$$(u\,,\,v)\,(x,y) \;=\; (U_0\,,\,0) \tag{4.15}$$

$$p(x,y) \;=\; \begin{cases} \dfrac{\sigma}{R_0} & \text{in the bubble} \\ 0 & \text{outside} \end{cases} \tag{4.16}$$

In this test case, the time is made dimensionless with the characteristic advection time $t_0 = D/U_0$.

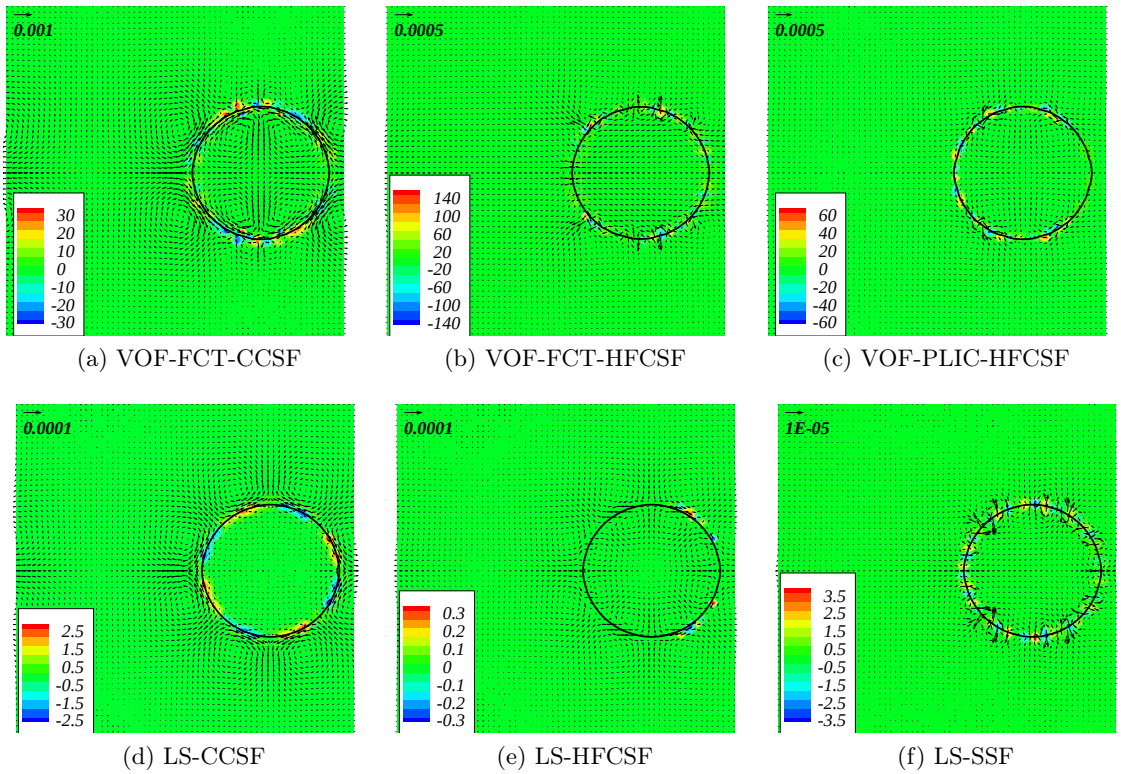

(a) VOF-FCT-CCSF (b) VOF-FCT-HFCSF (c) VOF-PLIC-HFCSF

(d) LS-CCSF (e) LS-HFCSF (f) LS-SSF

Figure 4.6: Intensity of the source term $|\nabla\kappa \times \nabla C|$ in the vorticity equation 4.11 and velocity field after the translation of a distance $1.25D$ in the frame of reference moving with the bubble (by decreasing spurious currents from (a) to (f)) for $R_0/\Delta x = 12.8$, $La = 12000$ and $We = 0.4$.

The spurious velocity and the vorticity production fields obtained with the different methods are shown in figure 4.6. Similarly to the static case, the maximum intensities of vorticity production and spurious velocity are collocated. It is observed that the maximum intensity of spurious currents in VOF-FCT-HFCSF simulation does not

tend towards machine accuracy in this test case and is of the same order of magnitude than in the VOF-FCT-CCSF simulation. However, while the spurious velocities are uniformly spread around the interface in the VOF-FCT-CCSF method, the spurious currents are localized in space when using the height function technique for the curvature calculation. This different behaviour between the different curvature calculation techniques is also observed with the VOF-PLIC and LS transport schemes. Therefore, the average intensity of spurious currents is decreased with the height function curvature calculation whereas the maximum intensity of spurious currents is of same order with both height function and curvature calculation from the divergence of the unit normal to the interface for a given transport scheme.

4.6.1 Time evolution of spurious currents

The temporal evolution of the maximum velocity of spurious currents is reported in figure 4.7. For a given transport scheme (VOF-FCT, VOF-PLIC or LS), the estimation of the curvature from the height function (HFCSF) leads to similar intensities of spurious currents as those obtained with the calculation of the curvature from the divergence of the unit normal to the interface (CCSF and SSF). The spurious currents obtained with CCSF and SSF methods are in good agreement with those obtained in the static case. On the other hand, with the height function curvature calculation (VOF-FCT-HFCSF, VOF-PLIC-HFCSF, LS-HFCSF), spurious currents are enhanced in this test case when compared with the static case. The accuracy of the height function curvature calculation is therefore highlighted since spurious currents are very sensitive to the errors in the shape that are introduced in the advection step, especially with VOF-FCT and VOF-PLIC schemes. In this test, it is seen that spurious velocities are dominated by the method used to capture and advect the interface. Indeed, this flow configuration shows that VOF-FCT and VOF-PLIC transport schemes generate almost similar spurious currents, with a stronger intensity than that obtained with a LS method, whatever the method used to calculate the curvature and the surface force (continuous or sharp).

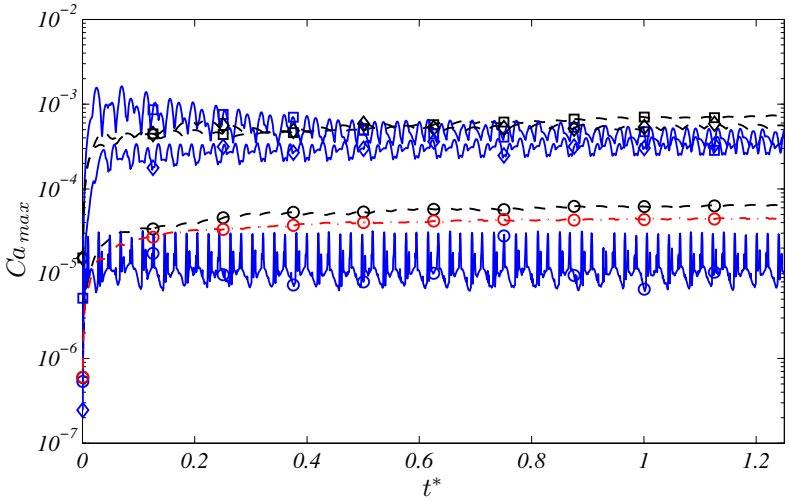

Figure 4.7: Temporal evolution of the maximum spurious currents velocity in the frame of reference moving with the bubble for $R_0/\Delta x = 12.8$, $La = 12000$, $We = 0.4$.
Legend : (–□–) VOF-FCT-CCSF ; (□) VOF-FCT-HFCSF ; (–◇–) VOF-PLIC-CCSF ; (◇) VOF-PLIC-HFCSF ; (–◯–) LS-CCSF ; (◯) LS-HFCSF ; (⊙ ·) LS-SSF.

4.6.2 Effects of the Laplace number

The effects of fluid properties on the intensity of the spurious currents have first been considered by varying the Weber number. Our results obtained with the VOF-PLIC-HFCSF method are close to those obtained with the *Gerris* collocated finite-volume code in Popinet [2009] that uses a geometrical VOF transport scheme of the interface (PLIC) and the CSF method is coupled to the height function curvature calculation. With most of the methods, the capillary number based on the maximum intensity of spurious currents does not depend strongly on the Weber number, as mentioned in Popinet [2009]. Since approximately the same evolution is found with all the methods, we focused on the effects of the Laplace number on the spurious currents.

The evolution of the spurious velocities, in terms of capillary number, as a function of the Laplace number is reported in figure 4.8(a), which also includes results from Popinet [2009]. Note that in Popinet [2009], the velocities are made dimensionless with the advective velocity U_0. To compare these results with the present study in terms of characteristic capillary number, the velocities from Popinet [2009] have been adapted ($Ca_{max}^{Popinet\ [2009]} = U_{max}^{Popinet\ [2009]}/U_0\sqrt{We_0/La}$). The trend observed in Popinet [2009] ($U_{max}/U_0 \sim La^{1/6}$) then leads to $Ca_{max} \sim La^{-1/3}$ for a given advective Weber number We_0. Our results obtained with the VOF-PLIC-HFCSF method are in good agreement with the results from Popinet [2009], despite a slightly lower influence of the fluid properties ($Ca_{max} \sim La^{-\frac{1}{4}}$). Whatever the transport scheme, VOF-PLIC, VOF-FCT or LS, the spurious currents generated with the CCSF method show almost no dependency with the fluid properties and are close to those obtained in the static case. The LS-SSF method also gives similar spurious current intensities and trends to the LS-CCSF method. However, the HFCSF method coupled with either VOF-PLIC, VOF-FCT or LS shows approximately the same trend, with a decrease in the spurious capillary number as the Laplace number increases ($Ca_{max} \sim La^{-\frac{1}{4}}$).
From a general point of view, in the range of Laplace and Weber numbers simulated in the present work ($1.2 < La < 12000$ and $0.4 < We < 30$) with 12.8 cells per bubble radius, VOF-FCT-CCSF and VOF-PLIC-CCSF are almost equivalent since the errors in the advection are smoothed. The spurious currents generated with the VOF-PLIC-HFCSF are of the same order of magnitude. The height function coupled with the VOF-FCT transport scheme leads to enhanced spurious currents when compared with the same curvature calculation coupled with the VOF-PLIC transport scheme and this is attributed to the slight interface diffusion. Finally, the spurious currents obtained in a LS framework are reduced by a factor between 2 ($La = 1.2$ and $We = 0.4$) and approximately 100 ($La = 12000$ and $We = 30$) when compared with the minimum ones obtained in a VOF framework. It is also interesting to point out that the intensity of the spurious currents in this test case is essentially driven by the transport scheme, *i.e.* LS schemes give better results than VOF-PLIC and finally VOF-FCT transport schemes, whereas the tendencies observed when increasing the Laplace number appear to depend on the method for the curvature calculation, *i.e.* almost no dependency on the Laplace number for the curvature derived from the interface normal and a slight decrease with the height function curvature calculation.

Figure 4.8(b) shows the maximum intensity of the vorticity source term and confirms that the vorticity production mainly depends on the transport scheme and the discretization. Indeed, the vorticity production in LS methods is smaller than in VOF methods, except with the LS-HFCSF method where strong curvature gradients, which are localized both in time and space, appear. As expected, the spurious currents production for a given method is constant in a first approximation throughout the range of Laplace numbers considered despite slight variations due to the coupling between spurious velocities, advection errors, curvature gradients and vorticity production. These

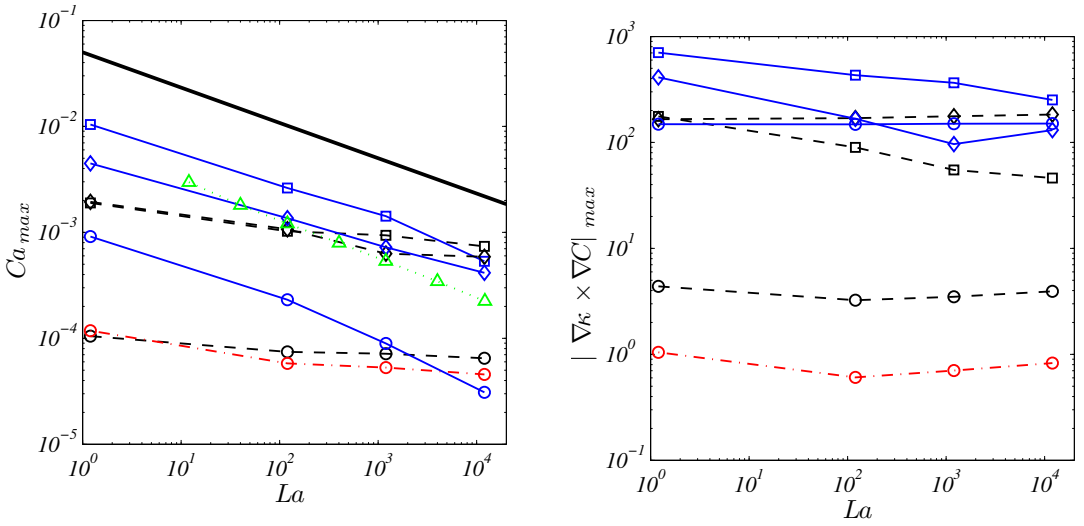

(a) Spurious currents intensity

(b) Spurious currents production

Figure 4.8: Maximum spurious currents capillary number (a) and vorticity production (b) versus the Laplace number for $R_0/\Delta x = 12.8$ and $We = 0.4$.
Legend : (–□–) VOF-FCT-CCSF ; (□) VOF-FCT-HFCSF ; (–◇–) VOF-PLIC-CCSF ; (◇) VOF-PLIC-HFCSF ; (–◯–) LS-CCSF ; (◯) LS-HFCSF ; (◯ ·) LS-SSF ; (·△·) VOF-PLIC-HFCSF *@Gerris* (Popinet [2009]) ; (—) $Ca_{max} \sim La^{-1/3}$.

observations show that the decrease in spurious currents as the Laplace number increases is not related to a decrease in vorticity production. Thus, the development of the vorticity source term into spurious currents and the balance between them depends on the Laplace number.

4.6.3 Convergence with spatial resolution

Intensity of spurious currents

The convergence with spatial resolution of the maximum velocity is shown in figure 4.9 for a given Laplace number ($La = 12000$) and two different Weber numbers ($We = 0.4$ and $We = 30$). As oberved in Dupont and Legendre [2010] for the static case, VOF-FCT-CCSF does not converge with spatial resolution and this is also true for the VOF-PLIC-CCSF method since both methods behave similarly. It is not surprising that a slight increase in spurious currents with increasing the number of nodes is observed since the number of smoothing iterations is kept constant and thus, the filtering procedure acts over a thinner region. VOF-FCT-HFCSF does not converge either when the number of nodes is increased and the trend is even worse with the LS-HFCSF method. VOF-PLIC-HFCSF presents almost a first order convergence rate. These different behaviours with a given curvature calculation and different transport schemes show the importance of the errors introduced in the advection step that are captured with an accurate curvature calculation, such as the height function method. Finally, LS-CCSF and LS-SSF present near second order convergence rates. The methods show similar trends within the range of Weber numbers considered. The differences reside in slightly lower rates of convergence at $We = 30$ and the spurious velocities obtained with the VOF-FCT scheme are greater than those at $We = 0.4$. Since there is no major difference and the calculation time is found to decrease when the bubble velocity increases (*i.e.* for high Weber numbers), all other spatial convergence studies have been

carried out at $We = 30$.

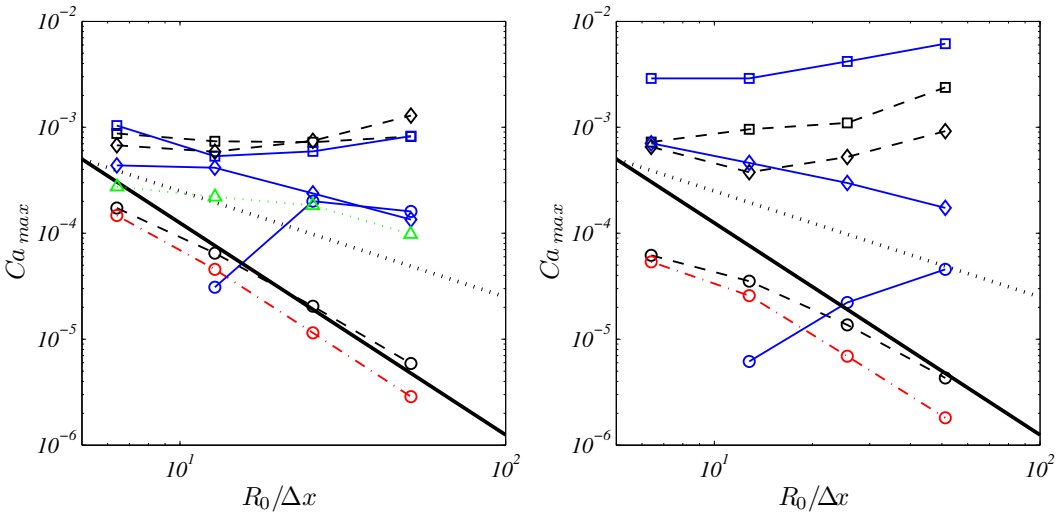

(a) $We = 0.4$ (b) $We = 30$

Figure 4.9: Maximum spurious currents capillary number as a function of spatial resolution for $La = 12000$.
Legend : (–□–) VOF-FCT-CCSF ; (□) VOF-FCT-HFCSF ; (–◇–) VOF-PLIC-CCSF ; (◇) VOF-PLIC-HFCSF ; (–◯–) LS-CCSF ; (◯) LS-HFCSF ; (◯ ·) LS-SSF ; (·△·) VOF-PLIC-HFCSF *@Gerris* (Popinet [2009]) ; (• • •) $Ca_{max} \sim (R_0/\Delta x)^{-1}$; (—) $Ca_{max} \sim (R_0/\Delta x)^{-2}$.

Shape errors

It is interesting to note the consistency between the previous observations about spurious currents and the errors on the shape of the bubble, E_{max} and its curvature, $E(\kappa)_{max}$ after translation. Indeed, it is shown in figure 4.10(a) that the error on the shape is minimized with the LS method and is maximum with the VOF-FCT transport scheme. Despite the different shape errors obtained with VOF-FCT-CCSF and VOF-PLIC-CCSF methods, the errors on the calculated curvature are similar due to the smoothing procedure used. However, with the height function curvature calculation, spurious currents arise due to the advection of the interface and it is not surprising to observe an increase in the curvature errors with the VOF-FCT-HFCSF method when compared with the VOF-PLIC-HFCSF method, which minimizes the advection errors in a VOF framework. While the error on the shape decreases with grid refinement with the LS-HFCSF method, the maximum error on the curvature and the vorticity source term increase, as it is the case with the maximum spurious velocity. It is observed with the LS-CCSF that the maximum curvature errors are enhanced when compared with LS-SSF or VOF-PLIC-HFCSF methods whereas the spurious currents generated are lower to those obtained with the VOF-PLIC-HFCSF method and similar to those obtained with the LS-SSF method. This can be due to the fact that the same accuracy is achieved in the curvature calculation for both the sharp and continuous formulations but the difference resides in the interpolation of the curvature at the interface in the sharp formulation. Thus, the LS-CCSF introduces a gradient of curvature normal to the interface, while the main contribution in the generation of spurious currents comes from the tangential gradient (see equation 4.10).

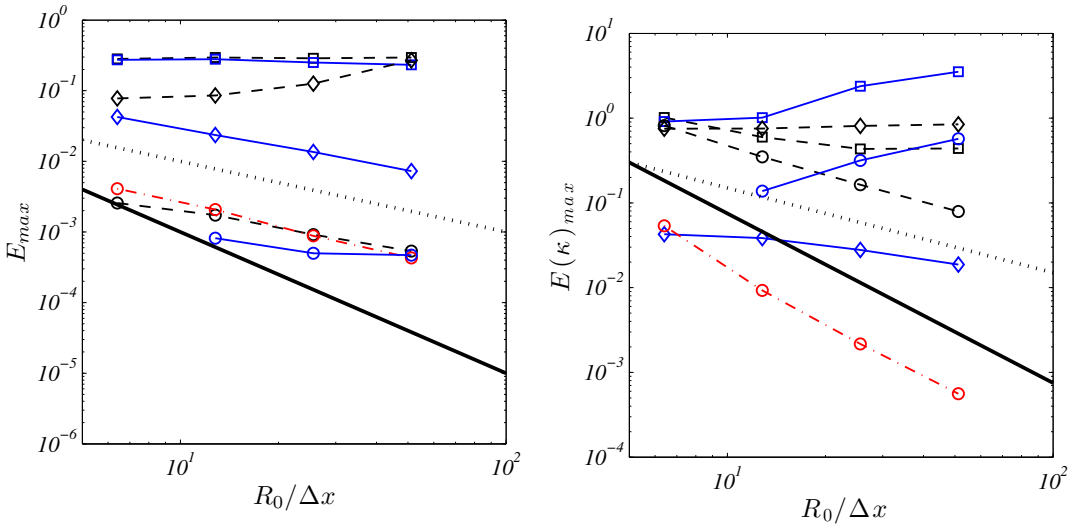

(a) Maximum shape error

(b) Maximum curvature error

Figure 4.10: Shape errors (a); curvature errors (b) as a function of spatial resolution for $La = 12000$ and $We = 30$.
Legend : (–□–) VOF-FCT-CCSF ; (□) VOF-FCT-HFCSF ; (–◇–) VOF-PLIC-CCSF ; (◇) VOF-PLIC-HFCSF ; (–○–) LS-CCSF ; (○) LS-HFCSF ; (○ ·) LS-SSF ; (• • •) $E \sim (R_0/\Delta x)^{-1}$; (—) $E \sim (R_0/\Delta x)^{-2}$.

In addition, the rates of convergence of the maximum curvature error for the different methods are close to those obtained for the maximum spurious currents intensity. Indeed, going back over the dimensional analysis presented in section 4.4 using the mesh size as the characteristic length rather than the bubble diameter, the rates of convergence with spatial resolution of the velocity, vorticity production and curvature can be related. The use of this characteristic length is justified since the present analysis concerns spurious flows where the derivatives in the vorticity equation 4.11 quantify errors over the mesh (discretization errors, as well as spurious velocity and vorticity fields gradients) instead of variations due to physical phenomena, which would be related to physical characteristic lengths (*e.g.* the bubble diameter). Thus, the vorticity source term is written as a function of the error in the curvature calculation as follows:

$$\nabla\kappa \times \nabla C \sim \frac{E(\kappa)}{\Delta x^2} \tag{4.17}$$

In addition, the balance between vorticity production and the viscous term can then be written as:

$$\mu\frac{\omega_{max}}{\Delta x^2} \sim \sigma\nabla\kappa \times \nabla C \tag{4.18}$$

$$i.e. \qquad \frac{Ca_{max}}{\Delta x^3} \sim \nabla\kappa \times \nabla C \tag{4.19}$$

Figure 4.11(a) shows the ratio of vorticity production to curvature error as a function of the mesh size. Good agreement with equation 4.17 is observed (divergence of order 2) for all the methods. It is interesting to point out that for a given curvature error, the vorticity source term is minimized with standard curvature calculations when compared with height function since the curvature errors are localized in space and the curvature gradient is enhanced while it is spread along the interface with smoothed

methods (CCSF). Figure 4.11(b) shows the ratio of maximum spurious currents intensity to the vorticity source term as a function of the spatial resolution. It is seen that this ratio decreases as the mesh size decreases whereas the rate of convergence is approximately one order lower then the one expected from equation 4.19, *i.e.* close to second order convergence instead of third order. This decrease in the rate of convergence is attributed to non linear effects in the vorticity equation. As a consequence, curvature errors and maximum spurious currents intensity show similar rates of convergence with spatial resolution ($\sim |\nabla\kappa \times \nabla C|\Delta x^2$). Finally, note that for a given vorticity production, the VOF methods minimize the spurious capillary number when compared with LS methods (see figure 4.11(b)) except for the LS-HFCSF method where strong oscillations of the curvature and the vorticity source term occur instantaneously and lead to a decreased ratio of spurious currents intensity to vorticity source term. These observations allow to conclude that spurious currents, vorticity production and curvature gradients are closely related. The sensitivity of the vorticity production on the transport scheme and the advection errors is enhanced with the height function curvature calculation when compared with the smoothed standard curvature calculation.

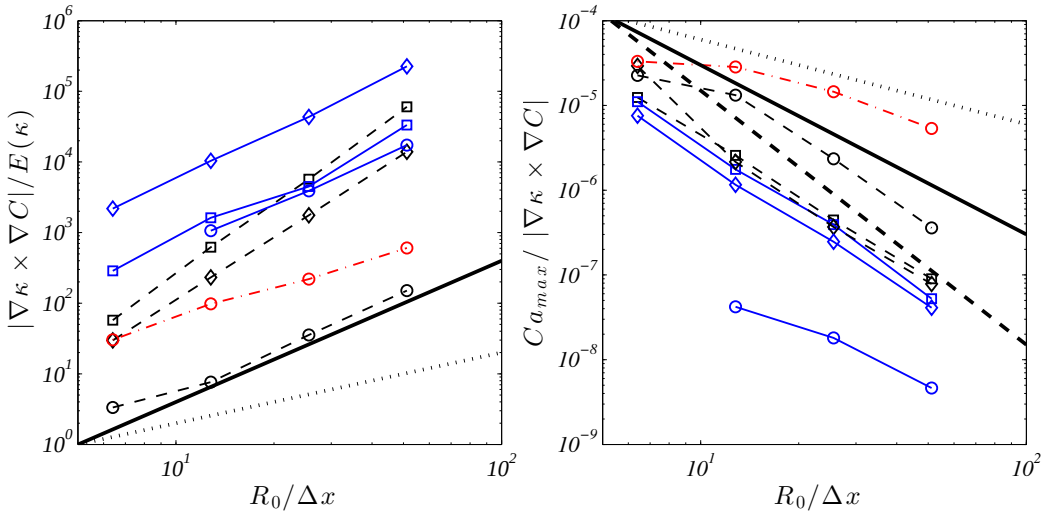

(a) Vorticity source vs curvature error

(b) Velocity vs vorticity source

Figure 4.11: Ratio of vorticity source term to curvature error (a) and ratio of spurious currents capillary number to vorticity source term (b) as a function of the spatial resolution $La = 12000$ and $We = 30$.
Legend : (–□–) VOF-FCT-CCSF ; (□) VOF-FCT-HFCSF ; (–◇–) VOF-PLIC-CCSF ; (◇) VOF-PLIC-HFCSF ; (–◯–) LS-CCSF ; (◯) LS-HFCSF ; (◯ ·) LS-SSF.
(a) (· · ·) $(R_0/\Delta x)$; (—) $(R_0/\Delta x)^2$.
(b) (· · ·) $(R_0/\Delta x)^{-1}$; (—) $(R_0/\Delta x)^{-2}$; (- - -) $(R_0/\Delta x)^{-3}$.

Laplace pressure jump

Another feature of the coupling between the surface tension scheme, the curvature calculation and the transport scheme is the accuracy in the pressure jump estimation. The decrease in spurious velocities does not always lead to a better pressure jump calculation. Indeed, Dupont and Legendre [2010] show that increasing the number of iterations in the filtering procedure of the volume fraction leads to a decrease in

spurious velocities but the numerical thickness of the pressure jump increases with filtering and a compromise therefore needs to be found to accurately calculate the Laplace pressure jump. In the present simulations, the errors in the pressure jump were generally insensitive to the changes in the Weber number and no explicit tendency was observed with the Laplace number. Figure 4.12 shows the pressure profile through the bubble along the horizontal plane of symmetry. It is seen in figure 4.12(a) that the pressure at the center of the bubble is better calculated within a LS framework (less than 0.3% error) than in a VOF framework. Although the pressure at the center of the bubble with the VOF-PLIC-HFCSF method is not so far from the pressure estimated in the LS simulations, the pressure field has peaks around the interface, whereas it is much more uniform in a LS framework.

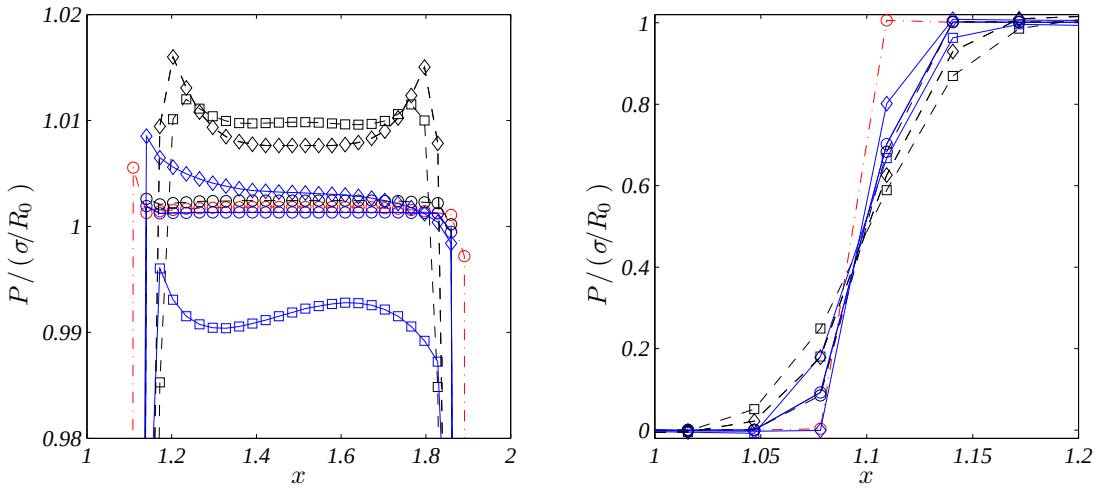

(a) (b)

Figure 4.12: Normalized pressure jump. Close up of (a) the pressure in the bubble ; (b) the pressure jump at the bubble rear cap.
Legend : (–□–) VOF-FCT-CCSF ; (□) VOF-FCT-HFCSF ; (–◇–) VOF-PLIC-CCSF ; (◇) VOF-PLIC-HFCSF ; (–◯–) LS-CCSF ; (◯) LS-HFCSF ; (⊙) LS-SSF.

Figure 4.13(a) reports the maximum pressure jump errors as a function of spatial resolution. No convergence with grid spacing is observed with any method. The importance of the transport scheme when using the height function curvature calculation is again highlighted. The VOF-PLIC transport scheme allows the maximum pressure jump errors to be significantly decreased when compared with the VOF-FCT advection scheme. However, the errors remain greater than those obtained with either VOF-FCT-CCSF and VOF-PLIC-CCSF methods, which are again similar. The LS methods and mainly the LS-CCSF method allows the maximum pressure jump errors in the domain to be minimized. Finally, the transition region of the pressure jump across the interface at the bubble rear cap is illustrated in figure 4.12(b) and quantified with the spatial convergence of the error on the total pressure jump $\Delta P_{total}/(\sigma/R_0)$ in figure 4.13(b). It is seen that compared with the continuous formulation of the surface tension force, the height function reduces the transition region and especially within a VOF framework since the smoothing procedure applied to reduce spurious currents in the CCSF methods spreads the pressure jump. However, it is clear that the sharp surface force is

the most accurate since there is no numerical thickness of the interface. The LS-SSF method also shows a better rate of convergence (slightly less than 2) than all the other methods, which all converge with first order.

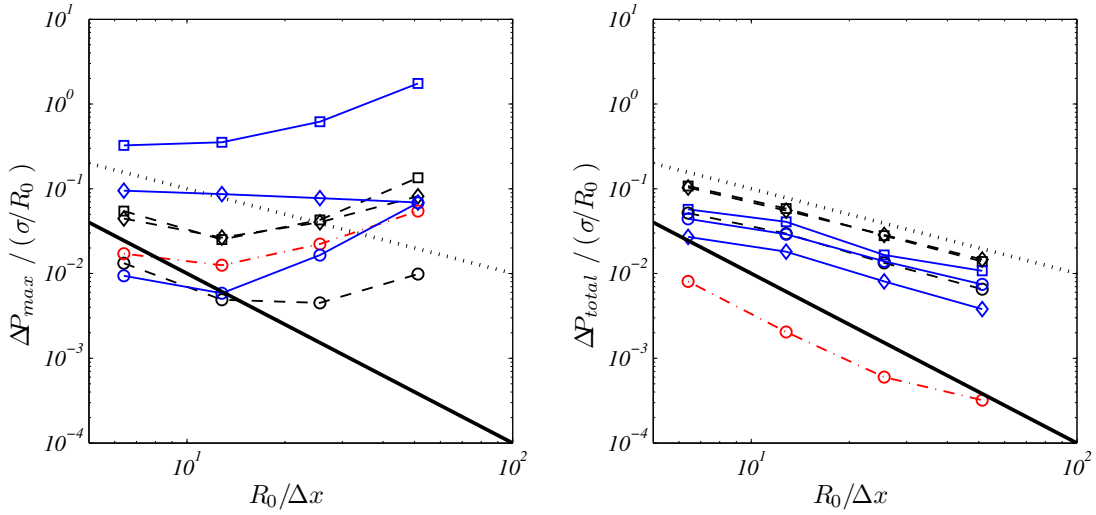

(a) $\Delta P_{max}/(\sigma/R_0)$ (b) $\Delta P_{total}/(\sigma/R_0)$

Figure 4.13: Pressure errors as a function of spatial resolution for $La = 12000$ and $We = 30$.
Legend : (–□–) VOF-FCT-CCSF ; (□) VOF-FCT-HFCSF ; (–◇–) VOF-PLIC-CCSF ; (◇) VOF-PLIC-HFCSF ; (–◯–) LS-CCSF ; (◯) LS-HFCSF ; (◯ ·) LS-SSF ; (• • •) $(R_0/\Delta x)^{-1}$; (—) $(R_0/\Delta x)^{-2}$.

4.7 Rotating bubble

A bubble placed in a rotating flow has been used previously to characterize the efficiency of the transport scheme Benkenida [1999] but not to study the efficiency of the coupling between interface advection and the surface tension force. This test is interesting since the displacement is not uni-directional like in the translating bubble, which moves along the mesh direction. Theoretically, the velocity in the frame of reference moving with the bubble should be zero, providing there are no spurious currents. Although the pressure in each phase is not constant due to the advective terms of the Navier-Stokes equations, which are not null in this case, the pressure jump at the interface should still obey the Laplace law since no shear is imposed. The theoretical velocity and pressure fields are given by equations 4.20-4.21. Images of the configuration and the spurious currents generated in such a flow after one revolution are illustrated in figure 4.14.

$$(u\,,\,v)\,(x,y) \;=\; (\,U_0 \times y\,,\,-U_0 \times x) \tag{4.20}$$

$$p(x,y) \;=\; \frac{\rho U_0^2}{2}\left((x-x_0)^2+(y-y_0)^2\right) \;+\; \begin{cases} \dfrac{\sigma}{R_0} & \text{in the bubble} \\ 0 & \text{outside} \end{cases} \tag{4.21}$$

The evolution of the maximum intensity of spurious currents with time is reported in figure 4.15. In this test case, which is slightly more complex, the predominant ef-

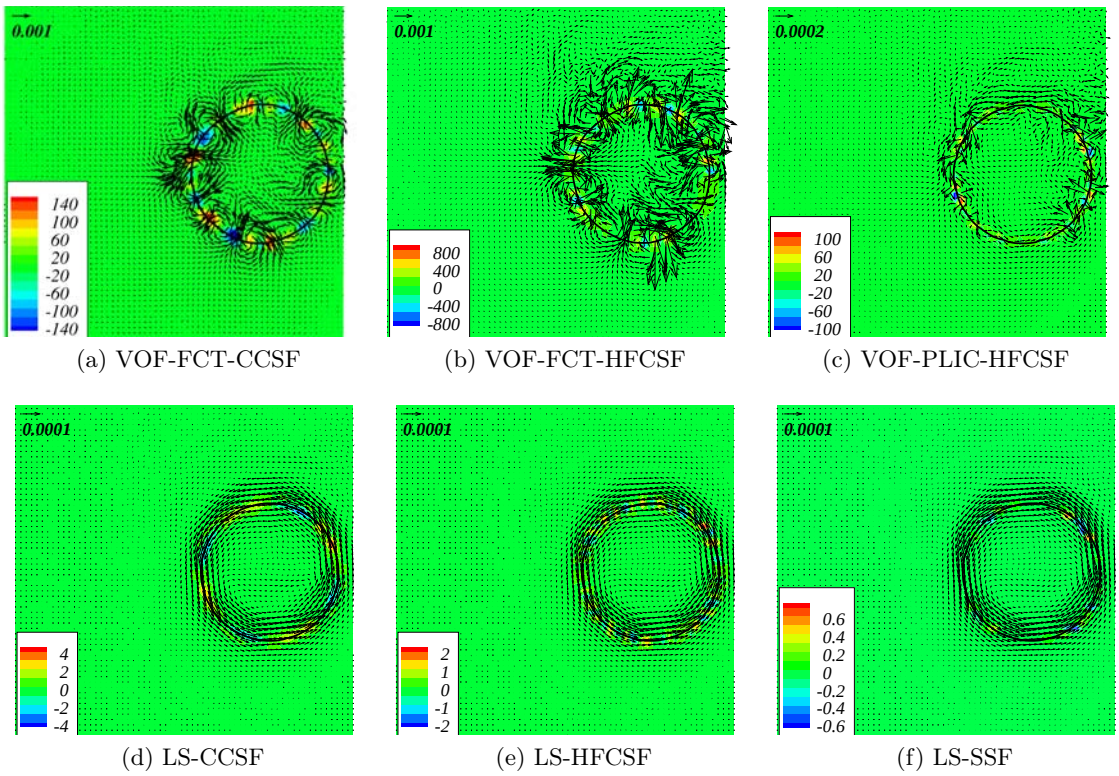

(a) VOF-FCT-CCSF (b) VOF-FCT-HFCSF (c) VOF-PLIC-HFCSF

(d) LS-CCSF (e) LS-HFCSF (f) LS-SSF

Figure 4.14: Intensity of the source term $|\nabla\kappa \times \nabla C|$ in the vorticity equation 4.11 and velocity field after the translation of a distance $1.25D$ in the frame of reference moving with the bubble (by decreasing spurious currents from (a) to (f)) for $R_0/\Delta x = 12.8$, $La = 12000$ and $We = 0.4$.

fects of the transport scheme on the spurious currents that have been observed with the translating case are enhanced. Figure 4.15 shows that the spurious currents are clearly dominated by the transport scheme. Indeed, with both curvature calculations, the use of the VOF-PLIC scheme leads to decreased spurious currents when compared with those obtained with the VOF-FCT scheme. This decrease is accentuated when compared with the translating case. Despite the smoothing procedure, spurious currents obtained with the VOF-PLIC-CCSF are reduced when compared with the VOF-FCT-CCSF method. This means that the shape errors introduced by the advection step are captured in the curvature calculation and overcome the errors associated with smoothed curvature calculations. Nevertheless, the spurious currents obtained with the VOF-PLIC transport schemes remain approximately 3 to 4 times greater than those obtained within a LS framework where both continuous methods (LS-HFCSF and LS-CCSF) and the sharp method (LS-SSF) give identical spurious velocities.

Similarly to what happens in the translating case, the maximum and mean velocities generally do not depend on the Weber number. The trends observed for the evolution of the intensity of spurious currents with the Laplace number are also qualitatively similar than in the translating case. However, they are more homogeneous than in the translating case, and the velocity scales approximately as $Ca_{max} \sim La^{-1/4}$ for most of the methods, except LS-CCSF and LS-SSF ($Ca_{max} \sim La^{-1/6}$).

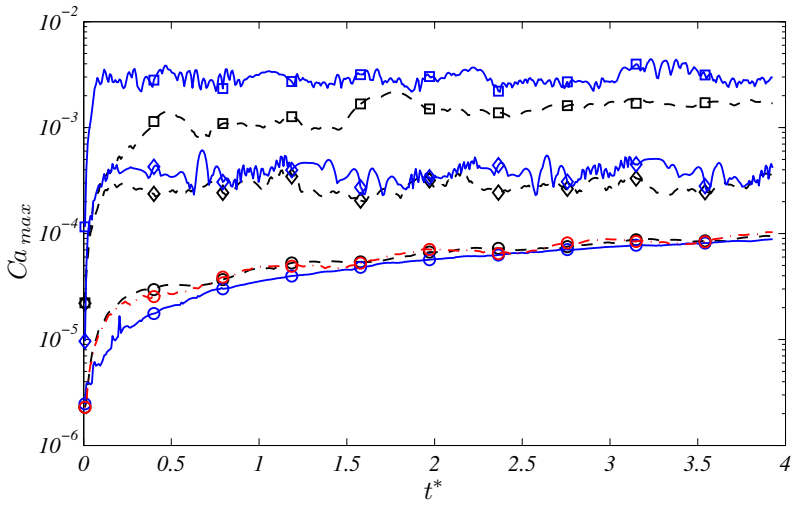

Figure 4.15: Temporal evolution of the maximum velocity of spurious currents in the frame of reference moving with the bubble for $R_0/\Delta x = 12.8$, $La = 12000$ and $We = 30$.
Legend : (–□–) VOF-FCT-CCSF ; (□) VOF-FCT-HFCSF ; (–◇–) VOF-PLIC-CCSF ; (◇) VOF-PLIC-HFCSF ; (–◯–) LS-CCSF ; (◯) LS-HFCSF ; (◯ ·) LS-SSF.

4.7.1 Convergence with spatial resolution

The convergence of the different methods with spatial resolution is presented in figure 4.16, which shows the capillary number based on the maximum velocity as a function of the grid resolution. As previously observed with the translating case, with the VOF-FCT-HFCSF scheme, the intensity of spurious currents is maximum and increases with mesh resolution. Within a VOF without reconstruction framework (VOF-FCT), the intensity of spurious currents is lower with the CCSF model than with the HFCSF scheme but the same trend with mesh refinement is observed. Similarly, the intensity of spurious currents increases as the mesh is refined with the VOF-PLIC-CCSF. At low resolution, the same intensity of spurious currents is found with the VOF-PLIC-HFCSF method but it decreases with mesh resolution. However, the rate of convergence is approximately one third, which is smaller than in the translating case (close to one). Concerning the LS transport scheme that minimizes spurious currents, while the LS-CCSF and LS-SSF methods showed a rate of convergence about 1.5 in the translating case, the magnitude of the spurious currents decreases in this flow configuration as long as the number of cells per bubble radius is lower than 13 but then stabilizes when refining the mesh further. The LS-HFCSF method shows the same trend as in the translating case and exhibits no convergence with spatial resolution.

Concerning the pressure errors and their convergence with grid refinement, the observations do not differ from the translating case, except that the differences between VOF-FCT and VOF-PLIC transport schemes are again enhanced. As it has been observed with the spurious velocities, the rate of convergence for the pressure jump decreases in this test case when compared with the translating one. The LS-CCSF method allows the maximum pressure jump error to be minimized but none of the methods converge with spatial resolution. The errors obtained with the VOF-FCT-HFCSF and LS-HFCSF methods increase when decreasing the cell size. It is interesting to note a difference with the translating case, although the Sharp Surface Force formulation still imposes a sharp pressure jump, this method does not appear to

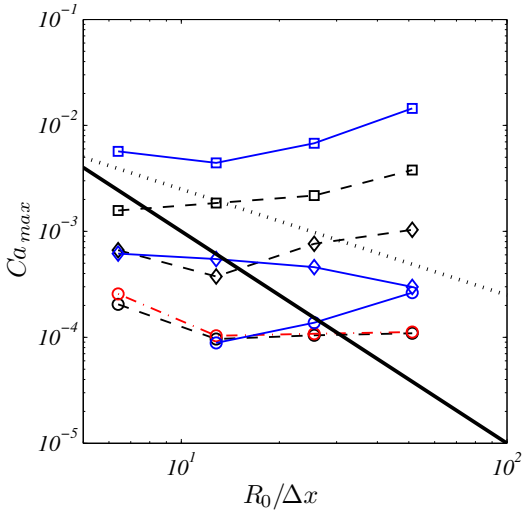

Figure 4.16: Dimensionless maximum velocity of spurious currents as a function of spatial resolution for $La = 12000$ and $We = 30$.
Legend : (–□–) VOF-FCT-CCSF ; (□) VOF-FCT-HFCSF ; (–◇–) VOF-PLIC-CCSF ; (◇) VOF-PLIC-HFCSF ; (–◯–) LS-CCSF ; (◯) LS-HFCSF ; (◯ ·) LS-SSF ; (• • •) $Ca_{max} \sim (R_0/\Delta x)^{-1}$; (—) $Ca_{max} \sim (R_0/\Delta x)^{-2}$.

be superior to the VOF-PLIC-HFCSF, LS-CCSF or LS-HFCSF methods, which give the best results in this rotating flow regarding the total average pressure jump. Finally, the LS-CCSF method seems to be a good compromise between spurious currents intensity and pressure jump calculation. The VOF-PLIC-HFCSF method also shows good results concerning the pressure jump estimation that are close to those obtained with the LS-CCSF method.

4.8 Summary of static, translating and rotating cases

A summary of the range of spurious currents observed in this study for the different methods and test cases is reported in figure 4.17 and in table 4.1 through approximate correlations with the Laplace number and spatial resolution. The superiority of VOF-PLIC-HFCSF and VOF-FCT-HFCSF methods in the static case show that the accurate curvature calculation achieved with the height function method is of main importance. Figures 4.18(a)-(b) show the ratio of maximum spurious currents intensity in dynamic cases over that obtained in the static case. This ratio is close to one for all the CCSF methods, as well as the SSF method. This indicates that for these methods, the errors in the curvature calculation after advection in these cases are of same order of magnitude than those obtained in a static case. With these methods, although the transport scheme can play a non negligible role in the generation of spurious currents, these observations indicate that the main spurious currents magnifiers are the curvature calculation (and the redistancing step in LS methods) rather than the transport scheme. On the other hand, with VOF-PLIC-HFCSF and VOF-FCT-HFCSF methods, and to a lesser extent with LS-HFCSF, the spurious currents are clearly magnified by the transport errors. Indeed, the difference between the static and dynamic cases highlights the strong interaction between interface advection and the spurious currents with an accurate curvature calculation like the height function. From a general point of view, the dynamic cases show that the curvature errors are dominated by advection errors

rather than inaccurate curvature calculation and LS methods minimize the spurious currents.

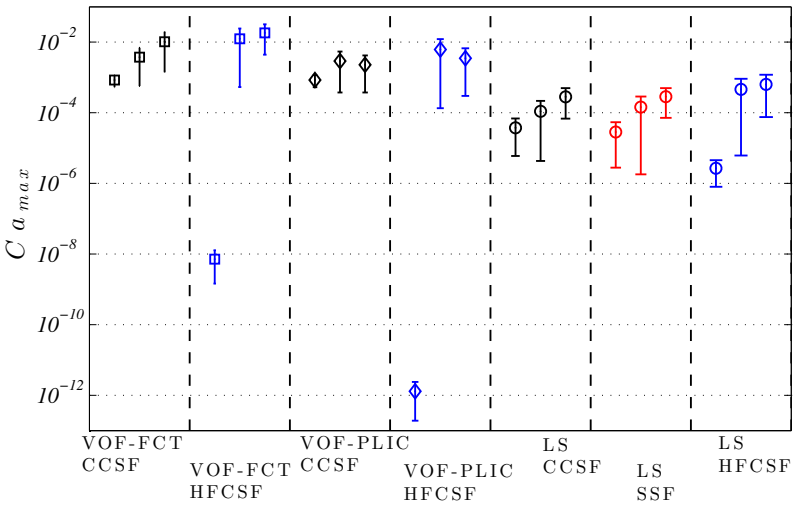

Figure 4.17: Range of maximum spurious capillary number generated with the different methods for $1.2 \leq La \leq 12000$; $0.4 \leq We \leq 30$ and $6.4 \leq R_0/x \leq 51.2$. For each method, the static, translating and rotating cases are reported from left to right. The symbols represent the average values of spurious velocities obtained within the range of fluid properties and spatial resolution covered and the error bar corresponds to the minimum and maximum values of spurious velocities obtained.

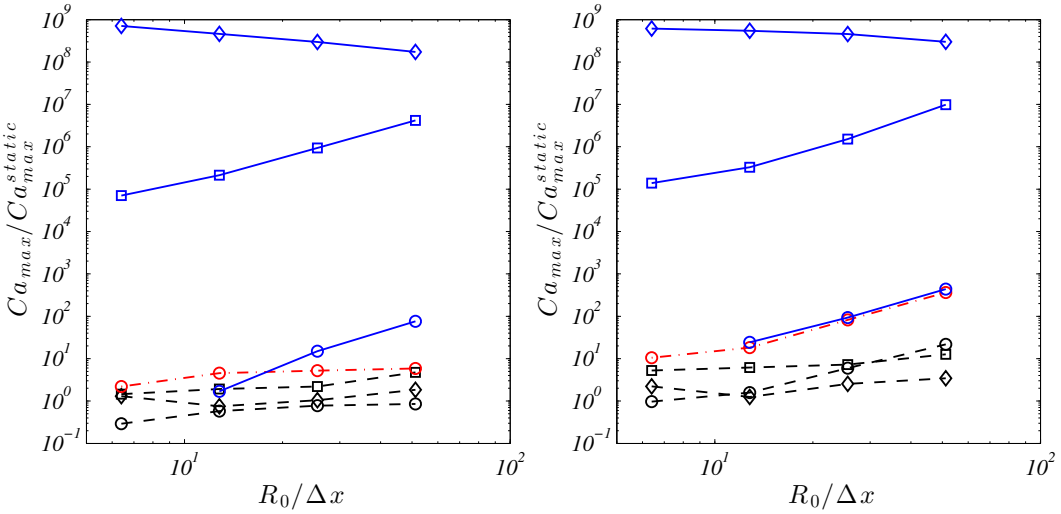

(a) Translation

(b) Rotation

Figure 4.18: Ratio of maximum spurious currents intensity in the translating (a) and rotating (b) cases over spurious currents intensity in the static case.
Legend : (–□–) VOF-FCT-CCSF ; (□) VOF-FCT-HFCSF ; (–◇–) VOF-PLIC-CCSF ; (◇) VOF-PLIC-HFCSF ; (–◯–) LS-CCSF ; (◯) LS-HFCSF ; (◯ ·) LS-SSF.

method	- spurious currents magnifier	Ca_{max} static case	Ca_{max} translating case	Ca_{max} rotating case
VOF-FCT-CCSF	- curvature calculation	10^{-3}	$1 \times 10^{-3} \left(\frac{R_0^*}{\Delta x}\right)^{0.4}$	$2 \times 10^{-2}\, La^{-\frac{1}{4}} \left(\frac{R_0^*}{\Delta x}\right)^{0.4}$
VOF-FCT-HFCSF	- advection errors	$1.4 \times 10^{-8} \left(\frac{R_0^*}{\Delta x}\right)^{-1.6}$	$2 \times 10^{-2}\, La^{-\frac{1}{4}} \left(\frac{R_0^*}{\Delta x}\right)^{0.4}$	$6 \times 10^{-2}\, La^{-\frac{1}{4}} \left(\frac{R_0^*}{\Delta x}\right)^{0.4}$
VOF-PLIC-CCSF	- curvature calculation	see VOF-FCT-CCSF	$7 \times 10^{-4} \left(\frac{R_0^*}{\Delta x}\right)^{0.2}$	$7 \times 10^{-3}\, La^{-\frac{1}{4}} \left(\frac{R_0^*}{\Delta x}\right)^{0.2}$
VOF-PLIC-HFCSF	- advection errors	10^{-12}	$5 \times 10^{-3}\, La^{-\frac{1}{4}} \left(\frac{R_0^*}{\Delta x}\right)^{-0.7}$	$5 \times 10^{-3}\, La^{-\frac{1}{4}} \left(\frac{R_0^*}{\Delta x}\right)^{-0.3}$
LS-CCSF	- curvature calculation and redistancing step	$6.1 \times 10^{-5} \left(\frac{R_0^*}{\Delta x}\right)^{-1.8}$	$4 \times 10^{-5} \left(\frac{R_0^*}{\Delta x}\right)^{-1.4}$	$5 \times 10^{-4}\, La^{-\frac{1}{6}}$
LS-HFCSF	- redistancing step and advection errors	$3.6 \times 10^{-6} \left(\frac{R_0^*}{\Delta x}\right)^{-1.3}$	$3 \times 10^{-4}\, La^{-\frac{1}{4}} \left(\frac{R_0^*}{\Delta x}\right)^{1.4}$	$10^{-3}\, La^{-\frac{1}{4}} \left(\frac{R_0^*}{\Delta x}\right)^{0.8}$
LS-SSF	- redistancing step	$5.7 \times 10^{-5} \left(\frac{R_0^*}{\Delta x}\right)^{-2.1}$	$5 \times 10^{-5} \left(\frac{R_0^*}{\Delta x}\right)^{-1.7}$	$5 \times 10^{-4}\, La^{-\frac{1}{6}}$

Table 4.1: Summary of the main characteristics of the transport schemes and calculations of the surface tension force used for the static, translating and rotating test cases. The rates of convergence with spatial resolution, as well as the dependencies on the Laplace number, have been simplified to make the comparison easier and stress only the major differences. In order to allow an easy comparison between the methods at a common resolution of 12.8 cells per bubble radius, the spatial resolution is expressed with a modified dimensionless bubble radius $R_0^*/\Delta x = R_0/(12.8\Delta x)$. The coefficient of the scaling laws therefore corresponds to the spurious currents intensity for $R_0/\Delta x = 12.8$ and $La = 1$.

4.9 Taylor bubble dynamics

The present section deals with the numerical simulation of Taylor flow in microchannels, which is of practical interest since it is encountered in many applications *e.g.* lab-on-a-chip devices, flow boiling, film coating, micro chemical reactors, etc. The motion of Taylor bubbles in microchannels is investigated with particular attention to the effects of the scalar field representing the interface and the transport scheme (VOF-FCT and LS) with a given surface tension scheme (CCSF). The LS-CCSF which appears to be a good compromise between spurious currents generation, convergence with grid refinement and pressure calculation, is compared with the method initially implemented in *JADIM*. This flow configuration appears to be very sensitive to spurious currents since the capillary forces are often predominant (usually $Ca << 1$ and $We << 1$). In addition, the flow tends towards a stationary solution in the frame of reference moving with the bubble and spurious currents can appear when the flow is developing. The case considered here is an axisymmetric tube with periodic boundary conditions in order to simulate a bubble train in a channel filled with a liquid. The dimensionless radius of the channel is $R^* = 1$ and the length is $L_x^* = 8$. A pressure gradient is imposed across periodic boundary conditions to induce the motion of the fluids initially at rest. The Laplace number is $La = 280$ and the capillary and Reynolds numbers vary with the imposed pressure gradient. For $Ca \geq 0.05$, the Laplace number has been reduced to $La = 2.8$ so that the Reynolds number remains lower than 10 in the present simulations. In order to correctly resolve the flow, the mesh needs to be fine enough close to the walls in order to capture the thin liquid film between the bubble and the channel wall. Furthermore, the bubble caps also need to be well resolved in order to accurately estimate the pressure jump at the rear and front caps of the bubble. The characteristics of the meshes that have been tested are summarized in table 4.2 and the time step constraint due to capillary forces is indicated by making it dimensionless with the time needed for a bubble (with $Ca \sim 0.005$) to cross the domain. This dimensionless capillary time step constraint then corresponds approximately to the number of iterations that are necessary to complete one cycle in the periodic domain. The capillary time step constraint is based on the minimum cell size containing the interface instead of the minimum cell size in the whole domain.

mesh	$N_x \times N_y$	$\Delta y_{j+1}/\Delta y_j$	Δy_{min}	$(L_x^*/U_B)/\Delta t_{cap,min}$
M1	128×32	0.9	3.967×10^{-3}	739400
M2	128×64	0.94	1.242×10^{-3}	2473000

Table 4.2: Different meshes used and corresponding numerical parameters.

As long as the bubble velocity is lower than the maximum velocity in the slug, which is observed at low capillary numbers, the flow in the liquid slug should be composed of a recirculation loop and a film flow. When the bubble velocity is close to the mean flow velocity in the slug, the recirculation loop occupies a major part of the channel and the film is very thin (Taylor [1961], Abadie et al. [2013]). Although this structure is observed qualitatively in all the LS-CCSF and the VOF-FCT-CCSF simulations for $Ca \geq 0.01$, at lower capillary numbers, the VOF-FCT-CCSF simulations present an additional liquid recirculation loop in the vicinity of the bubble nose cap as can be seen in figure 4.19. This phenomenon is enhanced when the number of smoothing iterations is decreased. Decreasing the capillary number, *i.e.* increasing the surface tension effects when compared to viscous forces, also enhances this phenomenon. These additional local recirculation loops are attributed to spurious currents since the vorticity generated

numerically looks very similar to the spurious currents generated in the translating bubble case. The additional recirculation loop that is present in VOF-FCT-CCSF simulations decreases in size when increasing the capillary number and vanishes for a capillary number $Ca \sim 0.02$, which is in agreement with previous observations and characterization of spurious currents made with the VOF-FCT-CCSF method developed in *JADIM* (Dupont and Legendre [2010], Abadie et al. [2012]). While the authors did not comment this additional recirculation loop in Taylor flow, it was also present in Hoang et al. [2013] in which the CCSF method is used coupled to a VOF scheme with an artificial compression term to keep a sharp interface in a VOF without geometrical reconstruction framework. On the other hand, with both an accurate curvature calculation based on height function and an accurate VOF-PLIC transport scheme, the correct flow structure was captured in Afkhami et al. [2011] at low capillary numbers, down to $Ca = 0.005$, with the *Gerris* code.

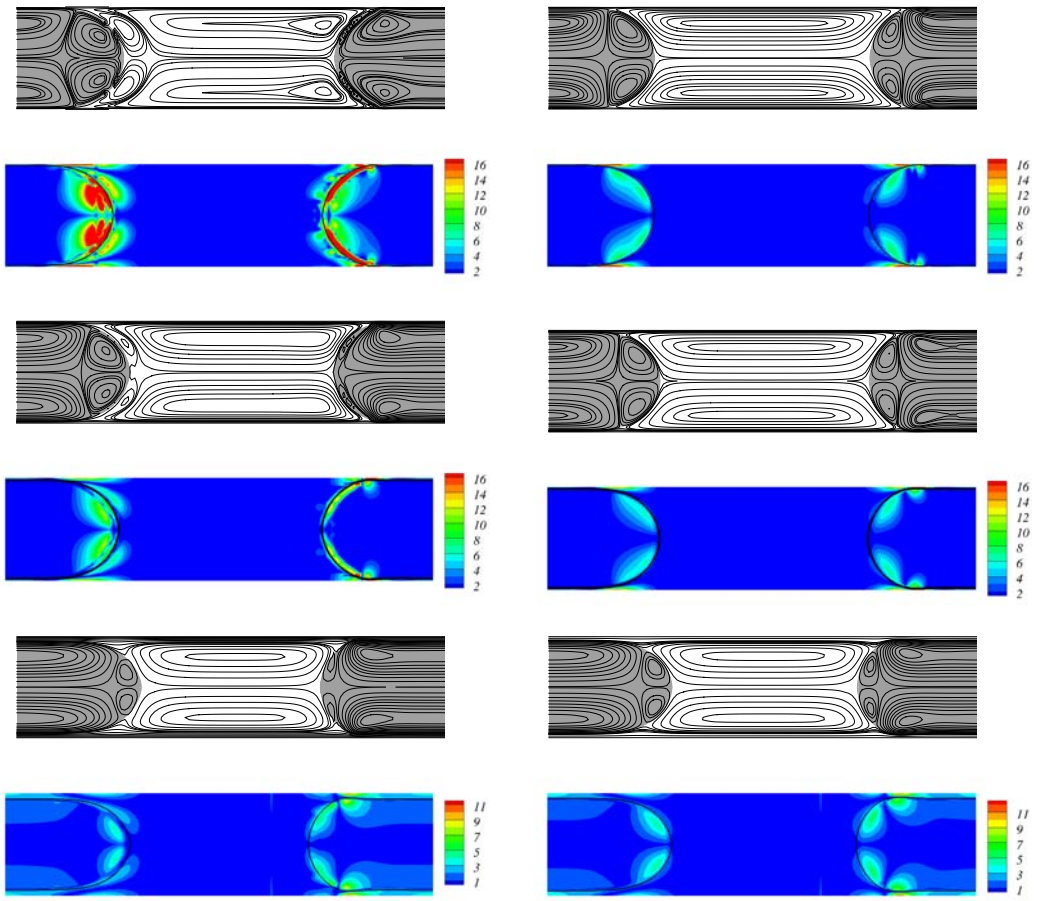

Figure 4.19: Streamlines and vorticity field in Taylor flow in a microchannel. From top to bottom : $Ca = [0.002; 0.005; 0.025]$; left : VOF-FCT-CCSF, mesh 128×32 ; right : LS-CCSF, mesh 128×32. The vorticity field of the equivalent single phase flow of mean velocity U_{TP} has been subtracted.

Although Harvie et al. [2006] were not able to conclude on the effects of spurious currents on the study of free bubble rise, these effects on the local velocity field in Taylor flow are clearly illustrated here. Figure 4.20 shows the effects of spurious currents on the slip velocity between the bubble and the mean velocity in the slug $W = (U_B - U_{TP})/U_B$, where $U_{TP} = U_{GS} + U_{LS}$ is the sum of the gaz and liquid su-

perficial velocities. The aptitude of a method to correctly estimate this dimensionless velocity is evaluated by comparing the values obtained with the correlation proposed by Aussillous and Quéré [2000] (given in chapter 6, equation 6.5) who extended Bretherton s theoretical lubrication analysis (Bretherton [1961]) to higher capillary numbers. As it was qualitatively observed with the local velocity field in figure 4.19, the difference between VOF-FCT-CCSF and LS-CCSF simulations is enhanced when the capillary number decreases. Figure 4.20 shows that the LS method allows the bubble slip velocity to be accurately predicted in a wide range of capillary numbers, while the VOF-FCT-CCSF method overestimates the slip velocity and thus, the liquid film thickness since they are directly related due to the zero velocity in the liquid film surrounding the bubble. However, with both the VOF-FCT-CCSF and LS methods, the pressure drop at the nose and rear caps of the bubble estimated from our simulations is in good agreement with the results from Hazel and Heil [2002] who simulated the propagation of a semi-infinite bubble by solving the free surface Stokes equations with a finite-element method. The difference between the two methods at the lowest capillary number simulated, which is the most sensitive to spurious currents, is only 2.4% while the difference in the slip velocity is about 30%. An advantage of the LS method is that no smoothing needs to be introduced to reduce spurious currents, whereas 12×6 smoothing iterations were employed for the computation of the curvature and orientation/spreading of the capillary force, respectively, in VOF-FCT-CCSF method as recommended in Dupont and Legendre [2010]. As a result, the pressure drop is sharper in the LS simulations than in the VOF-FCT-CCSF simulations.

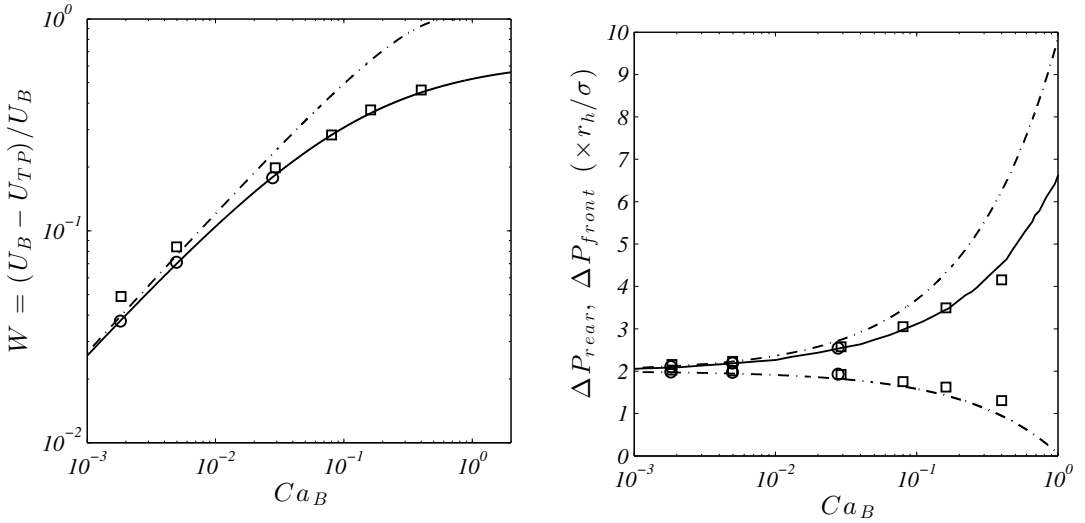

Figure 4.20: (a) Dimensionless slip velocity W versus the capillary number Ca_B. Legend : (□) VOF-FCT-CCSF ; (∘) LS-CCSF ; (dash-dotted line) Bretherton [1961] ; (straight line) Aussillous and Quéré [2000] . (b) Pressure drop at the front and rear caps of the bubble. Legend : (□) VOF-FCT-CCSF ; (∘) LS-CCSF ; (dash-dotted line) Bretherton [1961] ; (straight line) Hazel and Heil [2002].

It has generally been shown in the static, translating and rotating bubble cases that the intensity of the spurious currents obtained with the VOF-FCT-CCSF method does not decrease with spatial resolution. As a result, it is not surprising to see that the non-physical recirculation loop is not reduced with mesh size, as shown in figure 4.21

for $Ca = 0.005$. In fact, the vorticity intensity generated at the front cap of the bubble actually increases when the mesh is refined in the VOF-FCT-CCSF simulations.

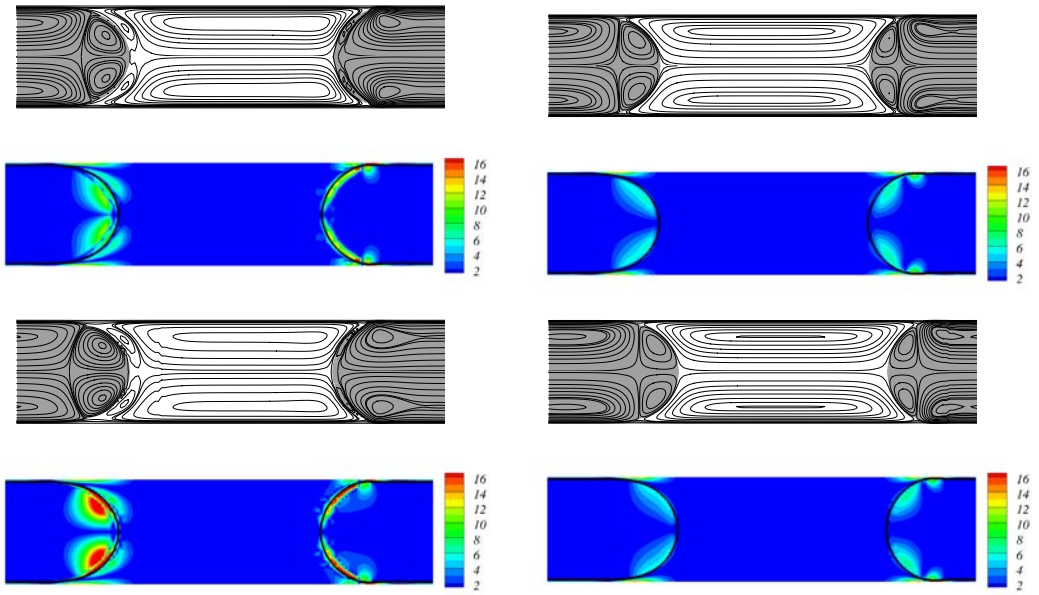

Figure 4.21: Streamlines and vorticity field in Taylor flow in a microchannel ($Ca = 0.005$) . Top left : VOF-FCT-CCSF, mesh 128×32 ; top right : LS-CCSF, mesh 128×32 ; bottom left : VOF-FCT-CCSF, mesh 128×64 ; bottom right : LS-CCSF, mesh 128×64. The vorticity field of the equivalent single phase flow of mean velocity U_{TP} has been subtracted.

The errors obtained on the dimensionless slip velocity in comparison with Aussillous & Quéré correlation are given in table 4.3. It is shown that the error for a capillary number $Ca \sim 0.005$ is significant with the VOF-FCT-CCSF simulations and does not decrease significantly with mesh refinement. However, the results obtained with a LS-CCSF formulation are satisfactory even with the coarsest mesh and are in very good agreement with the correlation of reference (Aussillous and Quéré [2000]) when the number of grid points is increased.

mesh	$E(W)$(VOF-FCT-CCSF)	$E(W)$(LS-CCSF)
M1	20.44%	1.88%
M2	18.71%	0.31%

Table 4.3: Error on the dimensionless slip velocity for a capillary number $Ca \sim 0.005$.

Finally, it is expected that the effects of spurious currents on the Taylor bubble dynamics can also significantly alter computations of heat and mass transfer phenomena since the non-physical recirculation loop will produce a kind of buffer zone and limit the transfer from the bubble to the slug when transfer is dominated by convective effects.

4.10 Conclusion

The generation of spurious currents and their effects on the velocity field in multiphase microfluidics has been investigated through the analysis of several numerical

methods. A comparison of numerical methods comprising the transport scheme (VOF-FCT, VOF-PLIC and LS), the surface tension scheme (continuum or sharp surface force) and the curvature calculation (height function or divergence of the normal to the interface) with the same flow solver has been carried out. It can be concluded that the height function curvature calculation is very accurate and is particularly interesting for the case of static bubbles and near-static bubble or oscillating bubbles (Herrman [2008], Fuster et al. [2009]). However, since the errors generated during the advection step are captured while they are smoothed with the convolution method, the height function method needs to be coupled to an accurate transport scheme, as it has been shown with the translating and rotating cases in this study. Otherwise, the classic CSF formulation with a smoothing of the volume fraction gives better results in terms of maximum spurious currents intensity. Although, when using the Level Set formulation, the exact balance between pressure and capillary forces reached with the VOF-HFCSF methods is not achieved due to the redistancing step, it has been shown that the spurious currents are decreased in dynamic cases. Similarly to the VOF-HFCSF methods, the sharp surface force that interpolates the position of the interface and the height function technique require accurate transport and redistancing schemes since they also precisely capture the slight errors created in these steps. Finally, it is shown that these test cases are well adapted to the characterization of spurious currents in Taylor flow. The spurious currents generated in VOF-FCT simulations are shown to significantly modify the structure of the flow by producing an additional recirculation zone. The LS-CSF method is shown to be able to estimate the bubble slip velocity and the pressure drop across the bubble with good accuracy in a wide range of capillary numbers. In addition, since only one bubble is simulated, the global mass redistribution allows mass conservation problems to be avoided. However, cases involving several bubbles (or drops) still require additional work to resolve this mass conservation problem. Two possible solutions may be considered in future work: the improvement of the transport scheme in a VOF framework coupled to height function curvature calculation; and the coupling between VOF and LS methods (Sussman and Puckett [2000]). An other topic that should be considered for the simulation of Taylor flows is the (semi-)implicitation of the surface tension force (Raessi et al. [2009]).

In the following, the VOF-FCT-CCSF method has been used for the simulation of Taylor flow for Capillary number $Ca_B \geq 0.08$ and the LS-CCSF method has been used for the simulation of Taylor flow at low capillary numbers $Ca_B < 0.08$.

Chapter 5

Bubble dispersion

Contents

5.1 State of the art

The generation of Taylor bubble trains has been extensively studied in the literature and especially experimentally. Much work has been dedicated to the development of flow pattern maps which define the transition between the regimes presented in figure 1. Slug flow is generated for a wide range of gas and liquid velocities and this gas-liquid dispersion is very regular, leading to a flow with homogeneous bubble break-up frequencies, volumes, and velocities. Depending on the operating conditions and the microchannel geometry, the bubble volume and length vary.

In the literature, many ways to merge the gas and liquid phases exist, including co-flowing systems, flow-focusing devices through a contraction (Anna et al. [2003], Ganan-Calvo [2004]), flow-focusing devices in a cross (Cubaud et al. [2005], Fu et al. [2009]), and T-junctions, where the fluids merge either front to front or with a right angle (Garstecki et al. [2006], Van Steijn et al. [2007, 2010], Fu et al. [2010b], Abadie et al. [2012]). Detailed reviews about the different methods to generate droplet or bubbles in microfluidic systems and the observed flow regimes can be found in Christopher and Anna [2007], Zhao and Middleberg [2011], Nunes et al. [2013].

Simple flow focusing devices were first implemented by Anna et al. [2003] and Ganan-Calvo [2004] to produce small droplets and bubbles, respectively. Two immiscible fluids initially flow into separate channels and then both fluids merge and enter a contraction where a jet is formed. The instability of this jet leads to its rupture and the formation of droplets or bubbles whose sizes are comparable with the size of the orifice. Ganan-Calvo [2004] correlated their experimental results (in the range $0.1 < Re < 20$ and $40 < We < 1000$) with the gas to liquid flow rate ratio:

$$\frac{D_B}{D} = 1.1 \left(\frac{Q_G}{Q_L} \right)^{0.4} \tag{5.1}$$

where D_B is the bubble diameter.

5.1.1 Flow focusing devices in a cross-junction

Flow-focusing devices in a cross-junction were introduced by Cubaud et al. [2005]. Experiments and numerical simulations were conducted at the junction of four square channels. The formation of monodisperse bubbles was achieved and the bubble size was related to the channel size and the volume fraction of liquid with a linear decrease. The simple mechanism will be developed in the next section since it is the basis of the bubble generation mechanism that will be analyzed further in this chapter.

Recently, Fu et al. [2009, 2010a] performed experiments in a cross-junction with square microchannels. Experimental visualization and $\mu-$PIV measurements were used to investigate the bubble formation mechanism which was divided into three steps: the expansion of the gas phase, the squeezing of the gas phase and the rapid collapse or pinch-off of the gas thread. The effects of gas and liquid flow rates, as well as the effects of fluid properties on the squeezing of the gas thread and its rapid collapse at the end of the bubble formation were analyzed. The bubble length was correlated with the gas to liquid flow rate ratio and the Reynolds number.

Numerical simulations using a Lattice Boltzmann method were carried out to model the droplet formation in a microfluidic cross-junction at low capillary numbers by Liu and Zhang [2011]. The droplet length was found to evolve linearly with the gas to liquid

flow rate ratio in the squeezing regime and both coefficients of the linear relationship were shown to obey a unique scaling law with the capillary number. The exponent on the capillary number appeared to vary with both the aspect ratio of the channel and the gas to liquid entrance width ratio.

5.1.2 T-shaped junctions

Bubble formation in T-shaped junctions has been widely studied over recent years. Garstecki et al. [2006] investigated the formation of droplets and bubbles in side-entering T-junctions. A discussion of the forces involved in the mechanism of break-up at low capillary number was provided. The three main forces acting on the bubble tip are the surface tension force, the shear stresses and the squeezing pressure. Indeed, as the dispersed phase obstructs the main channel, the continuous phase flows in the lubrication film and the pressure upstream the bubble or droplet increases. The estimation of this squeezing pressure is based on the lubrication analysis (Bretherton [1961], Stone [2005]). The estimation and the balance of these forces under the assumption that the squeezing pressure dominates the shear stress force lead to a simple scaling law to estimate the droplet length:

$$\frac{L_B}{w} = 1 + \frac{w_{in}}{w}\frac{Q_G}{Q_L} \ . \tag{5.2}$$

Bubble and droplet formation present similarities in the squeezing regime and this correlation was compared with experiments in both liquid-liquid and gas-liquid systems.

Van Steijn et al. [2007, 2010] performed $\mu-$PIV measurements of the bubble formation in side-T junctions. They confirmed that the bubble formation depends on the gas to liquid flow rate ratio and the geometry. They extended this model (equation 5.2) to a wide variety of side-T junctions geometries comprising channel aspect ratio and gas to liquid inlet width ratio.

Christopher et al. [2008] conducted experiments on the droplet break-up in a T-junction and studied the transition between the squeezing regime that occurs at very low capillary number and the dripping regime where the influence of the viscous stresses cannot be neglected. They present a model for the estimation of the minimum droplet length (or volume) generated in a T-junction that is based on a similar force balance than that in Garstecki et al. [2006]. Both the shear stresses and squeezing pressures are considered and the minimum droplet length is written as a function of the capillary number:

$$\left(1 - \frac{L^{min}_{droplet}}{w}\right)^3 = \frac{L^{min}_{droplet}}{w} Ca_L \ . \tag{5.3}$$

However, they showed that their model generally underestimates the droplet lengths obtained experimentally.

Numerous numerical simulations have been carried out using different numerical techniques to gain insight on the bubble or droplet formation mechanism: VOF method to study 2D channels (Arias et al. [2011]) and droplet break-up in symmetrical diverging T-junctions (Afkhami et al. [2011]); Lattice-Boltzmann method (Van der Graaf et al. [2006], Gupta and Kumar [2010]) to study the effects of capillary number and channel aspect ratio on the bubble lengths; and phase-field model (De Menech et al. [2008]) to study the transition between squeezing and dripping regimes in square channels.

The aim of this chapter is to characterize the bubble dispersion generated with three different geometries shown in figure 5.1. We firstly focus on a flow-focusing

(a) cross-junction (b) side-T junction (c) T-junction

Figure 5.1: Illustration of the three junctions studied.

device where the fluids merge in a cross-junction. The mechanism of break-up is briefly described with respect to the literature for this fluid contacting method. The effects of fluid properties and aspect ratio ($1 \leq \alpha \leq 4$) are then studied. The gas-liquid flow generated in this flow-focusing device is then compared with that generated in two other different T-shaped junctions.

5.2 Flow focusing devices

5.2.1 Bubble generation mechanism

According to the experimental work carried out by Cubaud et al. [2005], at low capillary numbers, bubble dispersion in flow-focusing devices is controlled by the gas and liquid flow rates. It is argued that due to the viscosity ratio between both phases, the resistance of the gas to the liquid flow at the intersection is negligible and the time necessary for the liquid to pinch the gas finger of width w is inversely proportional to the liquid flow rate. Thus, this pinching time is estimated as $t_{pinching} = \frac{w}{U_L}$. During this pinching time, the bubble growth can be estimated from the average bubble velocity as $L_B = U_B t_{pinching} \sim (U_L + U_G) t_{pinching}$. This leads to the following expression for the bubble length:

$$\frac{L_B}{w} \sim 1 + \frac{U_G}{U_L}. \tag{5.4}$$

Expression 5.4 should be used carefully since the estimation of the average bubble velocity as $U_B = U_L + U_G = U_{TP}$ is valid at low capillary numbers only. Indeed, the ratio of the bubble velocity to the average two-phase velocity U_{TP} increases with the capillary number (Bretherton [1961]).

Similarly to the bubble formation in T-junctions, the bubble generation mechanism in the cross-junction can be split into two main steps:

- the filling stage where the bubble enters the main channel while the liquid flows around the bubble until the gas fills a major part of the cross-sectional area of the channel (figure 5.2(a)-(d)),

- the squeezing stage where the bubble occupies almost the whole cross-section of the channel and the liquid barely flows around the bubble, which is then squeezed (figure 5.2(d)-(f)).

A third stage corresponding to the rapid collapse of the gas thread, which was studied in Fu et al. [2009, 2010a] and Dollet et al. [2008], could be considered but its characteristic time is much smaller than that of the two other mechanisms and it will be considered that below a certain distance, the break-up occurs instantaneously in the experiments.

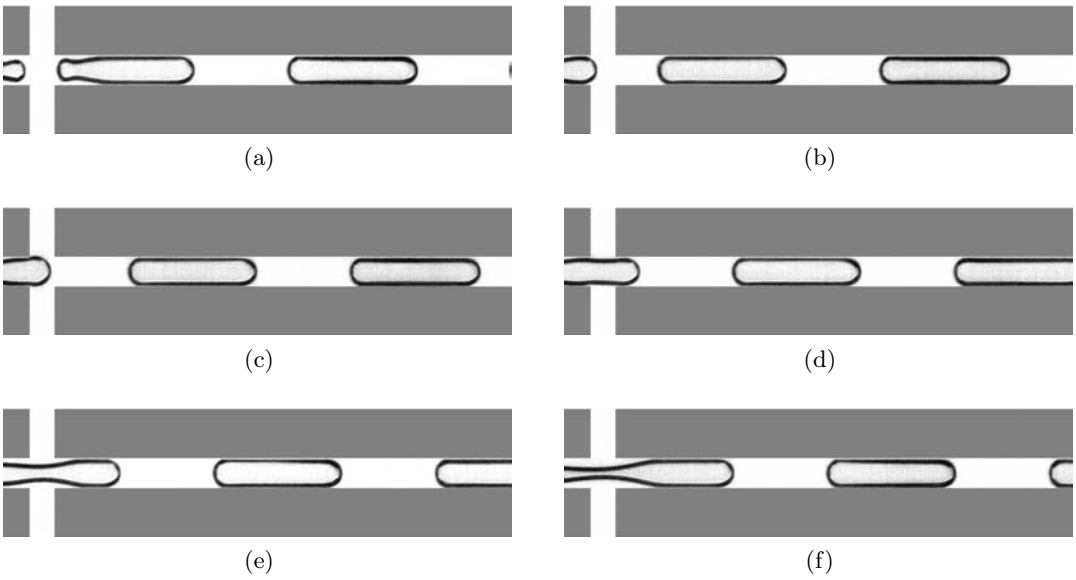

Figure 5.2: Bubble generation sequence in a cross-junction.

These steps are deduced from the competition between three forces: the capillary force prevents the bubble to break while the viscous stress and the squeezing pressure in the side channels act on the bubble to deform the interface. During the first step, while the bubble grows in the cross-junction, the pressure increases in the side channels since the available cross-sectional area for the liquid to flow is reduced. The forces acting on the bubble then grow and finally overcome the capillary force and the squeezing stage starts. Figure 5.3 shows the position where the neck of the bubble is estimated and its evolution in time for a fixed liquid velocity and three different gas velocities. This figure illustrates the two steps where the width of the bubble at the intersection grows until filling almost the entire section. Once the maximum neck size is reached, the bubble neck starts to collapse.

The period of bubble generation is then the sum of these two characteristic times:

$$\frac{1}{f} = t_{growth} = t_{filling} + t_{squeezing} \tag{5.5}$$

It is seen in figure 5.3 that the time needed to reach the maximum neck width is a function of the gas velocity. Indeed, at fixed liquid velocity, the time of the filling stage is inversely proportional to the gas velocity. Concerning the squeezing stage, the duration is constant with the three flow rate ratios, *i.e.* the time of the squeezing stage is inversely proportional to the liquid velocity. These characteristic times can then be estimated from the operating conditions and the geometry:

$$t_{growth} \sim \frac{L_B}{u_{growth}} \tag{5.6}$$

$$t_{filling} \sim \frac{w}{u_{filling}} \tag{5.7}$$

$$t_{squeezing} \sim \frac{w_{neck}}{u_{squeezing}} \tag{5.8}$$

where w_{neck} is the width of the filament of air where the bubble is pinched.

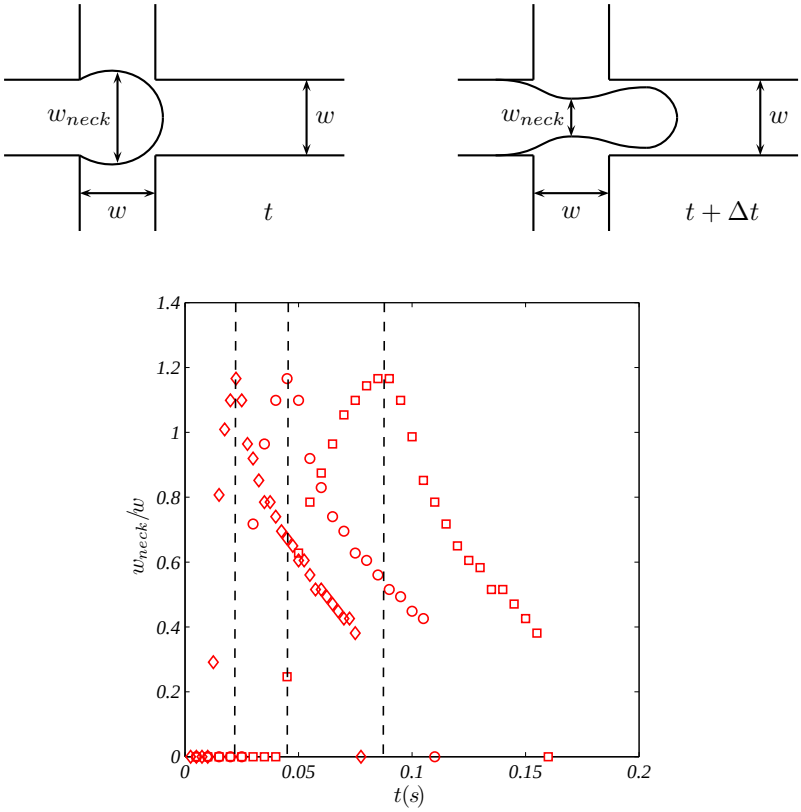

Figure 5.3: Schematic representation of the bubble formation in a cross-junction and definition of the neck width. Temporal evolution of the bubble neck size in a cross-junction for $Ca_L = 0.002$ and different flow rates ratio. The channel aspect ratio is $\alpha = 2.5$
Legend: ($\diamond$) $U_G/U_L = 2$; ($\circ$) $U_G/U_L = 1$; ($\square$) $U_G/U_L = 0.5$.

The three corresponding characteristic velocities are:

$$u_{growth} \sim \frac{Q_G}{A_{ch}} \tag{5.9}$$

$$u_{filling} \sim \frac{Q_G}{A_{ch}} \tag{5.10}$$

$$u_{squeezing} \sim \frac{Q_L}{A_{ch}} \tag{5.11}$$

Finally, from equation 5.5, the bubble length is correlated as:

$$\frac{L_B}{w} \sim 1 + \frac{w_{neck}}{w}\frac{Q_G}{Q_L} \tag{5.12}$$

Equation reduces to 5.2 with $w_{neck} = w_{in}$. A more general relation is given by the following expression:

$$\frac{L_B}{w} \sim \lambda_1 + \lambda_2\frac{Q_G}{Q_L} \tag{5.13}$$

where $\lambda_{1,2}$ are coefficients that depend on the geometry and the operating conditions, as will be shown in the next section.

The bubble dispersion is characterized by two asymptotic behaviours:

- $\frac{Q_G}{Q_L} \to 0$: bubbles are generated with a constant length $\lambda_1 w$ and the frequency of break-up increases with the gas to liquid flow rate ratio,
- $\frac{Q_G}{Q_L} \to \infty$: bubbles are generated with a fixed frequency and the bubble length increases with the gas to liquid flow rate ratio with a growth rate λ_2.

5.2.2 Effects of operating conditions in a square channel

Bubble lengths

The volume fraction of gas in the system or the ratio of gas to liquid flow rates is a key parameter for the control of bubble sizes. From the two-step bubble generation mechanism it is expected that the bubble length is a linear function of the flow rate ratio. Figure 5.4 shows the bubble length obtained with two liquids of different fluid properties and in particular different viscosities (ethanol and glycerol 60% (vol.) in ethanol), as a function of the gas to liquid superficial velocity ratio. The experiments have been performed by fixing the liquid flow rate and then increasing the gas flow rate step by step. Each set of points represents a set of experiments where the liquid flow rate is constant. Based on the relationship 5.13, it is observed that a linear fit of the experiments (red dashed line on the figure) agrees well with the obtained data. It is clearly shown that the coefficients of equation 5.13 and the minimum bubble length in particular appear to be dependent on the liquid velocity and the fluid properties. Indeed, the value λ_1 cannot reproduce all the experimental data presented here and it is observed that the minimum bubble length that can be produced decreases as the liquid velocity increases. In addition, it can be seen that for a fixed liquid velocity (*i.e.* a given symbol in figures 5.4(a) and (b)), the bubble lengths are greater when the Laplace number is increased. It should be noted that at high flow rate ratios ($U_G/U_L \gtrsim 8$), the linear model slightly overestimates the bubble lengths. This has not been further analyzed since the bubbles are approximately 10 times longer than the channel width in these cases and the flow structure approaches annular flow.

The effects of operating conditions on the minimum bubble length and the growth rate of the bubbles λ_2 with the gas to liquid flow rate ratio are now analyzed separately. The squeezing stage is characterized by geometrical parameters only and the operating conditions are not expected to play a major role. Figure 5.5(a) shows the growth rate λ_2 of the bubble length as a function of the gas to liquid velocity ratio. Only the squeezing stage is taken into account, *i.e.* without considering the minimum bubble length which corresponds to the first expansion stage. Data for the liquids with the lowest and the highest Laplace numbers are shown (i.e. glycerol 60% (vol.) in ethanol and pure ethanol, respectively) and it is seen that the data collapse onto a single line. A constant growth rate can then be fitted giving:

$$\frac{L_B}{w} - \lambda_1 = 1.6 \frac{U_G}{U_L} \, . \tag{5.14}$$

It is very interesting to note that the same trends are observed within a very wide range of dimensionless numbers. Indeed, the liquid capillary numbers vary from approximately 6×10^{-4} to 1×10^{-2} and the liquid Reynolds numbers between 0.1 and 200. It can then be concluded that the fluid properties and the operating conditions (the liquid velocity in particular) do not affect the squeezing stage in a square microchannel with the cross-junction contacting geometry.

The effects of the liquid velocity and the fluid properties on the minimum bubble length λ_1 are shown in figure 5.5(b). The minimum bubble length corresponds to the

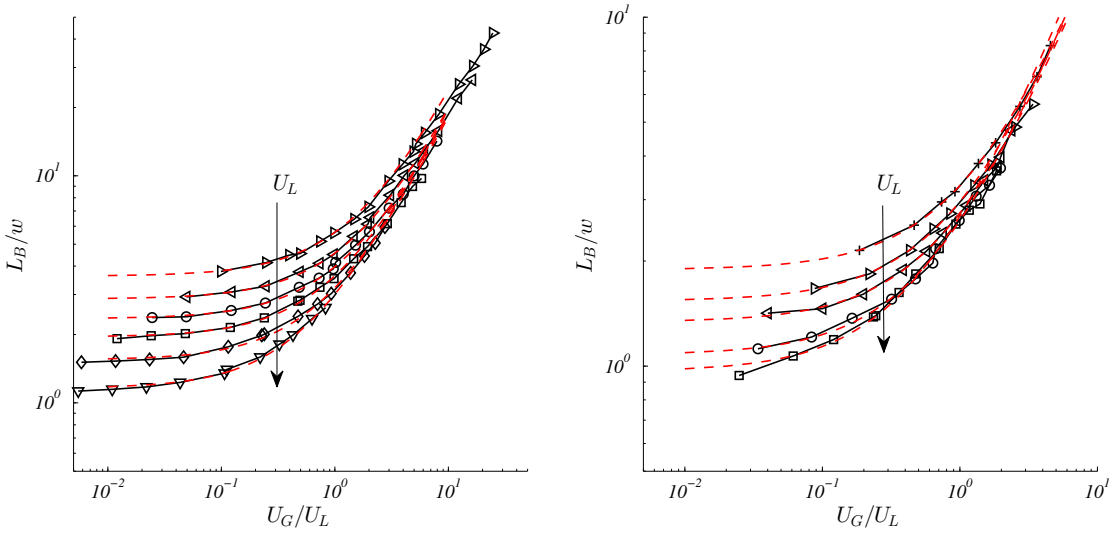

(a) Ethanol ($La = 5440$)

(b) Glycerol 60% (vol.) in ethanol ($La = 33$)

Figure 5.4: Dimensionless bubble lengths as a function of the gas to liquid superficial velocity ratio.
Legend : (+) $U_L \simeq 0.0055\,m/s$; ($\triangleright$) $U_L \simeq 0.011\,m/s$; ($\triangleleft$) $U_L \simeq 0.022\,m/s$; ($\circ$) $U_L \simeq 0.044\,m/s$; ($\square$) $U_L \simeq 0.088\,m/s$; ($\diamond$) $U_L \simeq 0.176\,m/s$; ($\triangledown$) $U_L \simeq 0.353\,m/s$; (dashed red line) experimental fittings (equation 5.13).

length reached during the first stage of the mechanism, *i.e.* the expansion stage until the bubble fills a major part of the channel. The minimum bubble length (obtained as the gas to liquid flow rate ratio vanishes) decreases as the liquid velocity increases. It is also shown that the bubbles produced with a viscous fluid, *e.g.* glycerol / ethanol solutions in this case, are smaller than those produced in pure ethanol. This phenomenon increases as the glycerol concentration of the solution increases, or in other words as the viscous effects increase when compared with the inertial and capillary effects. Since the first step of the bubble generation occurs until the pressure and viscous forces overcome the interfacial force (Garstecki et al. [2006], Christopher et al. [2008]), it can be expected that when the capillary number is increased, the bubble deformation is easier and the second step, *i.e.* the squeezing stage, starts earlier.

Figure 5.6 shows the influence of the liquid capillary number on the minimum bubble length that can be formed in a square microchannel with a cross junction. As it has been mentioned earlier, the bubble length decreases with the capillary number. It is observed that the scaling law given in equation 5.15, which is only based on the liquid capillary number correctly fits this minimum bubble length.

$$\lambda_1 = \frac{L_B^{min}\,(U_G/U_L \to 0)}{w} = \frac{Ca_L^{-0.25}}{2.1} \tag{5.15}$$

It should be mentioned that the $Ca^{-0.25}$ exponent describes the experiments at low Laplace numbers very well while it approaches $Ca^{-0.3}$ at higher Laplace numbers. Note that the influence of inertia is negligible since the differences between bubble lengths obtained at fixed capillary number remain small over the wide range of Reynolds and Weber numbers that have ben covered ($0.1 \lesssim Re_L \lesssim 200$ and $6 \times 10^{-4} \lesssim We_L \lesssim 10$). The exponent $Ca_L^{-0.25}$ is very close to the observations of Liu and Zhang [2011] who

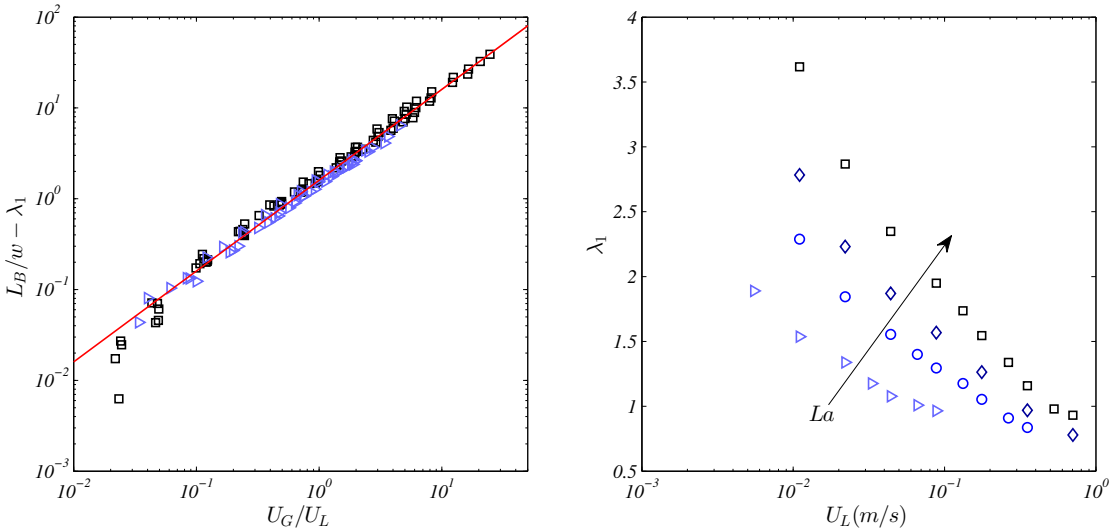

(a) (b)

Figure 5.5: (a) Growth rate of the bubble as a function of the gas to liquid velocity ratio. (b) Minimum bubble length formed as a function of the liquid superficial velocity. Legend : (□) $La = 5440$; (◇) $La = 1130$; (○) $La = 223$; (▷) $La = 33$.

found numerically with a Lattice-Boltzmann method that droplet lengths scale with $Ca_L^{-0.245}$ for droplet formation in a cross-junction and a square channel. The difference with their observations resides in the squeezing stage; they found that it was accelerated by increasing the capillary number, *i.e.* the coefficient of the linear part of the model was also found to decrease as $Ca_L^{-0.245}$. However, the effects of the liquid capillary number on the squeezing stage did not appear to be significant in the experiments in this work.

The relationship between the minimum bubble length formed and the capillary number in the symmetrical cross-shaped geometry can also be related to droplet break-up in symmetrical diverging T-junctions (Leshansky and Pismen [2009], Leshansky et al. [2012], Afkhami et al. [2011]). Indeed, based on geometrical approximations and the lubrication theory, Leshansky and Pismen [2009] found that at a given droplet/bubble capillary number, the transition between non-breaking and breaking drops occurs for a dimensionless length $L_B/w \simeq 1.3\,Ca_B^{-0.21}$. The slight difference in the exponent on Ca could be due to the droplet or bubble curvatures that differ in our experiment and symmetrical diverging T-junctions. Indeed, liquid is flowing on one side of the bubble and there is a lubrication film in the T-junction while the bubble is symmetrical in the cross-junction. Despite the differences in the microfluidics device, this is still interesting to relate the break-up phenomena in different microfluidic devices.

Break-up frequencies

Break-up frequency is another important parameter for characterising gas-liquid slug flow. Indeed, knowledge of the rate of bubble formation allows the prediction of the volume of the bubbles. While some geometrical approximations enable bubble volumes and bubble lengths to be related, they are generally valid at very low capillary numbers where the lubrication film is of negligible thickness. Knowing the bubble velocity, which is close to the sum of the superficial velocities at low capillary numbers,

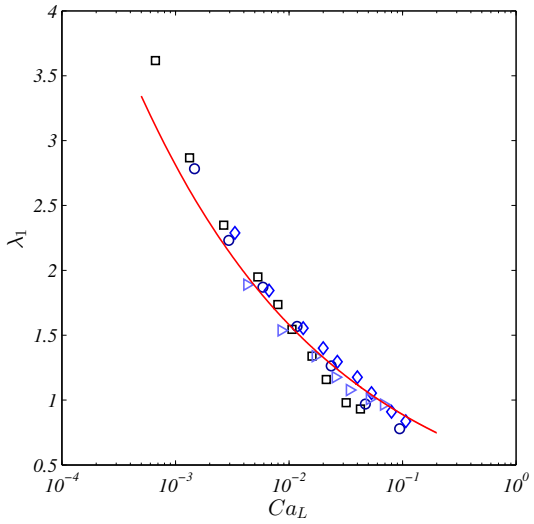

Figure 5.6: Minimum bubble length formed as a function of the liquid capillary number. Legend : (□) $La = 5440$; (◇) $La = 1130$; (○) $La = 223$; (▷) $La = 33$; (red solid line) $Ca_L^{-0.25}/2.1$.

together with the break-up frequency allows the unit cell length and thus the slug length to be estimated.

In order to better understand the influence of the operating conditions on the bubble generation mechanism, the rate of bubble formation can be made dimensionless with the advective time $f_L = w/U_L$ corresponding to the time needed for a liquid particle to travel a distance equal to the characteristic channel dimension, *i.e.* its width. The characteristic time is expected to be equal to the maximum break-up frequency when the gas to liquid flow rate ratio is much greater than unity. Indeed, this is the time needed for the fluid to squeeze a gas finger with a length equal to the width of the channel. This corresponds to the second stage in the two-step model presented in section 5.2.1 when the filling time is not considered.

The dimensional and dimensionless bubble detachment frequencies are shown in figure 5.7 and figure 5.8, respectively, as a function of the gas to liquid flow rate ratio for two liquids (ethanol and glycerol 60 % (vol.) in ethanol). It is seen that the break-up frequency increases with the gas to liquid flow rate ratio. Indeed, since for a fixed liquid velocity, the time needed to squeeze the bubble is expected to be independent of the gas velocity while the time needed to fill the channel cross-section is decreased as the gas flow rate increases. In addition, it is seen that the frequencies are higher when the liquid velocity is increased. For a fixed liquid velocity the frequency also increases when the ratio of capillary to viscous effects decreases (comparison between ethanol and glycerol 60% in ethanol at fixed velocity). This is relevant to the results on bubble lengths, which showed that an increase in the liquid velocity, or more generally, an increase in the capillary number leads to decreased bubble sizes. Indeed, the time needed to reach a decreased volume is also reduced, thereby increasing the break-up frequency.

Figure 5.9 shows that the dimensionless bubble detachment frequency can be roughly

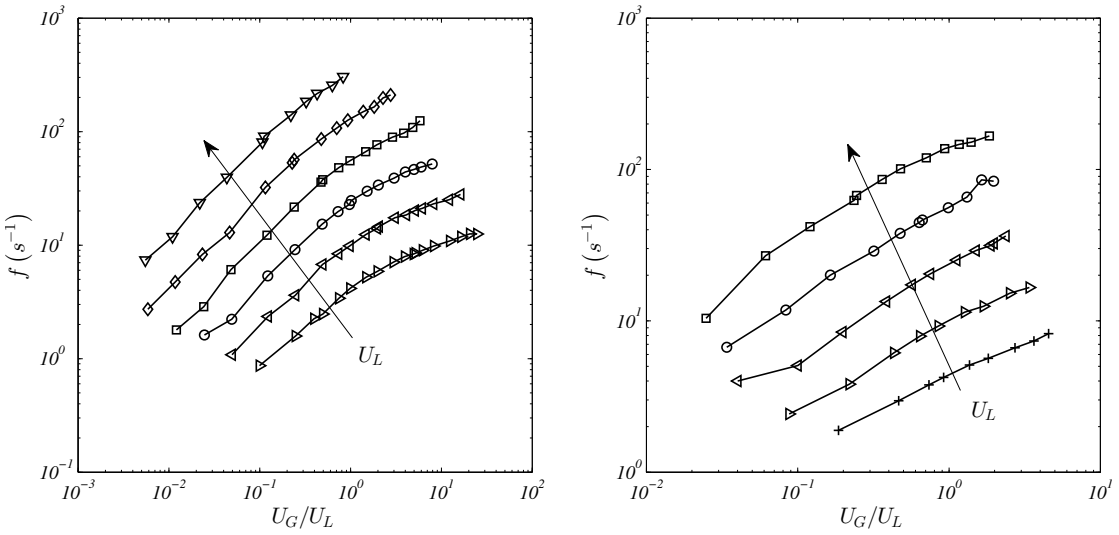

(a) Ethanol ($La = 5440$) (b) Glycerol 60% (vol.) in ethanol ($La = 33$)

Figure 5.7: Dimensional bubble detachment frequencies as a function of the gas to liquid superficial velocities ratio.
Legend : (+) $U_L \simeq 0.0055 m/s$; ($\triangleright$) $U_L \simeq 0.011 m/s$; ($\triangleleft$) $U_L \simeq 0.022 m/s$; ($\circ$) $U_L \simeq 0.044 m/s$; ($\square$) $U_L \simeq 0.088 m/s$; ($\diamond$) $U_L \simeq 0.176 m/s$; ($\triangledown$) $U_L \simeq 0.353 m/s$.

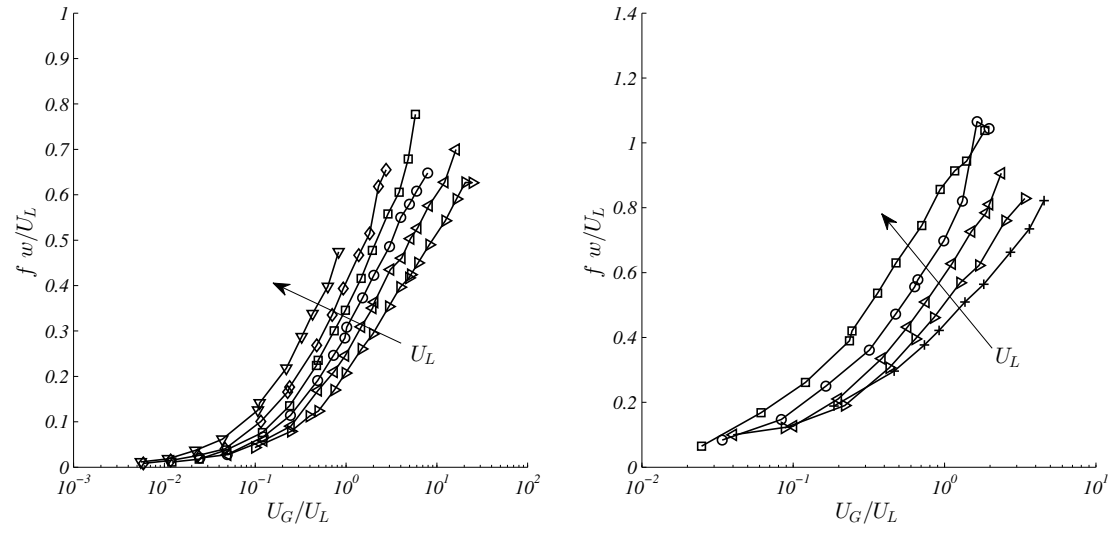

(a) Ethanol ($La = 5440$) (b) Glycerol 60% (vol.) in ethanol ($La = 33$)

Figure 5.8: Dimensionless bubble detachment frequencies as a function of the gas to liquid superficial velocities ratio.
Legend : (+) $U_L \simeq 0.0055\, m/s$; ($\triangleright$) $U_L \simeq 0.011\, m/s$; ($\triangleleft$) $U_L \simeq 0.022\, m/s$; ($\circ$) $U_L \simeq 0.044\, m/s$; ($\square$) $U_L \simeq 0.088\, m/s$; ($\diamond$) $U_L \simeq 0.176\, m/s$; ($\triangledown$) $U_L \simeq 0.353\, m/s$.

scaled with $Ca^{0.25}$:

$$\frac{f\,w}{U_L} \simeq Ca_L^{0.25} \left(6 \frac{\left(U_G/U_L + (U_G/U_L)^2 \right)}{\left(1 + 5U_G/U_L + 1.25\,(U_G/U_L)^2 \right)} \right) \tag{5.16}$$

This scaling is expected as the flow rate ratio vanishes since the bubble frequency is inversely proportional to the bubble length which scales approximately as $Ca_L^{-0.25}$. However, the influence of the capillary number on the bubble length was not significant at high flow rate ratios and therefore it may be expected that the maximum frequency does not depend on the capillary number. The maximum frequency, however, was not reached as the flow became unstable and sometimes annular. Another possibility is that the approximation that the frequency is inversely proportional to the bubble length suggests that the liquid fraction is close to zero, *i.e.* the bubble occupies the entire cross section. The scaling could then come from the appropriate relationship for an infinite gas to liquid flow rate ratio, *i.e.* $f \sim Q_G/(A_B L_B) \sim U_G/((1-W)L_B)$.

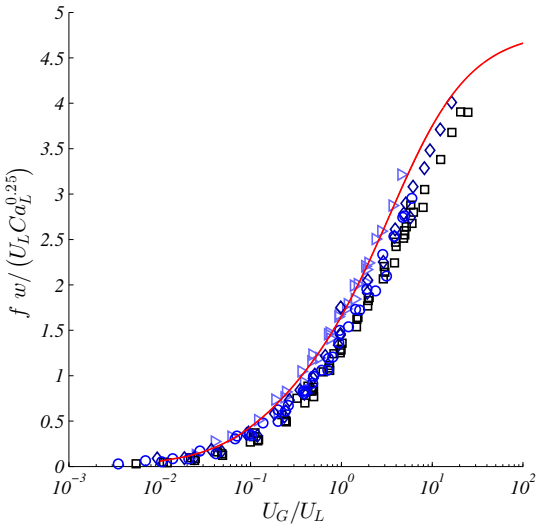

Figure 5.9: Dimensionless bubble break-up frequencies scaled with $Ca_L^{0.25}$ as a function of the gas to liquid superficial velocity ratio.
Legend : (□) $La = 5440$; (◇) $La = 1130$; (○) $La = 223$; (▷) $La = 33$; (red solid line) equation 5.16.

Unit cell lengths

The bubble and slug lengths are of main importance to characterize the hydrodynamics of Taylor flow and especially the pressure drop in the channel as it will be detailed in section 6.3.5.

Many studies deal with the bubble lengths as mentioned previously but less attention has been paid to the characterization of the unit cell or slug lengths. From a simple model that neglects the slip velocity and that assumes rectangular bubbles and no liquid film, the bubble and slug lengths can be related to the flow rates ratio:

$$\frac{L_S}{L_B} = \frac{Q_L}{Q_G} \ . \tag{5.17}$$

Using this, Volkel [2009] suggested a relationship between slug length and liquid to gas flow rates ratio from equations 5.13 and 5.17:

$$\frac{L_S}{w} \sim \lambda_2 + \lambda_1 \frac{Q_L}{Q_G} \tag{5.18}$$

This means that the bubble length relative to the unit cell length would be equal to the volume fraction of gas:

$$\frac{L_B}{L_{UC}} = \frac{U_G/U_L}{1 + U_G/U_L} \tag{5.19}$$

Although it has been observed that equation 5.17 can be used to correctly estimate slug lengths (Volkel [2009], Abadie et al. [2012]), the coefficients obtained from the bubble lengths ($\lambda_{1,2}$) cannot be used without being adapted slightly (Abadie et al. [2012]).

Figure 5.10 shows the bubble length relative to the unit cell length as a function of the gas to liquid flow rate ratio. It is very interesting to note that for all capillary and Reynolds numbers, the bubble length relative to the slug length as a function of the gas to liquid flow rate ratio follow the same trend. Indeed, all the data collapse following the form of equation 5.20, evolving linearly with the flow rate ratio at vanishing gas volume fraction and tends towards unity when the channel is essentially filled with gas:

$$\frac{L_B}{L_{UC}} = \frac{U_G/U_L}{0.6 + U_G/U_L} \tag{5.20}$$

It is not surprising that equation 5.20 is slightly different than equation 5.19 and this is due to the liquid surrounding the bubble caps and the non-zero liquid film thickness.

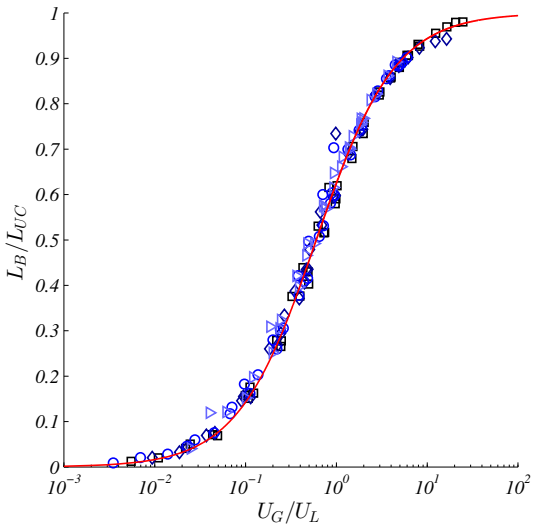

Figure 5.10: Ratio of the bubble length to unit cell length as a function of the gas to liquid superficial velocity ratio.
Legend : (□) $La = 5440$; (◇) $La = 1130$; (○) $La = 223$; (▷) $La = 33$; (red solid line) equation 5.20.

Figure 5.11 shows the dimensionless unit cell length as a function of the gas to liquid flow rate ratio. The relationship between the frequency of bubble formation, the bubble velocity and the unit cell length is:

$$L_{UC} = \frac{U_B}{f} \tag{5.21}$$

At low flow rate ratios, we observe a decrease in the unit cell length with increasing gas fraction since the bubble lengths are formed with a volume that is almost contant and the frequency increases. In other words, as the flow rate ratio vanishes, the bubble

velocity is close to the liquid velocity and the frequency increases with U_G/U_L. The opposite trend is found at high flow rate ratios: the bubble frequency tends towards a maximum and the bubble velocity is close to the gas velocity thereby leading to an increase in the unit cell length.

In section 5.2.2, it has been shown that the bubble length can be estimated from the flow rate ratio, the geometry and the liquid capillary number. Thus, the unit cell length can be deduced from equations 5.14 and 5.20 by:

$$\frac{L_{UC}}{w} = \lambda_1 + 0.6 \times \lambda_2 + \lambda_2 \frac{U_G}{U_L} + 0.6 \times \lambda_1 \frac{1}{U_G/U_L}, \tag{5.22}$$

where expressing λ_1 and λ_2, we obtain:

$$\frac{L_{UC}}{w} = \frac{1}{2.1\, Ca_L^{0.25}} + 0.6 \times 1.6 + 1.6 \frac{U_G}{U_L} + \frac{0.6}{2.1\, Ca_L^{0.25}} \frac{1}{U_G/U_L} \tag{5.23}$$

in the square microchannel with a cross-junction.

From the above equation, the flow rate ratio that leads to the minimum unit cell length can be derived as:

$$\frac{U_G}{U_L}(L_{UC}^{min}) = \sqrt{\frac{0.6}{1.6 \times 2.1\, Ca_L^{0.25}}} \tag{5.24}$$

The corresponding evolution is reported in figure 5.11.

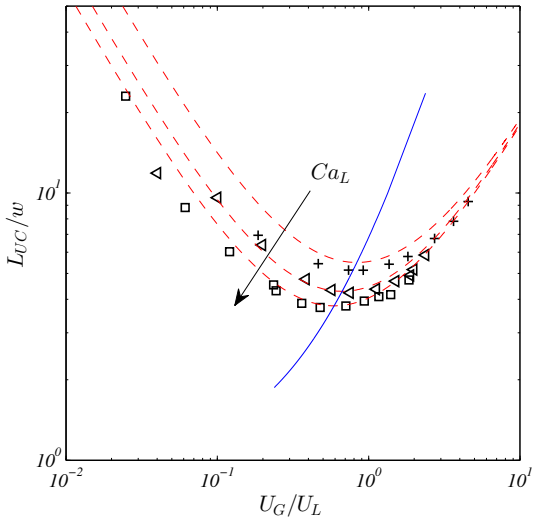

Figure 5.11: Dimensionless unit cell lengths as a function of the gas to liquid superficial velocity ratio.
Legend : (+) $Ca_L \simeq 0.043$; ($\triangleleft$) $Ca_L \simeq 0.0086\, m/s$; ($\square$) $Ca_L \simeq 0.0684 m/s$; (dashed red lines) equation 5.22 ; (blue solid line) equation 5.24 .

Partial conclusion

The key parameters that characterize the bubble formation in a cross-junction with a square cross-section have been clearly identified according to the two-step model which is widely used in T-junctions (Garstecki et al. [2006], Van Steijn et al. [2007, 2010]).

- The bubble length is found to evolve as $\frac{L_B}{w} = \lambda_1 + \lambda_2 \frac{U_G}{U_L}$.
- In addition to the effects of geometry and flow rate ratio, the minimum bubble size generated has been shown to depend on the liquid capillary number following the scaling law $L_B^{min}/w = \lambda_1 = \frac{Ca_L^{-0.25}}{2.1}$.
- The linear growth rate of the bubble length with the flow rate ratio has been found to be constant $\lambda_2 = 1.6$.
- The dimensionless bubble generation frequency and the bubble volume scale with $Ca_L^{0.25}$ and $Ca_L^{-0.25}$, respectively.
- The bubble length relative to the unit cell length is a function of the gas to liquid velocity ratio only and is given by: $L_B/L_{UC} = \frac{U_G/U_L}{0.6+U_G/U_L}$

5.2.3 Effects of cross-sectional aspect ratio

Bubble lengths

In channels with moderate aspect ratios, the break-up mechanism is expected to be similar to that in square microchannels. However, the aspect ratio is known to have effects on the liquid area fraction (Hazel and Heil [2002], De Lozar et al. [2008]) and also on the pressure drop since the radii of curvatures differ in the height and the width of the channel. It is therefore expected that the aspect ratio plays a role in the dynamics of break-up at the junction during the different stages.

As the capillary number has been previously identified as the dimensionless number that governs the bubble generation mechanism for fixed flow rate ratios, we compare the geometries at a given capillary number. Figure 5.12(a) shows the bubble lengths as a function of the gas to liquid flow rate ratio for two different capillary numbers and two aspect ratios. It is observed that at low capillary numbers, the dimensionless bubble length increases with the aspect ratio while this trend is inverted when the capillary number increases (around $Ca \simeq 0.01$).

Another observation is that the minimum bubble length produced at a given liquid capillary number and scaled by the channel width does not seem to depend significantly on the cross-sectional geometry. However, the growth rate during the squeezing stage, which corresponds to the slope λ_2 in the two-step model defined by equation 5.13, seems to evolve with the capillary number. In the square geometry the coefficient barely varies with the operating conditions however, in the rectangular geometry at low capillary numbers ($Ca_L \simeq 0.0042$ in figure 5.12) the bubble length increases more rapidly with the flow rate ratio than in the square geometry, while the opposite trend is observed at a higher capillary numbers ($Ca_L \simeq 0.067$ in figure 5.12). This is confirmed in figure 5.12(b), which represents the growth rate of the bubble as a function of the gas to liquid velocity ratio. The red line is the relationship found for the square geometry. It is seen that at low capillary numbers in the rectangular channel, the increase in bubble length with the gas velocity is greater than in the square channel. This trend decreases until the bubble lengths become less dependent on the flow rate ratio than in the square channel.

A close inspection of the dependency of these two coefficients, *i.e.* the minimum bubble length that can be formed and the growth rate with increasing gas volume fraction, is provided in figures 5.13(a) and (b), respectively.

Figure 5.13(a) shows that the minimum dimensionless bubble length scaled by the channel width is equal whatever the cross-sectional geometry, *i.e.* the minimum bubble

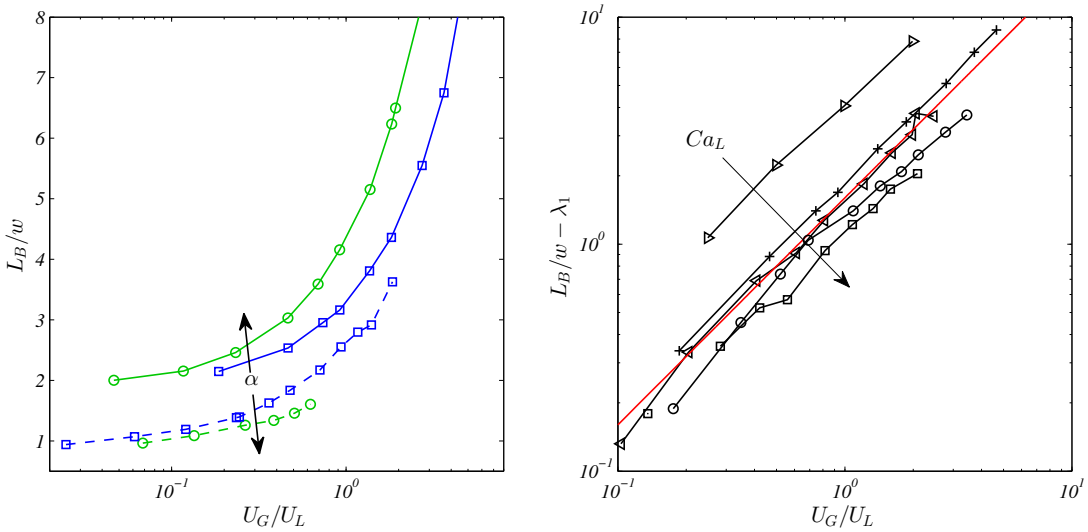

(a) (b)

Figure 5.12: (a) Dimensionless bubble lengths as a function of the gas to liquid superficial velocity ratio. (b) Growth rate of the bubble length as a function of the flow rate ratio.
(a) Legend : (solid line) $Ca_L \simeq 0.0042$; (dashed lines) $Ca_L \simeq 0.067$; (blue squares) $\alpha = 1$; (green circles) $\alpha = 4$.
(b) Legend : (red solid line) square channel $L_B/w - \lambda_1 = 1.6 U_G/U_L$; ($\triangleright$) $Ca_L \simeq 0.0004$; (+) $Ca_L \simeq 0.0026$; ($\triangleleft$) $Ca_L \simeq 0.0106$; ($\circ$) $Ca_L \simeq 0.0211$; ($\square$) $Ca_L \simeq 0.0422$.

length is: $L_B = \lambda_1 \times w$ with λ_1 independent of the geometry. For a fixed hydraulic diameter, the width of the channel increasing with the aspect ratio, the minimum dimensional bubble length increases with the aspect ratio. Similarly to the observations made for the square channel, the minimum bubble length is more dependent on the capillary number when the inertia is increased, as observed when working with ethanol. This trend is enhanced in the rectangular microchannel with aspect ratio $\alpha = 4$, where for the highest liquid capillary number $Ca_L \simeq 0.025$ the bubble length is approximately half the length of that obtained with a more viscous liquid, *e.g.* glycerol 60% (vol.) in ethanol. These differences can be explained by the fact that this corresponds to a regime that approaches the jetting regime. In addition, the bubbles are formed in pairs with two main break-up frequencies instead of being generated regularly with the same period.

Figure 5.13(b) reports the growth rate of bubbles as a function of the capillary number in rectangular channels. It clearly appears that an increase in the capillary number leads to a decrease in the linear growth of the bubble lengths for rectangular microchannels. The blue line indicates the constant results that were obtained in the square microchannel and the solid black line, the fit used for the minimum bubble length $\lambda_1 \sim Ca_L^{-0.25}/2.1$, is given as an element of comparison. It is interesting to note that the capillary number at which the dimensionless bubble lengths in the rectangular channels become smaller than those in the square channel is around $Ca_L \simeq 0.01$. This also corresponds to the cross point where the liquid area fraction in a rectangular channel becomes greater than that in a square channel (De Lozar et al. [2008]).

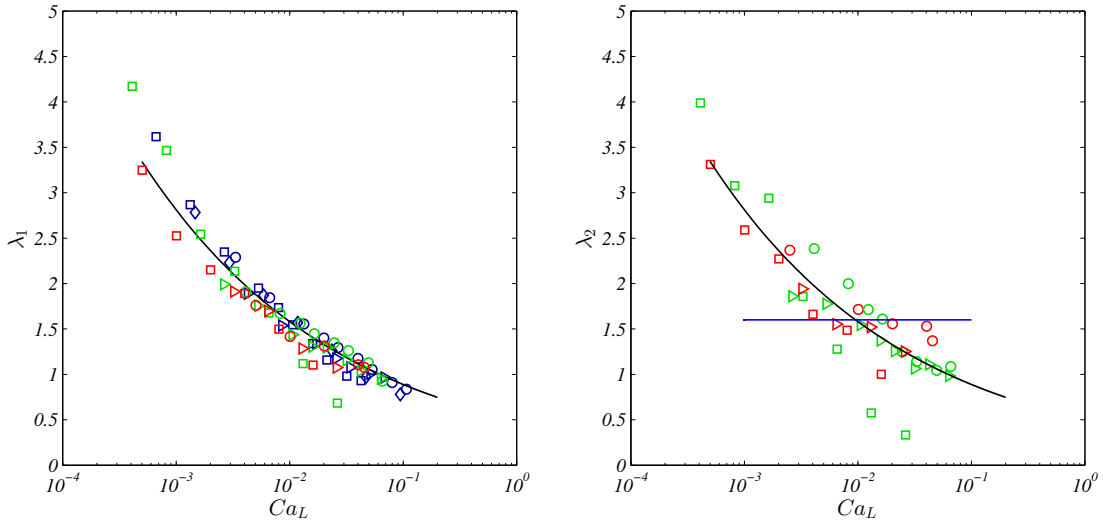

(a) (b)

Figure 5.13: (a) Minimum bubble lengths generated in channels of aspect ratio $\alpha = [1; 2.5; 4]$ as a function of the liquid capillary number. (b) Linear growth rate of the bubble length as a function of the capillary number Ca_L for $\alpha = [1; 2.5; 4]$..
(a) Legend : (blue) $\alpha = 1$; (red) $\alpha = 2.5$; (green) $\alpha = 4$; (□) $La = 5440$; (◇) $La = 1130$; (○) $La = 223$; (▷) $La = 33$; (black line) $Ca_L^{-0.25}/2.1$.
(b) Legend : (blue line) $\alpha = 1$; (red) $\alpha = 2.5$; (green) $\alpha = 4$; (□) $La = 5440$; (○) $La = 223$; (▷) $La = 33$; (black line) $Ca_L^{-0.25}/2.1$.

Break-up frequencies

Figure 5.14(a) shows the dimensionless bubble generation frequency as a function of the gas to liquid flow rate ratio for two different capillary numbers and two aspect ratios. At low capillary number ($Ca_L \simeq 0.0042$ in figure 5.14(a)), the dimensionless detachment frequency is lower when the aspect ratio is increased while the bubble length and the bubble volume, which are inversely proportional to the frequency, are increased. On the other hand, when the capillary number is increased ($Ca_L \simeq 0.067$ in figure 5.14(a)), the bubble deformation is made easier and this leads to an increase in the frequency while the bubble lengths decrease with the aspect ratio. This increase of bubble formation rate with the capillary number is enhanced with the aspect ratio. These observations are in agreement with the observations made on the bubble lengths. Figure 5.14(b) represents the bubble formation frequency as a function of the capillary number for different flow rate ratios ($U_G/U_L = [0.25; 0.5; 1; 2]$). It confirms the enhanced effects of the capillary number on the frequency of bubble formation when the aspect ratio is increased. In this range of capillary numbers, the same trend is observed for the liquid area fraction: the bubble slip velocity decreases with the aspect ratio at capillary numbers up to $Ca \simeq 0.01$, above which the opposite trend is found.

Although the dimensionless bubble formation rate scaled with $Ca_L^{0.25}$ provided a good estimation of the bubble formation frequency in a square channel, it appears to be no longer valid for the rectangular channels as illustrated in figure 5.15(a). Figure 5.15(b) shows that for the rectangular channel of aspect ratio $\alpha = 4$, the dimensionless bubble detachment frequency can be scaled approximately with $Ca^{0.4}$. It has been

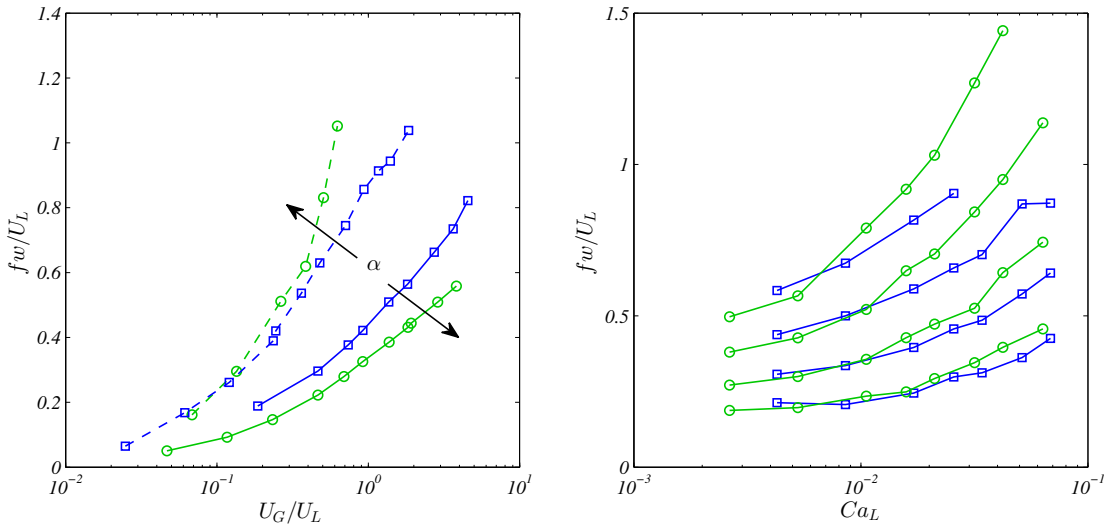

Figure 5.14: Dimensionless bubble formation frequency as a function of the (a) gas to liquid superficial velocity ratio ; (b) the capillary number for $U_G/U_L = [0.25; 0.5; 1; 2]$ from bottom to the top.
Legend : (solid line) $Ca_L \simeq 0.0042$; (dashed lines) $Ca_L \simeq 0.067$; (blue squares) $\alpha = 1$; (green circles) $\alpha = 4$.

seen that the linear growth rate of bubble length decreases when the capillary number is increased in rectangular cross-sections while it was almost constant in the square channel. Since the bubble formation frequency is inversely proportional to its volume, it is then not surprising to find an enhanced dependency on the liquid capillary number in rectangular channels at high gas to liquid flow rate ratio. However, the aspect ratio was not found to play a major role in the minimum bubble length and its dependency on the liquid capillary number. Thus, the dependency of the bubble formation frequency on the capillary number at low gas to liquid flow rate ratio is not yet well explained.

Unit cell lengths

Although the mechanisms of bubble generation in a flow-focusing device are qualitatively similar in both square and rectangular channels of various aspect ratios, it has been observed that the influence of the capillary number is increased as the aspect ratio increases. However, it is worth noting in figures 5.16(a) and (b) for aspect ratios $\alpha = 2.5$ and $\alpha = 4$ respectively that whatever the geometry and the capillary number, the bubble length relative to the unit cell length follow the same simple law given by equation 5.20.

The bubble and the unit cell lengths are related with the same equation whatever the geometry and depend only on the gas to liquid flow rate ratio. As a consequence, the observations made for the bubble lengths and the combined effects of aspect ratio and capillary number remain valid.

Figure 5.17 shows that the unit cell length for the aspect ratio $\alpha = 2.5$ and $\alpha = 4$ follow similar trends with the gas to liquid flow rate ratio to that observed for the square channel. However, although the minimum bubble length at a given capillary

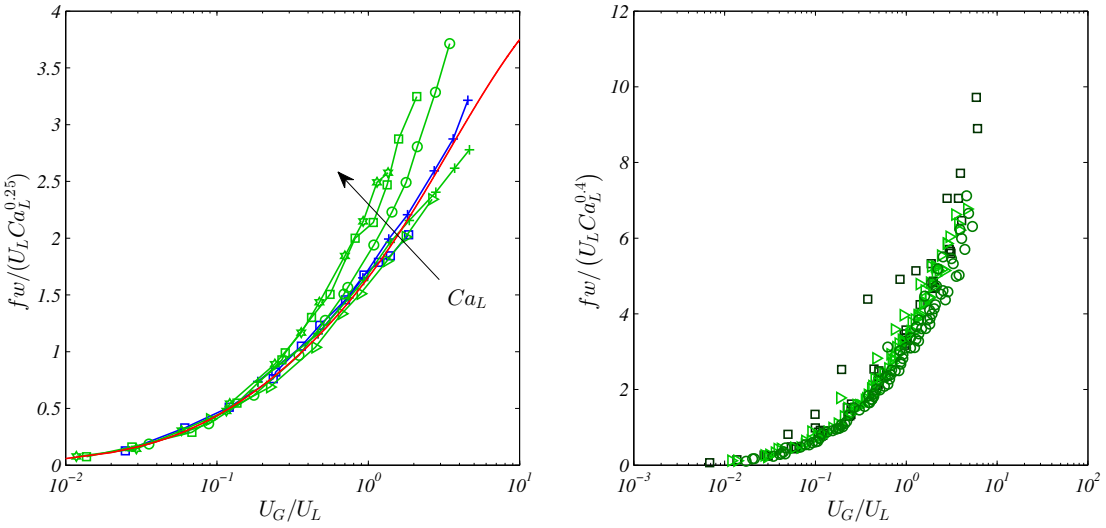

(a) (b)

Figure 5.15: Dimensionless bubble formation frequency in the rectangular channel $\alpha = 4$ scaled with (a) $Ca^{0.25}$ and (b) $Ca^{0.4}$ as a function of the gas to liquid superficial velocity ratio.
(a) Legend : (blue) $\alpha = 1$; (red solid line) experimental fit for $\alpha = 1$; (green) $\alpha = 4$;
(b) Legend : (□) $La = 5440$; (○) $La = 223$; (▷) $La = 33$;

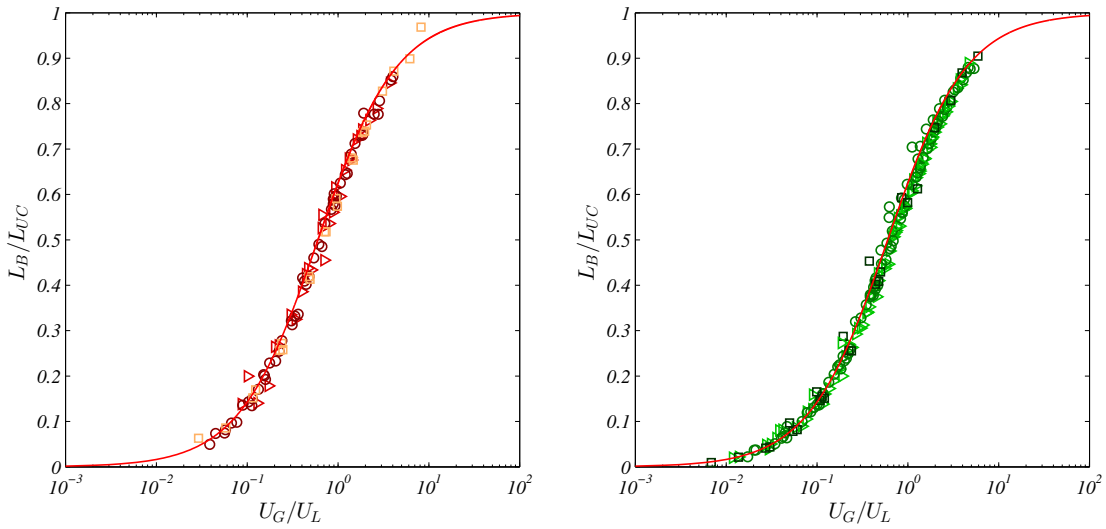

(a) Aspect ratio $\alpha = 2.5$ (b) Aspect ratio $\alpha = 4$

Figure 5.16: Bubble to unit cell length ratio as a function of the gas to liquid superficial velocities ratio.
Legend : (□) $La = 5440$; (○) $La = 223$; (▷) $La = 33$; (solid line) equation 5.20.

number does not depend on the aspect ratio, the influence of the capillary number on the growth rate of the bubble length is slightly less clear and the unit cell length has not been correlated in these geometries. It is still interesting to note that the unit

cell length always decreases at low flow rate ratios until it reaches a minimum value for a flow rate ratio of about one and then increases as the bubble velocity increases and the frequency approaches its maximum value. An estimation of the position of the minimum unit cell length can be calculated with the assumption that the coefficients of the linear two-step model (equation 5.13) follow the same dependency on the the capillary number. This leads to $U_G/U_L\left(L_{UC}=L_{UC}^{min}\right)=\sqrt{0.6}$. The corresponding evolution is plotted in figure 5.17 for the two aspect ratios $\alpha=2.5$ and $\alpha=4$.

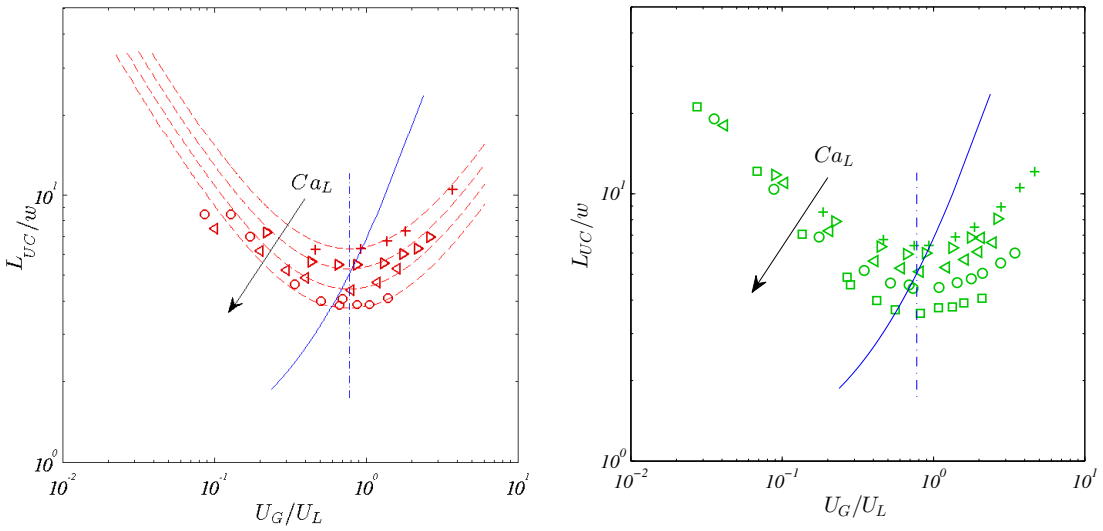

(a) Aspect ratio $\alpha=2.5$

(b) Aspect ratio $\alpha=4$

Figure 5.17: Dimensionless bubble length as a function of the gas to liquid superficial velocities ratio.
Legend : (a) (+) $Ca_L\simeq 0.0032$; ($\triangleright$) $Ca_L\simeq 0.0065$; ($\triangleleft$) $Ca_L\simeq 0.013$; ($\circ$) $Ca_L\simeq 0.026$; (red dashed lines) equation 5.20 with $L_B/w=(1+U_G/U_L)\,Ca_L^{-0.25}/2.1$; (blue solid line) equation 5.24.
(b) (+) $Ca_L\simeq 0.0026$; ($\triangleright$) $Ca_L\simeq 0.0053$; ($\triangleleft$) $Ca_L\simeq 0.0106$; ($\circ$) $Ca_L\simeq 0.021$; ($\square$) $Ca_L\simeq 0.042$; (blue solid line) equation 5.24.

Partial conclusion

The similarities and the differences between the bubble formation in a cross-junction with a square cross-section and rectangular cross-section have been clearly underlined.

- The minimum bubble size generated scaled by the width of the channel has been shown to be independent of the aspect ratio, $L_B^{min}/w=\lambda_1=\frac{Ca_L^{-0.25}}{2.1}$.
- The linear growth rate has been found to decrease with the liquid capillary number in rectangular channels. The dependency on the the capillary number seems to be enhanced when increasing the aspect ratio.
- The dimensionless bubble generation frequency scales with Ca_L^m where m is an increasing function of the aspect ratio. $m=0.25$ for $\alpha=1$ and $m=0.4$ for $\alpha=4$.
- The bubble length relative to the unit cell length does not depend on the aspect ratio and is given by: $L_B/L_{UC}=\frac{U_G/U_L}{0.6+U_G/U_L}$.

5.3 T-shaped junctions

In this section, the aspect ratio of the channel is fixed at $\alpha = 2.5$ and the effects of the geometrical shape of the contacting mode on the bubble lengths are studied. Two different T-shaped junctions are used: a side-T junction (figure 5.18) and a front-T junction (figure 5.20).

5.3.1 Bubble generation mechanism

Figure 5.18 illustrates the bubble formation in a side-T junction with ethanol as the continuous phase during one period. During this period, the position where the bubble neck thickness and its evolution in time are shown in figure 5.19 for one liquid flow rate and three gas flow rates. As it has been detailed for the cross-junction, the bubble formation comprises two main stages: the filling stage until the neck reaches a given thickness and the squeezing stage which depends on the liquid velocity.

For the front-T junction, a sequence is shown in figure 5.20 while the position where the neck thickness is evaluated and its evolution in time are shown in figure 5.21. The two-step mechanism of bubble formation appears to be valid in this geometry too.

From figures 5.18 and 5.20 for which the operating conditions are identical, the first qualitative observation is that the bubbles and the slugs generated in a front-T junction are longer than the ones produced in a side-T junction. However, under these operating conditions, the bubbles generated in the front-T junction remain smaller than the ones generated in the cross-junction (figure 5.2).

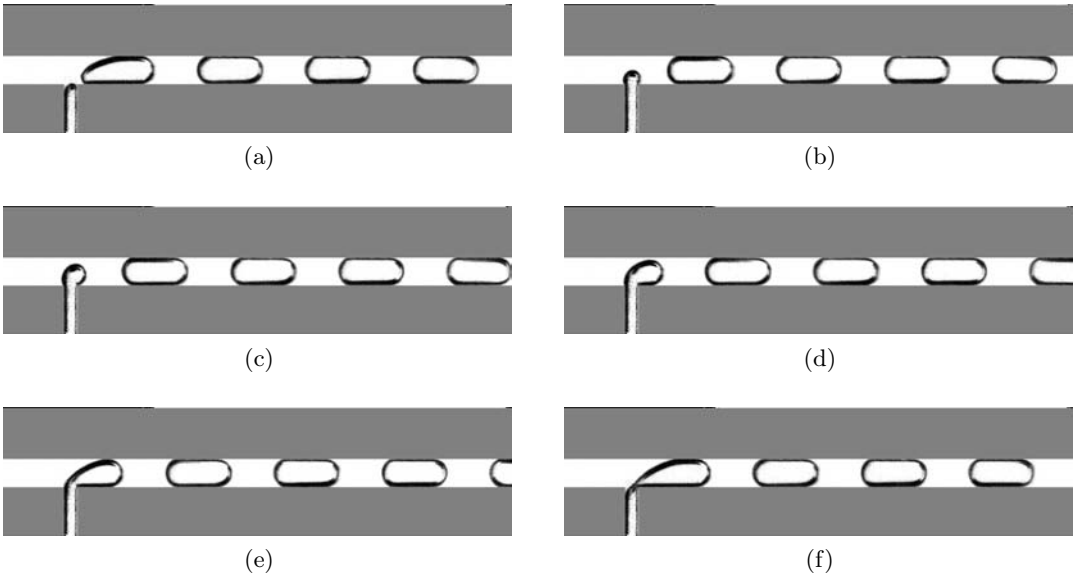

Figure 5.18: Bubble generation sequence in a side T-junction.

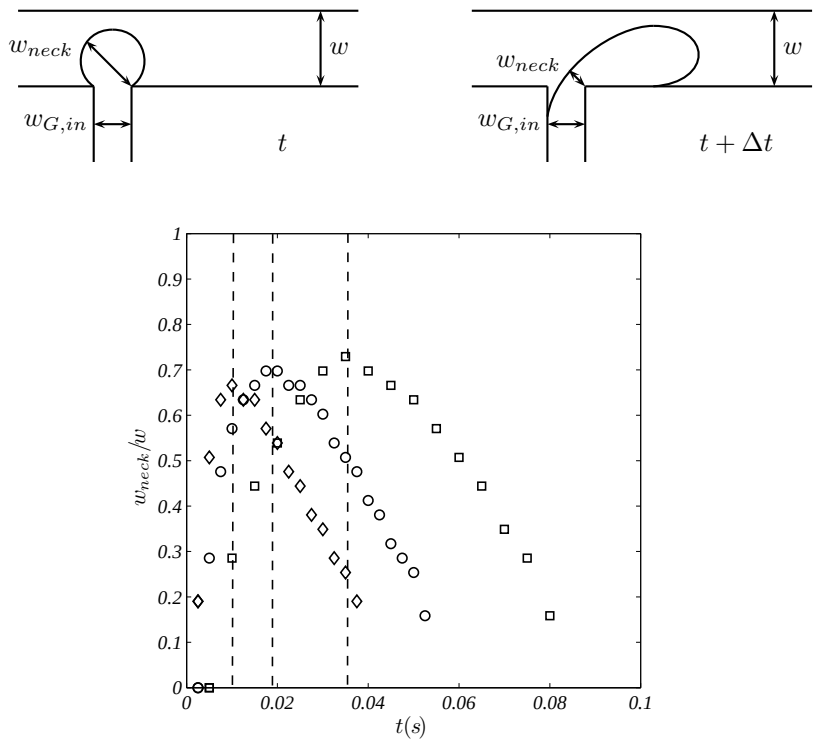

Figure 5.19: Schematic representation of the bubble formation in a cross-junction and definition of the neck width. Temporal evolution of the bubble neck size in a cross-junction for $Ca_L = 0.002$ and different flow rate ratios. The channel aspect ratio is $\alpha = 2.5$
Legend: ($\diamond$) $U_G/U_L = 2$; ($\circ$) $U_G/U_L = 1$; ($\square$) $U_G/U_L = 0.5$.

5.3.2 Effects of operating conditions in a rectangular channel ($\alpha = 2.5$)

Bubble lengths

With the previous observations and considering the work from the literature (Garstecki et al. [2006], Van Steijn et al. [2007, 2010], Christopher et al. [2008], Abadie et al. [2012]), the bubble lengths can be approximated with the linear relationship 5.13. The two coefficients λ_1 and λ_2 have been shown to depend on the capillary number in flow focusing devices while inertial effects did not play a major role in the bubble generation process in the regimes studied.

Figure 5.22(a) shows the effects of the liquid capillary number on the minimum bubble length that can be formed in each contacting geometry and figure 5.22(b) shows the rate at which the bubble length grows with the gas to liquid velocity ratio as a function of the liquid capillary number. Whatever the geometry, the minimum bubble length and the growth rate decrease when the liquid capillary number is increased. However, although this decrease scales approximately with $Ca_L^{-0.25}$ in the flow focusing device (red line and symbols), indicating that infinitely long bubbles would be generated at vanishing capillary number, the bubble length in the T-shaped geometries appear to tend towards a finite value when the capillary number is decreased that corresponds to the squeezing regime described by Garstecki et al. [2006], Van Steijn et al. [2007]. This

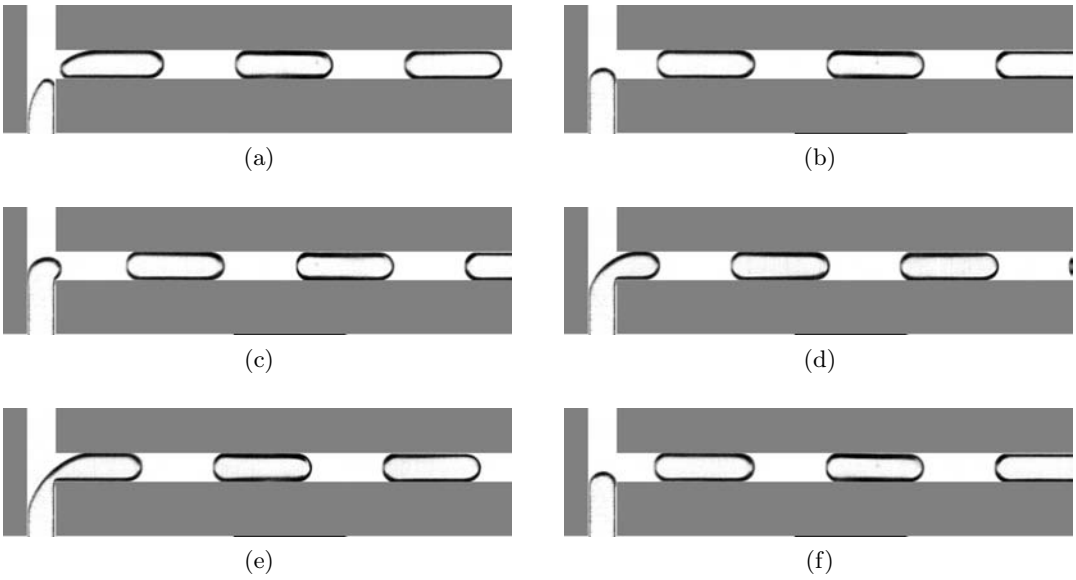

Figure 5.20: Bubble generation sequence in a T-junction.

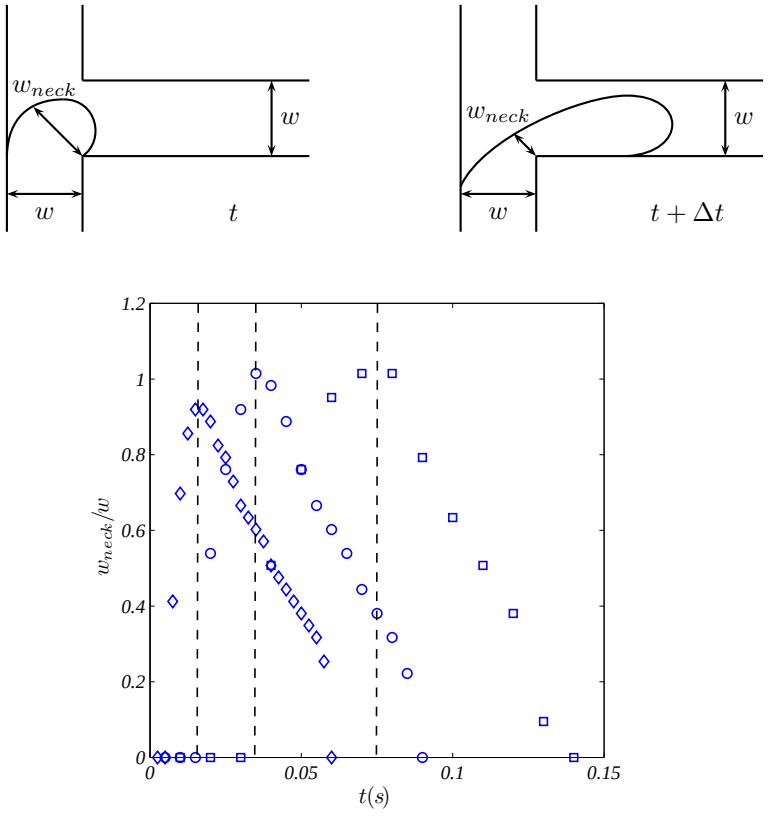

Figure 5.21: Schematic representation of the bubble formation in a cross-junction and definition of the neck width. Temporal evolution of the bubble neck size in a cross-junction for $Ca_L = 0.002$ and different flow rate ratios. The channel aspect ratio is $\alpha = 2.5$
Legend: ($\diamond$) $U_G/U_L = 2$; ($\circ$) $U_G/U_L = 1$; ($\square$) $U_G/U_L = 0.5$.

is in agreement with the model proposed by Christopher et al. [2008] developed for the formation of droplets in side-T junctions and described by equation 5.3. This model underestimates the bubble lengths in their work and it is also the case here (black dashed line). However, by correcting slightly this model, it agrees relatively well with the experimental data in the side-T junction. Firstly, since equation 5.3 represents the inverse problem, an explicit expression of the minimum bubble length $L_B^{min}/w = \lambda_1$ is given. Indeed, as the capillary number Ca_L tends towards zero, the dimensionless bubble length tends towards 1. Equation 5.3 then reduces to:

$$(1 - \lambda_1)^3 \sim Ca_L \tag{5.25}$$

Thus, at vanishing liquid capillary number, the minimum bubble length in a side T junction would obey:

$$\lambda_1 \sim 1 - Ca_L^{1/3} \tag{5.26}$$

To prevent the bubble length λ_1 from being negative above a certain capillary number, the second member on the right hand side of equation 5.26 should be limited and tend towards zero at infinite capillary number according to 5.3. In addition, as the model was found to underestimate the minimum bubble length, a factor slightly greater than one is introduced and the minimum bubble length can be written:

$$\lambda_1 \sim 1.1 \left(1 - \frac{Ca_L^{1/3}}{1 + Ca_L^{1/3}} \right) \tag{5.27}$$

It is shown in figure 5.22 (black line and symbols) that there is good agreement between this corrected model and the experimental data in the side-T junction. However, no simple scaling law was found for the evolution of the linear growth rate λ_2 of the bubble as a function of the liquid capillary number.

The observations that the bubbles are longer in a cross-junction than those formed in the front-T junction and side-T junctions can be seen in figures 5.22(a) and (b) since both the minimum bubble length and the growth rate are minimum in the side-T junction and maximum in the cross-junction. It is interesting to point out that the differences in bubble lengths and growth rates are mainly observable at low capillary numbers while the differences between the bubbles lengths generated with different contacting geometries reduce when the capillary number is increased. This means that the generation mechanism is governed almost uniquely by geometrical effects at low capillary numbers and especially in T-shaped junctions where the capillary number does not seem to affect significantly the bubble lengths below a critical capillary number. However, when increasing the capillary number, the capillary number governs the bubble generation mechanism and the effects of the geometrical entrance are reduced. Indeed, a bubble follows the shape of the channel at low capillary numbers while it separates from the walls when the capillary number is increased.

5.4 Conclusion and outlooks

The bubble dispersion generated in a cross-junction in channels of different aspect ratios ($\alpha = [1; 2.5; 4]$) has been characterized experimentally. The two-step model which is widely used in T-junctions, has been extended to cross-junctions. The effects of the liquid capillary number on the two stages of bubble formation mechanism have been identified. The effects of the liquid capillary number are often neglected in gas-liquid flow to characterize the bubble formation (Cubaud et al. [2005], Garstecki et al. [2006], Van Steijn et al. [2007]) although they are taken into account in droplet

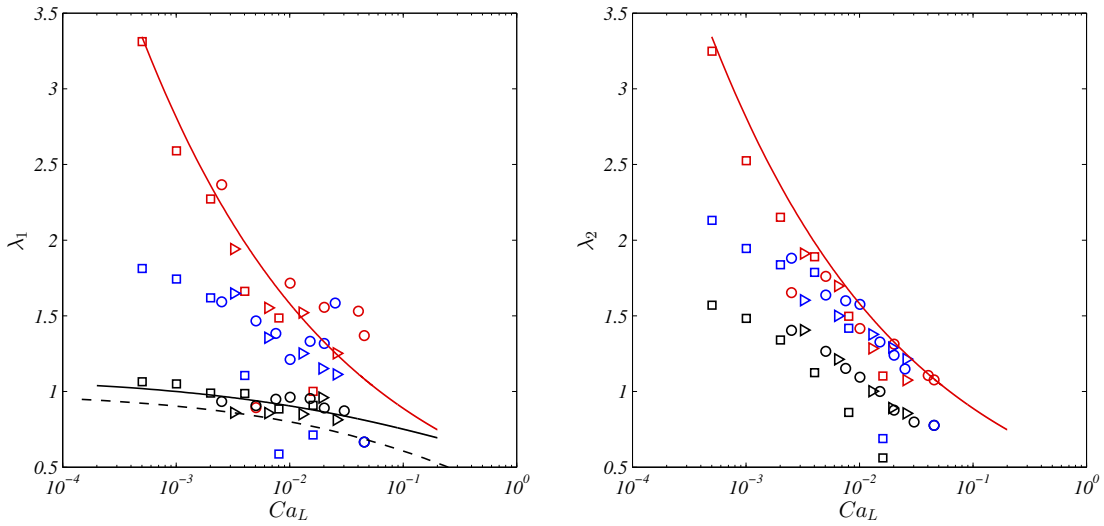

(a) (b)

Figure 5.22: (a) Minimum bubble length produced with the different contacting modes as a function of the liquid capillary number. (b) Linear growth rate with the gas to liquid flow rate ratio as a function of the liquid capillary number.
Legend: (red symbols) cross-junction ; (blue symbols) front-T junction ; (black symbols) side-T junction ; (□) $La = 5440$; (○) $La = 223$; (▷) $La = 33$; (red line) equation 5.15 ; (black solid line) equation 5.27 ; (black dashed line) equation 5.3 from Christopher et al. [2008]

formation Christopher et al. [2008]). The minimum bubble length has been shown to depend on the capillary number independently of the aspect ratio. The growth rate of bubble length has been found to decrease when the liquid capillary number is increased in rectangular microchannels whereas it is constant in a square microchannel. The bubble formation frequency increases with the gas to liquid flow rate ratio and with the liquid capillary number. The increase in bubble formation frequency is enhanced in rectangular channels when the aspect ratio is increased. It has been pointed out that the bubble to unit cell length ratio follows a unique law as a function of the gas to liquid flow rate ratio independently of the capillary number, the Reynolds number and the geometry of the channel.

The gas-liquid flows generated in a cross-junction and two different T-shaped junctions have been compared. Bubble formation in these three geometries can be split into two main steps but the effects of the capillary number on these steps has been shown to differ from one contacting section to another. Indeed, the minimum bubble length at vanishing capillary numbers in a cross-junction would diverge with the proposed scaling law while it seems to tend towards a finite value in T-junctions. The minimum bubble length in a side-T junction can be evaluated with the model proposed by Christopher et al. [2008]. It is smaller than the minimum bubble length obtained in a frontal T-junction and a cross-junction. Similarly, the growth rate of bubble length is reduced in T junctions when compared with cross-junctions. An interesting point is that the bubble lengths are less dependent on the geometry at high capillary numbers where the effects of the walls are reduced.

It could be interesting to perform numerical simulations of bubble formation in cross-junction with different aspect ratio to understand the details of the mechanism and in particular the growth rate for which the effects of the aspect ratio are still not accurately understood.

Chapter 6

Taylor bubble hydrodynamics

Contents

6.1 Introduction

6.1.1 State of the art

In the previous chapter, the bubble generation has been studied under different operating conditions including liquid capillary and Reynolds numbers, liquid to gas flow rate ratios, cross-sectional aspect ratios and contacting geometries. Once the bubble is formed, in straight channels, the bubble and the liquid quickly reach a stationary motion in the frame of reference moving with the bubble. The dynamics of bubble trains appear very similar to that of a single bubble moving in a stationary or flowing liquid, at least when the slug is long enough such that fully developed single phase flow occurs in the liquid slug. The motion of Taylor bubbles in circular channels have been studied since the first experiments by Taylor [1961] and the theoretical work by Bretherton [1961] based on the lubrication approximation. In capillary flows, the bubble with nearly spherical caps occupies a major part of the cross-sectional area of the channel and a thin film separates the bubble from the wall. The dimensionless number that best describes the flow is the capillary number based on the bubble velocity Ca_B:

$$Ca_B = \frac{\mu_L U_B}{\sigma} \tag{6.1}$$

U_B is the bubble velocity, μ_L is the dynamic viscosity of the liquid and σ is the surface tension.

With the lubrication analysis, Bretherton [1961] estimated the liquid film thickness between the bubble and the wall at vanishing capillary numbers, as well as the pressure drops at the bubbles caps (front and rear):

$$\frac{\delta}{R} = 1.34\ Ca_B^{2/3} \tag{6.2}$$

$$\Delta P_{nose} = \frac{2\sigma}{R}\left(1 + 3.72 Ca_B^{2/3}\right) \tag{6.3}$$

$$\Delta P_{rear} = \frac{2\sigma}{R}\left(1 - 0.97 Ca_B^{2/3}\right) \tag{6.4}$$

However, equation 6.2 is only valid at low capillary numbers and diverges as the capillary number increases. More recently, Aussillous and Quéré [2000] extended Bretherton s correlation to higher capillary numbers:

$$\frac{\delta}{R} = \frac{1.34\ Ca_B^{2/3}}{1 + 2.5 \times 1.34\ Ca_B^{2/3}} \tag{6.5}$$

The coefficient 2.5 in the denominator was found empirically while the general form of equation 6.5 was found with a simple balance between the Laplace pressure jump at the cap of the bubble and in the dynamic meniscus.

Less attention has been paid to square and rectangular channel cross-sections even though these geometries appear interesting when dealing with transport phenomena and applications related to chemical engineering and multiphase reactors. Wong et al. [1992, 1995a] also used the lubrication approximation to study the shapes of bubbles and contact lines in polygonal capillaries for nearly static bubbles as the capillary number tends towards zero. The pressure drop ahead of the bubble was related to the capillary number in a square channel of height $2h$ (Wong et al. [1995b]):

$$\Delta P_{nose} = \frac{\sigma}{h}\left(1.8862 + 2.75\ Ca_B^{2/3}\right) \tag{6.6}$$

$$\Delta P_{rear} = \frac{\sigma}{h}\left(1.8862 - 1.00\ Ca_B^{2/3}\right) \quad \text{for} \quad \frac{L_B}{h} << Ca_B^{-1} \tag{6.7}$$

Semi-inifinite bubbles in square and rectangular capillaries have been studied numerically with a finite-element method that solves the free-surface Stokes equations (Hazel and Heil [2002], De Lozar et al. [2008]). The effects of cross-sectional geometry on the liquid area fraction that separates the bubble from the walls and the pressure drop ahead of the bubble have been highlighted. They also investigated the effects of gravity on the loss of symmetry of the shape of the bubble and the flow structure.

Eulerian methods have also been used to simulate the dynamics of fully developed slug flow in 2D or axisymmetrical cases (Gupta et al. [2009, 2010a,b], Afkhami et al. [2011], Abadie et al. [2012]). The use of eulerian methods to perform three dimensional numerical simulations of Taylor flow in square or rectangular microchannels is restricted to only a few studies (Oztaskin et al. [2009], Taha and Cui [2006], Liu and Wang [2008], Abadie et al. [2013]).

In this chapter, we focus on fully developed Taylor flow; the entrance effects are not considered. The effects of the liquid capillary and cross-sectional geometry will be discussed in the first part concerning the results at low Reynolds numbers. The effects of bubble and slug lengths in bubble train flow will then be shown to be of negligible importance and the effects of the Reynolds numbers for the different geometries studied will then be considered in terms of bubble velocity, liquid area fraction and pressure drop.

6.1.2 Circular channels at low Reynolds numbers liquid film thickness and bubble velocity

Although this chapter mainly focuses on square and rectangular capillaries, the shape and the velocity of bubbles in a circular channel have been widely studied and can be well estimated in visco-capillary regimes, *i.e.* where inertial effects are weak. The results presented in this chapter are therefore compared to those predicted by the correlations for Taylor flow in circular channels, which is described below.

Bretherton [1961] considered the capillary driven motion of a bubble in a circular tube. This theoretical analysis based on the lubrication approximation leads to the estimation of the liquid film thickness, the bubble velocity and the pressure jumps at very low capillary numbers. However, this theory is based on the bubble velocity and its corresponding capillary number so that the hydrodynamic parameters cannot be deduced from the parameters of control of an experimental set-up, which are generally the flow rates of each phase. It is therefore interesting to relate the liquid film thickness and thus the bubble slip and absolute velocity to the two-phase velocity.

A key point of the following analysis relies on the flow in the liquid film. In circular tubes, the pressure in the bubble is uniform due to the low viscosity of the bubble and the annular film around the bubble has a constant thickness. As a result, the pressure in the liquid film is uniform and the velocity is zero. The stagnant film allows the bubble velocity to be calculated from the two-phase velocity and the liquid film thickness via a volume balance:

$$\frac{U_B}{U_{TP}} = \frac{1}{\left(1 - \left(\frac{\delta}{R}\right)^2\right)} \tag{6.8}$$

Order 0

In circular tubes, the relations 6.8 and 6.5 indicate that in the limit of small bubble capillary numbers,

$$Ca_B \sim Ca_{TP},$$

where $Ca_B = \frac{\mu_L U_B}{\sigma}$ and $Ca_{TP} = \frac{\mu_L U_{TP}}{\sigma}$ are the capillary number based on the bubble and the mean velocities, respectively. A first approximation would therefore consist in replacing the bubble capillary number Ca_B by the mean capillary number Ca_{TP} in relation 6.5. This leads to the following dimensionless liquid film thickness:

$$\frac{\delta}{R} = \frac{1.34\ Ca_{TP}^{2/3}}{1 + 2.5 \times 1.34\ Ca_{TP}^{2/3}} \tag{6.9}$$

This relation is a first approximation and it is seen in figure 6.1 that it is valid in the limit of small capilary numbers, typically $Ca_{TP} \leq 2 \times 10^{-2}$. It is also seen that it gives a good approximation as the liquid film thickness tends towards its maximum value, typically $Ca_{TP} \geq 2 \times 10^2$.

Order 1

At low capillary number, the bubble slip velocity approaches zero, *i.e.* the bubble velocity is close to the mean velocity in the liquid slug. We can then write as a first approximation :

$$U_B = U_{TP}\left(1 + \alpha Ca_{TP}^{\beta}\right) \tag{6.10}$$

where α and β are constant.
From Bretherton s analysis, the asymptotic solution of the dimensionless liquid film thickness at vanishing capillary number is :

$$\frac{\delta}{R} = 1.34 Ca_B^{2/3} \tag{6.11}$$

From equation 6.10, the film thickness is:

$$\begin{aligned} \frac{\delta}{R} &= 1.34 Ca_{TP}^{2/3}\left(1 + \alpha Ca_{TP}^{\beta}\right)^{2/3} && (6.12)\\ &\sim 1.34 Ca_{TP}^{2/3}\left(1 + \frac{2}{3}\alpha Ca_{TP}^{\beta}\right) && (6.13) \end{aligned}$$

Equations 6.8 and 6.12 allow the bubble velocity to be calculated from the two-phase velocity and the liquid film thickness:

$$\begin{aligned} \frac{U_B}{U_{TP}} &\sim 1 + 2\frac{\delta}{R} && (6.14)\\ &\sim 1 + 2 \times 1.34 Ca_{TP}^{2/3}\left(1 + \frac{2}{3}\alpha Ca_{TP}^{\beta}\right) && (6.15)\\ &\sim 1 + 2 \times 1.34 Ca_{TP}^{2/3} + 2 \times 1.34 \frac{2}{3}\alpha Ca_{TP}^{2/3+\beta} && (6.16) \end{aligned}$$

By considering low capillary numbers and keeping the leading order terms, we can then identify α and β from equations 6.10 and 6.16 as follows:

$$\begin{aligned} \alpha &= 2 \times 1.34 && (6.17)\\ \beta &= \frac{2}{3} && (6.18) \end{aligned}$$

With the values of α and β and as Ca_B tends towards zero, equation 6.10 then becomes :

$$\frac{U_B}{U_{TP}} = 1 + 2 \times 1.34 Ca_{TP}^{2/3} \tag{6.19}$$

and the liquid film thickness is:

$$\frac{\delta}{R} = 1.34 Ca_{TP}^{2/3} \left(1 + \frac{4}{3} \times 1.34 Ca_{TP}^{2/3}\right) \tag{6.20}$$

These corrections are valid at low capillary numbers but the liquid film thickness still needs to be limited when the capillary number increases in order to avoid divergence. From Aussillous and Quéré [2000], it is known that the dimensionless film thickness tends toward a maximum at 0.4 so it is possible to restrict the liquid film thickness at high capillary numbers with the following relation :

$$\frac{\delta}{R} = \frac{1.34 Ca_{TP}^{2/3} \left(1 + \frac{4}{3} \times 1.34 Ca_{TP}^{2/3}\right)}{1 + 1.34 Ca_{TP}^{2/3} \left(1 + \frac{4}{3} \times 1.34 Ca_{TP}^{2/3}\right)} \tag{6.21}$$

However, it is seen that the evolution of the liquid film thickness at intermediate and high capillary numbers is not exactly recovered and a slight correction in the denominator allows a better prediction of the liquid film thickness as a function of the two-phase capillary number.

$$\frac{\delta}{R} = \frac{1.34 Ca_{TP}^{2/3} \left(1 + \frac{4}{3} \times 1.34 Ca_{TP}^{2/3}\right)}{1 + 1.34 Ca_{TP}^{2/3} \left(1.2 + \frac{4}{3} \times 1.34 Ca_{TP}^{2/3}\right)} \tag{6.22}$$

From equations 6.8 and 6.22, the bubble velocity is written as a function of the mean velocity and the two-phase capillary number:

$$\frac{U_B}{U_{TP}} = \left[1 - \left(\frac{1.34 Ca_{TP}^{2/3} \left(1 + \frac{4}{3} \times 1.34 Ca_{TP}^{2/3}\right)}{1 + 1.34 Ca_{TP}^{2/3} \left(1.2 + \frac{4}{3} \times 1.34 Ca_{TP}^{2/3}\right)}\right)^2\right]^{-1} \tag{6.23}$$

Numerical results obtained from 2D axisymmetrical simulations similar to those described in chapter 4 are reported in figure 6.1 and agree well with the predicted film thickness.

Finally, as it is seen in figure 6.2, the bubble velocity in axisymmetric flows can be well estimated from the operating parameters and the numerical results again show very good agreement with the proposed correction to estimate the liquid film thickness and the bubble velocity as a function of the two-phase capillary number.

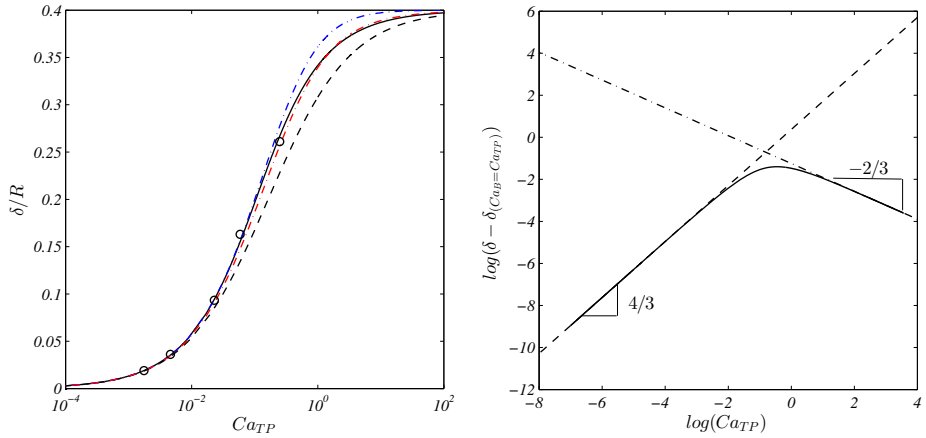

(a) (b)

Figure 6.1: (a) Evolution of the liquid film thickness in a tube as a function of the two-phase capillary number Ca_{TP}. (b) Log-Log representation of the difference between δ/R and δ/R (order 0) to reveal the power law.
Legend: (∘) numerical results ; (black solid line) δ/R obtained from Ca_B with equation 6.5 (Aussillous and Quéré [2000]) ; (black dashed line) δ/R obtained from equation 6.9 (correction order 0) ; (blue dash-dotted line) δ/R obtained from equation 6.20 (correction at low Ca) ; (red dash-dotted line) δ/R obtained from Ca_{TP} with equation 6.21.

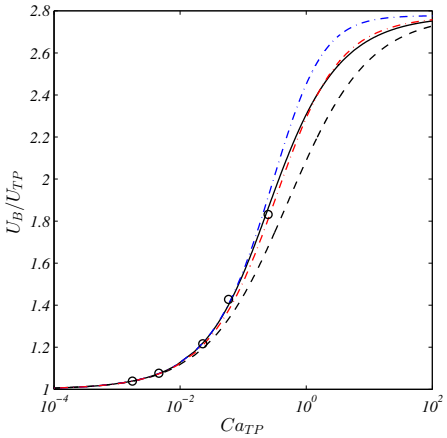

Figure 6.2: Evolution of the ratio of the bubble velocity to the two-phase velocity as a function of the two-phase capillary number Ca_{TP} in a tube.
Legend: (∘) numerical results ; (black solid line) U_B/U_{TP} from equations 6.5, 6.8 (Aussillous and Quéré [2000]) ; (black dashed line) U_B/U_{TP} from equations 6.9, 6.8 (correction order 0) ; (blue dash-dotted line) U_B/U_{TP} from equations 6.20, 6.8 (correction at low Ca) ; (red dash-dotted line) U_B/U_{TP} from equations 6.23.

6.2 Numerical set-up

In microchannels, the effects due to gravity can generally be neglected. Indeed, independently of the operating conditions in terms of mass or volumetric flow rates, the maximum Bond number achieved in our experiments is much lower than unity ($Bo \leq 0.1$), which indicates that the effects due to gravity are negligible when compared with capillary effects. This observation allows a symmetrical bubble shape to be considered and only a quarter of the channel is simulated throughout this study as shown in figure 6.3. As a consequence, the gravitational force is also set to zero in the simulations. The effects of the gravitational force on the symmetry of Taylor bubbles in circular microchannels for Bond number close to unity have been studied in the literature both experimentally (Leung et al. [2012]) and numerically (Gupta et al. [2013], De Lozar et al. [2008]).

The bubble is placed in the domain and a pressure gradient along the $z-$direction between two periodic boundary conditions is imposed to induce the motion until the flow reaches steady state (see figure 6.3(a)) . The periodic boundary conditions allow the simulation of a bubble train with bubbles translating through the boundaries. No-slip wall conditions are imposed on the planes $x = w$ and $y = h$ and a symmetry boundary condition is set at $x = 0$ and $y = 0$. The grids used consist of $32 \times 32 \times 256$, $48 \times 32 \times 256$ and $64 \times 32 \times 256$ cells in the $x-$, $y-$ and $z-$direction for microchannels with aspect ratios $\alpha = 1,\ 2.5$ and 4, respectively. Note that in this part, w represents half the channel width while it was the total width of the channel in chapter 5. An example of the mesh for the square cross-section can be seen in figure 6.3(b).

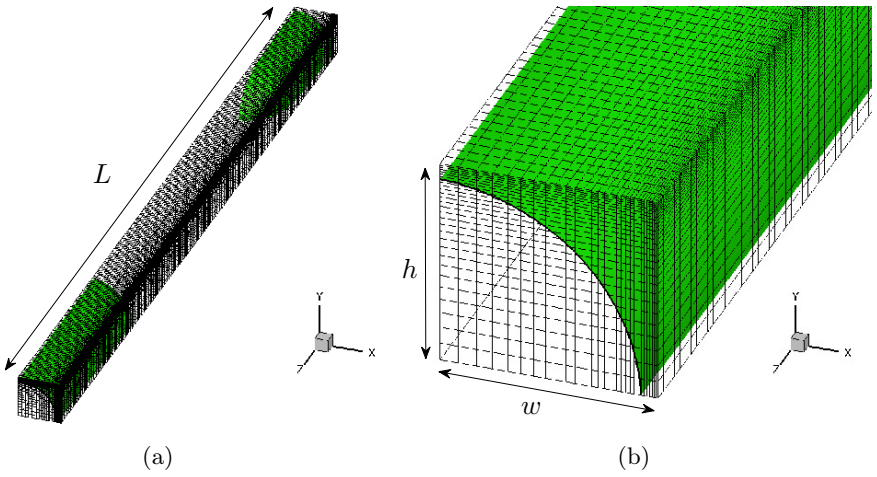

Figure 6.3: (a) Illustration of the computational domain and the mesh used in a square capillary. (b) Close-up view - the bubble interface is shown to reveal the flim thickness.

In order to correctly resolve the thin liquid film between the bubble and the wall (with a minimum of 5 cells as recommended in Gupta et al. [2009]), these grids are refined at the walls using a geometric evolution that decreases cell size in the last 32 cells in the x and y directions. In the axial direction, regular grid spacing is used and the length of the unit cell is $L = 17 \times h$. Depending on the case, the length of the domain has been varied: as the capillary number increases, the bubble length increases too and the unit cell length has been doubled. At low capillary numbers $Ca \leq 0.06$, the axial grid spacing has been refined and the unit cell length has been reduced to $L = 8.5 \times h$.

The ratio of liquid to gas viscosities and densities have been set to $\rho_L/\rho_G = 10^3 = \mu_L/\mu_G$. The fluid properties have been varied to cover a wide range of capillary and Reynolds numbers resulting in eight different Laplace numbers:

$$La = \frac{\rho_L \sigma D_h}{\mu_L^2} = [2.8\,;\ 28\,;\ 280\,;\ 1000\,;\ 2000\,;\ 5000\,;\ 10000\,;\ 20000].$$

It should be mentioned that for capillary numbers above $Ca = 0.08$, the VOF-FCT-CCSF method has been used while for low capillary numbers where spurious currents arise and are not negligible when compared with the velocity field around the bubble, the LS-CCSF method has been used.

6.3 Results at low Reynolds numbers

6.3.1 First observations

Bubble shapes obtained from 3D numerical simulations are reported in figure 6.4. It is observed that the bubble shape follows the cross-sectional shape of the channel. Indeed, the bubbles are flattened in the smallest dimension and curved in the greatest dimension. In addition, it is seen that the bubble caps exhibit different curvatures in the height and the width of the channel. Figure 6.5 reports the velocity magnitude relative to the bubble velocity on the interface for the three aspect ratios considered ($\alpha = [1; 2.5; 4]$). For all the geometries in this study, the velocity around the caps is close to the bubble velocity and approaches zero around the bubble body. With this representation, the confinement in the different directions of the channels is highlighted. Indeed, the velocity rapidly tends towards zero in the height while the nose and rear regions are elongated in the width of the channel. This trend is accentuated as the aspect ratio increases. It is also interesting to point out that the same tendency is found in the diagonal of the square channel.

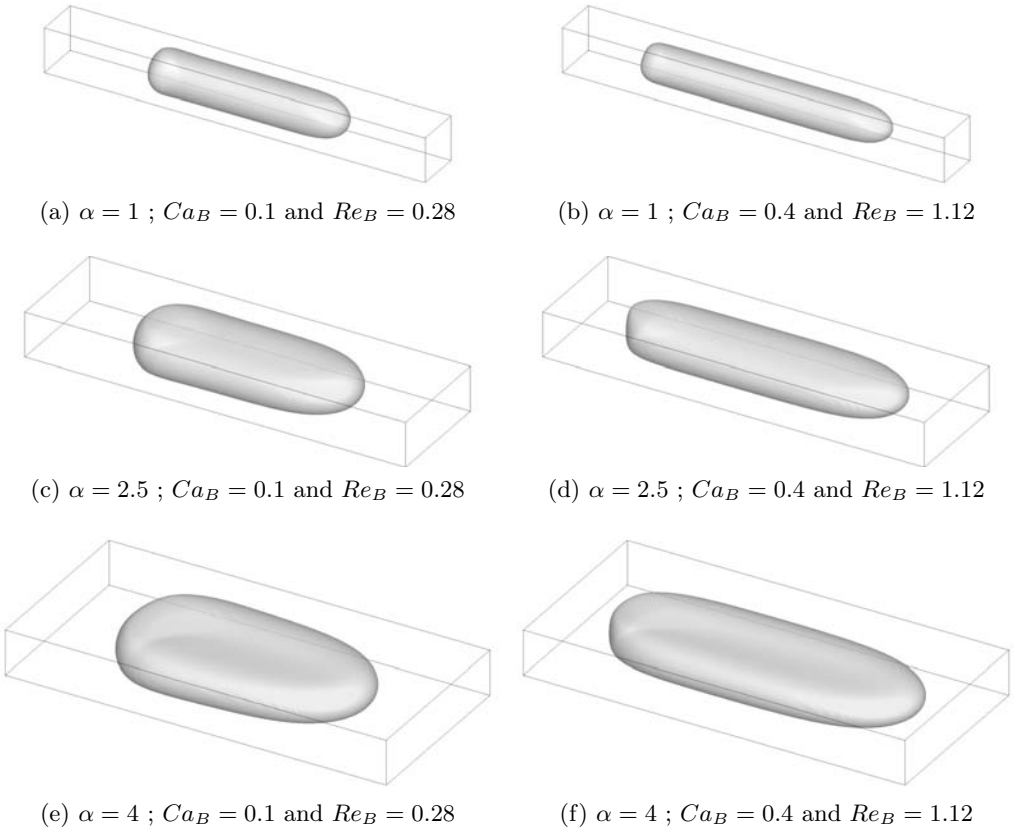

(a) $\alpha = 1$; $Ca_B = 0.1$ and $Re_B = 0.28$

(b) $\alpha = 1$; $Ca_B = 0.4$ and $Re_B = 1.12$

(c) $\alpha = 2.5$; $Ca_B = 0.1$ and $Re_B = 0.28$

(d) $\alpha = 2.5$; $Ca_B = 0.4$ and $Re_B = 1.12$

(e) $\alpha = 4$; $Ca_B = 0.1$ and $Re_B = 0.28$

(f) $\alpha = 4$; $Ca_B = 0.4$ and $Re_B = 1.12$

Figure 6.4: Bubble shapes for $Ca_B = 0.1$ in the channels of aspect ratio $\alpha = [1; 2.5; 4]$.

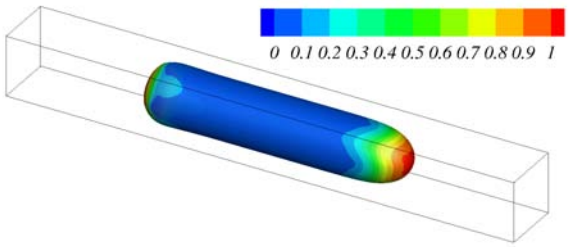

(a) $\alpha = 1$; $Ca_B = 0.1$ and $Re_B = 0.28$

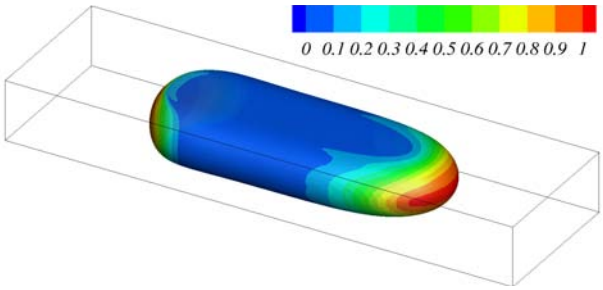

(b) $\alpha = 2.5$; $Ca_B = 0.1$ and $Re_B = 0.28$

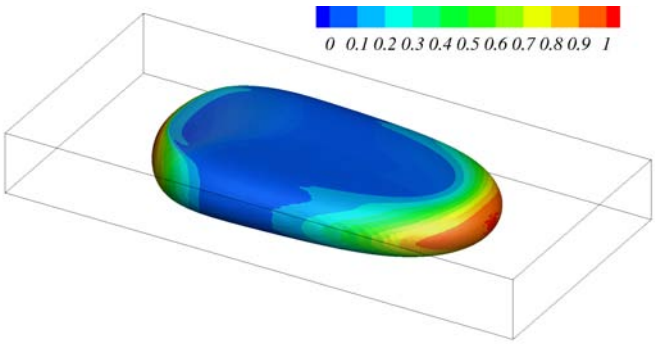

(c) $\alpha = 4$; $Ca_B = 0.1$ and $Re_B = 0.28$

Figure 6.5: Illustration of the bubble shapes for $Ca_B = 0.1$ in the channels of aspect ratio $\alpha = [1; 2.5; 4]$. The interface is colored with the magnitude of the dimensionless velocity U/U_B.

6.3.2 Flow field around the bubble

Since the bubble velocity increases with the capillary number, the flow structure also evolves with the capillary number and the velocity field around the bubble is modified. The bubble shapes and the flow pattern are illustrated for different capillary numbers in figures 6.6 and 6.7 for a square channel $\alpha = 1$ and a rectangular channel with aspect ratio $\alpha = 4$, respectively.

For the square channel, the streamlines represented in figure 6.6 in the frame of reference moving with the bubble indicate that the flow is affected by the bubble in the vicinity of the interface but the velocity in the slug rapidly tends towards the velocity profile of a single-phase flow with a mean velocity equal to the two-phase velocity. Indeed, the flow appears to be fully developed at a distance of approximately one diameter from the bubble caps. As the maximum velocity at the centerline of the channel is generally greater than the bubble velocity, the relative velocity at the center of the channel is positive while it decreases when approaching the walls and becomes negative at a certain distance from the center of the channel. This gives rise to a recirculation motion in the central zone of the channel and a by-pass flow close to the walls. This recirculation zone occupies a major part of the channel cross-section at low capillary numbers and the recirculating volume decreases as the capillary number increases until if finally vanishes (see figure 6.6(e)). Further details about the characteristics of this recirculation motion and the by-pass flow are given in chapter 7.

In the channel with aspect ratio $\alpha = 4$, similar structures are observed: at low capillary number ($Ca_B = 0.02$) recirculation motion occurs and at high capillary numbers complete by-pass flow occurs. However, the evolution of the flow around the bubble between these two extreme flow structures appear to be more complex in rectangular channels. It has been observed by De Lozar et al. [2008] that the stagnation point seems to detach from the bubble surface and moves towards the slug ahead of the bubble. It is interesting to observe similar behaviour at the rear cap of the bubble, which was not simulated in the work by De Lozar et al. [2008]. In addition, the other cross-section in the more confined direction was not shown in their study and it is interesting to point out that the recirculation pattern is similar to that in square capillaries.

It is also seen in figures 6.6 and 6.7 that the bubble shape changes significantly with the capillary number as it is the case in circular tubes. Indeed, the liquid film thickens as the capillary number increases, whatever the geometry. The thickening of the liquid film is particularly seen in the less confined direction (width) of rectangular channels. In addition, the length necessary for the liquid film to develop is increased as the aspect ratio increases. The bubble shape in the square channel presents a nearly constant film thickness, while it varies along the bubble length in the rectangular channel of aspect ratio $\alpha = 4$. The shape of the bubbles in an axial cross-section will be discussed further in section 6.3.4.

6.3.3 Bubble velocity

Since the experiments of Taylor [1961] and the theoretical analysis of Bretherton [1961] based on the lubrication approximation, the bubble capillary number has been identified as the dimensionless number that characterizes confined bubbles in small channels driven by surface tension effects and where the Reynolds number is generally very low, *i.e.* the inertial effects are negligible. Thus, the capillary number has been chosen to make the velocities dimensionless in order to compare the numerical

(a) $Ca_B = 0.02$ and $Re_B = 0.56$

(b) $Ca_B = 0.06$ and $Re_B = 1.68$

(c) $Ca_B = 0.1$ and $Re_B = 0.28$

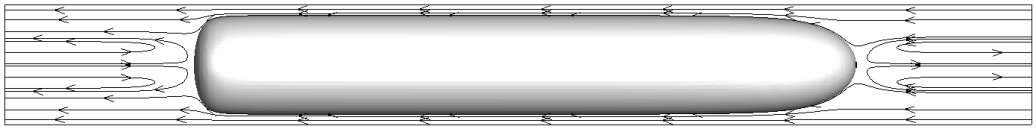

(d) $Ca_B = 0.4$ and $Re_B = 1.12$

(e) $Ca_B = 1$ and $Re_B = 2.8$

Figure 6.6: Bubble shapes and flow structures in the symmetry planes of the channel of aspect ratio $\alpha = 1$ for $Ca_B = [0.02; 0.06; 0.1; 0.4; 1]$.
The line on the bubble surface represents the separation between recirculation and by-pass zones.

simulations with the experiments. Figure 6.8 shows the bubble capillary number as a function of the two-phase capillary number based on the mean velocity in the channel. The results from the correlation of Aussillous and Quéré [2000], which is valid in tubes, is given as a comparison and in a first approximation, the bubble velocity in rectangular channels of moderate aspect ratio appears to be close to that in circular

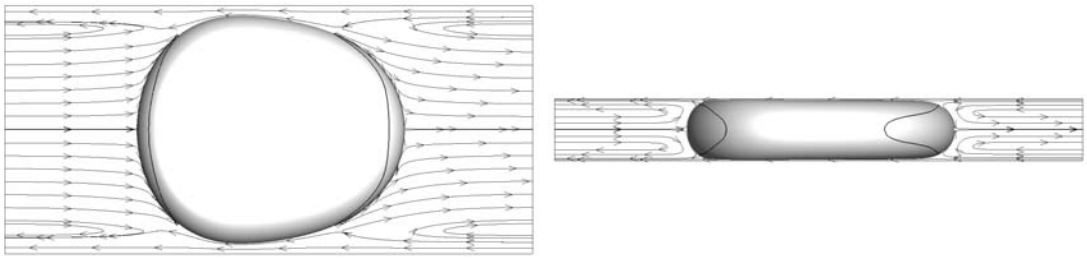

(a) $Ca_B = 0.02$ and $Re_B = 0.56$

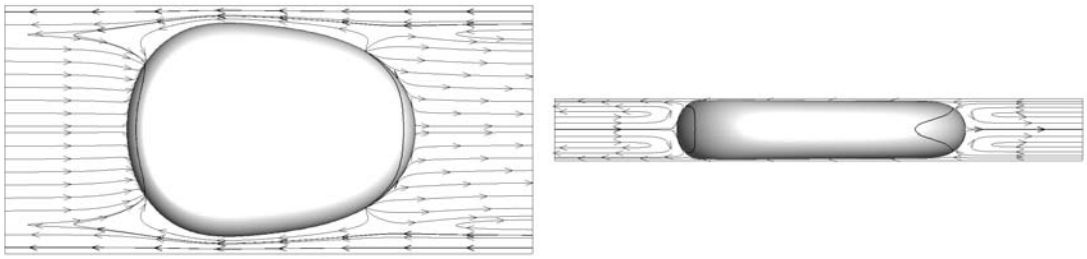

(b) $Ca_B = 0.04$ and $Re_B = 1.12$

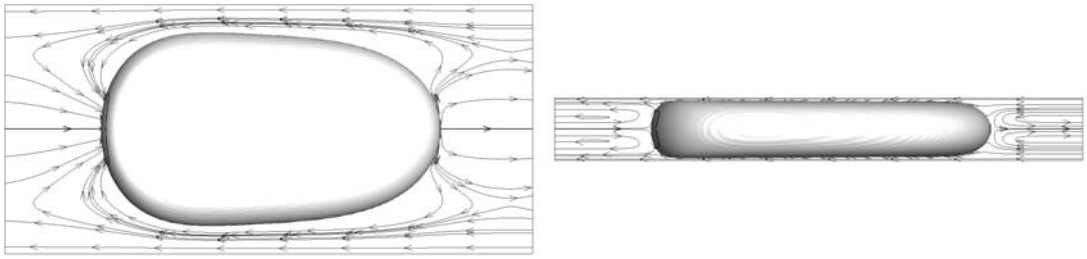

(c) $Ca_B = 0.1$ and $Re_B = 0.28$

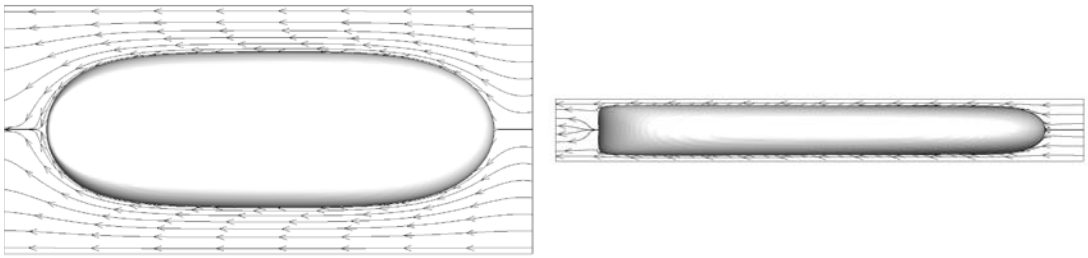

(d) $Ca_B = 0.6$ and $Re_B = 1.68$

Figure 6.7: Bubble shapes and flow structures in the symmetry planes of the channel of aspect ratio $\alpha = 4$ for $Ca_B = [0.02; 0.04; 0.1; 0.6]$.
Left: top view of the channel in the width of the channel ; right: lateral view in the depth of the channel. The line on the bubble surface represents the separation between recirculation and by-pass zones.

capillaries. Good agreement between the velocities from the experimental data (filled symbols) and the velocities obtained from the numerical simulations (open symbols) is found. It is observed that the bubble capillary number remains greater than the mean capillary number, which is in agreement with the predictions available in capillary tubes (Bretherton [1961], Aussillous and Quéré [2000]) and with the numerical results of semi-infinite bubbles in square and rectangular capillaries (Hazel and Heil

[2002], De Lozar et al. [2008]). It is also observed that the ratio of bubble velocity to mean velocity increases with the capillary number. Indeed, similarly to what happens in circular channels, the bubble velocity can be well estimated by the mean velocity in the liquid slug at vanishing capillary numbers. However, the slip velocity between the bubble and the mean velocities increase with the capillary number and when the viscous forces dominate the capillary forces, the ratio of bubble to mean velocities tends towards a constant value ($U_B/U_{TP}(Ca \to \infty) \simeq 2.78$ in circular capillaries).

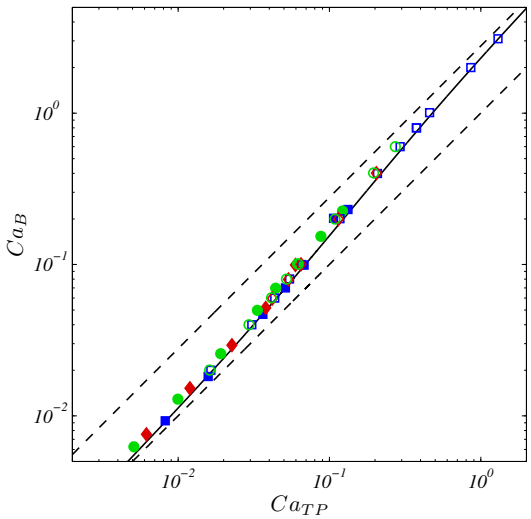

Figure 6.8: Bubble capillary number Ca_B as a function of the two-phase capillary number Ca_{TP}.
Legend: (filled symbols) experiments ; (open symbols) numerical simulations ;
(□, blue) $\alpha = 1$; (◇, red) $\alpha = 2.5$; (○, green) $\alpha = 4$; (dashed lines) $Ca_B = Ca_{TP}$ and $Ca_B = 2.78\,Ca_{TP}$; (solid line) equation 6.23.

Figure 6.9 shows the ratio of bubble velocity to the mean velocity in the liquid slug as a function of the bubble capillary numbers Ca_B and Ca_{TP} for the three aspect ratios $\alpha = [1; 2.5; 4]$. The bubble to two-phase velocity ratio increases with the capillary number in all the geometries and it is seen that the trends are close to those in a circular channel. Close inspection of the ratio of bubble velocity to mean velocity shows that at a given bubble capillary number greater than approximately $Ca_B = 0.01$, this ratio increases, *i.e.* the slip velocity between the bubble and the mean velocity increases with the aspect ratio. Both the experimental and numerical data are in very good agreement with the numerical results from De Lozar et al. [2008] in the range of capillary numbers covered. De Lozar et al. [2008] further showed that below this capillary number $Ca_B = 0.01$, the liquid area fraction and thus, the bubble velocity decreases when the aspect ratio increases. This was not possible in the current numerical simulations due to the computational effort needed to compute the very thin liquid film between the bubble and the walls (see appendix B for details on the required computational times). As it has been discussed in section 6.1.2, it is interesting to report the bubble to mean velocity ratio as a function of the two-phase capillary number Ca_{TP} as shown in 6.9(b). The observations are similar to the bubble to mean velocity ratio as a function of the two-phase capillary number. Indeed, at low capillary numbers, the bubble velocity tends towards the mean velocity and the increase in bubble velocity becomes sharper with this representation as the bubble to two-phase velocity increases.

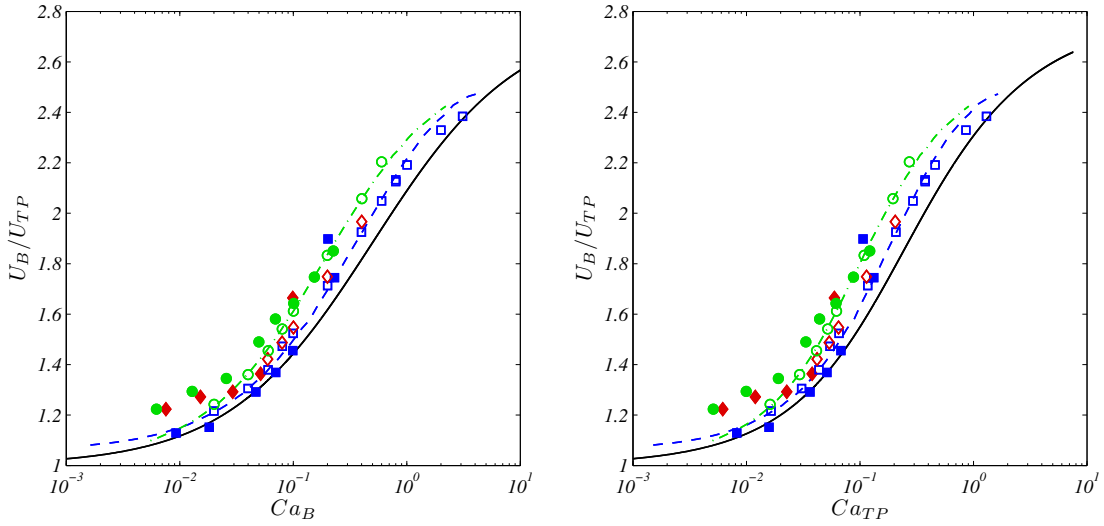

(a) (b)

Figure 6.9: Ratio of the bubble velocity to the mean velocity U_B/U_{TP} as a function of (a) the bubble capillary number Ca_B ; (b) the two-phase capillary number Ca_{TP}. Legend: (□, blue) $\alpha = 1$; (◇, red) $\alpha = 2.5$; (○, green) $\alpha = 4$; (blue dashed line) $\alpha = 1$ De Lozar et al. [2008] ; (green dash-dotted line) $\alpha = 4$ De Lozar et al. [2008] ; (solid line) equation 6.23.

6.3.4 Liquid area fraction

In circular tubes, the pressure in the bubble is uniform due to the low viscosity of the bubble and the annular film around the bubble has a constant thickness; as a result the pressure in the liquid film is uniform and the velocity is zero. Figure 6.5 illustrates that the absolute velocity on the interface along the bubble body is zero. Athough surface tension usually forces the interfaces to be spherical in three dimensions, the shape of the bubble is not cylindrical and approaches the shape of the channel at low capillary numbers in polygonal capillaries due to the confinement (Wong et al. [1992, 1995a]). Thus, due to the non-uniform radius of curvature in a cross-section, the pressure jumps differ from one direction to another. Indeed, close to the walls, the interface is flattened and the pressure jump is reduced while the curvature is maintained in the corners and in the less confined direction (if $\alpha \neq 1$) thereby leading to a pressure drop between the walls and the corners. The liquid film between the bubble and the walls is then drained towards the corners or the greatest dimension where the pressure is lower. An example of drainage flow is shown in figure 6.10 for a rectangular channel of aspect ratio $\alpha = 4$. It is seen that the maximum axial velocity is about $0.035 \times U_B$ and the velocity in a cross-section can reach around 5% of the bubble velocity. Wong et al. [1995a] suggested that in the case of gas fingers or semi-infinite bubbles at low capillary numbers, an axial flow persists in the corners and the bubble shape evolves in the axial direction. Hazel and Heil [2002] and De Lozar et al. [2008] also observed this draining flow in rectangular shaped channels but they estimated that this flow becomes negligible after a distance that is approximately four times the aspect ratio of the channel.

In this work, we focus on bubble trains with finite bubble and slug lengths. It is shown in figure 6.11 that the liquid flow rate is equal to the two-phase flow rate in the

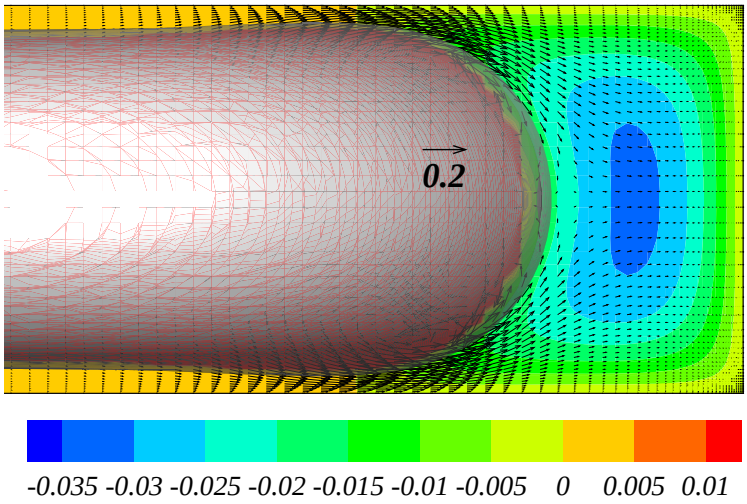

Figure 6.10: Drainage flow in a cross-section for $Ca_B = 0.1$ in a rectangular channel ($\alpha = 4$) at a distance 1.8α from the nose, where the liquid flow rate is minimum. Legend: The reference vector represents a velocity $0.2U_B$. The axial velocity field is reported in color.

liquid slug and decreases at the nose of the bubble until reaching less than 1% of the total flow rate along the bubble body. It is observed that even if the bubble is not much longer than the channel width and the bubble shape does not attain a uniform film thickness, the liquid flow rate decreases from the bubble nose to a position that is approximately at a distance of one width from the rear bubble cap. As the liquid flow rate vanishes at a certain position in the case of finite bubble lengths, a mass balance allows the liquid area fraction to be related to the bubble and mean velocities as in circular channels despite the draining flow in polygonal capillaries.

The liquid flow rate vanishes at a distance from the bubble nose that depends on the capillary number and its length. The cross-sectional shape of the bubble has been reported at this position since this would be the cross-sectional shape along the body of a developed bubble and it corresponds to the quantity of liquid that would remain on the walls of the channel in the case of a longer bubble emptying the channel. Figure 6.12(a) and (c) show the cross-sectional shape of bubbles in square and rectangular channels depending on the capillary number. The bubble shapes approach the shape of the channel when the capillary number is very low. In a square channel, the liquid film thickness increases with the capillary number and it increases more rapidly across the diagonal since the cross-section of the bubble becomes circular (see figures 6.12(a)-(b)). The bubble radius in a square channel is shown in figure 6.12(b) and confirms that the shape is not circular at low capillary numbers where the radius across the diagonal can be greater than the height of the channel. For capillary numbers around $Ca_B = 0.1$, the bubble body becomes cylindrical. It is interesting to note that the radius of the bubble in these cases can be fitted with a sinusoidal function where the amplitude corresponds to the difference between the radii in the horizontal (r_B^{wall}) and

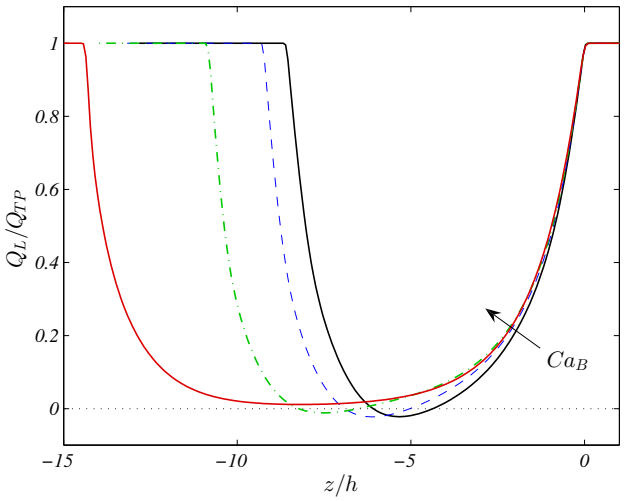

Figure 6.11: Liquid flow rate as a function of the axial position in a channel of aspect ratio $\alpha = 4$ for differetent capillary numbers.
Legend: (black solid line) $Ca_B = 0.02$; (blue dashed line) $Ca_B = 0.04$; (green dash-dotted line) $Ca_B = 0.1$; (red solid line) $Ca_B = 0.6$.

the diagonal (r_B^{diag}) directions:

$$r_B(\theta) = \frac{r_B^{wall} + r_B^{diag}}{2} + \frac{r_B^{wall} - r_B^{diag}}{2} cos\,(4\theta) \qquad (6.24)$$

with $[r_B^{diag}; r_B^{wall}] = [1.07; 0.973]$ for $Ca_B = 0.02$ and $[r_B^{diag}; r_B^{wall}] = [0.979; 0.942]$ for $Ca_B = 0.04$. However, this is yet to be confirmed at lower capillary numbers. In a rectangular channel, the bubble shape is more complex. It is seen that the liquid film thickness is greater in the less confined direction. It is interesting to point out that the bubble does not have an elliptical cross-section or a flat shape in the center part with two circular caps on the sides. In addition the film thickness is not minimal in the plane $x = 0$ but it decreases slightly until a distance from the symmetry plane that is approximately the maximum bubble radius minus the height of the channel.

The slip velocities between the bubble and the mean flow in the slug (or the liquid area fraction $W = 1 - U_{TP}/U_B$ as defined in Bretherton [1961] and De Lozar et al. [2008]) obtained from the numerical simulations at low Reynolds numbers are shown in figure 6.13 where the numerical results from De Lozar et al. [2008] are also reported. It has been qualitatively observed and it is confirmed here that an increase in the capillary number leads to an increase in the liquid area fraction. In addition, for $Ca_B \gtrsim 0.01$, the liquid area fraction increases with the aspect ratio. However, the opposite trend is found at lower capillary numbers as we can see with the results from De Lozar et al. [2008]. The agreement between our results and the results for semi-infinite bubbles is very good. Slight deviations can be observed at high capillary numbers but this corresponds to cases where the Reynolds numbers were greater than 5 since the Laplace number is fixed and $Re_B = La \times Ca_B$. These differences can then be attributed to the inertial effects that were not taken into account in the simulations of De Lozar et al. [2008]. Since the liquid area fraction is directly related to the velocities, the results are similar to those in section 6.3.3.

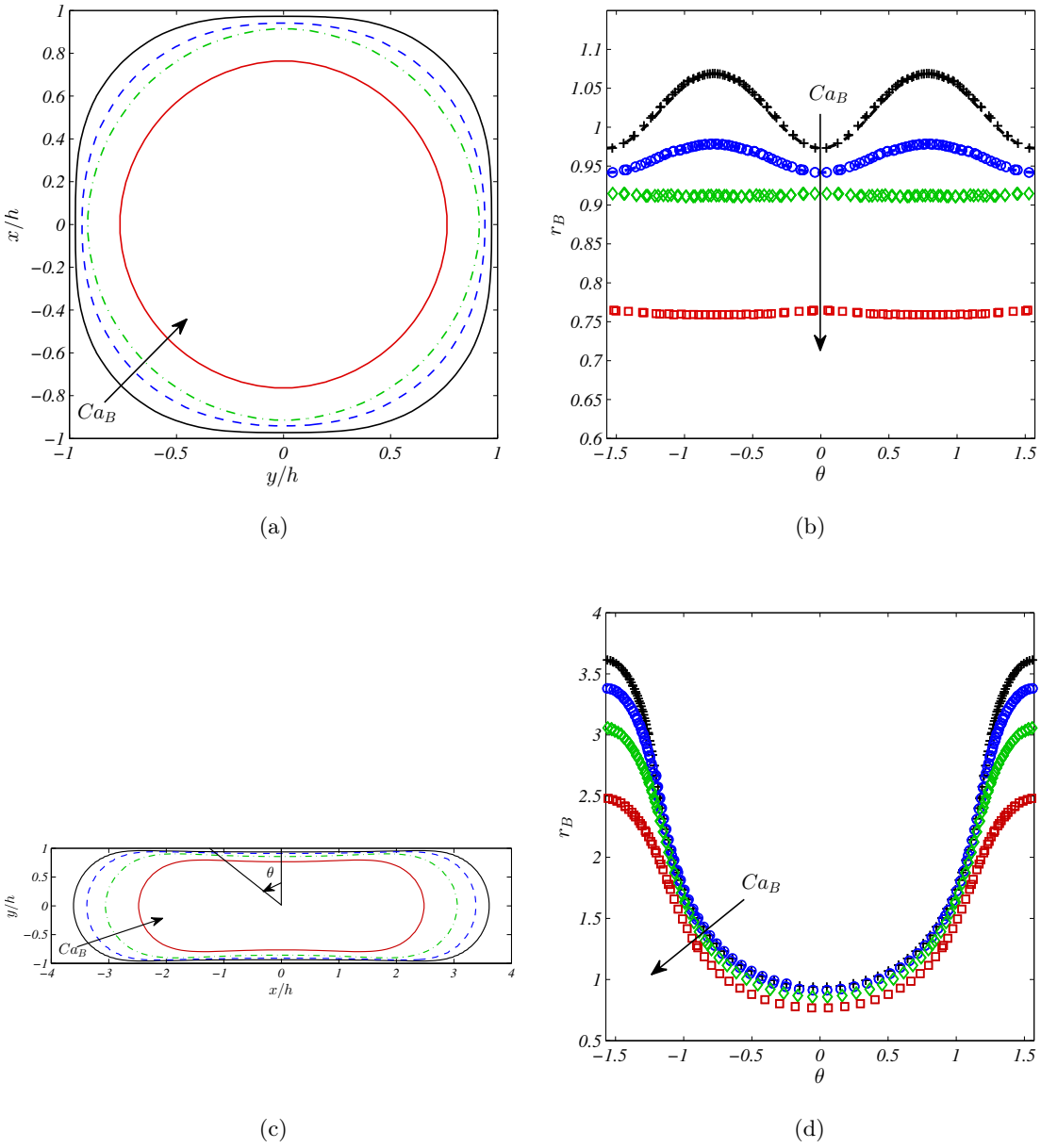

Figure 6.12: Cross-sectional shape of bubbles in (a) a square and (c) a rectangular channel of aspect ratio $\alpha = 4$. Cross-sectional bubble radii as a function of the angle formed with the vertical for (b) a square channel and (d) a rectangular channel of aspect ratio $\alpha = 4$

Legend: (a)-(b) (black, solid line and +) $Ca_B = 0.02$; (blue dashed line and $\circ$) $Ca_B = 0.04$; (green dash-dotted line and $\diamond$) $Ca_B = 0.1$; (red solid line and $\square$) $Ca_B = 1$. Legend: (c)-(d) (black, solid line and +) $Ca_B = 0.02$; (blue dashed line and $\circ$) $Ca_B = 0.04$; (green dash-dotted line and $\diamond$) $Ca_B = 0.1$; (red solid line and $\square$) $Ca_B = 0.6$.

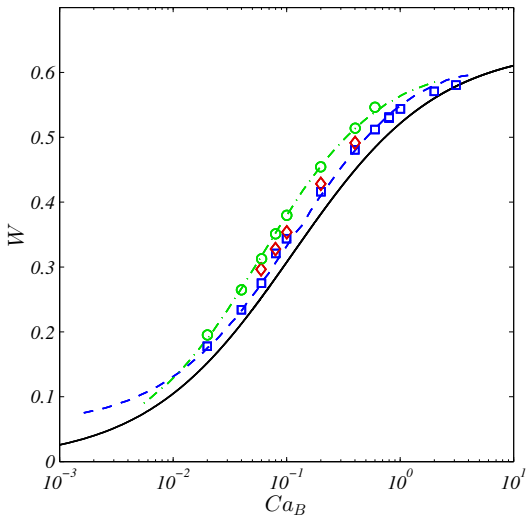

Figure 6.13: Slip velocity or liquid area fraction $W = 1 - U_{TP}/U_B$ as a function of the bubble capillary number Ca_B for aspect ratios $\alpha = [1; 2.5; 4]$ at low Reynolds number. Legend: ($\square$, blue) $\alpha = 1$; ($\diamond$, red) $\alpha = 2.5$; ($\circ$, green) $\alpha = 4$; (blue dashed line) $\alpha = 1$ De Lozar et al. [2008] ; (green dash-dotted line) $\alpha = 4$ De Lozar et al. [2008] ; (solid line) W deduced from equation 6.23.

6.3.5 Pressure drop

Bubble pressure drop

The evolution of the bubble shapes and notably the liquid area fraction are related to the bubble velocity, while the evolution of the shape of the bubble caps is related to the Laplace pressure jumps at the interface. Indeed, figures 6.6 and 6.7 show that the bubble nose is elongated as the capillary number increases and the rear bubble cap is flattened. The pressure drop across the bubble caps and the total pressure drop are shown in figure 6.14 as a function of the bubble capillary number Ca_B. As the surface tension forces are preponderant, the pressure drop is made dimensionless with a capillary pressure based on the minimum characteristic dimension of the channel $p_{cap} = \sigma/h$ (De Lozar et al. [2008]), which is the asymptotic pressure drop at low capillary number in a plane flow. The asymptotic values of both pressure jumps at vanishing capillary numbers in a square channel is 2, which is the value obtained with a sphere of diameter equal to the height of the channel. The pressure drop at the front cap of the bubble increases with the capillary number while the pressure drop at the rear cap decreases when the capillary number is increased. This is in agreement with the observations made previously about the bubble shapes, where the bubble nose had been seen to elongate (*i.e.* the front curvature increases) while the rear cap flattens (*i.e.* the rear curvature decreases). The total pressure jump then increases with the capillary number as the difference between the pressure jumps at the front cap and the rear cap increases. The relations 6.6 and 6.7 that have been built on the lubrication approximation at vanishing capillary numbers appear to give a correct estimation of the pressure drop at very low capillary numbers, however the variations with the capillary number are underestimated. Indeed, it underestimates the pressure jump at the front cap when the capillary number increases and overestimates the pressure drop at the rear cap. The pressure jumps obtained in a square channel are again in good agreement with the results of De Lozar et al. [2008] despite a slight overestimation of the pressure

jump at the front cap. The aspect ratio decreases both pressure drops at the front and rear caps. Indeed, as the channel width is not considered in the capillary pressure, due to the less confined direction in which the radius of curvature of the bubble is increased, the absolute value of the pressure drops decreases. This difference in the curvatures is clearly seen in figure 6.7(d). Indeed, in the depth of the channel, the bubble is flat while in the width of the channel, the rear shape remains circular.

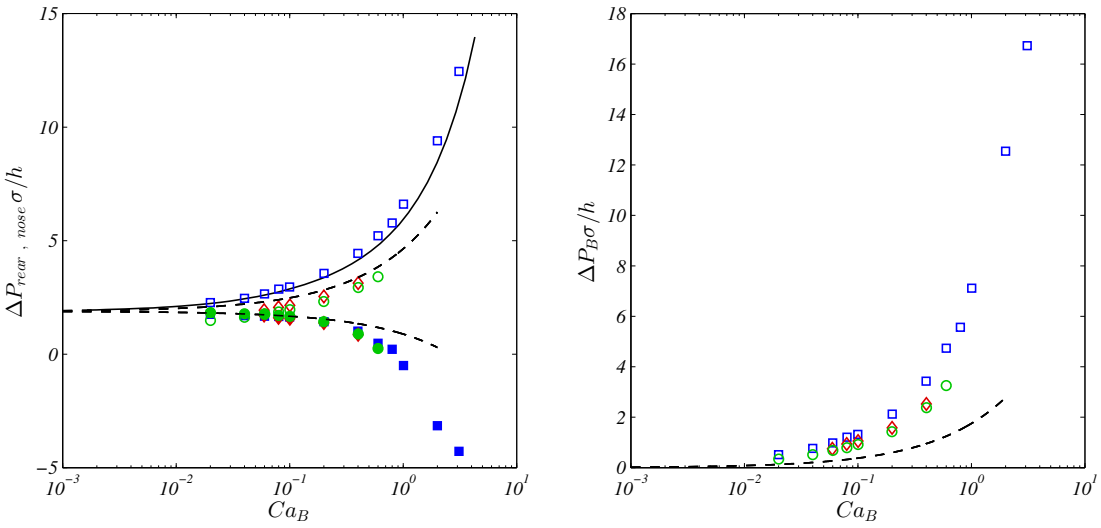

Figure 6.14: (a) Laplace pressure differences at bubble caps as a function of the capillary number for aspect ratios $\alpha = [1; 2.5; 4]$. (b) Total pressure drop across the bubble as a function of the capillary number for aspect ratios $\alpha = [1; 2.5; 4]$.
Legend: (open symbols) front cap ; (filled symbols) rear caps ;
($\square$, blue) $\alpha = 1$; ($\diamond$, red) $\alpha = 2.5$; ($\circ$, green) $\alpha = 4$; (dashed lines) $\alpha = 1$ (Wong et al. [1995b]) : (solid line) $\alpha = 1$ (De Lozar et al. [2008]).

The effects of the rectangular shape of the channel can be taken into account by considering a capillary pressure where the two main curvatures are the height and the width of the channel:

$$p^*_{cap} = \sigma\,[1/(2h) + 1/(2w)] = p_{cap}\,[1/2 + 1/(2\alpha)]\ . \tag{6.25}$$

Figure 6.15 presents the pressure drops as a function of the capillary number. With this representation, all the results resported in figure 6.15 almost collapse. It is seen that an increase in the aspect ratio leads to a slight increase in the pressure drop at the front cap of the bubble and a slight decrease at the rear cap.

The pressure drop across bubble caps depends strongly on the capillary number and it therefore appears relevant to compare it with capillary pressures, as it has been done in figures 6.14 and 6.15. However, the characterization of the whole flow also comprises the pressure drop in the slug.

Unit cell pressure drop

It is seen in figure 6.16 that the pressure drop in the slug is linear. It can be modified close to the bubble caps but it does not appear to be significant, at least at

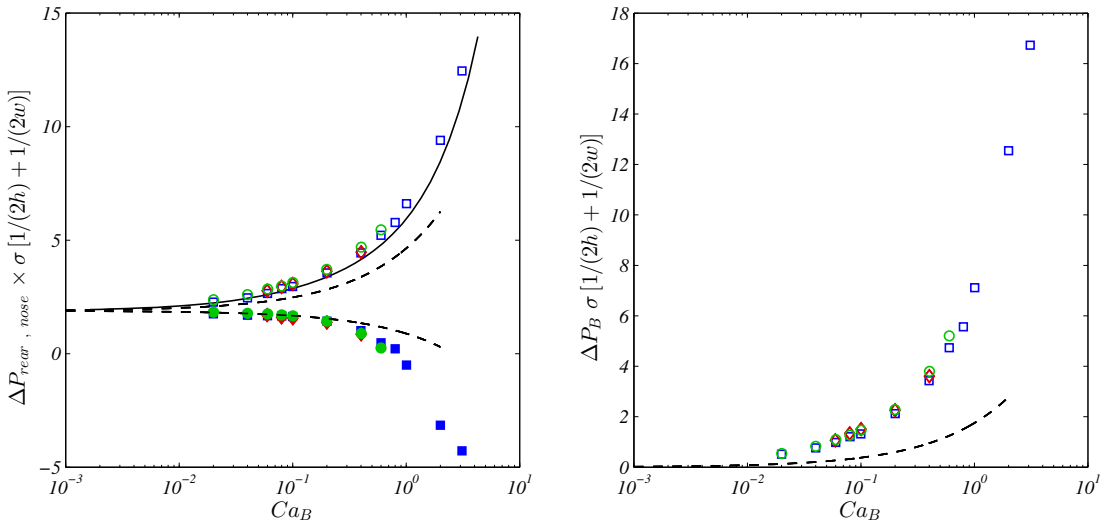

Figure 6.15: (a) Laplace pressure differences at bubble caps as a function of the capillary number for aspect ratios $\alpha = [1; 2.5; 4]$. (b) Total pressure drop across the bubble as a function of the capillary number for aspect ratios $\alpha = [1; 2.5; 4]$.
Legend: (open symbols) front cap ; (filled symbols) rear caps ;
($\square$, blue) $\alpha = 1$; ($\diamond$, red) $\alpha = 2.5$; ($\circ$, green) $\alpha = 4$; (dashed lines) $\alpha = 1$ (Wong et al. [1995b]) : (solid line) $\alpha = 1$ (De Lozar et al. [2008]).

low Reynolds number. The linear pressure drop in a single-phase flow in rectangular channels has been studied and a correlation that estimates the friction factor as a function of the Reynolds number and the aspect ratio exists in the literature (see appendix A). Simulations of single-phase flows have been carried out to check the applicability of the correlation in the cases studied here in terms of channel aspect ratios and Reynolds numbers. This indicates that the pressure drop in the slug is:

$$\Delta P_{slug} = \left(\frac{dP}{dz}\right)^{1-phase} = \frac{\lambda \rho U_{TP}^2}{2D_h} \times L_S \tag{6.26}$$

where λ is the friction factor estimated from the correlation given by equation A.4. In the geometries considered here, the friction factor is:

$$\lambda Re_{TP} = \begin{cases} 56.9 & \text{for} \quad \alpha = 1 \\ 65.5 & \text{for} \quad \alpha = 2.5 \\ 72.9 & \text{for} \quad \alpha = 4 \end{cases} \tag{6.27}$$

As the pressure in the bubble is uniform and the pressure drop across the bubble does not depend on its length once it is confined, the pressure drop across a unit cell with a fixed length that contains one bubble and one slug will decrease as the bubble length increases (see figure 6.16). Indeed, it is seen that very long bubbles allow the pressure drop to decrease significantly (figure 6.16(a)) when compared with single-phase flow. When the bubble length is decreased, the total pressure drop increases until reaching the equivalent pressure drop of single-phase flow (figure 6.16(c)). By decreasing further the bubble length, the presence of the bubble enhances the pressure drop when compared with a single-phase flow.

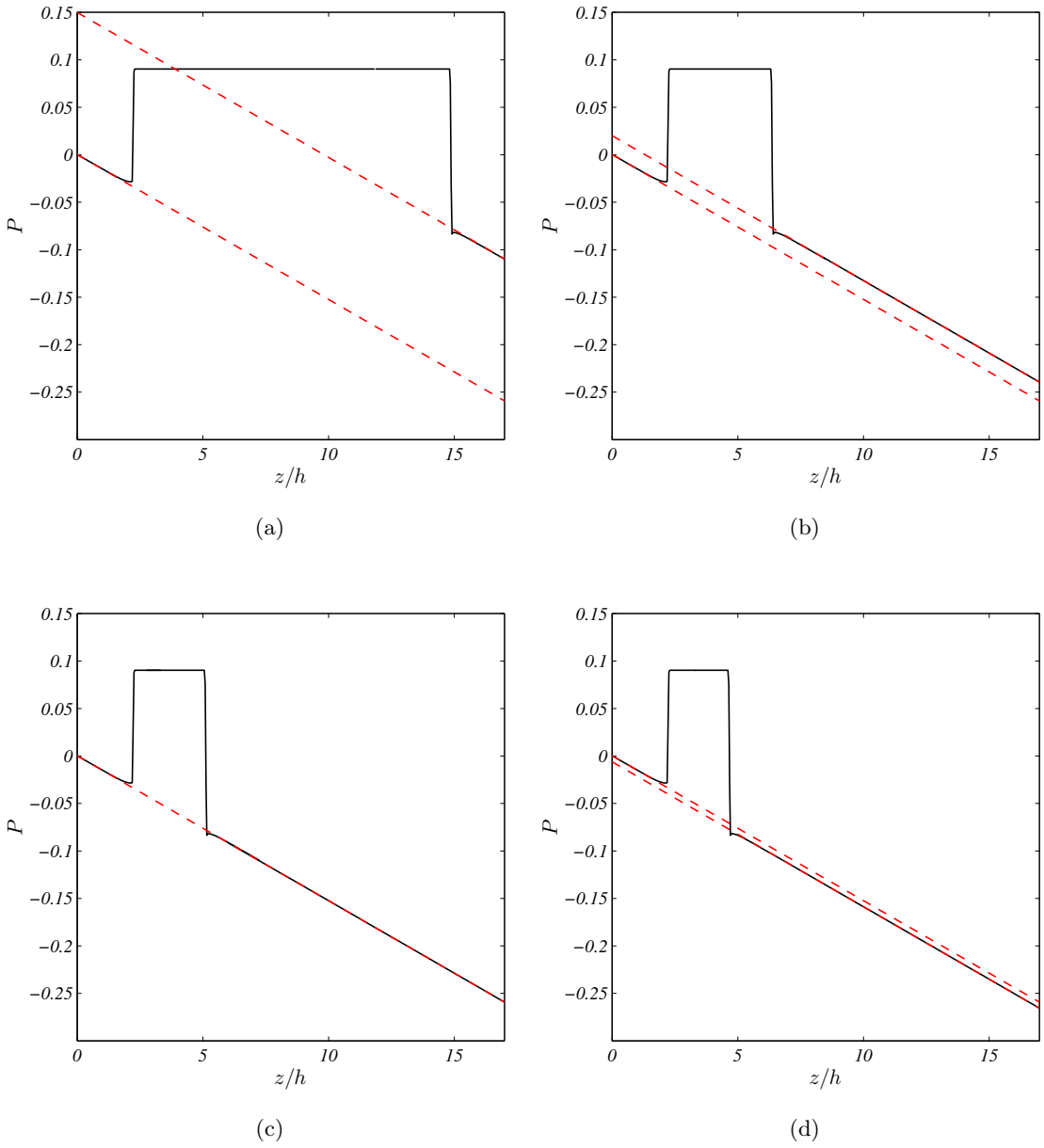

Figure 6.16: Evolution of the pressure on the centerline along a square channel for varying bubble lengths and void fractions. The capillary number is $Ca_B = 0.04$ and the Reynolds number is $Re = 1.12$.
Legend: (solid black line) pressure in the two-phase flow (DNS) ; (dashed red lines) pressure in a single-phase flow.

To summarize, assuming that the transition region between bubble caps and developed linear pressure drop is negligible, the pressure drop at low Reynolds number in Taylor flow can be expressed by a first approximation:

$$\Delta P_{UC} = \left(\frac{dP}{dz}\right)^{1-phase} \times L_S \quad + \Delta P_B \tag{6.28}$$

$$\Delta P_{UC} = \frac{\lambda \rho U_{TP}^2}{2D_h} \times L_S \quad + \Delta P_B \tag{6.29}$$

where λ is the friction factor that depends on the two-phase Reynolds number and the aspect ratio.

Finally, the equivalent pressure gradient in Taylor flow is estimated as:

$$\left(\frac{dP}{dz}\right)^{TF} = \frac{\lambda \rho U_{TP}^2}{2D_h} \times \frac{L_{UC} - L_B}{L_{UC}} + \Delta P_B \frac{1}{L_{UC}} \tag{6.30}$$

In the previous case, the void fraction in the channel is not fixed and it seems normal that an increase in the void fraction leads to a decrease in the pressure drop. However, it is clearly seen that for a given void fraction and fixed channel length, the pressure drop across the channel will be greater with a number of small bubbles than in the case of a few long bubbles. The pressure gradient is shown as a function of the void fraction in figure 6.17 for different bubble lengths. Figure 6.17 represents the case of a square channel for capillary numbers $Ca_B = 0.04$ and $Ca_B = 1$.

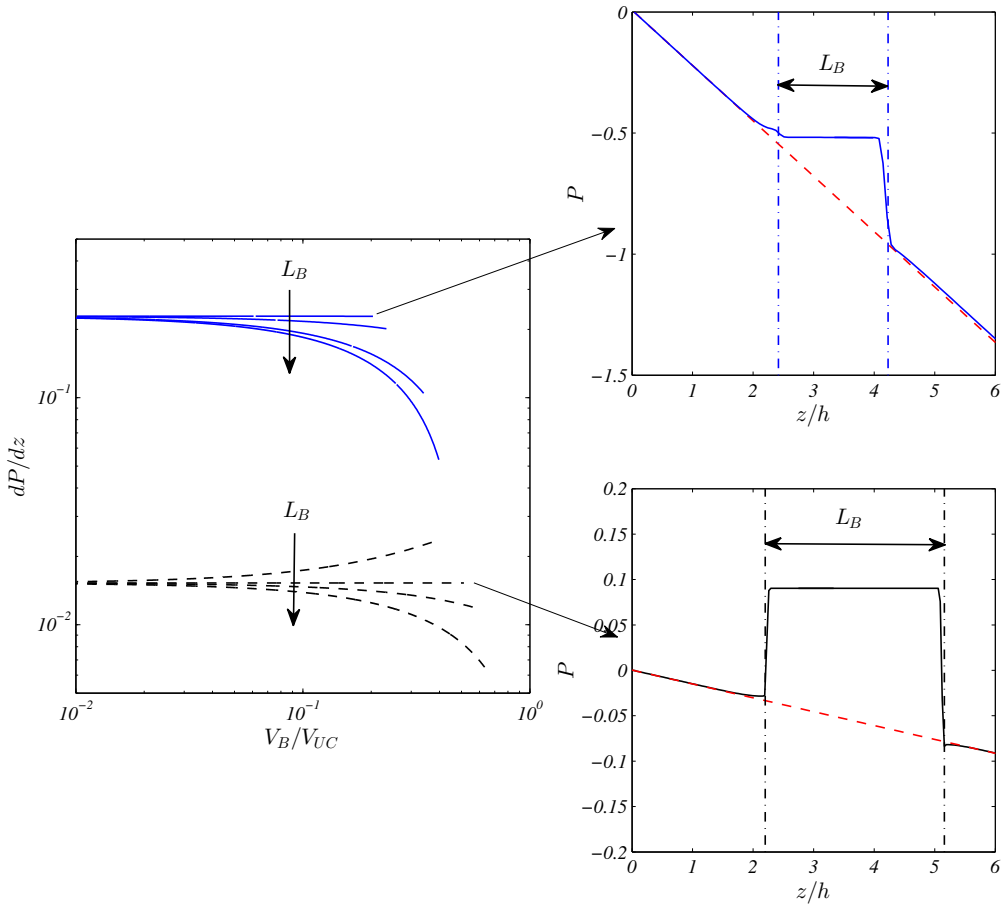

(a)

Figure 6.17: Left: Equivalent pressure gradient across a unit cell with 4 different bubble length $L_B/h = [1.75; 3; 4; 8]$. Right: Pressure on the centerline of the channel for $Ca_B = 1$ (top) and $Ca_B = 0.04$ (bottom) in the case where ΔP_B balances the single-phase pressure drop.
Left legend: (dashed black lines) $Ca_B = 0.04$; (solid blue lines) $Ca_B = 1$. Right legend : (solid black line) pressure in the two-phase flow (DNS) ; (dashed red lines) pressure in a single-phase flow ; (dash dotted lines) bubble caps.

It is observed in figure 6.17 that the pressure gradient tends towards the pressure

gradient of the single-phase flow as the void fraction vanishes. As the volume fraction of gas in the channel increases, the influence of the pressure drop across the bubble increases. Again, for long bubbles, the equivalent pressure gradient across a unit cell is lower than that for small bubbles. In the cases presented in figure 6.17, is is shown that the bubble lengths that would balance the single-phase pressure drop are approximately $L_B^* = 3 \times h$ and $L_B^* = 1.75 \times h$ for capillary numbers $Ca_B = 0.04$ and $Ca_B = 1$, respectively. It is not intuitive since the pressure drop increases with the capillary number and it is expected that the bubble length necessary to balance the single-phase flow increases with the capillary number. However, as the capillary number increases, the velocity in the channel increases too and the single-phase pressure gradient then increases. This linear pressure drop increases faster than the capillary pressure drop across the bubble and this explains the tendency observed.

From equation 6.30, it is possible to estimate the theoretical bubble length that would balance the single-phase flows across its length.

$$L_B^* = \Delta P_B \, \frac{2D_h}{\lambda \rho U_{TP}^2} \tag{6.31}$$

These theoretical bubble lengths are reported in figure 6.18 as a function of the bubble capillary number for the three aspect ratios considered. It is observed that an increase in the capillary number leads to a decrease in the bubble length that balances the single-phase pressure drop. This means that as the capillary number increases, the resistance to the flow induced by the bubbles when compared with the pressure drop in the slug is reduced. It is also seen that at fixed hydraulic diameter, the bubble lengths do not depend significantly on the aspect ratio although the dimensionless bubble lengths for aspect ratio $\alpha = 4$ appear to be slightly smaller. However, it is not always possible to generate Taylor bubbles of this length or the bubble could be not confined and the pressure drop at its caps could differ, thereby limiting the range of validity of equation 6.34.

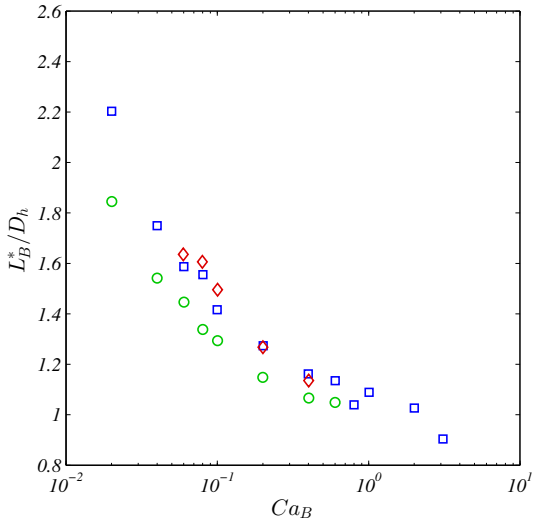

(a)

Figure 6.18: Dimensionless bubble lengths whose equivalent pressure drop balances the single-phase flow pressure drop.
Legend: (□, blue) $\alpha = 1$; (◇, red) $\alpha = 2.5$; (○, green) $\alpha = 4$;

6.4 Effects of bubble and slug lengths

For the aspect ratio $\alpha = 2.5$, 5 different bubble sizes have been simulated to study the influence of the bubble length or volume as well as the slug length on the dynamics of the bubble. It is shown that for this geometry and this capillary number $Ca = 0.1$, the bubble length is of negligible influence as long as the bubble is confined in both directions. This result, which is valid in 2D and axisymmetric cases due to the stagnant film around the bubble, is not obvious in 3D due to the flow in the corners. Indeed, Wong et al. [1995a] mentioned a film rearrangement along the bubble with an axial flow in the corners and a drainage flow from the walls to the corners. However, in our simulations, these flows are only about a few percents of the total flow rate and vanish when approaching the bubble rear cap. Above a certain length or volume, the liquid flow rate decreases until it reaches less than 1% of the total flow rate and reaches zero at a certain distance from the rear cap (see figure 6.11).

Figure 6.19 shows the evolution of the liquid area fraction as a function of the bubble volume. This volume is made dimensionless with the reference volume $4/3\pi h^3$ which corresponds to a bubble of diameter equal to the height of the channel.

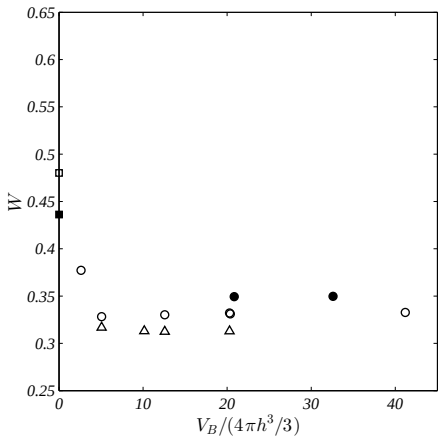

(a)

Figure 6.19: Liquid area fraction as a function of the bubble volume.
Legend: (open $\triangle$) $\alpha = 2.5$ and $Ca = 0.08$; (open $\circ$) $\alpha = 2.5$ and $Ca = 0.1$; (filled $\circ$) $\alpha = 4$ and $Ca = 0.1$; the squares represent value of the single-phase velocity on the centerline of the channel $W(V_B \to 0) = [0.4801; 0.4362]$ for $\alpha = [2.5; 4]$ respectively, corresponding to the asymptotic value in the limit $V_B = 0$.

We can see in figure 6.19 that the slip velocity of the bubbles decrease when the volume increases until reaching a constant value. Indeed, for these aspect ratios, when the volume of the bubble approaches five times the reference volume of a sphere with a diameter equal to the height of the channel, the liquid area fraction becomes independent of the bubble volume and length. A decrease in the bubble volume would lead to an increase in bubble velocity until reaching an infinitely small bubble that acts like a tracer with a velocity equal to the maximum velocity in the liquid slug (which depends on the geometry). However, in some cases, the velocity of a long bubble can overcome the maximum velocity in the liquid slug and thus, the opposite trend is expected: a decrease in bubble volume would lead to a decrease in velocity until reaching the velocity on the centerline of the channel in the slug.

The shapes of four of the bubbles that have been considered to study the effects of bubble length are shown in figure 6.20 and the interface is colored with the magnitude of the velocity. It is seen that except for the first tiny bubble, the velocity on the interface of the other ones is close to zero all around the bubble which means that there is almost no liquid flow. Finally, as long as the bubble is confined in both directions, its velocity does not depend on its volume (or length).

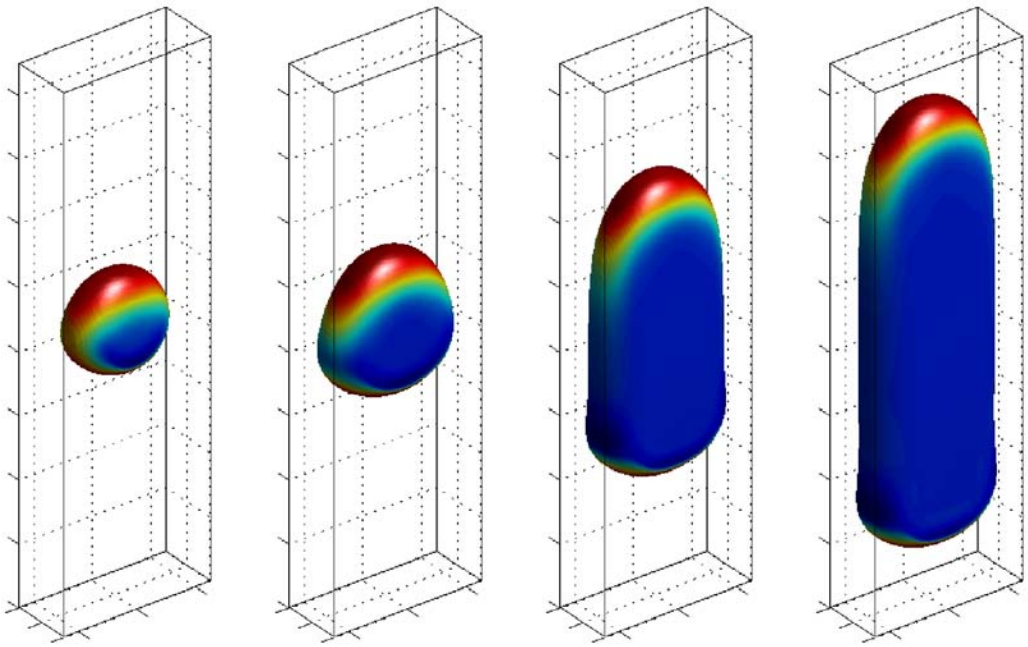

Figure 6.20: Illustration of the bubble shapes of different volumes for $\alpha = 2.5$, $Ca_B = 0.1$ and $La = 280$. The interface is colored with the magnitude of the dimensionless velocity U/U_B.
(red) bubble velocity ; (blue) zero.

6.5 Effects of inertia

6.5.1 First observations

The effects of inertia on the hydrodynamics of Taylor flow in microchannels are often neglected through numerical simulations of Stokes flow, for example Hazel and Heil [2002], De Lozar et al. [2008]. However, in micrometric and millimetric channels, the Laplace number for water flowing in a channel of diameter $100\mu m$ is approximately $La = 7000$. This means that for a capillary number of $Ca_B \simeq 0.01$ that is commonly encountered in experiments (see section 5), the Reynolds number would be $Re_B \simeq 70$. Although laminar, the flow and notably the bubble are subject to inertial effects that cannot be neglected. This section aims at understanding the effects of inertia on the hydrodynamics of Taylor flow. The same steps that have been used to characterize slug flow at low Reynolds numbers in the previous section are followed.

A summary of the ranges of Reynolds and capillary numbers that have been covered through 3D numerical simulations is given in figure 6.21. The capillary number which governs the bubble shapes and velocities has been varied from $Ca_B \simeq 0.02$ to $Ca_B \simeq 3$ and the Reynolds has been varied from $R_B \simeq 0.5$ to $Re_B \simeq 1000$. The different symbols represent a Laplace number that depends only on the geometry and the fluid properties.

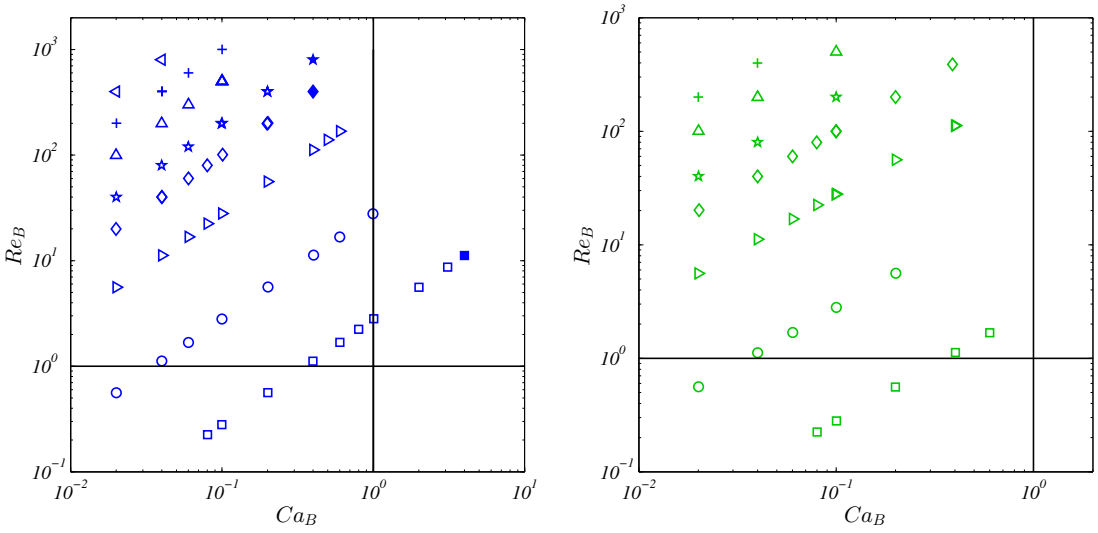

(a) $\alpha = 1$ (b) $\alpha = 4$

Figure 6.21: Summary of the numerical simulations performed in (a) a square channel and (b) a rectangular channel ($\alpha = 4$) in terms of Reynolds and capillary numbers. Legend: ($\square$) $La = 2.8$; ($\circ$) $La = 28$; ($\triangleright$) $La = 280$; ($\diamond$) $La = 1000$; ($\star$) $La = 2000$; ($\triangle$) $La = 5000$; ($+$) $La = 10000$; ($\triangleleft$) $La = 20000$.

The filled symbols in figure 6.21 represent the flows in which bubbles break at the rear cap. It is seen that the maximum capillary number that has been simulated is lower at high Laplace numbers. Indeed, at high Laplace numbers and fixed capillary number, the Weber number $We_B = La \times Ca_B^2$ is increased. The surface tension force is less dominant and is not sufficient to maintain the bubble shape. The rear bubble cap is dug out at the center of the channel and thin structure elongates close to the walls until it breaks. It is interesting to point out that the rupture is different depending on

the Laplace number. In the case of the low Laplace number, droplets are formed from a viscous jet at the rear of the bubble and travel across the bubble, while in the case of high Laplace number, bubbles detach at the rear cap and coalesce with the initial bubble. In these cases, as the pressure drop is fixed across the channel and the number of inclusions and their shapes change, the mean velocity of the gas phase varies over time. However, bubble rupture is very difficult to predict numerically, this phenomenon is often dependent on the mesh and it is difficult to ensure if the break-up is independent of the numerical parameters. These simulations have been repeated with a refined mesh ($64 \times 64 \times 960$) and bubble rupture has been observed. While the simulations performed give a first idea on transition points towards different regimes, this would need to be further investigated with more refined meshes. It should also be verified that bubble and/or slug lengths do not affect this mechanism. Such particular regime where drops travel inside the bubble at low Reynolds number and high capillary number has been observed in tubes with the numerical simulations of Dupont et al. [2007] and in the experiments of Nelissen et al. [2007], but also in porous media Olbricht [1996]. In addition, at low Reynolds number, the critical value of the capillary number where the break-up of the bubble occurs is in good agreement with previous studies, $Ca \sim O(1)$.

(a) Present simulation ($Ca_B = 4$ and $Re_B = 11.2$)

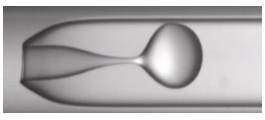

(b) Nelissen et al. [2007]

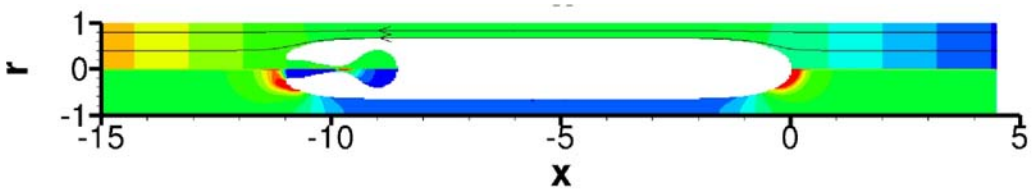

(c) Dupont et al. [2007] ($Ca_B = 5.3$ and $Re_B = 2.12$)

Figure 6.22: Droplet detachment at the bubble rear cap.

A map of the bubbles observed in a square channel is given in figure 6.23 to illustrate the different shapes that can occur. Figure 6.23 shows the influence of the capillary number (already discussed in the previous section) and the Laplace number that is equivalent to the Reynolds number at a given capillary number as $Re_B = La \times Ca_B$. It is clear that the shape of the bubble is also influenced by inertial effects.

Indeed, at a given capillary number, an increase in the Laplace number induces an elongation of the nose and the bubble evolves much less rapidly towards an equilibrium shape in a cross-section of the channel in the axial direction. The effects of inertia on the transition length between the nose and the film region are particularly significant at $Ca_B = 0.1$ and $La = 10000$, *i.e.* $Re_B = 1000$. At low capillary numbers, $Ca_B \leq 0.06$

approximately, waves on the interface near the rear bubble cap are observed at high Reynolds numbers as we can see in figure 6.23 for $Ca_B = 0.04$ and $La = 10000$, *i.e.* $Re_B = 400$. In addition, for capillary numbers lower than $Ca_B = 0.06$, the bubble starts to oscillate. This phenomena is related to the waves on the interface that appear around $Re_B = 400$, The bubble length therefore evolves in time as well as the curvatures of the bubble caps. These shape oscillations are mainly observed at the rear bubble cap while pressure jump at the front cap and the bubble velocity vary only slightly.

Figure 6.23: Illustration of the shape of the bubbles obtained in a square channel for various capillary numbers and Laplace numbers. The Laplace number $La = Re_B/Ca_B$ increases from the bottom to the top and the capillary number increases from the left to the right.

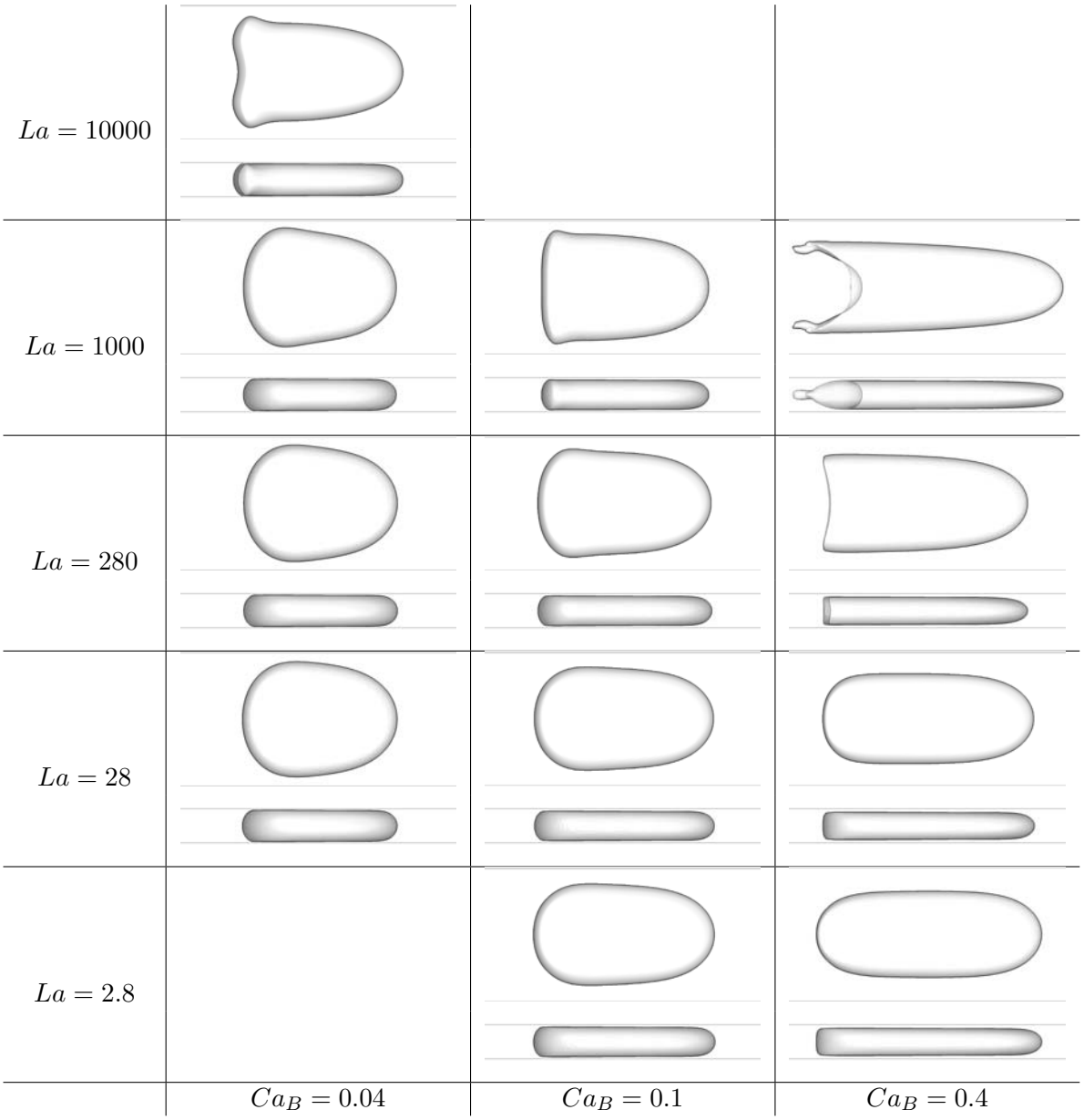

Figure 6.24: Illustration of the cross-sectional shapes of the bubbles obtained in a rectangular channel ($\alpha = 4$) for various capillary numbers and Laplace numbers. The Laplace $La = Re_B/Ca_B$ number increases from the bottom to the top and the capillary number increases from the left to the right.

6.5.2 Bubble velocity

The first observations when visualizing the flow indicate that the inertia of the liquid can play a non-negligible role in the dynamics of Taylor bubbles. The velocity of the bubble as a function of the mean velocity in the slug is shown in figures 6.25(a)-(b) in terms of capillary numbers for a square channel and a channel of aspect ratio $\alpha = 4$, respectively. It has been shown previously that the relationship between the bubble velocity and the two-phase velocity in the case of a circular tube gives a correct estimation of the bubble velocity in the rectangular capillaries considered here. This is still the case in the presence of inertia and particularly at low capillary numbers with both geometries. Indeed, it is seen around $Ca_{TP} = 0.04$ that the data collapse despite the Reynolds number being increased by over three orders of magnitude ($0.5 < Re_{TP} < 2000$). Indeed, at low capillary numbers, the liquid film is very thin and despite a high Reynolds number based on the channel diameter, the inertia is not so strong in the liquid film, which has a characteristic dimension that is much smaller than the channel hydraulic diameter. This reinforces that the capillary number is the dimensionless number that governs the flow structure. As the capillary number increases, slight deviations can be observed between the different Laplace numbers. This means that inertia influences the bubble velocity and particularly as both the capillary number and the liquid film thickness increase.

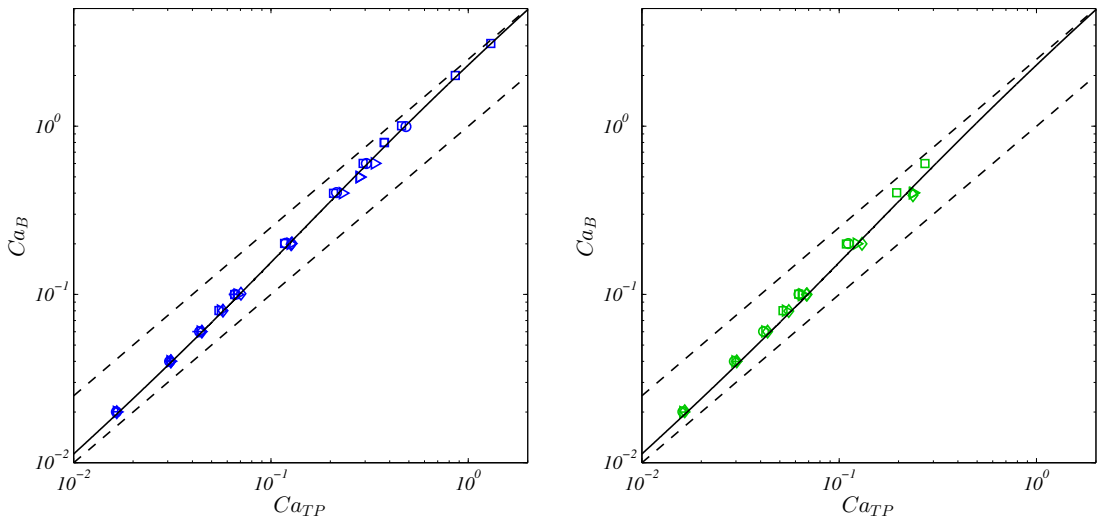

(a) $\alpha = 1$ (b) $\alpha = 4$

Figure 6.25: Bubble capillary number Ca_B as a function of the two-phase capillary number Ca_{TP}.
Legend: (black solid line) axisymmetric case (equation 6.36) ; (dashed lines) $Ca_B = Ca_{TP}$ and $Ca_B = 2.78\ Ca_{TP}$; (□) $La = 2.8$; (○) $La = 28$; (▷) $La = 280$; (◇) $La = 1000$; (+) $La = 10000$.

Figure 6.26 shows the ratio of bubble velocity to the mean velocity for the square and the rectangular channels as a function of the capillary number. Numerical results are reported only for Reynolds numbers up to $Re_B = 100$. The bubble slip velocity increases with the capillary number, whatever the Laplace number. As the Laplace number increases, we observe a decrease in the bubble to the mean velocity ratio. In other words, at a given two-phase capillary number, an increase in inertia, *i.e.* in the

Reynolds number, leads to a decrease in the bubble velocity. The same trend is observed in both square and rectangular microchannels. This is in contradiction with the results obtained by Aussillous and Quéré [2000] and Han and Shikazono [2009] who mentioned a thicknening of the liquid film as the inertia is increased via the Weber number. Similarly, Han and Shikazono [2009] proposed a correlation in which increasing inertia leads to a thickening of the liquid film.

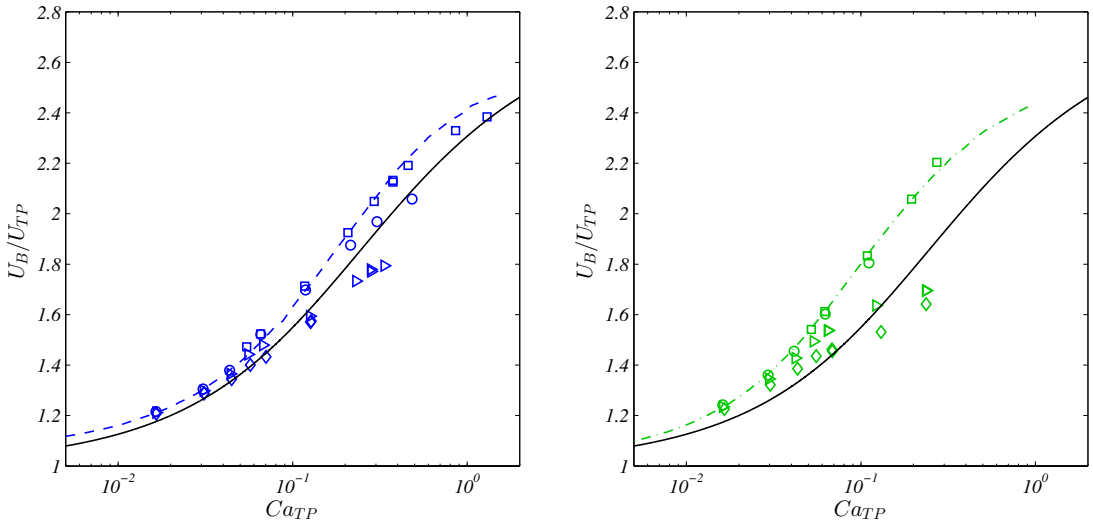

(a) $\alpha = 1$ (b) $\alpha = 4$

Figure 6.26: Bubble to mean velocity ratio as a function of the two-phase capillary number for $Re_{TP} \leq 100$ in (a) a square channel and (b) a rectangular channel ($\alpha = 4$). Legend: (black solid line) axisymmetric case (equations 6.36) ; (dashed blue line) $\alpha = 1$, $Re_B = 0$ (De Lozar et al. [2008]) ; (dash-dotted green line) $\alpha = 4$, $Re_B = 0$ (De Lozar et al. [2008]) ; ($\square$) $La = 2.8$; ($\circ$) $La = 28$; ($\triangleright$) $La = 280$; ($\diamond$) $La = 1000$.

Further investigation indicates that the evolution of the liquid film thickness and thus the ratio of bubble to slug velocity is not monotonic (Giavedoni and Saita [1997], Kreutzer et al. [2005] for the plane and axisymmetric cases). Figure 6.27 shows the bubble to mean velocity ratio as a function of the Reynolds number for different capillary numbers. It is interesting to note that the variations in the bubble velocity with the Reynolds number remain moderate, although the bubble shape changes significantly with inertia, as shown in figures 6.23 and 6.24. However, inertia promotes bubble deformation and break-up mainly at the rear cap while the front cap elongates slightly. This means that the rear bubble cap does not play a major role in the dynamics of Taylor bubbles even though it is important to characterize the pressure drop at the bubble tail as well as the velocity field to better understand transport phenomena. It is thought that such changes in the shape of the interface would disturb the flow in the wake of the bubble thereby modifying the velocity and pressure fields ahead of the next bubble in bubble train flow but it has been shown that the velocity does not change significantly as long as the slug length is greater than the characteristic dimension of the channel. We can see in figures 6.27(a) and (b) for the square and rectangular capillaries respectively that the bubble velocity decreases until $Re_{TP} \sim 100 - 200$ where a minimum is reached before increasing again. This is mainly seen in figures 6.27(c)-(d) at high capillary numbers while the variations at low capillary numbers, scaled by the slip velocity in Stokes flow, are weak up to $Re_{TP} \simeq 200$. At high Reynolds number, the velocity can

be greater than the bubble velocity in Stokes flow (*e.g.* $Ca_{TP} = 0.04$ and $Re_{TP} \gtrsim 400$ in figure 6.27). Even if higher Reynolds numbers cannot easily be reached in microchannels, the asymptotic behaviour at infinite Reynolds numbers can help in understanding the transition between the two observed regimes around $Re_{TP} \simeq 100 - 200$. In addition, the slip velocities obtained with a fine mesh ($64 \times 64 \times 512$) for $Ca = 0.1$ in a square channel are also reported in figures 6.27(a) and (c) and justify the use of the first mesh ($32 \times 32 \times 256$), the difference being less than 2%.

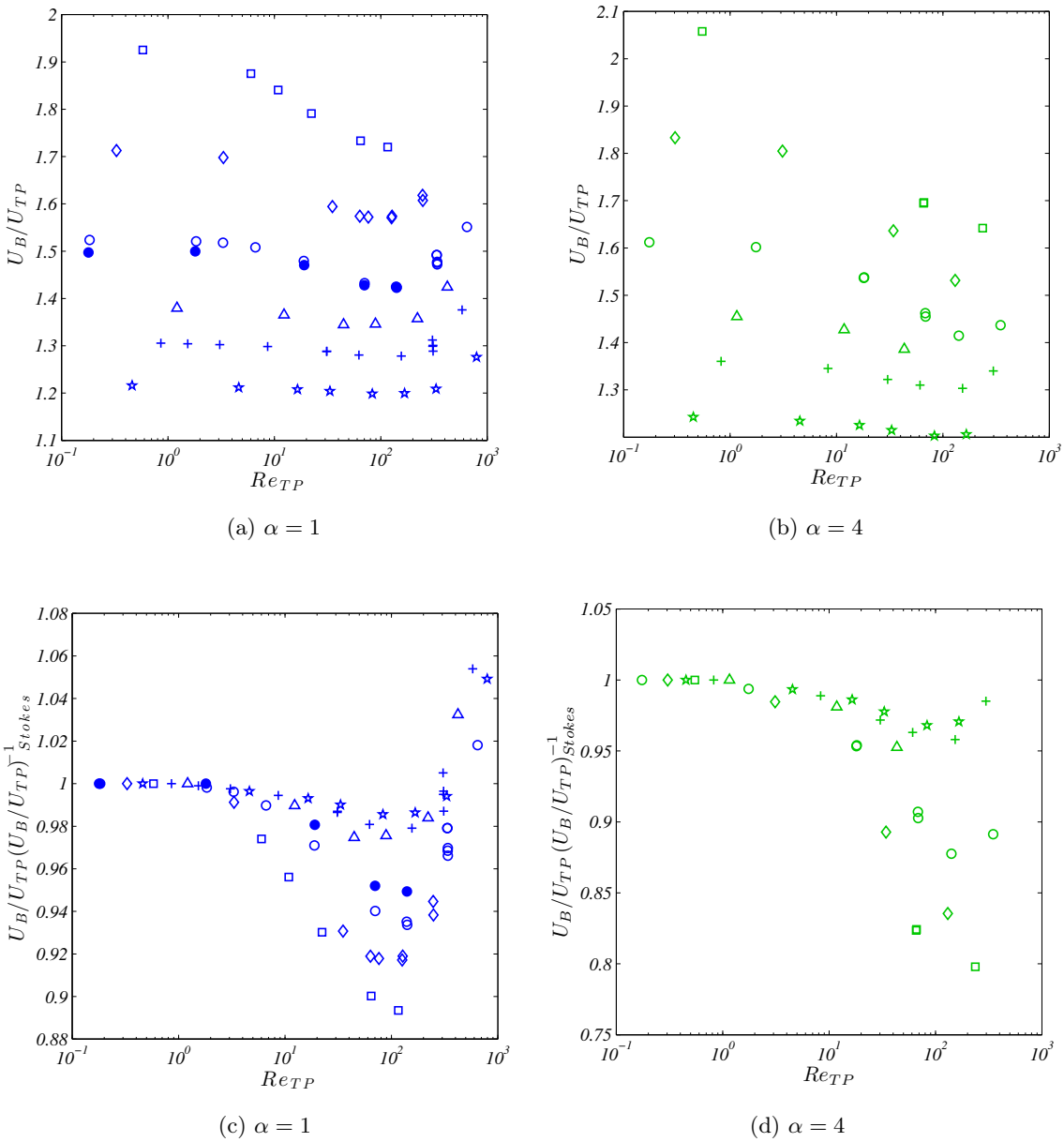

(a) $\alpha = 1$

(b) $\alpha = 4$

(c) $\alpha = 1$

(d) $\alpha = 4$

Figure 6.27: Bubble to mean velocity ratio U_B/U_{TP} as a function of the two-phase Reynolds number Re_{TP} in (a) a square channel and (b) a rectangular channel ($\alpha = 4$). Slip velocity U_B/U_{TP} scaled with the slip velocity in Stokes flow ($Re_B = 0$) as a function of the two-phase Reynolds number Re_{TP} in (c) a square channel and (d) a rectangular channel ($\alpha = 4$).
Legend: ($\star$) $Ca_B = 0.02$; (+) $Ca_B = 0.04$; ($\triangle$) $Ca_B = 0.06$; ($\circ$) $Ca_B = 0.1$; ($\bullet$) $Ca_B = 0.1$ (mesh $64 \times 64 \times 512$) ; ($\diamond$) $Ca_B = 0.2$; ($\square$) $Ca_B = 0.4$.

The velocity magnitude on the bubble interface at different bubble Reynolds numbers are shown in figure 6.28. It is seen that the bubble nose is elongated in the whole range of Re_B simulated and at $Re_B = 500$, there is no stagnant film anymore. Also, the velocity across the diagonal is increased as the inertia increases and Ca_B is fixed.

From figure 6.29 where the geometries are compared in terms of bubble velocities as a function of the Reynolds number, it is shown that increasing the aspect ratio enhances the effects of inertia on the bubble velocity. Indeed, the minimum ratio of bubble to mean velocity decreases when the aspect ratio is increased. In rectangular channels, the shear stress is less important in the less confined direction and inertial effects can therefore develop more easily and mainly affect the bubble shape in this direction.

6.5.3 Pressure drop

Since the effects of inertia have a great influence on the shape of the bubble, it appears relevant to look at the pressure drop that is directly related to the curvature of the bubble caps.

The Laplace pressure jumps and the total pressure jump are shown in figures 6.30 and 6.31 as a function of the two-phase Reynolds number for fixed capillary numbers. While a non-monotonic behaviour was reported for the bubble velocity, the pressure jump at the front cap increases with the Reynolds number throughout the range of Reynolds numbers covered and the pressure jump at the rear decreases monotonically. The changes in the pressure drop across the bubble are particularly impressive at high capillary numbers. This was expected since the main variations in the shape of the bubble were observed at high capillary numbers in figures 6.23 and 6.24. These respective increase and decrease in the front and rear pressure jumps lead to an increased total pressure drop across the bubble with the Reynolds number as it is shown in figures 6.31(a) and (b). For each capillary number, scaling the total pressure jump by the pressure jump at low Reynolds number allows the relative variations of the total pressure drop at a given capillary number as a function of the Reynolds number to be compared. It is shown that the pressure drop across the bubble evolves linearly with the Reynolds number:

$$\frac{\Delta P_B}{(\Delta P_B)_{Stokes}} = 1 + \frac{Re_{TP}}{200} \tag{6.32}$$

Although the data collapse quite well, the greatest variations are observed at high capillary numbers in the square microchannel. The coefficient 1/200 could be adapted and its dependency on the capillary number could be an improvement but the relation 6.32 is already satisfactory. Under the assumption that the flows ahead of and in the rear of the bubble develop over a short length when compared with the slug length, equations 6.30 and 6.32 can be combined to consider the effects of inertia on the total pressure drop across a unit cell:

$$\left(\frac{dP}{dz}\right)^{TF} = \frac{\lambda \rho U_{TP}^2}{2D_h} \times \frac{L_{UC} - L_B}{L_{UC}} + \frac{(\Delta P_B)_{Stokes}}{L_{UC}} \left(1 + \frac{Re_{TP}}{200}\right) \tag{6.33}$$

Similarly to the estimation made at low Reynolds number, the theoretical bubble length that would balance the single-phase flows across its length is:

$$L_B^* = (\Delta P_B)_{Stokes} \left(1 + \frac{Re_{TP}}{200}\right) \frac{2D_h}{\lambda \rho U_{TP}^2} \tag{6.34}$$

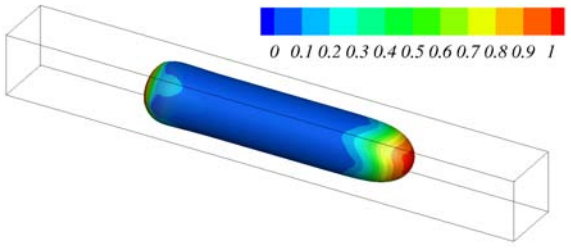

(a) $\alpha = 1$; $Ca_B = 0.1$ and $Re_B = 0.28$

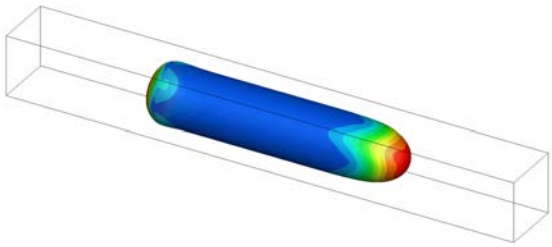

(b) $\alpha = 1$; $Ca_B = 0.1$ and $Re_B = 28$

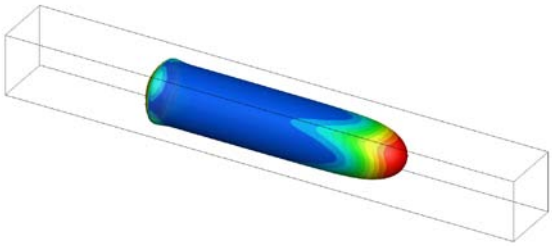

(c) $\alpha = 1$; $Ca_B = 0.1$ and $Re_B = 100$

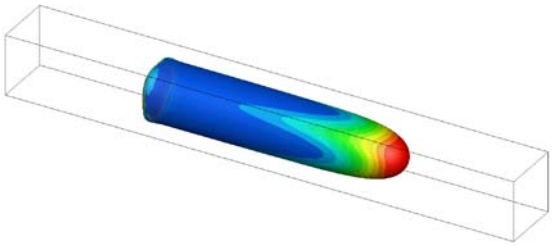

(d) $\alpha = 1$; $Ca_B = 0.1$ and $Re_B = 200$

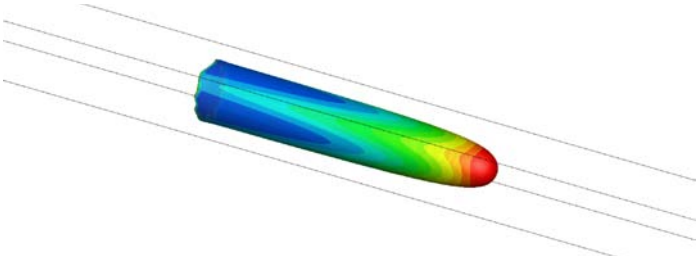

(e) $\alpha = 1$; $Ca_B = 0.1$ and $Re_B = 500$

Figure 6.28: Illustration of the bubble shapes for $Ca_B = 0.1$ in the square channel channels for $Re_B = [0.28; 28; 100; 200; 500]$. The interface is colored with the magnitude of the dimensionless velocity U/U_B.

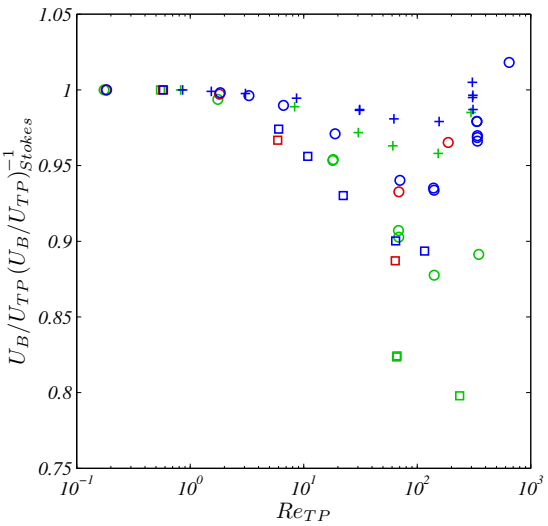

Figure 6.29: Ratio of slip velocity U_B/U_{TP} to the slip velocity in Stokes flow ($Re_B = 0$) as a function of the two-phase Reynolds number Re_{TP} for aspect ratios $\alpha = [1; 2.5; 4]$. Legend: (blue) $\alpha = 1$; (red) $\alpha = 2.5$; (green) $\alpha = 4$; Legend: (+) $Ca_B = 0.04$; ($\circ$) $Ca_B = 0.1$; ($\square$) $Ca_B = 0.4$.

6.6 Conclusion

In this chapter, a correction has been made to the correlation of Aussillous and Quéré [2000] to allow the direct prediction of the liquid film thickness in circular tubes as a function of the two-phase capillary number Ca_{TP} instead of the bubble capillary number Ca_B, which is not known *a priori* when starting an experiment or a process. Results of the slip velocity and the pressure drop at the front cap at low Reynolds number have been compared with the results from De Lozar et al. [2008] and it has been shown that the liquid flow rate vanishes around the bubble even if the bubble is not much longer than the width of the channel. New insights on the rear bubble cap and the decrease in the pressure drop with the capillary number have been given. This resulted in a comparison between two-phase and single-phase pressure drop where it has been shown that for a given bubble length, the pressure gradient evolves linearly with the void fraction. However, it has been seen that the coefficient of the linear evolution depends on the bubble pressure drop as well as the bubble length: long bubbles allow the pressure drop in the channel to decrease while small bubbles can lead to an increase in the pressure drop. It has also been shown that the bubble length that balances the single-phase linear pressure drop along the bubble length decreases with the capillary number and the aspect ratio of the channel.

The effects of inertia on the bubble dynamics have been highlighted. Inertia has been observed to promote bubble break-up at the rear cap. Also, although the effects of inertia on the bubble velocity are not very significant, the bubble slip velocity has been shown to follow a non-monotonic trend with the Reynolds number. The slight changes in the bubble velocities are related to the fact that inertial effects do not play a major role ahead of the bubble. However, inertial effects in the wake of the bubble modify its shape and thus the pressure drop thereby increasing the resistance to the

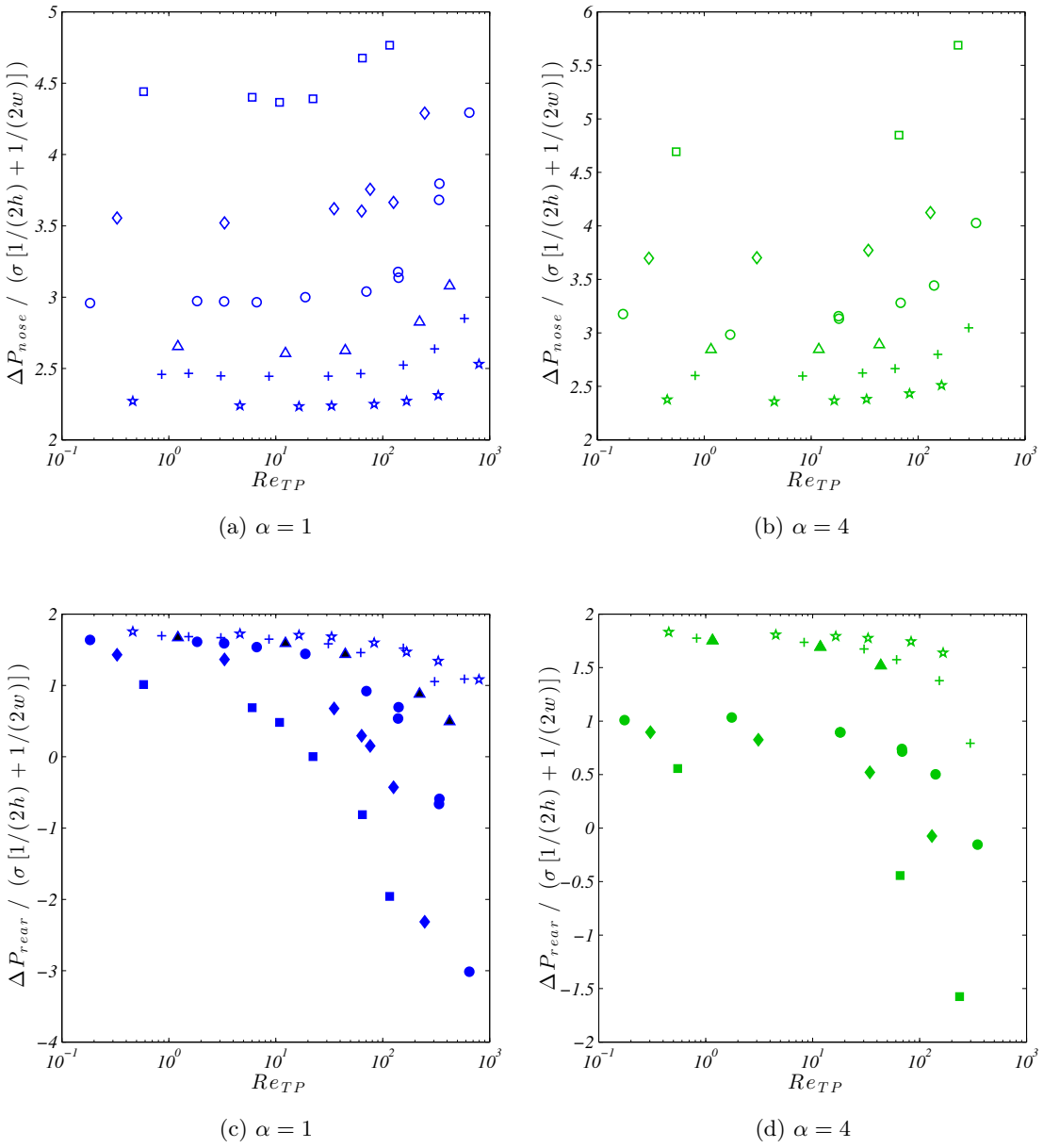

(a) $\alpha = 1$ (b) $\alpha = 4$

(c) $\alpha = 1$ (d) $\alpha = 4$

Figure 6.30: Dimensionless Laplace pressure jumps at the front and rear caps as a function of the two-phase capillary number in (a)-(c) a square channel and (b)-(d) a rectangular channel ($\alpha = 4$).
Legend: ($\star$) $Ca_B = 0.02$; (+) $Ca_B = 0.04$; ($\triangle$) $Ca_B = 0.06$; ($\circ$) $Ca_B = 0.1$; ($\diamond$) $Ca_B = 0.2$; ($\square$) $Ca_B = 0.4$.

flow linearly with the Reynolds number:

$$\frac{\Delta P_B}{(\Delta P_B)_{Stokes}} = 1 + \frac{Re_{TP}}{200} \tag{6.35}$$

Finally, the aspect ratio has been shown to enhance inertial effects on the bubble slip velocity. For all the cases considered, we have shown that the bubble velocity can

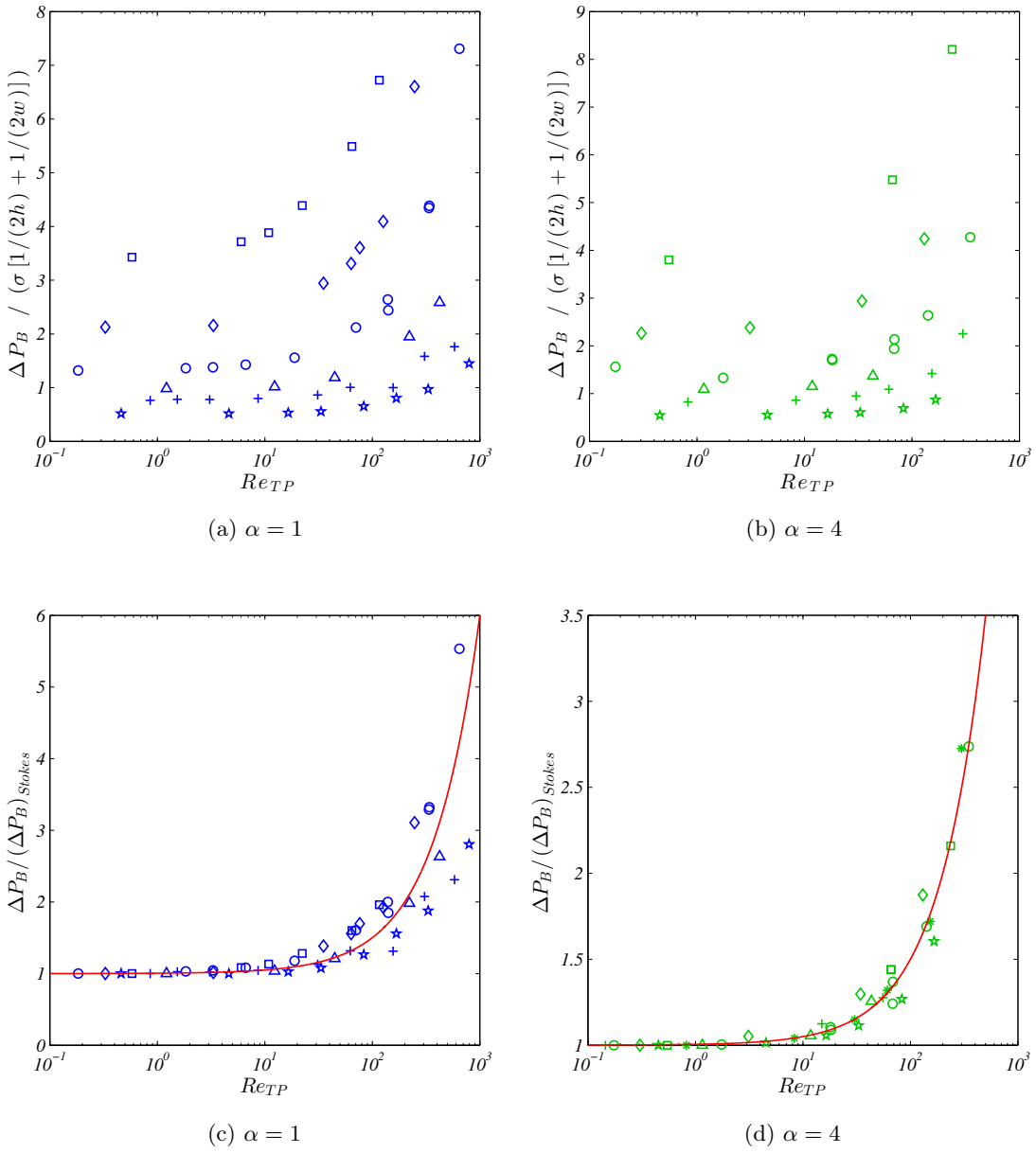

(a) $\alpha = 1$ (b) $\alpha = 4$

(c) $\alpha = 1$ (d) $\alpha = 4$

Figure 6.31: Bubble pressure drop as a function of the two-phase Reynolds number in (a) a square channel and (b) a rectangular channel ($\alpha = 4$). Bubble pressure drop scaled by the pressure drop in Stokes flow as a function of the two-phase Reynolds number in (c) a square channel and (d) a rectangular channel ($\alpha = 4$)
Legend: ($\star$) $Ca_B = 0.02$; ($+$) $Ca_B = 0.04$; ($\triangle$) $Ca_B = 0.06$; ($\circ$) $Ca_B = 0.1$; ($\diamond$) $Ca_B = 0.2$; ($\square$) $Ca_B = 0.4$; (red line) equation 6.32.

be described using:

$$U_B = U_{TP}\left[1 \ - \ \left(\frac{1.34Ca_{TP}^{2/3}\left(1+\frac{4}{3}\times 1.34Ca_{TP}^{2/3}\right)}{1+1.34Ca_{TP}^{2/3}\left(1.2+\frac{4}{3}\times 1.34Ca_{TP}^{2/3}\right)}\right)^2\right]^{-1} \tag{6.36}$$

Chapter 7

Mixing characteristics in the liquid slug

Contents

7.1 Introduction

Over the last decade, micro-reaction technology has become of much interest to both academics and the process industries for the intensification of chemical processes. Taylor or slug flow is a commonly encountered flow regime for gas-liquid microchannel flows and has the advantage of providing high interfacial area and good liquid mixing in the liquid slug, thereby enhancing transport processes. These features of microreactors are particularly interesting for fast and highly exothermic gas-liquid reactions amongst other applications and allow an increase in reaction performance whilst working under safe operating conditions (Hessel et al. [2005], Kashid and Kiwi-Minsker [2009]). A number of studies have focused on the understanding of hydrodynamics as well as heat and mass transfer enhancement in these flows (see reviews Kreutzer et al. [2005], Shao et al. [2009], Gupta et al. [2010b]) but often independently. Indeed the transport efficiency appears to be closely related to the recirculation in the liquid phase, which depends on the operating conditions, fluid properties and reactor geometry.

A major feature of gas-liquid Taylor flow is the recirculation flow pattern generated in the liquid slug in the moving frame of reference as shown in Figure 7.1 and detailed by Taylor [1961]. The recirculating flow pattern is characterized by the position of the center of the circulation loop $[x_0, y_0]$, and the position of the streamline separating the recirculation zone and the liquid film at the channel wall $[x_1, y_1]$. As the bubble velocity increases, both the loop center and the outer streamline of the recirculation zone move towards the center of the channel (Thulasidas et al. [1997]). This leads to a reduction of the volume of the recirculating zone and an increase in the volume of liquid in the film region until complete bypass flow occurs at $U_B \geq U_{max}$. Studies on the recirculating flow in circular and square capillaries have been conducted previously (Taylor [1961],Thulasidas et al. [1997]), however little information on the characteristics of the recirculation zone in rectangular channels is available. Recently, it has been shown theoretically (Kececi et al. [2009]) that the cross-sectional area occupied by the recirculation zone in the liquid slug is generally smaller for rectangular channels than for circular channels due to the increased film thickness in the channel corners.

The recirculation time in the liquid slug in Taylor flow is defined as the time required for an element of fluid to complete one revolution in the recirculating slug. This characteristic time is particularly relevant for transport processes occurring in the system, such as mass transfer between the bubble and slug or wall and slug, and heat transfer with the channel wall. The rate of flow recirculation can be calculated via the surface integration of the relative velocity profile across the microchannel cross-section, similarly to what is done in conventional stirred tanks to calculate circulation induced by the mechanical impeller Jaworski et al. [1996]. The recirculation flow rate through the microchannel can be divided into three parts (illustrated in Figure 7.1) :

- a positive flow rate, Q_0, in the main flow direction at central core of the microchannel occupying a volume V_0 with a cross-sectional area A_0,

- a negative flow rate, Q_1, with a volume V_1 and a cross-sectional area A_1 that corresponds to the recirculating liquid in the slug,

- a negative flow rate, Q_2 of volume V_2 in area A_2, that is close to the channel wall and contributes to axial mixing between slugs instead of radial mixing within the slug.

The recirculation time is then defined as $t_{rc} = V_{rc}/Q_{rc}$, where the recirculating volume V_{rc} corresponds to the volume of liquid within the limit of the separating streamline and Q_{rc} is the recirculation flow rate equal to Q_0 (and $|Q_1|$). t_{rc} can be

made non dimensional by dividing it by the time taken for the bubble to travel a distance equal to the slug length : $\tau_{rc} = t_{rc}/(L_S/U_B)$.

In our previous work we have explored the effects of fluid properties, operating conditions and microchannel geometry on the size of Taylor bubbles (Abadie et al. [2012]) and the flow patterns in the liquid slug using micro Particle Image Velocimetry ($\mu - PIV$) (Zaloha et al. [2012]). The objective of this work is to explore the effects of operating parameters (capillary, Ca_B, and Reynolds numbers, Re_B) and microchannel aspect ratio ($\alpha = w/h = [1; 2.5; 4]$) on the mixing and recirculation characteristics of the liquid slug in gas-liquid Taylor flow in microchannels. To do this, 3-dimensional VOF simulations of gas-liquid Taylor flow in microchannels have been performed. Using an approach that is analogous to the determination of circulation rate in stirred tanks, the recirculation rate in the liquid slug, as well as the size of the recirculating zone have been evaluated from the 3-dimensional numerical data. An attempt has been made to relate these characteristics of the recirculating liquid slug to the enhanced transport phenomena observed in Taylor flow in microreactors. Finally, recommendations on the design and operation of microreactors employing Taylor flow are given.

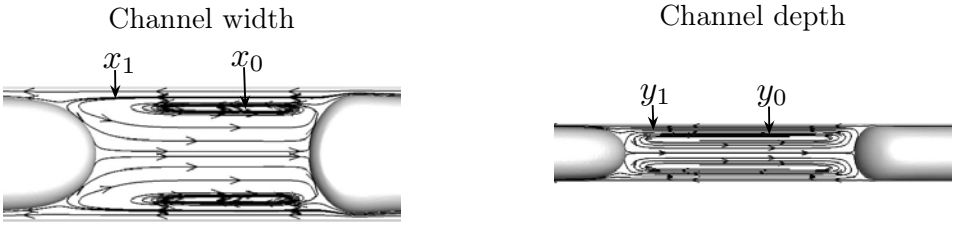

Figure 7.1: Streamline pattern in the frame of reference moving with the bubble ($Ca_B = 0.06$ and $Re_B = 16.8$). The flow is directed from the left to the right. The positive part of the recirculating pattern of volume V_0 is delimited by the coordinates $[x_0, y_0]$ in the channel width and depth; the negative part of the recirculating zone of volume $V_1 = V_{rc} - V_0$ is located between $[x_0, y_0]$ and $[x_1, y_1]$; and the film region of volume $V_2 = V_{slug} - V_{rc}$ is located between $[x_1, y_1]$ and the walls.

7.2 Methodology

7.2.1 Theoretical developed velocity profile in rectangular capillaries

In the limit of infinite slug length, the analytical solution of the velocity profile in a cross-section of a rectangular capillary can be derived. The velocity profile in a rectangular capillary is given in appendix A. This theoretical velocity profile has been used to evaluate the effects of aspect ratio and dimensionless bubble velocity on characteristic parameters of recirculation motion in gas-liquid Taylor flow: recirculating volumes and recirculation times. Under the assumption that the slug is long when compared with development lengths of velocity profile at the rear and the nose caps of the bubbles, the recirculation volume can be approximated by the cross-sectional area of the recirculating zone multiplied by the slug length: $V_{0,1} \sim A_{0,1} \times L_S$.

Numerical integration of the velocity profile (equations A.1 and A.2) for aspect ratios $\alpha = [1; 2.5; 4]$ have been performed on fine uniform grids of 400×400, 1000×400 and 1600×400, respectively, to calculate the area A_0 where the velocity in the moving coordinate system is positive. Following this, an iterative integration of A_1 (cross-section of the negative part of the recirculating liquid) has been performed until the flow rates

in the positive and negative parts of the recirculating zone are balanced. Integration of these profiles allows the prediction of recirculating volumes and recirculation times as a function of the aspect ratio and the dimensionless velocity $W = (U_B - U_{TP})/U_B$ assuming long liquid slugs.

7.2.2 Numerical simulations

The numerical code has been presented in chapter 2 and 3 and the numerical set-up has been detailed in section 6.2.
The parameters considered in this study have been chosen so that the Laplace number $La = Re_B/Ca_B = \frac{\rho_L D_h \sigma}{\mu^2}$ is constant in all the geometries and equal to $La = 280$ while it was varied in chapter 6. An illustration of the bubble shape and velocity field obtained in the 3D numerical simulations is given in figure 7.1.

7.3 Results and Discussion

In this section, the results concerning global observations about recirculation patterns, shapes of the recirculation zone in a cross-section of the slug, recirculating volumes, as well as recirculation times are given. As shown theoretically in circular channels (Thulasidas et al. [1997]), the recirculation characteristics of infinite slugs can be related to one parameter, which is the slip velocity $W = (U_B - U_{TP})/U_B$. Many studies dealing with the dynamics of gas-liquid Taylor flow relate W to the capillary number (Bretherton [1961], Aussillous and Quéré [2000]). In this study, the flow conditions were modified by varying the capillary number in the range $0.04 \leq Ca_B \leq 0.5$ and the corresponding Reynolds number in the range $11.2 \leq Re_B \leq 140$ whilst keeping the gas void fraction constant at 31%.
To study the effects of slug length on the recirculation characteristics, the geometry with an aspect ratio $\alpha = 2.5$ has been considered and the capillary number has been set to $Ca_B = 0.1 + / - 0.0005$ that leads to $W = 0.3303 + / - 0.0021$. Five different cases have been simulated by varying slug length from $2.90 \times h$ to $20.06 \times h$ and the corresponding volume fraction of gas phase ranges from 50% to 12.5%.

7.3.1 Recirculation pattern and local velocity field

The recirculation patterns in a rectangular channel with aspect ratio $\alpha = 2.5$ with varying capillary numbers are shown in Figure 7.2. The local velocity field is shown in terms of local liquid Péclet number $Pe_l = Re \times Sc = \frac{|U_l| D_h}{D_L}$ where $|U_l|$ is the local velocity magnitude in the frame of reference moving with the bubble, D_L is the mass diffusivity in the liquid and Sc is the Schmidt number and is set to 1.
It can be seen in Figure 7.2 that the maximum value of the local Péclet number is found in the liquid film between the bubble rear cap and the wall. Whatever the capillary number, the maximum value of the local Péclet number in the liquid slug is found close to the wall, decreases to zero at the center of the recirculation loop and then increases whilst approaching the center of the channel. Furthermore, as the Reynolds number increases, the boundary layer close to the bubble caps (where the Péclet number is very low) decreases in size. It can also be seen that recirculation loops through both the channel width and depth are formed. However, as the capillary number increases, the recirculation pattern in the less confined direction (channel width) diminishes until the closed loop is entirely lost. These changes in the streamline patterns are mainly observable in the wake of the bubble where the flow is particularly disturbed and

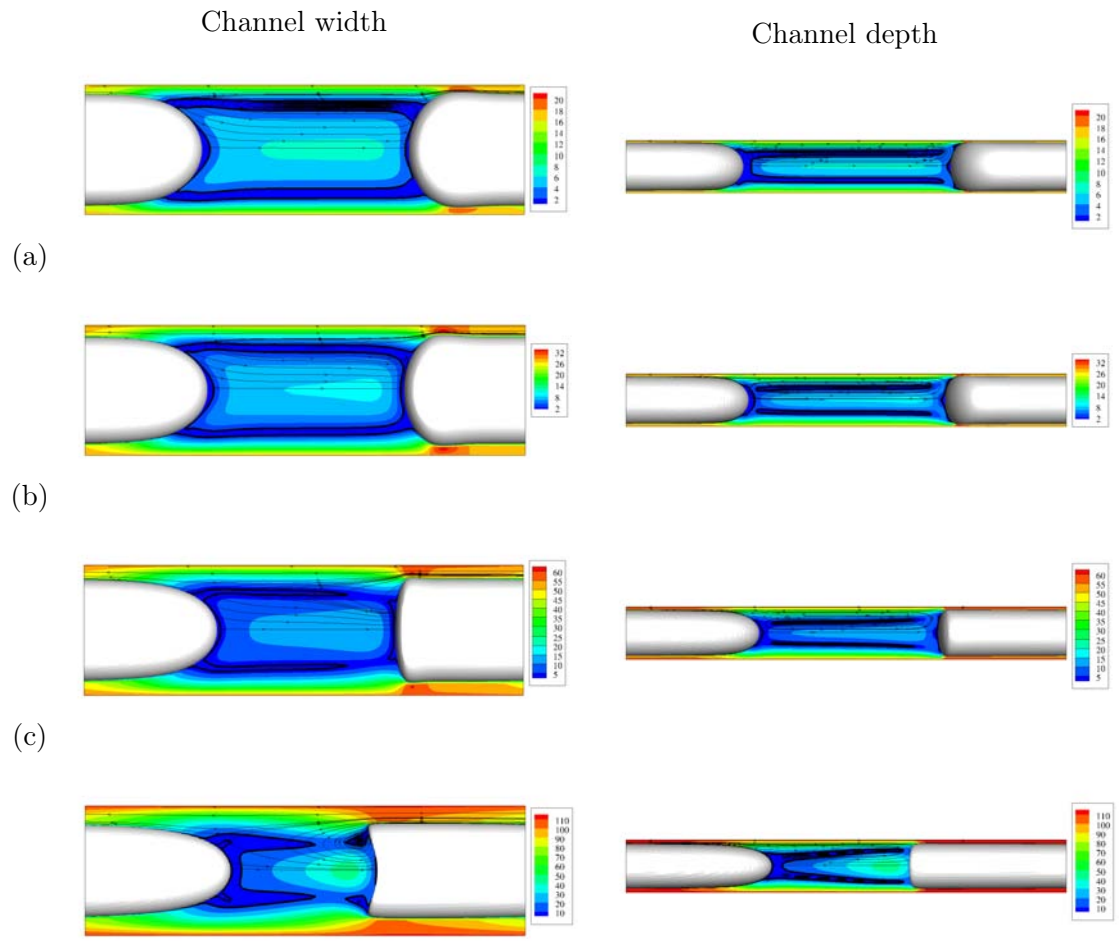

Figure 7.2: Local liquid Péclet numbers and streamlines through the channel width and depth for channel aspect ratio of 2.5. (a) $Ca_B = 0.06$, $Re_B = 16.8$; (b) $Ca_B = 0.1$, $Re_B = 28$; (c) $Ca_B = 0.2$, $Re_B = 56$; (d) $Ca_B = 0.4$, $Re_B = 112$. The bold line represents a Péclet number of 2 for (a)-(c) and 10 for (d) where $Ca_B = 0.4$ and $Re_B = 112$.

the streamlines do not follow the shape of the rear of the bubble in the less confined direction.

These observations also depend strongly on the cross-sectional shape of the channel and it can be seen in Figure 7.3 that the detachment of the streamlines is enhanced when the aspect ratio increases. Indeed, although the recirculation loop in the square geometry seems qualitatively similar to that in a circular geometry, strong 3-dimensional effects of the rectangular geometry on the velocity field in the wake of the bubble are observed. In addition to the streamline pattern in the wake of the bubble, the same phenomenon is observed at the front cap of the bubble in the very wide shallow channel (aspect ratio $\alpha = 4$). This is in agreement with previous works on semi-infinite bubbles at low Reynolds numbers (Hazel and Heil [2002]) in rectangular channels.

The effects of the capillary number and the aspect ratio on the dimensionless velocity at the channel centerline is illustrated in Figure 7.4 and Figure 7.5 respectively. It is seen that close to the bubble caps, the velocity at the channel centerline increases from the bubble velocity to the maximum velocity expected in the liquid slug that depends on the mean velocity (from equations A.1 and A.2, $U_{max} \sim [2.10\ ;\ 1.92\ ;\ 1.77] \times U_{TP}$ for channel cross-sections of aspect ratios $\alpha = [1\ ;\ 2.5\ ;\ 4]$). It is also observed (Fig-

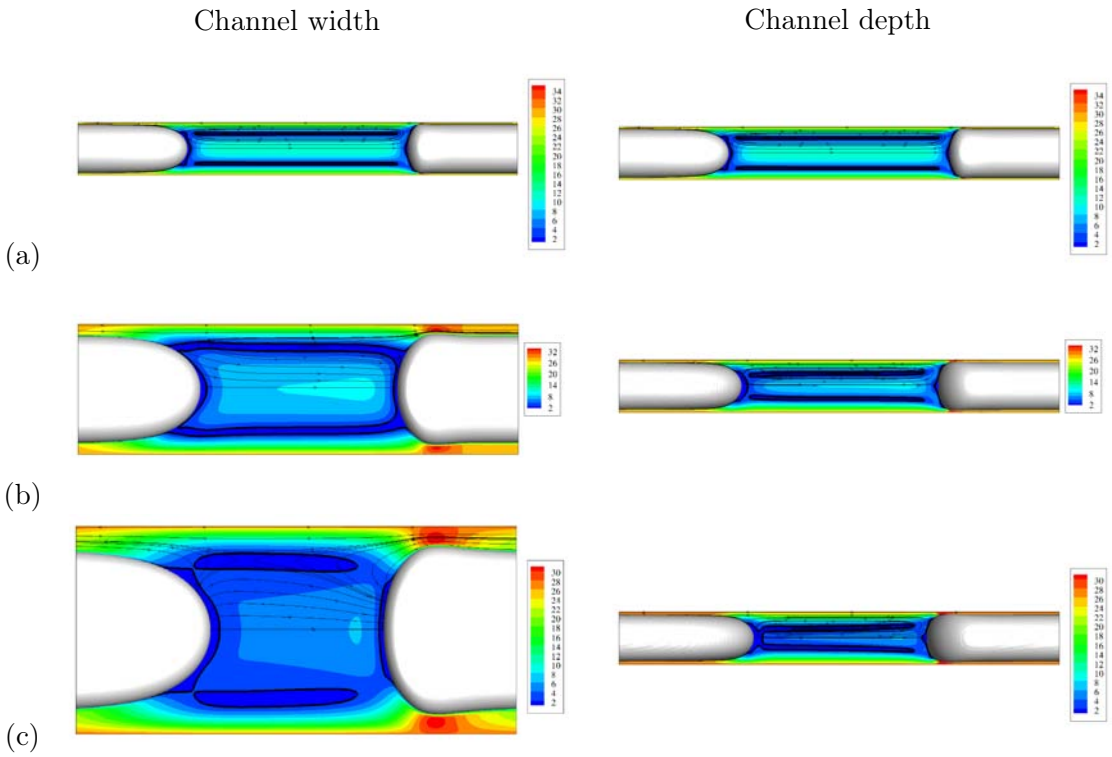

Figure 7.3: Local liquid Péclet numbers and streamlines through the channel width and depth for $Ca_B = 0.1$ and $Re_B = 28$. (a) $\alpha = 1$; (b) $\alpha = 2.5$; (c) $\alpha = 4$. The bold line represents a Péclet number of 2.

ures 7.4 and 7.5) that as the capillary number increases or the aspect ratio increases, there is a region in the wake of the bubble where the liquid velocity is greater than the maximum velocity of a laminar single-phase flow close to the bubbles caps.

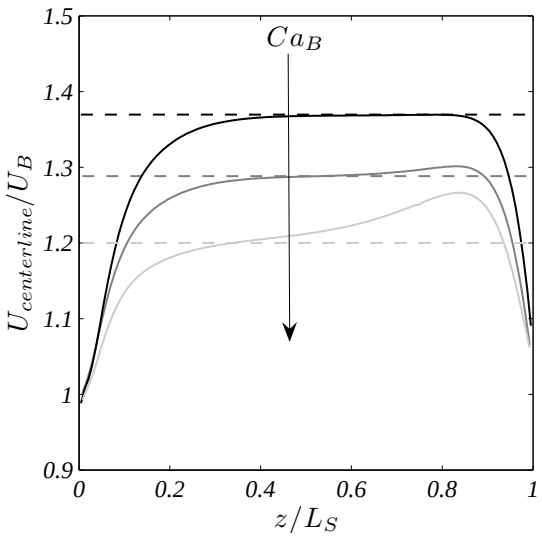

Figure 7.4: Dimensionless liquid velocity along the centerline of the channel between two bubbles for an aspect ratio of 2.5 and various capillary numbers. Legend : ( ) $U_{centerline}/U_B$; (−−) U_{max}/U_B evaluated from U_{TP} and equations A.1 and A.2 ; (black) $Ca_B = 0.06$; (gray) $Ca_B = 0.1$; (light gray) $Ca_B = 0.2$.

These observation suggest that the recirculation characteristics are not only gov-

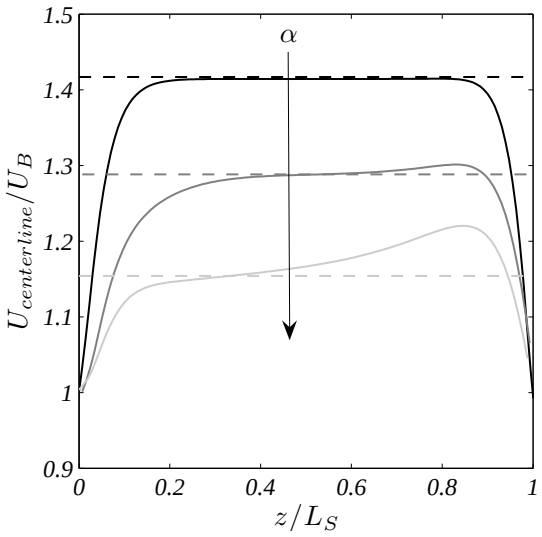

Figure 7.5: Dimensionless liquid velocity along the centerline of the channel between two bubbles for $Ca_B = 0.1$ and for aspect ratios 1, 2.5 and 4. Legend : ( ) $U_{centerline}/U_B$; $(--)$ U_{max}/U_B evaluated from U_{TP} and equations A.1 and A.2 ; (black) $\alpha = 1$; (gray) $\alpha = 2.5$; (light gray) $\alpha = 4$.

erned by the dimensionless slip velocity W but also by the slug length and this will be discussed in detail in section 7.3.3 and 7.3.4. The influence of slug length is expected when the development lengths at the rear and front caps of the bubbles are non negligible in comparison with the slug length, as illustrated with the streamlines and local Péclet numbers in Figures 7.2 and 7.3.

7.3.2 Shape of the recirculation zone

The cross-sectional area occupied by the recirculation zones as approximated by the theoretical fully-developed velocity profile (see section 7.2.1) has been calculated and is shown in Figure 7.6 for the three aspect ratios : $\alpha = [1; 2.5; 4]$. It can be seen that the recirculation areas follow the shape of the channel for low dimensionless velocities and reduce to circular and elliptical shapes as the velocity (or Ca_B) increases.

When the channel aspect ratio increases, the aspect ratio of the recirculation zone also increases. Furthermore, the center of the recirculation loop and the separating streamline both move faster towards the center of the channel in the less confined direction. As a result, the slug film thickness is greater in the width of the microchannel than in the height.

Mass transfer between the film and the recirculating regions will occur by molecular diffusion through the interface separating these regions. In a 2-dimensional representation through the channel cross-section, the perimeter that separates the recirculating and film regions can be used to understand transport processes between the recirculating and film regions. Figure 7.7 shows the evolution of the perimeter that separates the recirculating and film regions in Figure 7.6 as a function of the dimensionless slip velocity. To compare the three aspect ratios with circular channels, the perimeters are normalised by the perimeter of a circular channel with an equivalent hydraulic diameter D_h. It is clearly seen that the perimeter that links the recirculation zone and the film region is greater in square channels than in circular channels. As the aspect ratio increases, the perimeter that separates the recirculating and film regions also increases until a certain velocity W above which the opposite trend is observed. The velocity at

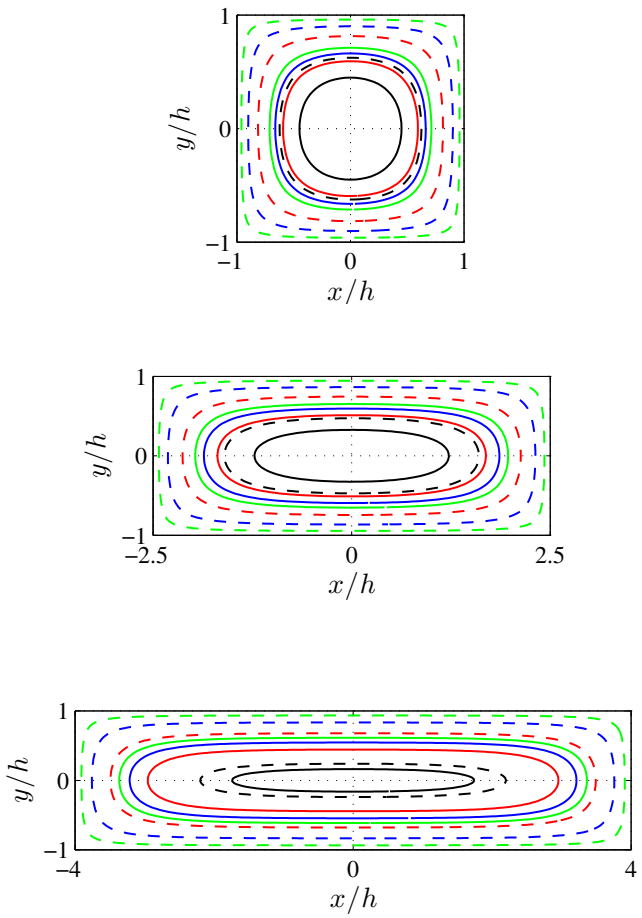

Figure 7.6: Cross-sectional shape of the recirculating zone for aspect ratios $\alpha = [1; 2.5; 4]$ for different slip velocities W. Legend : ( ) center of the recirculating loop; $(--)$ streamline separating the circulation loop and the film. From the walls to the center (green ; blue ; red ; black) : $W = [0.1; 0.2; 0.3; 0.42]$.

which the transition occurs decreases as the aspect ratio increases. As a consequence, it is expected that when dealing with wall to slug mass transfer, channels with a high aspect ratio will typically provide better mass transfer than channels with square or circular cross-section. However, mass transfer from the recirculation zone to the film will also depend on the time needed for a fluid element to travel the slug distance and more generally, mixing efficiency will depend on the total recirculation time, as well as the size of the recirculating volume.

7.3.3 Characteristic recirculating volumes

A characteristic parameter of the recirculation motion in Taylor flow is the volume of fluid recirculating in the slug. Unlike in cylindrical tubes where the volumes of positive flow and negative flow of the recirculation region are equal, it is not the case in square and rectangular ducts. Indeed, in the channel cross-section the ratio of total recirculation area over positive recirculation area increases with the aspect ratio and tends to $\sqrt{3}$ for the asymptotic behavior of an infinite aspect ratio. In addition, for a fixed geometry, the ratio of recirculation areas also varies with the dimensionless velocity W.

The size of the recirculation area at the center of the slugs for channel aspect

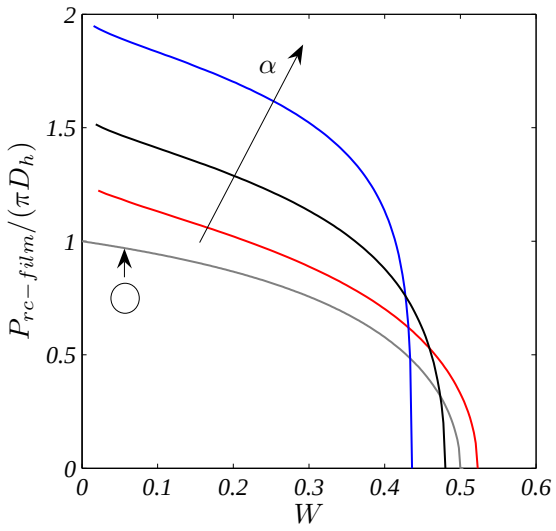

Figure 7.7: Perimeter of the recirculation zone through the channel cross-section (as depicted by dashed lines in Figure 7.6) normalised by the perimeter of a circular channel with an equivalent hydraulic diameter D_h in a cross-section of the slug as a function of the dimensionless velocity W. Legend : (gray) circular channels ; (red) $\alpha = 1$; (black) $\alpha = 2.5$; (blue) $\alpha = 4$.

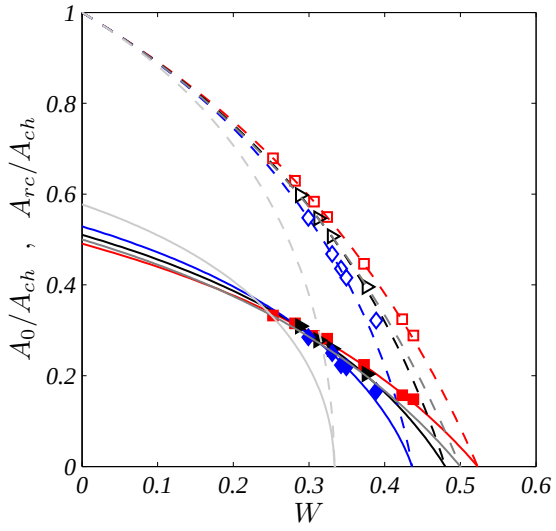

Figure 7.8: Dimensionless cross-section of the recirculating areas at the center of the slug versus the dimensionless bubble velocity. Legend : ( ) A_0/A_{ch}, infinite slug legnth assumption ; $(--)$ A_{rc}/A_{ch}, infinite slug length assumption ; (gray) circular channels ; (light gray) 2D channels ; (filled symbols) A_0/A_{ch} ; (open symbols) A_{rc}/A_{ch} ; $(\square, \text{red})$ $\alpha = 1$, numerical ; $(\triangleright, \text{black})$ $\alpha = 2.5$, numerical ; $(\diamond, \text{blue})$ $\alpha = 4$, numerical

ratios $[1; 2.5; 4]$ are shown in Figure 7.8. A_{rc} (cross-section of the reciculating liquid) and A_0 (cross-section of the positive part of the reciculating liquid) are normalised by the channel cross-section area A_{ch}. The results integrated from the analytical velocity profile corresponding to infinite slug length and the results obtained from the numerical simulations with finite slug length are compared and very good agreement between the computational and theoretical results is observed, as long as the liquid velocity profile is fully-developed at the center of the slug. The computations that show a slight

deviation from the theory correspond to cases where the velocity profile is not entirely fully-developed at the center of the slug. For short slugs, the laminar velocity profile is not fully-developed and the region where the flow is disturbed by the bubble is not negligible; therefore the recirculating volumes and times cannot be approximated by the theoretical velocity profile. In such cases, the recirculating volume is obtained from direct numerical simulations by integrating small slices of recirculating zones along the slug.

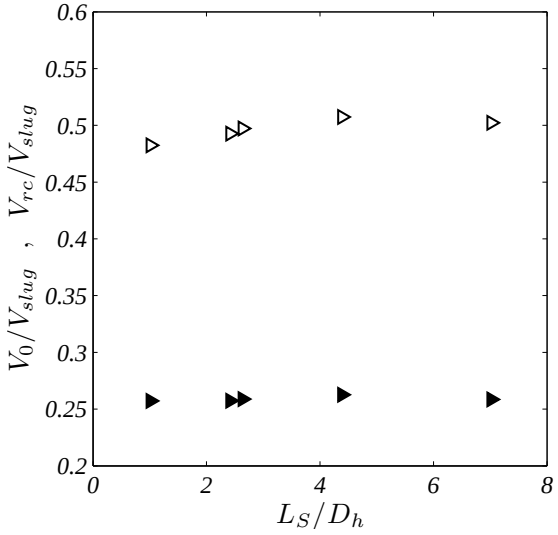

Figure 7.9: Dimensionless recirculation volumes as a function of dimensionless slug length. Legend : (filled symbols) V_0/V_{slug} ; (open symbols) V_{rc}/V_{slug}.

Figure 7.9 shows the influence of the slug length on the recirculating volume V_{rc} and the positive part of the recirculating volume V_0 normalised by the slug volume V_{slug}. In every simulation, care has been taken that the bubble is long enough and the dimensionless bubble velocity is constant whatever the slug and bubble lengths. From these data, it is clear that the regions close to bubble caps do not affect the ratio of recirculating volume over slug volume significantly.

Figure 7.10 shows the ratio of the recirculating volumes V_0 and V_{rc} over total slug volume V_{slug} as a function of the capillary number for the three rectangular microchannel geometries. The recirculating volume for the infinite aspect ratio and axisymmetrical cases are also given using the relation $W = f(Ca_B)$ from Aussillous and Quéré [2000] for the tubes and Abadie et al. [2012] for 2D cases; both assume long liquid slug in order to neglect the changes in the flow close to the bubble caps. It should also be kept in mind that axisymmetrical and planar cases are given as an indication only since the relations $W = f(Ca_B)$ for these cases are valid for negligible inertia, which is not the case in the present work since $Re_B \geq 10$. Experimental data obtained by $\mu - PIV$ in Zaloha et al. [2012] (obtained for a Laplace number $La = Re_B/Ca_B \sim 1000$) are also presented. As expected, the recirculating volumes are close to the slug volume at low capillary numbers ($Ca_{BB} \sim 10^{-3}$) due to the fact that the bypass flow is negligible compared with the total flow rate. In other words, almost all the liquid contributes to the recirculation motion. Then, as the capillary number increases, the recirculating volume significantly decreases in all the geometries. Although the volume of the positive recirculating flow is hardly dependent on the geometry, the total recirculating volume decreases as the aspect ratio increases.

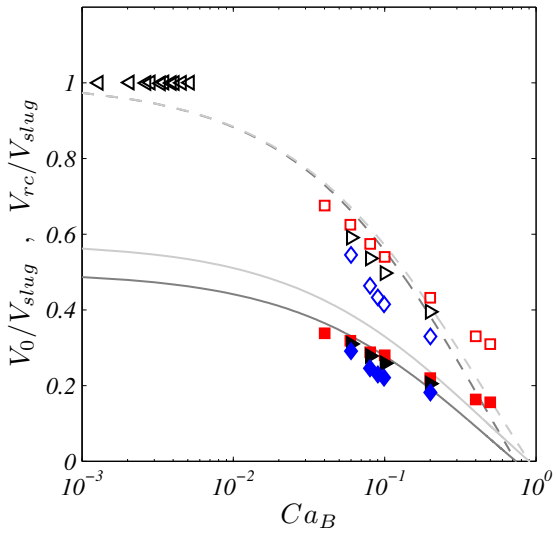

Figure 7.10: Dimensionless recirculating volume as a function of the capillary number. Legend : ( ) V_0/V_{slug}, infinite slug length assumption ; $(--)$ V_{rc}/V_{slug}, infinite slug length assumption ; (gray) circular channels ; (light gray) 2D channels ; (filled symbols) V_0/V_{slug} ; (open symbols) V_{rc}/V_{slug} ; $(\triangleleft, \text{black})$ $\alpha = 2.5$, experimental Zaloha et al. [2012] ; $(\square, \text{red})$ $\alpha = 1$, numerical ; $(\triangleright, \text{black})$ $\alpha = 2.5$, numerical ; $(\diamond, \text{blue})$ $\alpha = 4$, numerical

7.3.4 Characteristic recirculation times

The characteristic recirculation times τ_0 for the positive recirculation flow, τ_1 for the negative flow and τ_{rc} for the total recirculation as a function of the dimensionless velocity are plotted in Figure 7.11 in comparison with the infinite slug length assumption. The effects of slug length on positive (τ_0) and total (τ_{rc}) recirculation times are represented in Figure 7.12 and the recirculation times as a function of the capillary number are then plotted in Figure 7.13.

Although the recirculation areas show very good agreement with the theoretical predictions, the recirculation times τ_{rc} are greater than those determined using the infinite slug assumption (Figure 7.11), and mainly for aspect ratios 1 and 2.5 at low capillary numbers. Indeed, close to bubble caps where the flow is disturbed, the axial flow rate is reduced and the recirculation time is increased. However, as the capillary number or the aspect ratio increase, the velocity in the wake of the bubble increases (see Figures 7.4 and 7.5) and balances the lower velocities in the vicinity of the interface. It can be seen in Figure 7.11 that the recirculation time for the channel with aspect ratio of 4 (represented with diamonds in blue) is lower in our calculations compared with the inifinite slug assumption. The trends observed for all geometries are qualitatively similar and an increase in the aspect ratio leads to an increase in both the positive and negative recirculation times and thus in the total recirculation time until divergence when complete by-pass flow is attained.

Although the recirculating volume only depends on the dimensionless velocity W, it is shown in Figure 7.12(a) that the dimensionless recirculating times vary with the slug length. Indeed, whilst the disturbed flow around the bubble does not change the recirculating volume, it does cause an increase in the recirculation time when the slug length decreases, as mentioned in the previous paragraph. As expected, the recirculation times tend towards the value evaluated from the theoretical laminar single-phase flow representing the case of an infinite slug length. For the shortest slug considered

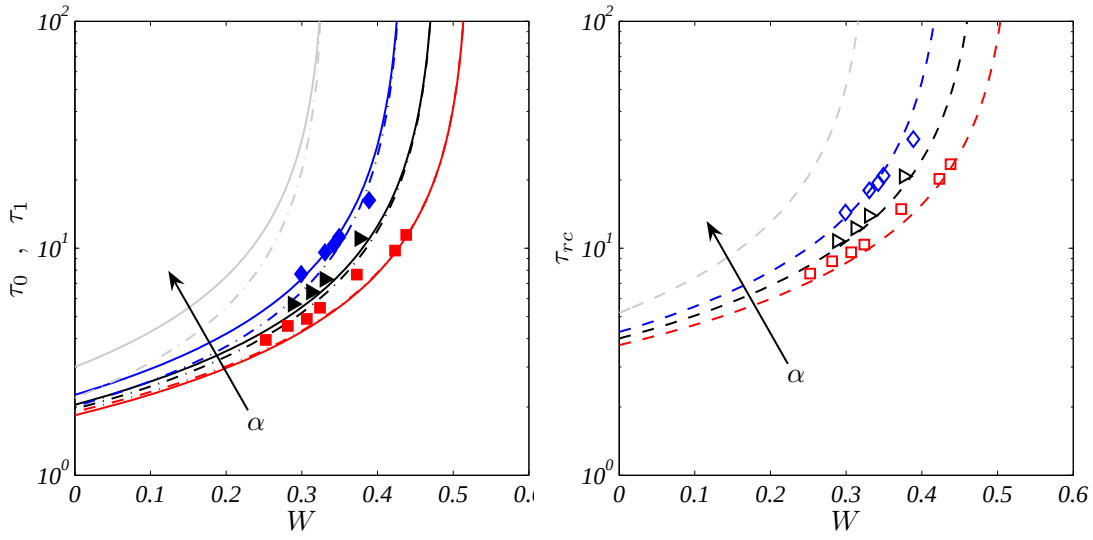

Figure 7.11: (a) Dimensionless recirculation times τ_0 and τ_1 versus the dimensionless bubble velocity. Legend : ( ) τ_0, infinite slug length assumption ; $(-.-)$ τ_1, infinite slug length assumption ; (light gray) 2D channels ; (filled symbols) τ_0, numerical $(\square, \text{red})$ $\alpha = 1$; $(\triangleright, \text{black})$ $\alpha = 2.5$; $(\diamond, \text{blue})$ $\alpha = 4$ (b) Dimensionless total recirculation time τ_{rc} versus the dimensionless bubble velocity. Legend : $(--)$ τ_{rc}, infinite slug length assumption ; (light gray) 2D channels ; (open symbols) τ_{rc}, numerical ; $(\square, \text{red})$ $\alpha = 1$; $(\triangleright, \text{black})$ $\alpha = 2.5$; $(\diamond, \text{blue})$ $\alpha = 4$

here, the total recirculation time is 20% longer than the asymptotic value. Leung et al. [2010] studied the effect of slug length on the Nusselt number with a constant heat flux on the wall of a circular tube and found an increase in the Nusselt number as the slug length decreases. Indeed, fluid elements will refresh the interface separating the recirculating and film regions more frequently in short slugs. The evolution of the mean time for a fluid element to complete a cycle can be represented in a dimensional form to illustrate this decrease in recirculation time as the slug length decreases. It is seen in Figure 7.12(b) that although the recirculation time is slightly underestimated with the infinite slug length assumption due to the increased time taken for a fluid element to travel the development length close to bubble caps, the recirculation time decreases as the slug length decreases.

In the cases presenting a recirculation motion in the liquid slug, the bubble velocity is lower than the liquid velocity at the centerline of the channel. Thus, around the bubble caps, there is a region where the velocity on the channel centerline decreases to the bubble velocity, as shown in Figures 7.4 and 7.5. This explains the increase in recirculation time when the slug length decreases since the ratio of development length over slug length increases. Here, it has been observed that in the development region close to the bubble caps, the centerline velocity can be greater than the expected velocity on the axis (*e.g.* $U_{max} = 1.92 \times U_{TP}$ for the 2.5 aspect ratio channel, Figure 7.4 for $Ca_B \geq 0.1$) before stabilizing if the slug is long enough. This local increase in the velocity can lead to a decrease in the recirculation time as the slug length decreases. This phenomenon is accentuated as the aspect ratio increases and it can be seen in Figure 7.11 that recirculation times evaluated in the numerical simulations are lower than that for an infinite slug length with the aspect ratio 4 and $W > 0.3$.

Figure 7.13 reports the evolution of the recirculation times as a function of the capillary number. It is shown that an increase in the capillary number also leads to

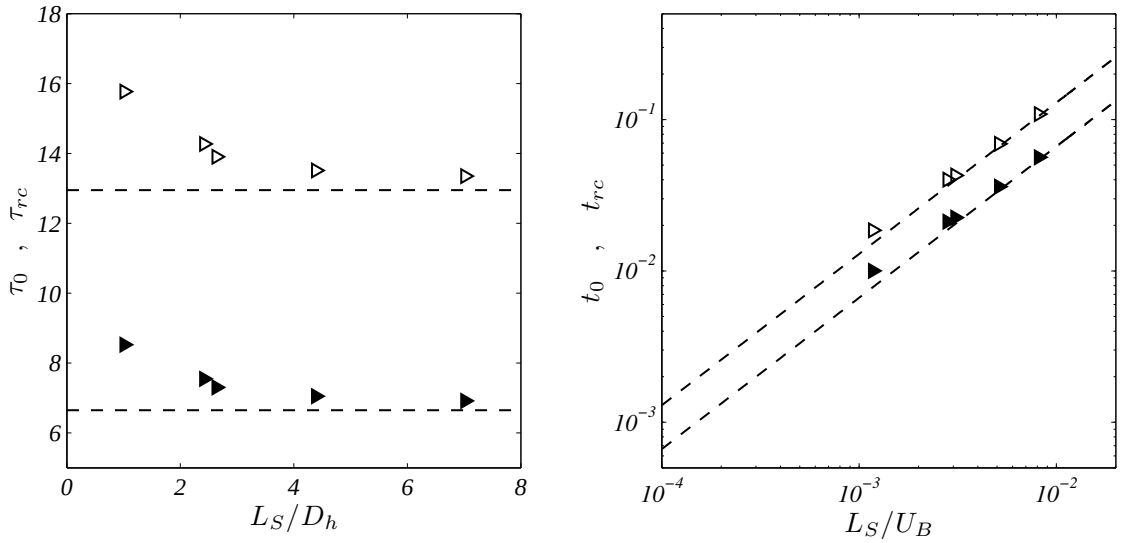

Figure 7.12: (a) Dimensionless recirculation times as a function of dimensionless slug length. Legend : (−−) asymptotic values τ_0 and τ_{rc} ; (filled symbols) τ_0 ; (open symbols) τ_{rc}. (b) Dimensional recirculation times t_0 and t_{rc} (with $D_h = 571\,\mu m$ and $U_B = 0.5\,m/s$) as a function of the time taken for a bubble to travel the slug length L_S/U_B. Legend : (−−) asymptotic values t_0 and t_{rc} ; (filled symbols) t_0 ; (open symbols) t_{rc}

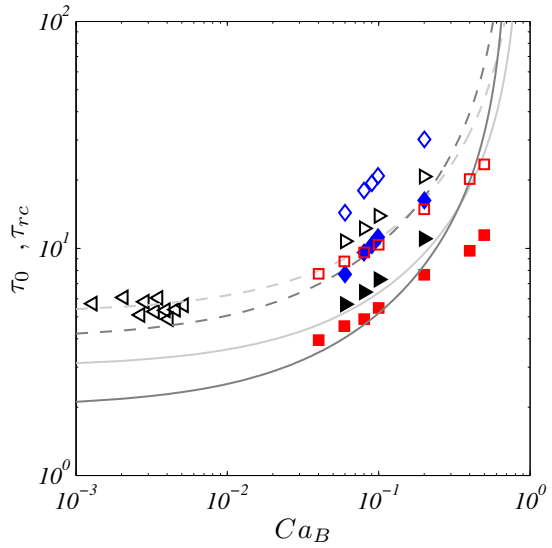

Figure 7.13: Dimensionless recirculation times versus the capillary number. Legend : ( ) τ_0, infinite slug length assumption ; (−−) τ_{rc}, infinite slug length assumption ; (gray) circular channels ; (light gray) 2D channels ; (filled symbols) τ_0; (open symbols) τ_{rc} ; ($\triangleleft$, black) $\alpha = 2.5$, experimental Zaloha et al. [2012] ; ($\square$, red) $\alpha = 1$; ($\triangleright$, black) $\alpha = 2.5$; ($\diamond$, blue) $\alpha = 4$, numerical.

an increase in the recirculation time for all the geometries considered. Thus, when the capillary number increases, the volume involved in the recirculation motion is reduced but the dimensionless time needed for a fluid element to travel the slug length is increased. It is also observed that the 2D theory is not a good approximation for high

aspect ratios. In addition, it can be seen that even if the recirculating volume shows a weak dependency on the channel geometry, the effect observed on the recirculation time is more significant. Indeed, at fixed operating conditions (Ca_B, Re_B and L_S), an increase in the aspect ratio leads to significantly longer recirculation times.

7.4 Concluding remarks

Direct numerical simulations of gas-liquid Taylor flow in microchannels have been performed. The effects of channel cross-section and operating conditions on mixing and recirculation in the liquid slug have been investigated. The results of the numerical simulations have been compared with theoretical approximations for the case of infinite slug length in terms of cross-sectional recirculation area, recirculating volume and recirculation times. It has been shown that as long as the slug is long, the recirculation area in the slug can be well predicted using the fully-developed velocity profile. Whatever the geometry, increasing the capillary number leads to a decrease in recirculating volume and an increase in recirculation time, which means that transport processes will be hindered. Radial mixing is then reduced while axial dispersion is enhanced with increasing the capillary number. It has been shown that when the aspect ratio increases for a given capillary number, the recirculating volume decreases slightly and the recirculation time increases while the exchange surface between film and recirculating regions is enhanced at low slip velocities, which is the case for capillary numbers lower than approximately $Ca_B \sim 0.1$. Indeed, high aspect ratio channels may appear attractive for heat transfer in plate microreactors, however the decrease in the recirculation rate and effective recirculation volume is disadvantageous for both heat and mass transfer operations. It is therefore expected that some intermediate aspect ratio geometry would be most effective. This would require a systematic study that investigates the effects of process parameters (aspect ratio, void fraction, capillary number, Reynolds number) on the efficiency of the gas-liquid system that could be expressed by a cost-function integrating global parameters (pressure drop, circulation volumes and times, mass transfer, heat transfer).
The disturbed flow close to the bubble caps has shown to generally increase recirculation time. It has also been shown that for certain cases in rectangular channels, the bubble wake causes a local increase in the velocity at the center of the channel and this phenomenon is enhanced in high aspect ratio channels and high capillary number flows. Although this increase in the axial velocity can lead to a slight decrease in the recirculation time, these wake effects do not balance geometrical effects and the recirculation times in wide shallow channels remain greater than the ones obtained in channels of lower aspect ratio.

Conclusion and future work

Conclusion

In order to contribute to the development of microstructured devices, this work has focused on obtaining fundamental knowledge of gas-liquid Taylor flow using both experimental and numerical approaches.

The first part of this work has aimed at contributing to the fundamental knowledge of bubble generation and controlling bubble lengths. Microchannels have been designed and visualization experiments have been conducted to investigate the role of the channel geometry and the effects of fluid properties on the bubble generation mechanism. The bubble dispersion generated in a cross-junction in channels of different aspect ratios ($\alpha = [1; 2.5; 4]$) has been characterized. The two-step model, which is widely used in T-junctions, has been extended to cross-junctions and the effects of the liquid capillary number on the two stages of bubble formation mechanism have been identified. The minimum bubble length has been shown to depend on the capillary number independently of the aspect ratio. The growth rate of bubble length has been found to decrease when the liquid capillary number is increased in rectangular microchannels whereas it is constant in a square microchannel. The bubble formation frequency increases with the gas to liquid flow rate ratio and with the liquid capillary number. The increase in bubble formation frequency is enhanced in rectangular channels when the aspect ratio is increased. It has also been pointed out that the bubble to unit cell length ratio follows a unique law as a function of the gas to liquid flow rate ratio, independently of the capillary number, the Reynolds number and the geometry of the channel.

The gas-liquid flows generated in a cross-junction and two different T-shaped junctions have been compared. Bubble formation in these three geometries can be split into two main steps but the effects of the capillary number on these steps has been shown to differ from one contacting section to another. Indeed, the minimum bubble length at vanishing capillary numbers in a cross-junction diverges with the proposed scaling while it tends towards a finite value in T-junctions. Similarly, the growth rate of bubble length is reduced in T-junctions when compared with cross-junctions. An interesting point is that the bubble lengths are less dependent on the geometry at high capillary numbers where the effects of the walls are reduced.

It has been shown that some limitations in the computational method of *JADIM* did not allow the accurate simulation of Taylor flow at low capillary numbers. Spurious currents arise in such simulations and it has been necessary to reduce their intensity to correctly simulate low capillary number flows. This part has consisted in two steps: the implementation of a Level Set method to capture the interface (chapter 3) and the characterization of its ability to perform the simulations at low capillary number. Chapter 4 has been dedicated to the analysis of spurious currents and it is demonstrated that the technique implemented is very well adapted to low capillary number

simulations and reduces spurious currents by approximately one order of magnitude in dynamic cases.

The third part of this work focused on the hydrodynamics of fully developed Taylor flow. Three dimensional numerical simulations have been carried out in different geometries. Firstly, results at low Reynolds numbers have been compared with data from the literature (Wong et al. [1995a,b], De Lozar et al. [2008]) and extended through an analysis of the pressure drop in microchannels as a function of the bubble length, the capillary number and the channel aspect ratio.

The transition to intermediate and high Reynolds number has then been investigated. It has been shown that an increase in the Reynolds number promotes bubble rupture at the rear cap. The bubble shape is significantly modified as the Reynolds number increases. However, it has also been shown that the available correlation for low Reynolds numbers in a circular channel gives a very good estimation of the bubble velocity in the aspect ratios considered here. A close inspection of the slip velocity between the bubble and the mean velocity has however shown some deviations between the results obtained with different aspect ratios. In addition, the slip velocity follows a non-monotonic behaviour as the Reynolds numbers increases. The pressure drop across the bubble has been characterized and follows a linear law with the two-phase Reynolds number.

Finally, the velocity field in the liquid slug has been analysed to characterize the mixing characteristics in the slug. Indeed, the effects of the capillary number and geometry on mean recirculation times in the liquid slug have been estimated from numerical simulations and compared with the case of infinite slug lengths obtained from the single-phase velocity profile in a rectangular duct. It has been shown that an increase in the capillary number leads to an increase in the recirculation time. This means that radial mixing is reduced. In addition, the by-pass flow is increased as the capillary number increases, therefore increasing the axial dispersion. It has been shown that although high aspect ratio channels increase the exchange surface for reactor-heat exchanger systems, the recirculation time is increased thereby reducing the radial mixing in a microchannel. This may indeed have negative effects on the heat transfer process.

From the above, it can be seen that this work has contributed to three key aspects of Taylor flow: bubble dispersion, dynamics of the fully-developed flow and mixing. However, much work still remains and the outlooks for future work are various and promising.

Future work

The direct outlooks of this work concerning the bubble generation are to determine the relationship between the capillary effects and the geometrical effects in a cross-junction geometry more accurately. This could be done by means of numerical simulations, which would also give the possibility to accurately control wettability of the channel walls. Another outlook is to scale-up such microchannel geometries in multichannel structures. This work has already been started at LOCIE in the framework of the project MIGALI. However, due to different pressure drops in every channel, the control of bubble dispersion remains very difficult.

Concerning the hydrodynamics of fully developed Taylor flow, the points that have been adressed but not clearly explained up to now need to be further analysed. This

concerns in particular the non-monotonic behaviour of the slip velocity as a function of the Reynolds number. Another point of interest for future work is the transition to flow regimes where droplet form at the rear of the bubble and cross the bubble. In addition, the extension of the current work to other geometries, as shown below, would be interesting. Indeed, the effects of the serpentine channel on the dynamics of the bubble and mixing in the slug play an important role in transport processes and still need to be thoroughly characterized.

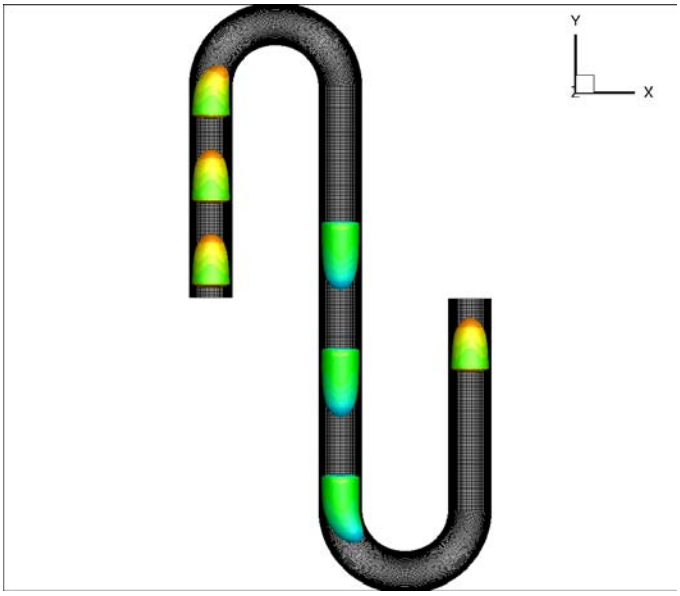

Figure 7.14: Illustration of bubbles in serpentine channel of square cross-section. Bubbles are colored by the $y-$component of the velocity.

Although mixing in the slug has been characterized, it is necessary to relate the characteristic times and volumes to mass and heat transfer processes. Some preliminary work on this subject has already been started in this PhD. Mass transfer within the VOF formulation developed by Haroun and Legendre [2010] has been validated in the case of bubble rising in a liquid and the results have been compared with data from the literature (Figueroa-Espinoza and Legendre [2010], see figure 7.15).

The agreement is very good and simulations of mass transfer from the bubble to the liquid slug are currently under way. In the first step, the concentration in the bubble is fixed and some preliminary results are shown in figure 7.16.

Finally, concerning the numerical developments in the JADIM code, the method implemented currently is very well adapted to the simulations of Taylor flow but still suffers from mass conservation problems. Although this can be easily solved for a single bubble, it remains a drawback when simulating a large number of inclusions (*e.g.* bubble swarms, atomization). It would be therefore very interesting to couple VOF and Level Set methods in a VOF without reconstruction framework. The use of Height Functions coupled to more accurate transport schemes is also a possibility. The time step constraint introduced by the capillary force in the Navier-Stokes equations is very limiting. An idea to pursue would be to make implicit the resolution of the surface tension force (Raessi et al. [2009]). Another option would be to decrease the time needed per iteration with the use of adaptive mesh refinement techniques which are available in the literature (Popinet [2009]).

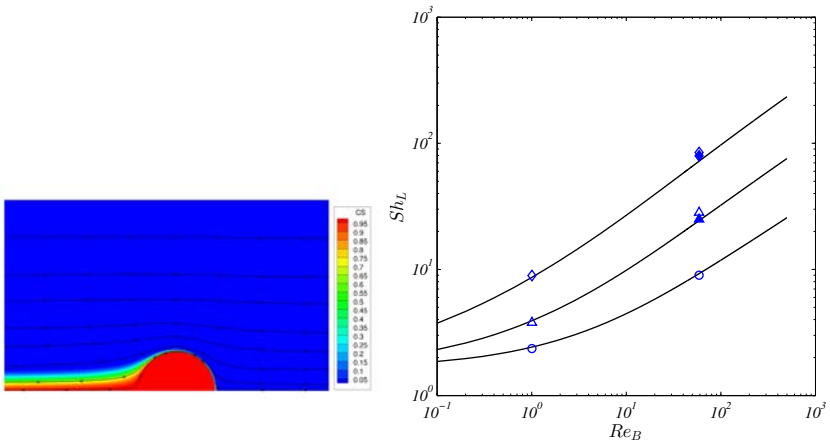

(a) (b)

Figure 7.15: (a) Bubble rise and mass transfer in a liquid at $Re \simeq 60$ and $Sc = 100$. (b) Sherwood number as a function of the Reynolds number for Schmidt numbers $Sc = [1; 10; 100]$.
Legend: ($\diamond$) $Sc = 100$; ($\triangle$) $Sc = 10$; ($\circ$) $Sc = 1$; (lines) see Figueroa-Espinoza and Legendre [2010] for more details on the available correlations.

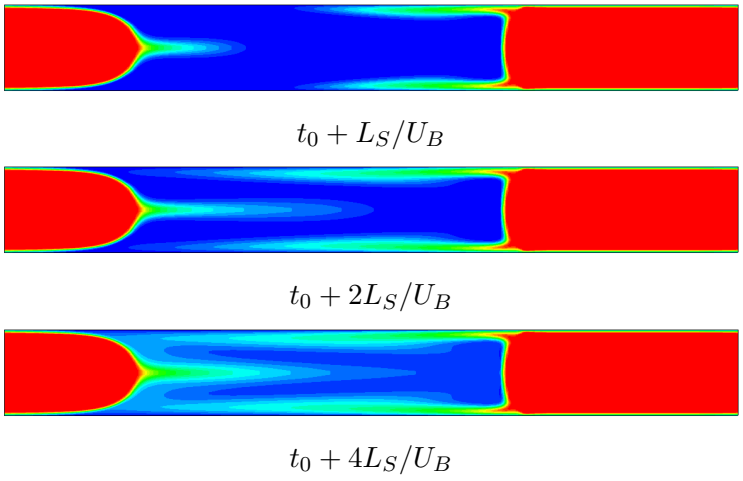

Figure 7.16: Illustration of mass transfer through the depth of a square microchannel. The resistance of the bubble to mass transfer is negligible, $Ca = 0.1$; $Re = 28$; $Pe = 1400$.

References

T. Abadie, J. Aubin, D. Legendre, and C. Xuereb. Hydrodynamics of gas-liquid Taylor flow in rectangular microchannels. *Micro uid Nano uid*, 12:355 369, 2012.

T. Abadie, J. Aubin, D. Legendre, and C. Xuereb. Mixing and recirculation characteristics of gas-liquid Taylor flow in microreactors. *Chem Eng Res Des*, page http://dx.doi.org/10.1016/j.cherd.2013.03.003, 2013.

S. Afkhami, A. M. Leshansky, and Y. Renardy. Numerical investigation of elongated drops in a microfluidics t-junction. *Phys Fluids*, 23:022002(14), 2011.

M. K. Akbar, D. A. Plummer, and S. M. Ghiaasiaan. On gas-liquid two-phase flow regimes in microchannels. *Int J Multiph Flow*, 29:855 865, 2003.

S. L. Anna, N. Bontoux, and H. A. Stone. Formation of dispersions using flow-focusing in microchannels. *Appl Phys Lett*, 82:364 366, 2003.

S. Arias, D. Legendre, and R. Gonzalez-Cinca. Numerical simulation of bubble generation in a T-junction. *Comput Fluids*, 56:49 60, 2011.

J. Aubin, J.-M. Commenge, L. Falk, and L. Prat. Miniaturisation des procédés. *Génie des Procédés durables: du concept à la concrétisation industrielle*, 2010.

P. Aussillous and D. Quéré. Quick deposition of a fluid on the wall of a tube. *Phys Fluids*, 12:2367 2371, 2000.

A. Benkenida. *Développement et validation d une méthode de simulation d écoulements diphasiques sans reconstruction d interface. Application à la dynamique des bulles de Taylor*. PhD thesis, INP Toulouse, 1999.

A. A. Blanco. *Quelques aspects de l écoulement d un uid visqueux autour d une bulle déformable: une analyse par simulation directe*. PhD thesis, INP Toulouse, 1995.

T. Bonometti. *Développement d une méthode de simulation d écoulements à bulles et à gouttes*. PhD thesis, INP Toulouse, 2005.

T. Bonometti and J. Magnaudet. An interface-capturing method for incompressible two-phase flows. Validation and application to bubble dynamics. *Int J Multiph Flow*, 33:109 133, 2007.

J. Brackbill, D. B. Kothe, and Zemach C. A continuum method for modeling surface tension. *J Comput Phys*, 100:335 354, 1992.

F. P. Bretherton. The motion of long bubbles in tubes. *J Fluid Mech*, 10:166 188, 1961.

R.D. Chambers, D. Holling, R.C.H. Spink, and G. Sandford. Elemental fluorine - part 13. Gas-liquid thin film microreactors for selective direct fluorination. *Lab Chip*, 1: 132 137, 2005.

Y. C. Chang, T. Y. Hou, B. Merriman, and S. Osher. A level set formulation of Eulerian interface capturing methods for incompressible fluid flows. *J. Comput. Phys.*, 124: 449 464, 1996.

G. F. Christopher and S. L. Anna. Microfluidics methods for generating continuous droplet streams. *J Phys D: Appl Phys*, 40:R319 R366, 2007.

G. F. Christopher, N. N. Noharuddin, J. A. Taylor, and S. L. Anna. Experimental observations of the squeezing-to-dripping transition in T-shaped microfluidics junctions. *Phys Rev E*, 78:036317(12), 2008.

E. Climent. *Dispersion de bulles et modi cation du mouvement de la phase porteuse dans des écoulements tourbillonaires*. PhD thesis, INP Toulouse, 1996.

F. Couderc. *Développement d un code de calcul pour la simulation d écoulements de uides non miscibles: application à la désintégration assistée d un jet liquide par un courant gazeux*. PhD thesis, ENSAE, 2007.

T. Cubaud, M. Tatineni, X. Zhong, and C-M. Ho. Bubble dispenser in microfluidics devices. *Phys Rev E*, 72:037302, 2005.

S. J. Cummins, M. M. Francois, and D. B. Kothe. Computing curvature from volume fraction. *Comput. Struct.*, 83:425 434, 2005.

A. De Lozar, A. Juel, and A. Hazel. The steady propagation of an air finger into a rectangular tube. *J Fluid Mech*, 614:173 195, 2008.

M. De Menech, P. Garstecki, F. Jousse, and H. A. Stone. Transition from squeezing to dripping in a microfluidics T-shaped junction. *J Fluid Mech*, 595:141 161, 2008.

B. Dollet, W. Van Hoeve, P. Raven, P. Marmottant, and M. Versluis. Role of the channel geometry on the bubble pinch-off in flow-focusing deices. *Phys Rev Lett*, 100:034504(4), 2008.

J.-B. Dupont and D. Legendre. Numerical simulation of static and sliding drop with contact angle hysteresis. *J Comput Phys*, 229:2453 2478, 2010.

J.-B. Dupont, D. Legendre, and J. Fabre. Motion and shape of long bubbles in small tubes at low re-number. *ICMF, Leipzig, Germany*, 2007.

H. Ehrich, D. Linke, K. Morgenschweis, M. Baerns, and K. Jahnisch. Application of microstructured reactor technology for the photochemical chlorination of alkylaromatics. *Chimia*, 56:647 653, 2002.

D. Enright, R. P. Fedkiw, J. Ferziger, and Mitchell I. A hybrid particle-level set method for improved interface capturing. *J. Comput. Phys.*, 183:83 116, 2002.

B. Figueroa-Espinoza and D. Legendre. Mass or heat transfer from spheroidal gas bubbles rising througha stationary liquid. *Chem Eng Sci*, 65:6296 6309, 2010.

M. M. Francois, S. J. Cummins, Dendy E. D., D. B. Kothe, J. M. Sicilian, and M. W. Williams. A balanced-force algorithm for continuous and sharp interfacial surface tension models within a volume tracking framework. *J. Comput. Phys.*, 213:141 173, 2006.

T. Fu, D. Funfschilling, M. Ma, Youguang, and H. Z. Li. Bubble formation and breakup mechanism in a microfluidic flow-focusing device. *Chem Eng Sc*, 64, 2009.

T. Fu, D. Funfschilling, M. Ma, Youguang, and H. Z. Li. Scaling the formation of slug bubbles in microfluidics flow-focusing devices. *Micro uid Nano uid*, 8, 2010a.

T. Fu, M. Ma, Youguang, D. Funfschilling, C. Zhu, and H. Z. Li. Squeezing-to-dripping transition for bubble formation in a microfluidic T-junction. *Chem Eng Sc*, 65, 2010b.

D. Fuster, G. Agbaglah, C. Josserand, S. Popinet, and S. Zaleski. Numerical simulation of droplets, bubbles and waves: state of the art. *Fluid Dyn. Res.*, 41:065001, 2009.

A. M. Ganan-Calvo. Perfectly monodisperse microbubbling by capillary flow focusng: an alternate physical description and universal scaling. *Phys Rev E*, 69:037301(3), 2004.

P. Garstecki, M. J. Fuerstman, H. A. Stone, and G. M. Whitesides. Formation of droplets and bubbles in a microfluidics T-junction - scaling and mechanism of break-up. *Lab Chip*, 6:437 446, 2006.

M. D. Giavedoni and F. A. Saita. The axisymmetric and plane cases of a gas phase steadily displacing a Newtonian liquid - A simultaneaous solution of the governing equation. *Phys Fluids*, 9:2420 2427, 1997.

D. Gueyffier, J. Li, A. Nadim, R. Scardovelli, and S. Zaleski. Volume-of-Fluid interface tracking with smoothed surface stress methods for three-dimensional flows. *J. Comput. Phys.*, 152:423 456, 1999.

A. Gupta and R. Kumar. Effect of geometry on droplet formation in the squeezing regime in a microfluidic T-junction. *Micro uid Nano uid*, 8:799 812, 2010.

R. Gupta, D. F. Fletcher, and B. S. Haynes. On the CFD modelling of Taylor flow in microchannels. *Chem Eng Sci*, 64:2941 2950, 2009.

R. Gupta, D. F. Fletcher, and B. S. Haynes. CFD modelling of flow and heat transfer in the Taylor flow regime. *Chem Eng Sci*, 65:2094 2107, 2010a.

R. Gupta, D. F. Fletcher, and B. S. Haynes. Taylor flow in microchannels: a review of experimental and computational work. *J Comput Multiph Flow*, 2:1, 2010b.

R. Gupta, S. S. Y. Leung, R. Manica, D. F. Fletcher, and B. S. Haynes. Three dimensional effects in Taylor flow in microchannels. *La Houille Blanche*, 2:60 67, 2013.

Y Han and N. Shikazono. Measurement of the liquid film thickness in micro square channel. *Int J Multiph Flow*, 30:896 903, 2009.

F. H. Harlow and J. E. Welch. Numerical calculation of time-dependent viscous incompressible flow of fluid with free surface. *Phys. Fluids*, 8:2182 2189, 1965.

Y. Haroun and D. Legendre. Volume of fluid method for interfacial reactive mass transfer: application to stable liquid film. *Chem Eng Sci*, 65:2896 2909, 2010.

D. J. E. Harvie, M. R. Davidson, and M. Rudman. An analysis of parasitic current generation in Volume of Fluid simulations. *Applied Mathematical Modelling*, 30: 1056 1066, 2006.

A. L. Hazel and M. Heil. The steady propagation of a semi-infinite bubble into a tube of elliptical or rectangular cross-section. *J Fluid Mech*, 470:91 114, 2002.

M. Herrman. A balanced force refined level set grid method for two-phase flows on unstructured flow solver grids. *J. Comput. Phys.*, 227:2674 2706, 2008.

V. Hessel, P. Angeli, and A. Gavriilidis. Gas-liquid and gas-liquid-solid microstructured reactors: contacting principles and applications. *Ind. Eng. Chem. Res.*, 44:9750, 2005.

C. W. Hirt and B. D. Nichols. Volume of Fluid (VOF) method for the dynamics of free boundaries. *J. Comput. Phys.*, 39:201 225, 1981.

D. A. Hoang, V. Van Steijn, Portela L. M., M. T. Kreutzer, and C. R. Kleijn. Benchmark numerical simulations of segmented two-phase flows in microchannels using the Volume of Fluid method. *Comput Fluids*, 86:28 36, 2013.

D. Jacqmin. Calculation of two-phase Navier-Stokes flows using phase-field modeling. *J. Comput. Phys.*, 155:96 127, 1999.

D. Jamet, D. Torres, and J. U. Brackbill. On the theory and computation of surface tension: the elimination of parasitic currents through energy conservation in the second-gradient method. *J. Comput. Phys.*, 182:262 276, 2002.

Z. Jaworski, A. W. Nienow, and K. N. Dyster. An LDA study of the turbulent flow field in a ba ed vessel agitated by an axial, down-pumping hydrofoil impeller. *Can. J. Chem. Eng.*, 74:3 15, 1996.

M. Kang, R. Fedkiw, and X. D. Liu. A boundary condition capturing method for multiphase incompressible flow. *J. Sci. Phys.*, 15:323, 2000.

M. H. Kashid and L. Kiwi-Minsker. Microstructured reactors for multiphase reactions: State of the art. *Ind. Eng. Chem. Res.*, 48:6465 6485, 2009.

S. Kececi, M. Worner, A. Onea, and H. S. Soyhan. Recirculation time and liquid slug mass transfer in co-current upward and downward Taylor flow. *Catalysis Today*, 147S:S125 S131, 2009.

J. Kobayashi, Y. Mori, K. Okamoto, R. Akiyama, M. Ueno, T. Kitamori, and Kobayashi S. A microfluidic device for conducting gas liquid solid hydrogenation reactions. *Science*, 304:1305 1308, 2004.

M. T. Kreutzer, F. Kapteijn, J. A. Moulijn, and J. J. Heizwolf. Multiphase monolith reactors: chemical reaction engineering of segmented flows in microchannels. *Chem. Eng. Sci.*, 60:5895 5916, 2005.

B. Lafaurie, C. Nardone, R. Scardovelli, S. Zaleski, and G. Zanetti. Modelling merging and fragmentation in multiphase flows with SURFER. *J. Comput. Phys.*, 113:134 147, 1994.

D. Legendre. *Quelques aspects des forces hydrodynamiques et des transferts de chaleur sur une bulle sphérique*. PhD thesis, INP Toulouse, 1996.

D. Legendre and M. Maglio. Numerical simulation of spreading drops. *Colloids and Surfaces A: Physicochemical and Engineering Aspects*, 432:29 37, 2013.

A. M. Leshansky and L. M. Pismen. Breakup of drops in a microfluidic T-junction. *Phys Fluids*, 21:023303(6), 2009.

A. M. Leshansky, S. Afkhami, M.-C. Jullien, and P. Tabeling. Obstructed breakup of slender drops in a microfluidic T-junction. *Phys Rev Lett*, 108:364502(5), 2012.

S. S. Y. Leung, Y. Liu, D. F. Fletcher, and B. S. Haynes. Heat transfer in well-characterised Taylor flow. *Chem. Eng. Sci.*, 65:6379 6388, 2010.

S. S. Y. Leung, R. Gupta, D. F. Fletcher, and B. S. Haynes. Gravitational effects on Taylor flow in horizontal microchannels. *Chem Eng Sci*, 69:553 564, 2012.

D. Liu and S. Wang. Hydrodynamics of Taylor flow in noncircular capillaries. *Chem. Eng. Process*, 47:2098 2106, 2008.

H. Liu and Y. Zhang. Droplet formation in microfluidics cross-junctions. *Phys Fluids*, 23:082101, 2011.

J. Lopez and J. Hernandez. Analytical and geometrical tools for 3d volume of fluid methods. *J Comput Phys*, 2008:5939 5948, 2008.

J. Magnaudet, M. Rivero, and J Fabre. Accelerated flows past a rigid sphere or a spherical bubble. Part 1: Steady straining flow. *J Fluid Mech*, 284:97 135, 1995.

C. Min and F. Gibou. A second order accurate level set method on non-graded adaptive cartesian grids. *J. Comput. Phys.*, 225:300 321, 2007.

R. Nelissen, R. Sidin, D. van den Ende, and J. Mellema. Drop behaviour and breakup by capillary waves in large capillaries. *ICMF, Leipzig, Germany*, 2007.

J. K. Nunes, S. S. H. Tsai, J. Wan, and H. A. Stone. Dripping and jetting in microfluidics multiphase flows applied to particle and fibre synthesis. *Chem Eng Sc*, 60, 2013.

W. L. Olbricht. Pore-scale prototypes of multiphase flow in porous media. *Annu. Rev. Fluid. Mech.*, 28:187 213, 1996.

M. Oztaskin, M. Worner, and H. S. Soyhan. Numerical investigation of the stability of bubble train flow in a square microchannel. *Phys Fluids*, 21:042108(17), 2009.

S. Popinet. An accurate adaptive solver for surface-tension-driven interfacial flows. *J Comput Phys*, 228(16):5838 5866, September 2009.

S. Popinet and S. Zaleski. A front tracking algorithm for accurate representation of surface tension. *Int J Numer Meth Fluids*, 24:775 793, 1999.

M. Raessi, M. Bussman, and J. Mostaghimi. A semi-implicit finite volume implementation of the CSF method for treating surface tension in interfacial flows. *Int. J. Numer. Meth. Fluids*, 59:1093 1110, 2009.

Y. Renardy and Renardy. PROST: A Parabolic Reconstruction of Surface Tension for the Volume-of-Fluid Method. *J Comput Phys*, 183:400 421, 2002.

W. J. Rider and D. B. Kothe. Reconstructing volume tracking. *J. Comput. Phys.*, 141: 112 152, 1998.

M. Rudman. Volume-tracking methods for interfacial flow calculations. *Int. J. Numer. Meth. Fluids*, 24:671 691, 1997.

M. Rudman. A volume-tracking method for incompressible multifluid flow with large density variations. *Int. J. Numer. Meth. Fluids*, 28:357 378, 1998.

R. Scadovelli and S. Zaleski. Direct numerical simulation of free-surface flow and interfacial flow. *Annu Rev Fluid Mech*, 31:567 603, 1999.

R. K. Shah and A. L. London. *Laminar ow forced convection in ducts.* Academic Press, 1978.

N. Shao, A. Gavriilidis, and P. Angeli. Flow regimes for adiabatic gas-liquid flow in microchannels. *Chem. Eng. Sci.*, 64:2749 2761, 2009.

S. Shin and D. Juric. Modeling three-dimensional multiphase flow using a level contour reconstrution method for front tracking without connectivity. *J Comput Phys*, 180: 427 470, 2002.

H. A. Stone. On lubrication flows in geometries with zero local curvature. *Chem Eng Sc*, 60, 2005.

M. Sussman and E. G. Puckett. A coupled level set and volume-of-fluid method for computing 3D and axisymmetric incompressible two-phase flows. *J. Comput. Phys.*, 162:301 337, 2000.

M. Sussman, P. Smerecka, and S. Osher. A level set approach for computing solutions to incompressible two-phase flow. *J. Comput. Phys.*, 114:146 159, 1994.

M. Sussman, E. Fatemi, P. Smerecka, and S. Osher. An improved level set method for incompressible two-phase flows. *Comp. Fluids*, 27:663 680, 1997.

T. Taha and Z.F. Cui. CFD modelling of slug flow inside square capillaries. *Chem. Eng. Sci.*, 61:665 675, 2006.

S. Tanguy. *Développement d une méthode de suivi d interface: application aux écoulements diphasiques*. PhD thesis, Faculté des Sciences de l université de Rouen, 2004.

S. Tanguy and A. Berlemont. Application of a Level Set for simulation of droplet collisions. *Int. J. Multiph. Flow*, 31:1015 1035, 2005.

G. I. Taylor. Deposition of a viscous fluid on the wall of a tube. *J Fluid Mech*, 10: 161 165, 1961.

T. C. Thulasidas, M. A. Abraham, and R. L. Cerro. Flow patterns in liquid slugs during bubble-train flow inside capillaries. *Chem. Eng. Sci.*, 52:2947 2962, 1997.

D. J. Torres and J. Brackbill. The Point-Set method : front-tracking without connectivity. *J Comput Phys*, 165:620 644, 2000.

K. A. Triplett, S. M. Ghiaasiaan, S. I. Abdel-Khalik, and D. L. Sadowsli. Gas-liquid two-phase flow in microchannels. Part 1: two-phase flow patterns. *Int J Multiph Flow*, 25:377 394, 1999.

S. O. Unverdi and G. Tryggvason. A front-tracking method for viscous, incompressible multi-fluid flows. *J. Comput. Phys.*, 100:25 37, 1992.

S. Van der Graaf, T. Nisisako, C. G. P. H. Schroen, R. G. M. Van der Sman, and R. M. Boom. Lattice Boltzmann simulations of droplet formation in a T shaped microchannel. *Langmuir*, 22:4144 4152, 2006.

V. Van Steijn, M. T. Kreutzer, and C. R. Kleijn. μ-PIV study of the formation of segmented flow in microfluidic T-junction. *Chem Eng Sci*, 62:7505 7514, 2007.

V. Van Steijn, C. R. Kleijn, and M. T. Kreutzer. Predictive model for the size of bubbles and droplets created in microfluidics T-junctions. *Lab Chip*, 10:2513 2518, 2010.

N. Volkel. *Design and characterization of gas-liquid microreactors*. PhD thesis, INP Toulouse, 2009.

S. Waelchli and P. R. Von Rohr. Two-phase flow characteristics in gas-liquid microreactors. *Int J Multiph Flow*, 32:791 806, 2006.

H. Wong, S. Morris, and C. J. Radke. Three dimensional menisci in polygonal capillaries. *J Colloid Interface Sci*, 148:317 336, 1992.

H. Wong, C. J. Radke, and S. Morris. The motion of long bubbles in polygonal capillaries. Part 1. Thin films. *J Fluid Mech*, 292:71 94, 1995a.

H. Wong, C. J. Radke, and S. Morris. The motion of long bubbles in polygonal capillaries. Part 2. Drag, fluid pressure and fluid flow. *J Fluid Mech*, 292:95 110, 1995b.

J. Yue, G.W. Chen, Q. Yuan, L.G. Luo, and Y. Gonthier. Hydrodynamics and mass transfer characteristics in gas liquid flow through a rectangular microchannel. *Chem. Eng. Sci.*, 62:2096 2108, 2007.

S. T. Zalesak. Fully multidimensional flux-corrected transport algorithms for fluids. *J Comput Phys*, 31:335 362, 1979.

P. Zaloha, J. Kristal, V. Jiricny, N. Volkel, C. Xuereb, and J. Aubin. Characteristics of liquid slugs in gas-liquid Taylor flow in microchannels. *Chem Eng Sci*, 68:640 649, 2012.

T. Zhang, B. Cao, Y. Fan, Y. Gonthier, L. Luo, and S. Wang. Gas-liquid flow in circular microchannel. Part 1: Influence of liquid physical properties and channel diameter on flow patterns. *Chem Eng Sci*, 66:5791 5803, 2011.

C.-X. Zhao and A. P. J. Middleberg. Two-phase microfluidics flows. *Chem Eng Sci*, 66:1394 1411, 2011.

Appendix A

Single phase flow in rectangular ducts

A.1 Velocity profile

The velocity profile in a single-phase flow in a rectangular duct of width w and height h is written (Shah and London [1978]):

$$u(x,y) = -\frac{16c_1w^2}{\pi^3}\sum_{n=1,3,\ldots}^{\infty}\frac{-1^{\frac{(n-1)}{2}}}{n^3}\left[1-\frac{cosh\left(\frac{n\pi h}{2w}\right)}{cosh\left(\frac{n\pi h}{2w}\right)}\right]cos\left(\frac{n\pi x}{2w}\right) \tag{A.1}$$

$$u_m = -\frac{c_1w^2}{3}\left[1-\frac{192}{\pi^5}\frac{w}{h}\sum_{n=1,3,\ldots}^{\infty}\frac{1}{n^5}tanh\left(\frac{n\pi h}{2w}\right)\right] \tag{A.2}$$

A.2 Pressure drop

The pressure drop in a channel can be written as a function of a friction factor λ:

$$\frac{\Delta p}{L} = \frac{\lambda\rho u_m^2}{2D_h}\ . \tag{A.3}$$

The friction factor may be approximated by the following equation (Shah and London [1978]):

$$\lambda = \frac{96}{Re}\left(1-1.3553\alpha^{-1}+1.9467\alpha^{-2}-1.7012\alpha^{-3}+0.9564\alpha^{-4}-0.2537\alpha^{-5}\right)\ , \tag{A.4}$$

with $\alpha = w/h$, the aspect ratio of the channel.

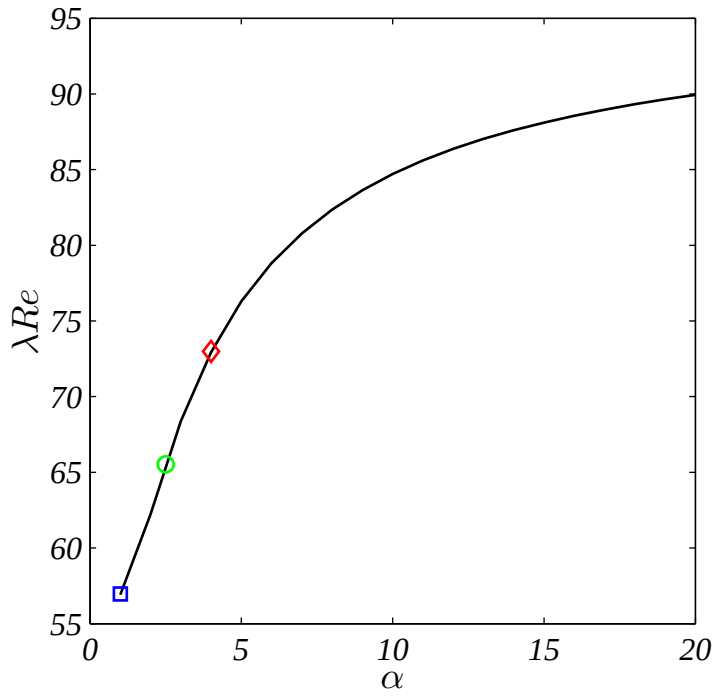

Figure A.1: Friction factor λRe as a function of the aspect ratio α.
Legend: (solid line) equation A.4 ; (□) $\alpha = 1$; (○) $\alpha = 2.5$; (◇) $\alpha = 4$.

Appendix B

Computational time - Parallel scaling

The parallel scaling analysis for the 3D simulations of Taylor flow has been performed for the cases presented in chapter 6.6 ($Ca = 0.1$ and $La = 280$). The numerical setup is described in section 6.2 and two meshes have been used: $32 \times 32 \times 256$ and $64 \times 64 \times 512$. The computations have been performed on the Hyperion (Altix Ice 8200) computational system at CALMIP and the time required for 10 iterations with both meshes and with both the VOF-FCT and LS methods presented in this thesis are reported in figure B.1.

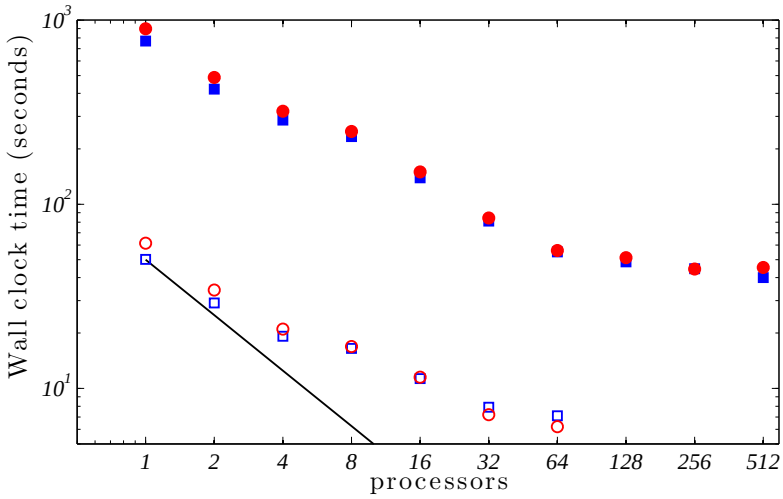

Figure B.1: Parallel scaling for 2 meshes with both VOF-FCT and LS interface capturing techniques.
Legend: (blue squares) VOF-FCT ; (red circles) LS ; (open symbols) mesh $32 \times 32 \times 256$; (filled symbols) mesh $64 \times 64 \times 512$; (straight line) 1/(n processors).

With the first mesh ($32 \times 32 \times 256$), a good scaling is obtained with both VOF-FCT and LS methods up to 16 processors, which corresponds to subdomains of size $32 \times 32 \times 16$ for which the communication time between processors becomes non-negligible when compared to the total computational time. Above 16 processors, the gain in the computational time is not very significant. It is seen with the second mesh that a good scaling is obtained up to 64 processors, which corresponds to approximately the same subdomain decomposition.

In addition, it is interesting to note that the same speed-up is obtained with both VOF-FCT and LS methods. The computational times of LS simulations are slightly longer than those required in VOF-FCT simulations (between 5% and 15%) and tend towards the same value as the number of processors increases.

Finally, most of the simulations have been run on 8 processors with the mesh $32 \times 32 \times 256$. The computational time for 10 iterations is about 15 seconds and depending on the Reynolds and capillary numbers, between 100000 iterations (for relatively large Ca and Re) and 2000000 iterations (for low Ca and Re) were required, which means computational times between 2 days and approximately one month.

With the second mesh $64 \times 64 \times 512$, the number of processors can be increased to 64 with a good speed-up but the computational time can exceed one month since the time step is reduced, thereby leading to an increase in the number of iterations required until reaching a fully-developed flow.

Appendix C

Microfluidics and Nanofluidics (Abadie et al. [2012])

Microfluid Nanofluid (2012) 12:355–369
DOI 10.1007/s10404-011-0880-8

RESEARCH PAPER

Hydrodynamics of gas–liquid Taylor flow in rectangular microchannels

Thomas Abadie · Joëlle Aubin · Dominique Legendre · Catherine Xuereb

Received: 11 June 2011 / Accepted: 30 August 2011 / Published online: 22 September 2011

Abstract The effect of fluid properties and operating conditions on the generation of gas–liquid Taylor flow in microchannels has been investigated experimentally and numerically. Visualisation experiments and 2D numerical simulations have been performed to study bubble and slug lengths, liquid film hold-up and bubble velocities. The results show that the bubble and slug lengths increase as a function of the gas and liquid flow rate ratios. The bubble and slug lengths follow the model developed by Garstecki et al. (Lab chip 6:437–446, 2006) and van Steijn et al. (Chem Eng Sci 62:7505–7514, 2007), however, the model coefficients appear to be dependent on the liquid properties and flow conditions in some cases. The ratio of the bubble velocity to superficial two-phase velocity is close to unity, which confirms a thin liquid film under the assumption of a stagnant liquid film. Numerical simulations confirm the hypothesis of a stagnant liquid film and provide information on the thickness of the liquid film.

Keywords Microchannel · Gas–liquid Taylor flow · Microreactor · Visualisation experiments · Numerical simulation

T. Abadie · D. Legendre
Institut de Mécanique des Fluides CNRS/INPT/UPS, University of Toulouse, Allée du Prof. Camille Soula, 31400 Toulouse, France

T. Abadie · J. Aubin (✉) · C. Xuereb
Laboratoire de Génie Chimique CNRS/INPT/UPS, University of Toulouse, 4 Allée Emile Monso, BP 84-234, 31030 Toulouse, France
e-mail: joelle.aubincano@ensiacet.fr

List of symbols

A	Cross-section area (m^2)
C	Color function (VOF) (−)
d	Diameter (m)
f	Break-up frequency (s^{-1})
$\mathbf{F}_\sigma$	Capillary force (Pa/m)
k	Constant (−)
$l_{1,\infty}$	norms in the spurious currents evaluation (m/s)
L	Length (m)
m	Constant (−)
$\mathbf{n}$	Normal to the interface (−)
P	Pressure (Pa)
Q	Flow rate (m^3/s)
r	Radius (m)
U	Velocity (m/s)
W	Dimensionless velocity (−)
w	Width (m)
x, y	Axis in 2D simulations (−)

Greek letters

α	Volume fraction (−)
$\beta_{1,2}$	Constant (−)
δ	Liquid film thickness (m)
δ_I	Dirac distribution (interface) (−)
ε	Fraction of area (−)
$\lambda_{1,2}$	Constant (−)
μ	Dynamic viscosity (Pa . s)
ρ	Density (kg/m^3)
σ	Surface tension (N/m)
$\mathbf{\Sigma}$	Viscous stress tensor (Pa)

Subscripts

B	Bubble
ch	Channel
G	Gas phase (air)

h Hydraulic
in Gas inlet
L Liquid phase
S Slug
SC Spurious currents
TP Two-phase

Dimensionless numbers

Bo_{TP} Bond number $Bo = \frac{(\rho_L - \rho_G) d_h^2 g}{\sigma}$
Ca_{TP} Capillary number $Ca = \frac{\mu_L U_{TP}}{\sigma}$
Re_{TP} Reynolds number $Re = \frac{\rho_L U_{TP} d_h}{\mu_L}$
We_{TP} Weber number $We = \frac{\rho_L U_{TP}^2 d_h}{\sigma}$

1 Introduction

The interest of the process industries in microreaction technology for process intensification has become increasingly important over the recent years. Amongst the different applications, microreactors are particularly interesting for fast highly exothermic and/or mass transfer limited gas–liquid reactions since heat and mass transfer are remarkably intensified. Although miniaturized devices are already implemented in industry, the engineering methodologies for the design and integration of microreactors in existing processes are still not clearly defined. The development of such methodologies requires fundamental understanding of the physical phenomena that control the process operation and the specificities of equipment design.

To date, research on gas–liquid flow in microchannels has mainly been dedicated to the study of flow patterns in a range of microchannel geometries and the development of flow pattern maps based on superficial gas and liquid velocities (e.g. Triplett et al. 1999; Waelchli et al. 2006; Yue et al. 2007, 2008) or superficial Weber numbers (Akbar et al. 2003). Slug or Taylor flow is the flow configuration that occurs for a large range of flow conditions, from low to average superficial gas and liquid velocities. Taylor flow is characterized by regular sized bubbles that are longer than the microchannel width or diameter and separated by slugs of liquid. The bubbles fill almost all the entire cross-section of the channel and are separated from the wall by a thin liquid layer. Taylor flow in microreactors is an interesting flow regime because it intensifies both mass and heat transfer due to the fluid recirculation generated in the liquid slug (Gupta et al. 2010; Leung et al. 2010; Sobieszuk et al. 2008; Yue et al. 2007, 2008). However, controlling the flow regime and the characteristic size of the gas–liquid dispersion remains a difficult task. These characteristics depend not only on the physical properties of the fluids but also on the operating conditions, the microchannel geometry and material of fabrication.

T-junction geometries are relatively popular for the production of bubbles in microchannels (Garstecki et al. 2006; van Steijn et al. 2007; Yue et al. 2008; Yun et al. 2010) and the correlation of bubble sizes as a function of the superficial gas and liquid flow rates generated in these geometries has been the subject of several works (Garstecki et al. 2006; van Steijn et al. 2007; Yue et al. 2008; Yun et al. 2010). Few studies, however, have dealt with the effects of fluid properties, such as viscosity and surface tension, on bubble generation (Garstecki et al. 2006; Qian and Lawal 2006; Pohorecki and Kula 2008). Under the flow conditions in these studies, bubble size has been shown to be slightly dependent or not at all on viscosity and surface tension.

The liquid film hold-up around Taylor bubbles is also of main importance for heat and mass transfer in microchannels. The knowledge of the amount of liquid surrounding bubbles in small tubes has been studied for a long time (Aussillous and Quéré 2000; Bretherton 1961; Giavedoni and Saita 1997; Han and Shikazono 2009a), since the first experiments in 1961 by Taylor in circular capillaries, and more recently in microchannels of different cross sections (Han and Shikazono 2009b; Kreutzer et al. 2005a, b; Wong et al. 1995; Yun et al. 2010) where correlations of liquid film thickness as a function of various dimensionless numbers have been developed. Nevertheless, the exact relationships between the microsystem parameters (e.g. geometry and fluid properties) and the characteristics of the gas–liquid flow (e.g. bubble velocity, bubble and slug lengths, and liquid film thickness) are still not clear.

The present work aims at improving the fundamental understanding of gas–liquid Taylor flow in microchannels, which will contribute to the design and development of microreactors for the chemical process industries. In particular, the objective of this study is to investigate the effects of the physical properties of the fluids and the flow rates on the characteristics of the Taylor dispersion generated in a T-junction microchannel. Visualisation experiments and direct numerical simulations have been performed to obtain information on the bubble generation mechanism, bubble velocity, bubble and slug lengths, as well as the liquid film surrounding the bubble body.

2 Experimental setup

2.1 Microchannel characteristics

Rectangular cross-section microchannels have been etched through a silicon wafer plate using the deep reactive ionic etching (DRIE) technique, sandwiched between glass wafers and bonded using anodic bonding. The gas and liquid are contacted using a side-entering T-junction as shown in Fig. 1 and the main channel has a meandering

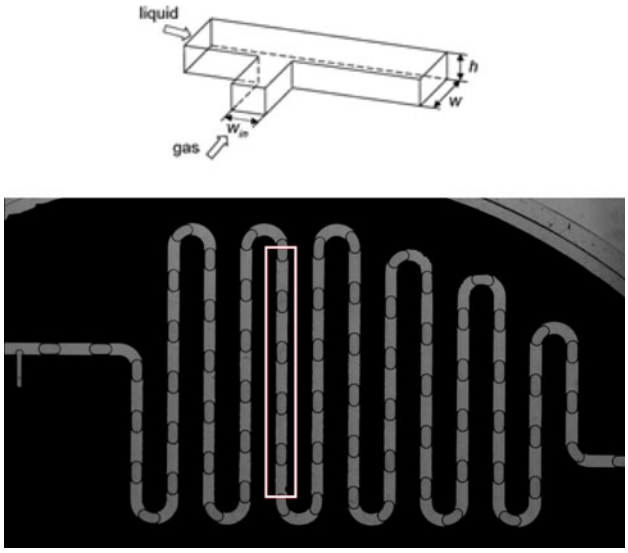

Fig. 1 Side entering T-junction, Meandering microchannel with curved bends, $w_{L,in} = 1$ mm $= w$, $w_{G,in} = 525$ µm, $h = 400$ µm, $d_{h\,=\,571\ \mu m}$, 1–30 cm

topology with curved bends for reasons of compactness. The liquid is flowing in the main channel while the gas is supplied perpendicularly via a narrower channel. The width of the main channel and the gas inlet are $w = 1$ mm and $w_{g,in} = 525$ µm, respectively. The ratio of the widths of the gas and liquid inlets corresponds to the lower limit recommended by Garstecki et al. (2006) for generating Taylor flow via the squeezing mechanism. The depth of the microchannel is fixed by the thickness of the silicon wafer, $h = 400$ µm and the total length is approximately 1–3 cm. These dimensions lead to a hydraulic diameter $d_h = 571$ µm and an aspect ratio $w/h = 2.5$.

2.2 Flow control equipment

Several liquids have been tested to cover a wide range of dimensionless numbers with the feeding equipment available and air has been used as the gas phase for all of the experiments. Air is supplied from a pressurized vessel and controlled by a mass-flow controller (HORIBA SEC 7320), which allows a volumetric flow rate ranging from 0.00 to 1.00 mL/min with a precision of 0.02 mL/min. Liquid flow is controlled using a syringe pump, which allows flow rates in the range of 0.000–1.000 mL/min with a precision of 0.002 mL/min. All experiments were conducted under room temperature and pressure. The temperature of the gas and liquid phases was monitored by thermocouples that are inserted in to the feeding tubes just before the microchannel inlets. The fluid properties are evaluated according to the temperatures measured in each experiment.

2.3 Measurement method

High speed imaging has been used to obtain characteristic information on the gas–liquid Taylor flow. Images have been recorded with a high-speed camera (CCD HCC-1000, VDS Vossmuller GmbH) with frame rates up to 462 fps at full resolution (1024 pix × 1024 pix) and a shutter time short enough to obtain a distinct gas–liquid interface (about 1 ms in our experiments). A backlight was employed to provide enough light throughout the exposure period. A significant number of image sequences were recorded to get a representative sample of bubbles passing through the observation window and to identify unsteady flow situations, which were characterized by irregular bubble lengths.

For the measurement of bubble and slug lengths and bubble velocities, images have been taken in a straight section between two bends and approximately halfway along the length of the channel defined by the rectangular zone shown in Fig. 1. As shown in Fig. 2, the bubble length is evaluated between the extremities of a bubble while the slug length is calculated as the average of the slugs immediately before and after the bubble. From the simulations, the liquid film thickness between the bubble and the walls is characterized by the averaged value along the bulk of the bubble δ, i.e. not including the bubble nose and rear end.

Mean bubble and slug lengths were determined using between 20 and 100 bubbles depending on the flow. Average bubble velocities were evaluated by following the gas–liquid interface at the bubble tip between the entrance and the exit of the observation window, averaging the data of 20–100 bubbles.

2.4 Fluid properties and operating conditions

Reference experiments were carried out using an ethanol-air system, which allows a regular and relatively easy bubble formation in the silicon-glass microchannel (Völkel 2009). The effects of surface tension on bubble generation and hydrodynamics have been studied using water and an ethanol/water solution. Sugarcane syrup solutions (SCS)

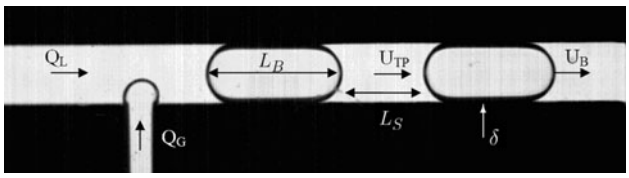

Fig. 2 Contacting section: bubble formation. The notations used are: $Q_{G,L}$ for gas and liquid flow rates, $L_{B,S}$ for bubble and slug lengths, δ the liquid film thickness, U_B the bubble velocity and U_{TP} the superficial two-phase velocity ($U_{TP} = U_L + U_G$)

Table 1 Fluid properties (at room temperature $T = 22$–$23°$ C)

Fluid	ρ_L (kg/m^3)	μ_L(Pa · s)	σ (N/m)
Air	1.204	1.815×10^{-5}	–
Water	998	1.34×10^{-3}	0.068
Ethanol	795	1.15×10^{-3}	0.022
Diluted ethanol (33%)	930	2.4×10^{-3}	0.037
Sugarcane syrup	1,318	1.4×10^{-1}	0.085
Diluted sugarcane syrup (50%)	1,163	4.6×10^{-3}	0.076

have been tested to change the viscosity of the carrier fluid. The properties of the fluids used have been measured and are reported in Table 1. The percentages indicated for ethanol/water and sugarcane syrup/water solutions are volume ratios.

Table 2 summarises the ranges of velocities and dimensionless numbers explored in the experiments. The two-phase dimensionless numbers are based on the physical properties of the liquid and the two-phase velocity, which is the sum of gas and liquid superficial velocities. The superficial velocity is defined as the ratio of the phase flow rate to the channel cross-sectional area, i.e. $U_{L,G} = Q_{L,G}/A_{ch}$.

In terms of dimensionless numbers, the values of the capillary number (ratio of the viscous effects to capillary effects) and the Weber number (ratio of the inertial effects to capillary effects) used in this study indicate that the dominant force in these flows is the capillary force. The Reynolds numbers show that for ethanol, water, ethanol/water and diluted sugarcane syrup, the inertial term dominates the viscous term, howerver this trend is inverted when sugarcane syrup is used. Finally, the Bond number (ratio of the gravitational effects to capillary effects) is less than unity ($Bo_{max} = 0.11$) for all cases and, therefore, the surface tension dominates the gravitational effects. Under these dimensionless flow conditions, and despite the low velocities used, Taylor flow is, therefore, expected since Akbar et al.'s (2003) universal criterion $We_{LS} \leqslant 3$ and $We_{GS} \leqslant 0.11 We_{LS}^{0.315}$ is respected.

3 Numerical simulations

3.1 Governing equations and numerical schemes

The numerical code used for this study is the JADIM code (Dupont and Legendre 2010), which has been developed to simulate dispersed two-phase flows. The interface capturing technique implemented in this code is the volume of fluid method (VOF), which consists of a Eulerian description of each phase on a fixed grid. Under the assumptions that (1) the fluids are Newtonian and incompressible, (2) there is no mass transfer at the interface, (3) the flow is isothermal and (4) the surface tension is constant, the fluid flow can be described by the classical one fluid formulation of the Navier–Stokes equations:

$$\nabla \cdot \mathbf{U} = 0 \tag{1}$$

$$\rho\left(\frac{\partial \mathbf{U}}{\partial t} + (\mathbf{U}\cdot\nabla)\mathbf{U}\right) = -\nabla P + \nabla\cdot\mathbf{\Sigma} + \rho\mathbf{g} + \mathbf{F}_{\sigma,\mathbf{s}} \tag{2}$$

where $\mathbf{\Sigma}$ is the viscous stress tensor ($\mathbf{\Sigma} = \mu(\nabla\mathbf{U} + \nabla\mathbf{U}^T)$), $\mathbf{g}$ is the acceleration due to gravity, $\mathbf{F}_{\sigma,\mathbf{s}} = -\sigma(\nabla\cdot\mathbf{n})\mathbf{n}\delta_I$ is the capillary contribution whose calculation is described below, σ is the surface tension, $\mathbf{n}$ the normal to the interface, δ_I is the Dirac distribution localizing the interface, and ρ and μ are the local density and dynamic viscosity, respectively. The density and viscosity are deduced from the volume fraction of one phase (or colour function) C by a linear interpolation:

$$\rho = C\rho_1 + (1-C)\rho_2 \tag{3}$$

$$\mu = C\mu_1 + (1-C)\mu_2 \tag{4}$$

where the volume fraction is $C = 1$ in cells filled with fluid 1, $C = 0$ in cells filled with fluid 2 and $0 < C < 1$ in cells that are cut by the interface. Additionally, the transport equation of the colour function is solved to capture the interface between the phases:

$$\frac{\partial C}{\partial t} + \mathbf{U}\cdot\nabla C = 0 \tag{5}$$

In many VOF methods employed to capture the interface, a reconstruction technique step is used to control the thickness

Table 2 Velocities and dimensionless numbers of the fluids used in the experiments

Fluids	Q_L (mL/min)	Q_G (mL/min)	U_L (10^{-2} m/s)	U_G (10^{-2} m/s)	Re_{TP}	Ca_{TP} 10^{-3}	We_{TP} 10^{-2}	Bo
Air–ethanol	0.2–1	0.04–1	0.83–4.2	0.17–4.2	4–32.9	0.52–4.35	0.21–14	0.115
Air–ethanol (33%)	0.3–1	0.06–1	0.83–4.2	0.17–4.2	3.3–18.5	0.97– 5.4	0.32–10	0.080
Air–water	0.2–1	0.04–1	0.83–4.2	0.17–4.2	10.6–35.5	0.49–1.64	0.52–5.8	0.047
Air-sugarcane syrup	0.002– 0.2	0.05–1	0.0083–0.83	0.213–4.2	0.03–0.07	10–21	0.035–0.14	0.050
Air-sugarcane syrup (50%)	1	0.2–1	4.2	0.83–4.2	7.2–12	3.03–5.04	2.2–6	0.049

of the interface. In JADIM, the interface location and thickness are both controlled by an accurate algorithm based on Flux-Corrected Transport schemes (Bonometti and Magnaudet 2007).

The equations are discretized on a staggered grid using a finite volume method and all spatial derivatives are approximated using second-order centered schemes. The time scheme used to compute the advective terms in the Navier–Stokes equations is a third-order Runge–Kutta type scheme, while the viscous stresses are solved using a semi-implicit Crank–Nicolson method. The incompressibility is ensured using a projection method, which consists in splitting the velocity field into two contributions: a rotational one, which gives a predicted velocity field calculated semi-implicitely, and a potential one, which is obtained from a pressure correction solution of a pseudo-Poisson equation whose divergence is null.

3.2 Capillarity contribution

3.2.1 Continuum surface force method

The capillary contribution $\mathbf{F}_{\sigma,\mathbf{s}}$ is of main importance in flows controlled by capillarity as is the case in microchannels. The numerical method used to solve the interfacial force is the continuum surface force (CSF) proposed by Brackbill et al. (1992). The localization of the interface is available through a non-zero gradient of volume fraction and the curvature is calculated from the volume fraction gradient. Thus, the surface force $\mathbf{F}_{\sigma,\mathbf{s}}$ is transformed into a volume force $\mathbf{F}_{\sigma,\mathbf{v}}$ by distributing its effects over grid points in the vicinity of the interface in a region of thickness of few cells where $\nabla C \neq 0$:

$$\mathbf{F}_{\sigma,\mathbf{v}} = -\sigma \underbrace{\nabla \cdot \left(\frac{\nabla C}{\|\nabla C\|}\right)}_{\text{curvature}} \underbrace{\nabla C}_{\text{localization/orientation}} \tag{6}$$

The discretization of the capillary force (Eq. 6) is well known to produce artificial vorticity in the vicinity of the interface and unphysical streams called 'spurious currents'. Following the method of Brackbill et al. (1992), a smoothing step on C is introduced to decrease the variations in the curvature and reduce spurious currents.

3.2.2 Characterization of spurious currents

The objective of this section is to characterize the spurious currents for microchannel geometries. The spurious velocities generated by the calculation of the capillary term are measured using two norms as introduced by Renardy and Renardy (2002) and Francois et al. (2006) corresponding to the maximum spurious velocity (l_∞) and the averaged spurious velocities in the domain (l_1), respectively:

$$l_\infty = \max_{i,j,k}\left(\|\mathbf{U}_{\mathbf{i},\mathbf{j},\mathbf{k}}\|\right) \tag{7}$$

$$l_1 = \frac{1}{N_x N_y N_z}\sum_{i,j,k}\|\mathbf{U}_{\mathbf{i},\mathbf{j},\mathbf{k}}\| \tag{8}$$

To characterize the intensity of these spurious currents, a simple configuration has first been analysed (Francois et al. 2006; Dupont and Legendre 2010). A circular drop of radius $R_0 = 1$ mm is placed at equilibrium at the center of a gas domain $l_x \times l_y = 4 \times 4$ mm^2. The computational domain is divided regularly in the x- and y-directions into 96 meshes which corresponds to a uniform spacing in both directions of $\Delta x = \Delta y = l_x/96 \sim 0.042$ mm. The condition imposed at the boundaries is zero velocity and the initial condition on the velocity field is zero. The fluid properties for this test are $\rho_L = 10^3$ kg/m^3, $\rho_G = 1$ kg/m^3 for the liquid and gas densities, $\mu_L = 10^{-2}$ Pa · s, $\mu_G = 10^{-5}$ Pa · s for the liquid and gas viscosities and $\sigma = 0.072$ N/m for the surface tension.

Secondary tests have been performed for the geometry, fluid properties and boundary conditions corresponding to the microchannel flows considered in this study. Half of a 2D Taylor bubble $l_{B,x} = 0.72$ mm and $l_{B,y} = 0.16$ mm is placed at equilibrium at the center of the domain $l_x \times l_y = 2 \times 0.2$ mm. A regular mesh is used in both directions $n_x \times n_y = 250 \times 50$ that leads to a grid spacing $\Delta x = 8$ μm and $\Delta y = 4$ μm. The conditions imposed at the boundaries are zero velocity on the north face, symmetry on the south face and periodicity on east and west faces. The fluid properties for this test are $\rho_L = 10^3$ kg/m^3, $\rho_G = 1.204$ kg/m^3 for the liquid and gas densities, $\mu_L = 10^{-1}$Pa · s, $\mu_G = 1.815 \times 10^{-5}$Pa · s for the liquid and gas viscosities and $\sigma = 0.07$ N/m for the surface tension.

Table 3 reports the stable spurious velocities obtained after a significant number of iterations for the different test cases. The spurious velocities, based on the norm l_∞, have been found to be proportional to:

$$u_{SC} \sim 0.01\frac{\sigma}{\mu_L} \quad \text{i.e. } Ca_{SC} \sim 0.01. \tag{9}$$

This magnitude is comparable to the simulations reported by Lafaurie et al. (1994) ($\sim 0.01\ \sigma/\mu_L$) and Dupont and Legendre (2010) ($\sim 0.005\ \sigma/\mu_L$). The spurious velocities thus appear at capillary numbers $Ca_{SC} \sim 0.01$ indicating that error-free numerical simulations can only be performed for $Ca > Ca_{SC}$.

3.3 Mesh and boundary conditions

Two-dimensional numerical simulations that simulate flow in an infinitely wide channel were performed in a plane 200 μm high to simulate half the height of the microchannel. Every 2D simulation is performed using the same

Table 3 Spurious velocities evaluated from a confined bubble at rest

Test case	l_∞ (m/s)	l_1 (m/s)	σ/μ_L (m/s)	Δt ($\times 10^{-6}$ s)	Iterations
2D circular bubble ($R_0 = l_x/4$)	0.0409	0.000239	7.2	1	20,000
2D long bubble 1 ($l_{B,x}/l_{B,y} = 4.5$)	0.00542	0.000123	0.7	0.25	200,000
2D long bubble 1	0.00702	0.000162	1.4	0.20	250,000
2D long bubble 1	0.00353	0.0000983	0.35	0.25	200,000
2D long bubble 2 ($l_{B,x}/l_{B,y} = 12$)	0.00459	0.000969	0.7	0.25	200,000

boundary conditions and the same fluid properties that were used to characterize the spurious currents. A pressure gradient is imposed between the two periodic boundaries to generate fluid flow. Two domains of simulation have been used: a short one (Domain 1: $l_x = 2$ mm) that allows bubble lengths about 1 mm to be simulated and a longer one (Domain 2: $l_x = 5$ mm) for the simulation of bubbles that are a few millimeters long. For each domain, simulations have been performed by varying the volume fraction of air at the initialization stage and by varying the pressure gradient across the domain.

Domain 1 is the computational domain described in the spurious currents characterization section and comprises 12,500 nodes. Since there were only about five grid cells in the liquid film, which is the lower limit for the correct simulation of the film (Gupta et al. 2009), the convergence has been tested with a second, finer mesh. This second grid is coarser in the bubble region and finer in the liquid film area compared with the first mesh, however, the total number of nodes (12,500) remained unchanged. This refined mesh consists in a uniform grid spacing along the channel ($n_x = 250, \Delta x = 8$ μm) and a non-uniform grid spacing across the width of the channel: $n_y = 50$ with a regular spacing for $y < 115$ μm (16 nodes) and irregular mesh with a factor 0.92 for 115 μm $< y$ (34 nodes). Thus, the grid spacing across the channel width varies between $\Delta y_{max} = 7.20$ μm and $\Delta y_{min} = 0.46$ μm. The simulations with both grids converged to the same velocity field, however, the number of iterations needed to converge is almost 20 times greater for the non-uniform mesh than for the regular mesh. The regular mesh is, therefore, considered adequate for the simulation of these flows and allows a much larger time step than the non-uniform mesh does. Domain 2 is meshed in the same way as domain 1, such that there are at least 5 grid cells in the liquid film and a regular mesh is used in both directions $n_x \times n_y = 500 \times 40$ (i.e. 20,000 nodes), which leads to a grid spacing $\Delta x = 10$ μm and $\Delta y = 5$ μm.

4 Results and discussion

Figure 3a summarises the numerical and physical experiments performed in this study to characterize the bubble lengths, shapes and velocities of gas–liquid Taylor flow in rectangular microchannels as a function of the Reynolds and capillary numbers. The numerical simulations were carried out with fluid properties such that the spurious velocities were lower than the physical velocities of the flow.

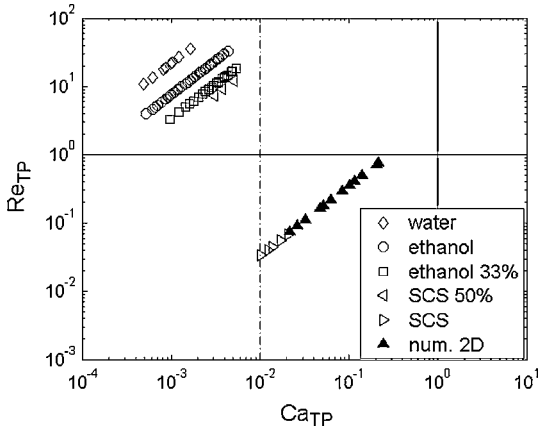

Fig. 3 Reynolds and capillary numbers of the experiments and numerical simulations performed. *Dash dot dash line* minimum capillary number available numerically to neglect spurious currents

4.1 Bubble generation

Figure 4 shows the bubble generation mechanism for the ethanol-air system. This mechanism can be divided into several steps: (a to b) the bubble starts growing in the side channel, perpendicularly to the direction of the liquid flow in the main channel; (b to d) as the bubble grows, the gas–liquid interface is distorted by the liquid in main channel and the radius of curvature upstream of the leading bubble cap increases; (d) during this time, the interface detaches from the upstream wall of the gas inlet and the contact line starts moving into the gas inlet; (d to e) the air fills the main channel and the bubble occupies the width of the main channel; (e to f) the gas–liquid interface coming from the gas inlet is pushed downstream until pinching off occurs and the bubble is formed.

In the majority of ethanol-air experiments, bubbles are pinched off at the T-junction and regular bubble trains are observed, as shown in Fig. 4. For these experiments, the

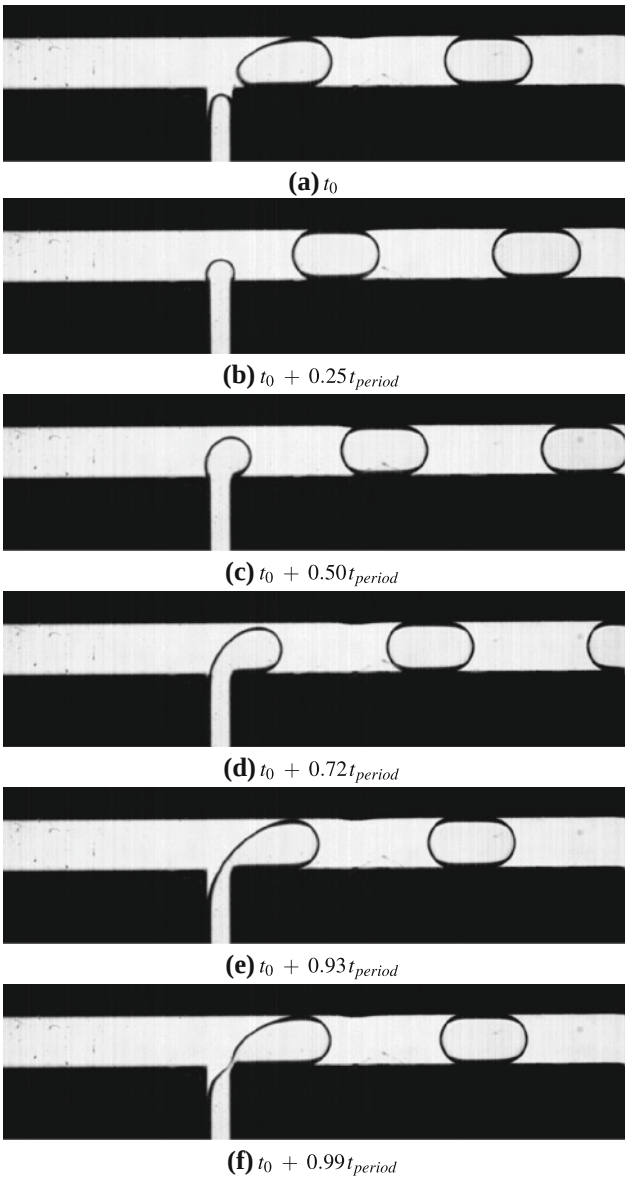

Fig. 4 Bubble generation in air–ethanol flows. $U_L = 0.021$ m/s and $U_G = 0.0105$ m/s, evolution of Taylor flow during a period where bubbles are generated every $t_{period} = 0.125$ s, i.e. with a frequency of formation about 8 Hz

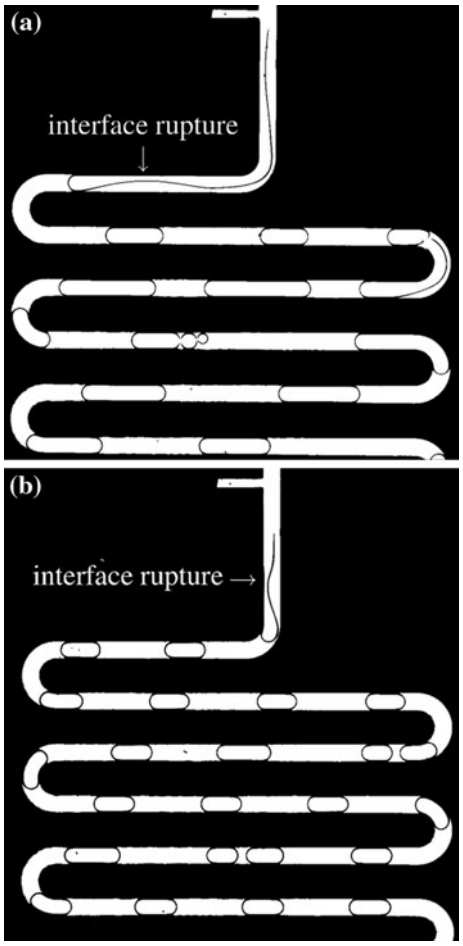

Fig. 5 Bubble generation and interface rupture in the main channel with **a** air–water system $U_L = 0.021$ m/s and $U_G = 0.0105$ m/s, bubble pinch-off occurs at the gas inlet every $t_{period} = 1.16$ s, i.e. with a frequency about 0.86 Hz; **b** air-sugarcane syrup system, $U_L = 0.042$ m/s and $U_G = 0.021$ m/s bubble pinch-off occurs at the gas inlet every $t_{period} = 0.97$ s, i.e. with a frequency about 1 Hz

standard deviation of the average bubble size is less than 5 %. In general, the fluctuations in the bubble velocities are only about 1–2% of the average value. Fig. 5 shows the generation of air bubbles in water and sugarcane syrup. For both the air–water and air-sugarcane syrup systems, an iterative break-up mechanism is observed. For the most part, the bubble generation occurs in the main channel, well after the T-junction. However, after the generation of several bubbles in the main channel far from the T-junction, a bubble is then pinched off at the T-junction before bubble break-up occurs in the main channel again. It is interesting to point out that for air-sugarcane syrup, this break-up mechanism results in a rather periodic structure, which is not so obvious with the air–water system. Nevertheless, for both the water and sugarcane syrup systems, these flows result in irregular bubble lengths with a standard deviation greater than 10% of the average length. Once the bubble train is established, the bubble velocities are constant. Similar irregular flows were also found to occur with ethanol/water solutions at low liquid flow rates.

We distinguish these two processes of bubble generation by naming the regular bubble flow as the squeezing regime (Garstecki et al. 2006) and the irregular bubble flow (with bubble generation in the main channel) as the leakage regime. The leakage regime described here looks similar to the parallel liquid–liquid flow that breaks in the microchannel to form droplets as observed by Guillot and Colin (2005). However, the flow conditions required for the transition between the squeezing regime and unstable parallel flow pinching in the channel remain unclear.

According to Akbar et al.'s (2003) criteria, bubble or slug flow is expected for all of the flow conditions studied here. However, the unstable leakage regime is observed for both viscous liquids (i.e. sugarcane syrup solutions), as well as low viscosity liquids (i.e. water). It is, therefore, thought that the wettability of the microchannel material by the liquids also plays an important role in the bubble generation process.

In addition, for equal gas and liquid flow rates, a decrease in the frequency of bubble formation was observed with air-diluted ethanol system when compared with the pure ethanol system. However, in both cases the bubble nose and rear are the same shape, which is in agreement with the corresponding values of the capillary and Weber numbers; under these conditions, the stabilizing effect of the capillary force is dominant and minimizes the bubble surface.

4.2 Bubble and slug lengths

Figure 6 shows the evolution of the dimensionless bubble lengths as a function of the Weber number for the air–ethanol

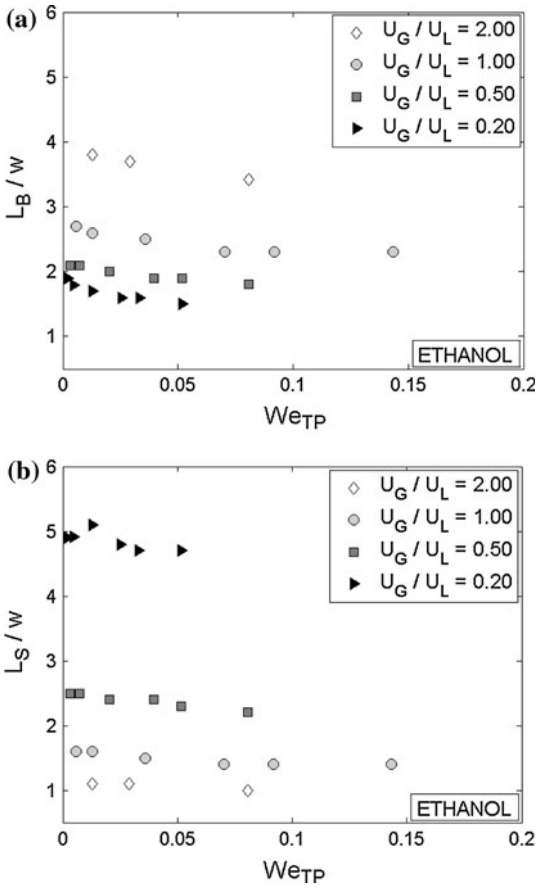

Fig. 6 Bubble and slug lengths versus the Weber number We_{TP} in air–ethanol system for volumetric flow rate ratios $U_G/U_L = [2;\ 1;\ 0.5;\ 0.2]$

systems. For a fixed flow rate ratio U_G/U_L, the bubble and slug lengths decrease slightly when the superficial two-phase velocity increases. This decrease in bubble and slug size can be explained by the increase in energy input to the system; similar observations have been made for drop formation in micromixers (Haverkamp et al. 1999). Thus, for a given gas hold-up, the frequency of bubble formation $f \sim U_B/(L_B + L_S)$ increases with inertia. Similar phenomena are observed for other fluid pairs, however, for fixed flow conditions, the bubble/slug period is shorter with ethanol than it is with the ethanol solution (33%), which is shorter than the bubble/slug periods for water alone. This is primarily due to the higher surface tension of water compared with ethanol.

Figure 7 shows the evolution of dimensionless bubble and slug lengths as a function of the flow rate ratios for different fluid pairs. The experiments were conducted by varying the gas flow rate at a fixed liquid flow rate ($U_L = 0.021$ m/s). For each fluid system, the bubble and slug lengths increase linearly with the gas-to-liquid and liquid-to-gas velocity ratios, respectively. It can be seen that the bubble and slug lengths are greater with water than they are with ethanol for the same flow rate conditions. Again, this shows that for a fixed flow rate ratio, the bubble and slug lengths decrease and the frequency of bubble break-up increases when the Weber number increases. It should be pointed out that for the results presented in Fig. 7a,b, the flow for the ethanol and diluted ethanol (33%) systems was regular and bubbles were formed via the squeezing mechanism, whilst the air–water flow was irregular (as suggested by the error bars) with bubble formation in the main channel (leakage regime).

The linear evolution of the bubble and slug lengths with the flow rate ratios is in agreement with the model proposed by Garstecki et al. (2006) for the estimation of drop and bubble lengths. According to the Garstecki model, the lengths of bubbles (and drops) generated in side-entering T-junction microchannels with rectangular cross-section can be determined from the continuous and dispersed phase flow rates. The model was developed using data obtained in microchannels with characteristic dimensions on the order of 100 μm at low capillary ($Ca_{TP} < 10^{-2}$) and Reynolds numbers ($Re_{TP} < 1$). Under these conditions, the effects of shear stress dominate the inertial effects and both are negligible compared with the interfacial stresses and pressure gradients. Garstecki et al. (2006) postulate that the dynamics of drop and bubble break-up is dominated by the pressure balance between the dispersed and continuous phases due to the interfacial stresses and the pressure drop generated by the resistance of the flow induced by the bubble or drop. The authors identified four stages of the break-up process for their model: (1) the tip of the bubble enters the main channel, (2) the filling stage where the

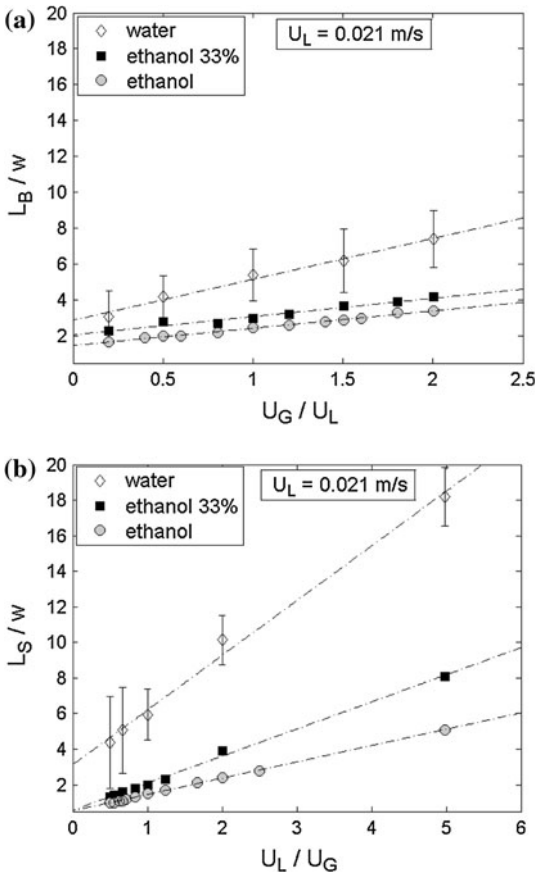

Fig. 7 **a** Dimensionless bubble lengths and **b** dimensionless slug lengths for varying gas phase velocities and a fixed liquid phase velocity $U_L = 0.021$ m/s for water, $We_L = 0.43$ (*open diamond*); diluted ethanol (33%), $We_L = 0.30$ (*open square*); and ethanol, $We_L = 0.18$ (*open circle*). *Error bars* represent the standard deviation for the water-air system; the standard deviation on bubble and slug lengths for the ethanol and the diluted ethanol (33%) systems was negligible with this liquid velocity. *Dash dot dash line* experimental fitting

bubble occupies almost all the cross-section, (3) the squeezing stage where the radius of curvature of the interface increases and the interface at the gas inlet is squeezed, (4) the break-up stage where the Laplace pressure reaches a maximum as the radius of curvature tends to infinity and the discontinuous phase pinches off. Following this, they suggest that the bubble or drop generation process can be divided into two main steps and that the time for bubble or drop formation t_{growth} is the sum of the filling and squeezing times. The scaling relation they proposed is $t_{growth} = t_{filling} + t_{squeezing}$ where $t_{growth} = L_B/u_{growth}, t_{filling} = w/u_{filling}$ and $t_{squeezing} = d_{neck}/u_{squeezing}$, where d_{neck} is the characteristic dimension of the neck of the bubble at the beginning of the squeezing stage. If the filling and squeezing stages are independent, it can be assumed that $d_{neck} \sim w_{in}$. The characteristic velocities of the different stages can be expressed as a function of the dispersed and continuous phase flow rates: $u_{growth} = Q_G/A_{ch}$, $u_{filling} = Q_G/A_{ch}$ and $u_{squeezing} = Q_L/A_{ch}$. Accordingly, the bubble length is given by:

$$\frac{L_B}{w} \sim 1 + \frac{w_{in}}{w}\frac{Q_G}{Q_L}. \tag{10}$$

However, in microchannels of rectangular cross-section, liquid flows around the dispersed phase during the squeezing stage thereby increasing the squeezing time. Van Steijn et al. (2007) improved the Garstecki model by taking this leakage flow into account and estimated the bubble length as:

$$\frac{L_B}{w} = \lambda_1 + \lambda_2\frac{U_G}{U_L}, \tag{11}$$

where $\lambda_1 = 1.5$ and $\lambda_2 = 1.5\ w_{in}/w$. Völkel (2009) suggested that the length of the liquid slug should follow a scaling law similar to the gas phase:

$$\frac{L_S}{w} = \lambda_2 + \lambda_1\frac{U_L}{U_G}. \tag{12}$$

Pohorecki and Kula (2008) also proposed a 'switching' mechanism to predict bubble lengths in Y-junction microchannels and presented a simple model: $L_B/w \sim \varepsilon_L^{-1}$, i.e. $L_B/w \sim 1 + U_G/U_L$. This model is almost identical to that proposed by Garstecki et al. (2006) with the difference that the gas-to-liquid inlet width ratio is not explicitly taken into account since the gas and liquid inlets used by Pohorecki and Kula (2008) were the same size. It is interesting to note that their experimental results, which were obtained in microchannels of square and circular cross sections as well as different materials, agree relatively well with this model. It is interesting to note that according to both Garstecki et al.'s (2006) and Pohorecki and Kula's (2008) models, the bubble lengths only depend on the continuous and dispersed phase flow rates and the microchannel dimensions; there appears to be no dependency on the physical properties of the fluids. Recently, Leclerc et al. (2010) also proposed a unique scaling law for bubble generation in various T-junction geometries. Again, it enables bubble lengths to be predicted from flow rates and microchannel dimensions only. It should be pointed out, however, that the effects of fluid and material properties on bubble generation were not investigated.

The results in Fig. 7 show that when $U_G \ll U_L$, the minimum bubble length is greater than the width of the microchannel w and appears to depend on the liquid phase properties. In fact, as shown in Fig. 4, the squeezing stage can start even if the bubble is not completely filling the cross-section area, which results in bubble lengths $L_B > w$. In this case, it appears that the same scaling relation can still be applied, however, the coefficients λ_1 and λ_2 may be

slightly different to the values found by van Steijn et al. (2007). It can also be pointed out that although Garstecki et al. (2006) presented their model for the estimation of both drop and bubble lengths, it only correctly estimates bubble lengths under certain operating conditions. In fact, although the bubble/drop generation process is apparently independent of fluid properties (i.e. viscosity, density and surface tension) under the conditions studied by Garstecki et al. (2006), a close inspection of their results suggests that other properties of the carrier liquid (e.g. wettability) play a non-negligible role in the generation process. As a result, it is not clear that all fluid pairs follow a single scaling law.

It also can be seen in Fig. 7 that the length of the liquid slug increases with U_L/U_G, as suggested by Völkel (2009). However, the coefficients λ_1 and λ_2 appear to depend on both the fluid properties and the liquid velocity, and do not appear to have the same value as the coefficients of Eq. (11). Indeed, the coefficients for ethanol are close to 1.5 in the squeezing regime but they appear to increase when the break-up mechanism changes and tends towards the leakage regime (Figs. 7, 8).

Qian and Lawal (2006) carried out 2D simulations of the break-up of Taylor bubbles in T-junctions and side-entering T-junctions. They proposed a correlation for the prediction of bubble lengths ($L_B/w = 1.637\varepsilon_G^{0.107}(1-\varepsilon_G)^{-1.05}Re_{TP}^{-0.075}Ca_{TP}^{-0.0687}$), which underlines the predominant contribution of the flow rate ratio and only a slight effect of surface tension and viscosity. Although a few points remain unclear in Qian and Lawal's (2006) study - they used a coarse grid that was inadequate to correctly detect the liquid film and no details on the surface tension conditions that determine bubble break-up - it is interesting to point out that the bubble lengths obtained in this study for the air–ethanol systems at various Weber numbers (Fig. 6) agree with the Qian and Lawal (2006) correlation. However, when water or sugarcane syrup are used as the carrier fluid, the squeezing mechanism does not occur. Instead, parallel flow develops before bubble generation occurs in the main channel and in this case the data do not agree with the Qian and Lawal (2006) correlation. Indeed, the dependency of the bubble lengths on the fluid properties has shown to be much more significant here than ever shown in previous studies. The transition from the squeezing regime to the leakage regime is difficult to detect based solely on the competition of capillary, viscous and inertial effects; it is thought that the wettability of microchannel by the liquid really plays a non-negligible role.

Figure 8 shows the evolution of the bubble and slug lengths as a function of the the flow rate ratios for the air-diluted ethanol (33%) system at fixed superficial liquid velocities. This figure highlights the linear evolution of the

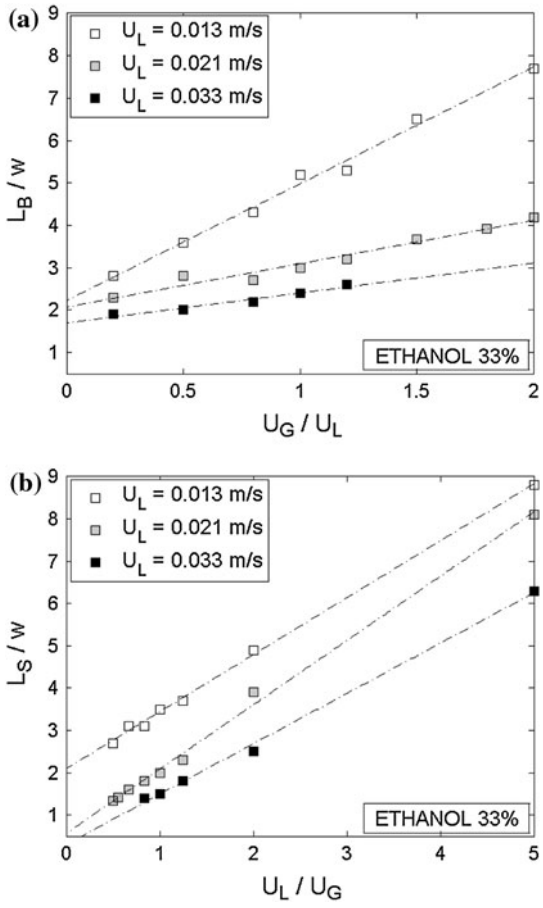

Fig. 8 Bubble and slug lengths versus ratio of air and liquid velocities U_G/U_L (**a**), and U_L/U_G (**b**) in ethanol 33%/air system for given liquid velocities: $U_L = [0.008; 0.021; 0.042]$ m/s. *Dash dot dash line* experimental fitting

bubble and slug lengths with the gas-to-liquid and liquid-to-gas velocity ratios respectively, which is in agreement with Eqs. (11) and (12). The coefficients λ_1 and λ_2 of the linear scaling law for this fluid pair decrease when the liquid velocity increases. It was observed that regular bubble sizes were generated at a high frequency with high liquid flow rates, whereas a decrease in the liquid flow rate leads to irregular flows of longer bubbles and slugs at a lower frequency. This transition from squeezing to leakage regime is also visible with water for which a similar linear evolution is also found. However, for the pure air–ethanol experiments, where the bubble generation was generally very regular, the bubble and slug lengths are not so dependent on the liquid velocities. Figure 8 also shows that for a fixed gas fraction, the bubble lengths decrease as the liquid velocity increases and the energy input into the system increases. Thus, the bubble and slug lengths, as well as the frequency of bubble generation, appear to be governed mainly by the competition between gas and liquid velocities, as well as the competition between inertial and capillary effects.

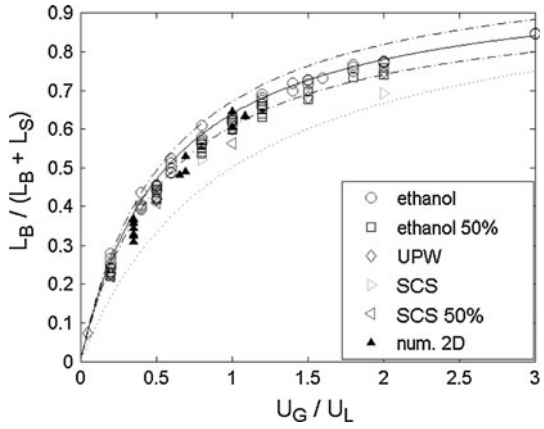

Fig. 9 Dimensionless bubble length versus ratio air/liquid flow rates. *Dotted line* relative bubble length in the case of a zero liquid film thickness. *Straight line* Experimental fitting from averaged values of coefficients λ_1 and λ_2 using the van Steijn representation (Eq. 11). *Dash dot dash line* deviation of 5% from the experimental fitting

Interestingly, when the bubble length relative to the total length of a bubble/slug unit is plotted as a function of the flow rate ratio, as shown in Fig. 9, the squeezing and leakage regimes observed seem to collapse; slight differences can be accounted for by the varying effects of capillarity, inertia and viscosity. This suggests that the relative quantity of liquid surrounding the bubble (in the liquid film and around the caps) is almost the same for the different fluid pairs at a given gas hold-up, whatever the bubble break-up frequency.

The difference between the experimental points and the curve for the relative bubble length in the case of zero liquid film shows that the quantity of liquid surrounding the bubble increases with U_G/U_L, reaches a maximum around $U_G/U_L = 1$ and then decreases slightly. Results from numerical simulations are also reported in this figure and their agreement with the experimental data is good despite their 2D nature.

4.3 Liquid film

The liquid film between the bubble and the microchannel wall has been evaluated with 2D simulations. This 2D representation is a simplified approach to the problem and does not take into account the liquid film in the corners of the channel. However, de Lózar et al. (2008) have shown that the liquid flow from the film to the corners is weak and does not significantly deform the gas–liquid interface. Although the 2D simulations do not provide detailed information on the varying liquid film thickness around the bubble and the 3D bubble shape, they nevertheless provide a useful information. The qualitative trends observed in 2D representation are expected to be similar to 3D cases. Indeed, Sarrazin et al. (2006) studied velocity field and mixing in liquid–liquid microsystems and they observed similar hydrodynamic flow structures in 2D and 3D rectangular cases (with an aspect ratio close to unity). Furthermore, the information obtained through these 2D simulations is also expected to be valid for high aspect ratio rectangular microchannels. In the following, the liquid film hold-up around a Taylor bubble is considered and defined as $\varepsilon_L = A_L/A_{ch}$ where A_L is the area occupied by the liquid. In the literature, the bubble velocity is often related to this liquid film hold-up (see Völkel 2009 for an overview). Under several conditions, such as constant surface tension and a flat annular liquid film, there is no pressure gradient along the bubble and the velocity in the liquid film is assumed to be zero. Thus, using the mass conservation relationship, the bubble velocity can be related to the liquid film hold-up and the two-phase velocity: $U_B/U_{TP} = 1/(1-\varepsilon_L)$.

Since the liquid film hold-up is typically very low in Taylor flow, the bubble velocities can be expected to be close to the sum of the gas and liquid superficial velocities. Although the linear plots of the bubble lengths given in Figs. 7 and 8 suggest information on the leakage flow around the bubble at the T-junction contacting section, the measurement of the liquid film thickness around Taylor bubbles is not straightforward experimentally. However, it can be quite easily obtained with correctly performed numerical simulations. Figure 10a shows the dimensionless liquid film thickness around the Taylor bubble obtained numerically as a function of the capillary number based on the bubble velocity, as suggested in the first studies of Taylor (1961) and Bretherton (1961). In this latter work, a correlation assuming the 'lubrication approximation' is proposed for the determination of the liquid film thickness from the capillary number in tubes or 2D planar geometries. This correlation is valid for flows where $Ca_B \ll 1$ and the inertial effects are negligible compared with the surface tension and viscous effects: $\delta/r_h = 1.34\ Ca_B^{2/3}$, where δ is the liquid film thickness, r_h is the hydraulic radius and Ca_B is the Taylor bubble capillary number based on the bubble velocity.

Aussillous and Quéré (2000) extended Bretherton's (1961) correlation to high capillary numbers in capillary tubes:

$$\frac{\delta}{r_h} = \frac{1.34 Ca_B^{2/3}}{1 + k \times 1.34 Ca_B^{2/3}}. \quad (13)$$

The coefficient 1.34 was derived by Bretherton (1961) and the coefficient $k = 2.5$ was found empirically (Aussillous and Quéré 2000). Thus, the liquid film thickness tends toward a maximum value of $1/2.5 \sim 0.4$ as the capillary number increases.

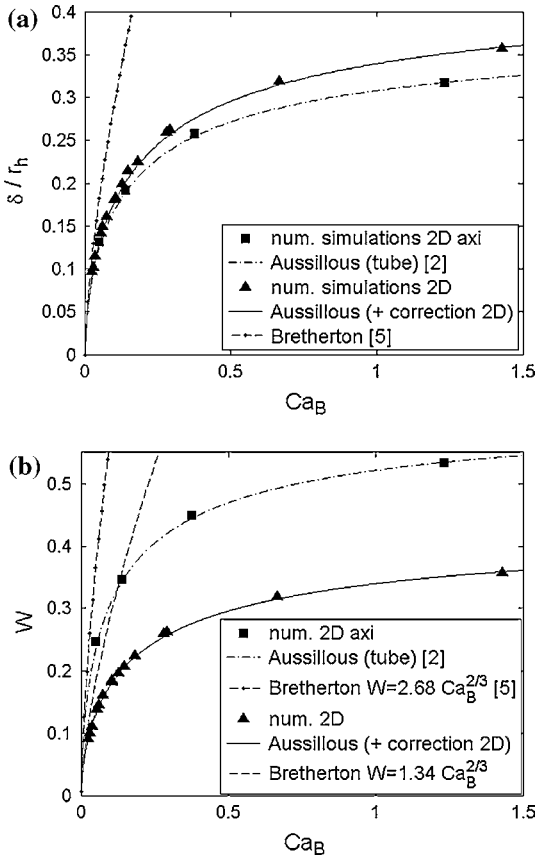

Fig. 10 **a** Dimensionless liquid film thickness determined from numerical simulations as a function of the capillary number. **b** Dimensionless bubble velocities $W = (U_B - U_{TP})/U_B$ versus the capillary number

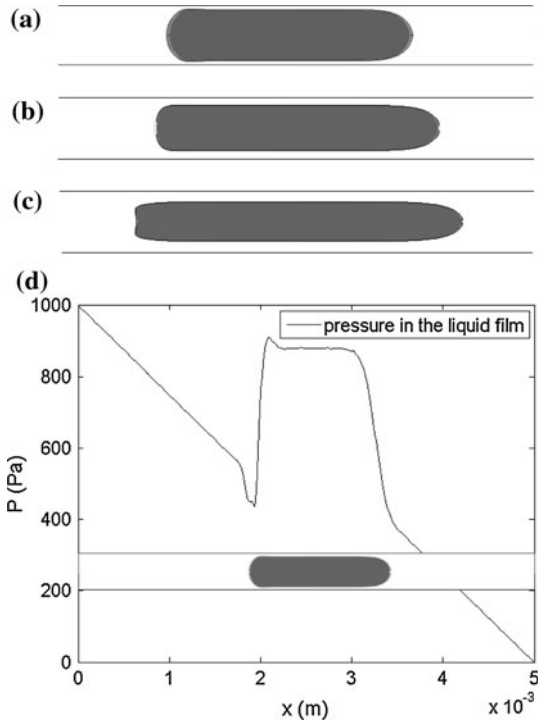

Fig. 11 Bubbles shapes obtained numerically under different conditions: **a** $Ca_B = 0.055$, **b** $Ca_B = 0.293$, **c** $Ca_B = 1.47$, gas hold-up is fixed $\alpha_G \sim 0.25$. **d** pressure field in the liquid film corresponding to case (**a**): P decreases linearly from $P_0 + 1000$ (Pa), capillary pressure jump, P remains constant along the bulk of the bubble, capillary pressure jump, P decreases linearly to P_0. Domain: $l_x \times l_y = 5 \times 0.2$ mm. *Blue* air, *red* liquid; the interface is distributed over about 3–4 meshes at the maximum elongation (tail and nose)

In Fig. 10a, it can be seen that the liquid film thickness obtained by the 2D axisymmetrical simulations is correctly described by Eq. (13). In the 2D geometry, the liquid film thickness increases with increasing capillary number, however the asymptotic value at large capillary numbers is higher than that obtained in tubes (1./2.2 $\sim$ 0.455). Therefore, an equation similar to Eq. (13) can be proposed for 2D geometries, whereby the coefficient $k = 2.2$. This equation, with corresponding coefficient k, shows that Bretherton's (1961) correlation is found as the asymptotic behaviour for low capillary numbers, while at higher capillary numbers the liquid film thickness tends towards a maximum value depending on the geometry. In square and rectangular microchannels, the film thickness around the bubble body varies due to the presence of the channel corners (Han and Shikazono 2009b; Hazel and Heil 2002; Liu and Wang 2008; Taha and Cui 2006; Wong et al. 1995). However, although the 3D aspects of the bubble shapes are not considered in these 2D simulations, the asymptotic behaviour of the liquid film is expected to be the same and particularly in channels with a high aspect ratio (i.e. wide shallow microchannels) where the shear rate along the channel width is negligible compared with the shear rate along the depth of the channel. These results are in very good agreement with the theory and allow bubble shapes to be roughly estimated so that the mesh for 3D simulations, which are much more computationally expensive, can be adapted to correctly capture the liquid film in Taylor flow.

In addition to the increase in the liquid film thickness, a flattening of the rear of the bubble and an elongation of the nose of the bubble can be seen with increasing capillary number in the simulated results as shown in Fig. 11a–c. Such a loss of symmetry was also observed in the experiments with sugarcane syrup solutions where the capillary number is of the order of 10^{-2} and the liquid film is visibly thick. Figure 11d shows the pressure field in the liquid film and there is indeed no pressure gradient along the bulk of the bubble, which statisfies the hypothesis of the stagnant film.

The changes in the shape of the bubbles rear and nose have also been observed in several other studies, including planar cases (Giavedoni and Saita 1997), circular

capillaries (Fouilland et al. 2010; Gupta et al. 2009; Triplett et al. 1999) and square channels (Liu and Wang 2008; Taha and Cui 2006). This phenomenon can be understood from the pressure drop across the bubble caps. In Bretherton's work (1961), the asymptotic behaviour of the pressure drop at vanishing Ca was studied. It was found that the pressure drop at the front cap of an axisymmetrical bubble is $\Delta p_{\text{front}} = \frac{2\sigma}{r_h}\left(1 + 3.72Ca_B^{2/3}\right)$ and the pressure drop at the rear cap is $\Delta p_{\text{rear}} = \frac{2\sigma}{r_h}\left(1 - 0.97Ca_B^{2/3}\right)$. From these relationships, it can be seen that the pressure drop at the front cap increases with the capillary number while it decreases at the rear cap. Even if this asymptotic behaviour can not be used at higher capillary numbers ($Ca_B > 10^{-2}$), Giavedoni and Saita (1997) and Hazel and Heil (2002) found similar trends in 2D and rectangular channels, respectively, where the pressure drop across the front tip of the bubble increases with Ca_B.

4.4 Bubble velocities

Since the liquid film thickness obtained by the numerical simulations in the visco-capillary regime is correctly described by Eq. (13), the dimensionless bubble velocity W can be deduced as the following, respecting the stagnant film hypothesis:

$$W = \frac{U_B - U_{TP}}{U_B} = 1 - \left(1 - \frac{\delta}{r_h}\right)^m, \quad (14)$$

where $m = 1$ for 2D cases and $m = 2$ for tubes. Figure 10b shows that both the 2D and axisymmetrical simulations are in good agreement with the scaling laws obtained from the liquid film thickness. The relationship for the evaluation of bubble velocity, as first proposed by Bretherton (1961), is also found at low capillary numbers ($Ca_B < 0.01$) where the liquid film is very thin: $W = m \times 1.34\ Ca_B^{2/3}$.

In this work, the experiments were performed for a range of low capillary numbers ($Ca_B < 0.01$) and moderate Reynolds numbers ($1 < Re_B < 100$). Under these conditions, the effects of inertia are not negligible compared with our numerical simulations and the conditions studied by Aussillous and Quéré (2000), which were both carried out in the visco-capillary regimes ($Ca_B > 0.01$ and $Re_B < 1$). Since the Weber numbers of the experiments in this study are much larger than those of the simulations and a simple model like relation (13) is not applicable to such conditions, the bubble velocity has been plotted versus the two-phase superficial velocities. Figure 12a shows a linear increase in the experimental bubble velocities with increasing two-phase superficial velocity for the air–ethanol system. This means that the liquid film is of more or less constant thickness along the bubble body in our experiments, which is in agreement with the results of Taha and Cui (2006) in square capillaries at low capillary numbers ($Ca_B \ll 1$). The ratio of the bubble velocity to the two-phase velocity is slightly greater than unity, which is coherent with the stagnant film hypothesis and suggests a thin liquid film. Similar results about bubble velocities were reported in Yun et al.'s (2010) study. Indeed, the liquid film between the bubble and the microchannel walls in these experiments was indistinguishable. Figure 12b shows a similar graph, which combines all of the bubble velocities measured experimentally with those obtained by the 2D simulations. The results of the 2D numerical simulations appear to agree relatively well with the experiments, although the bubble velocities increase slightly faster than experimental bubble velocities. In addition to the fact that different effects dominate in the experiments and the numerical simulations, this discrepancy is certainly due to the fact that the lateral walls of the microchannel were not taken into account in the simulations. Indeed, the lateral walls contribute to an increase in flow resistance and dissipation, which results in a reduction of the bubble velocity. 3D simulations are, therefore, necessary for a more accurate comparison with the experiments.

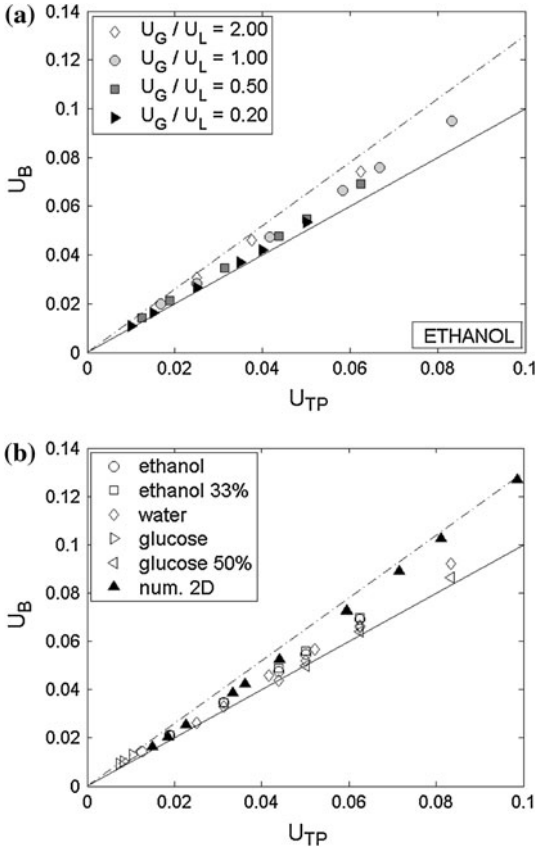

Fig. 12 **a** Bubble velocity versus two-phase velocity for ethanol. **b** Bubble velocity versus two-sphase velocity. *Straight line* $U_B = U_{TP}$ and *Dash dot dash line* $U_B = 1.3 \times U_{TP}$

It can also be pointed out that although the cross-sectional area occupied by the liquid film should increase with increasing capillary number (Bretherton 1961; Aussillous and Quéré 2000), the capillary numbers in the experiments were typically very low ($Ca_B < 0.01$) and, therefore, the bubble velocity should be approximately equal to the two-phase superficial velocity. However, inertia is assumed to be negligible in Bretherton's (1961) and Aussillous and Quéré's (2000) works, which is not the case in our experiments at moderate Reynolds numbers. It is, therefore, possible that the Weber number has some effect on the liquid film thickness and thus, the dimensionless bubble velocity. This was also mentioned by Aussillous and Quéré (2000) for conditions in the visco-inertial regimes. Even if the effective dependency of the liquid film thickness or bubble velocity upon the Weber number is not clear at present, these results highlight its possible effects on the hydrodynamics of Taylor bubbles in capillary-inertial regimes.

5 Conclusions

This study has focused on the generation and characteristics of gas–liquid Taylor flow formed in T-junction microchannels. Visualisation experiments using a high speed camera and 2D Volume of Fluid simulations have been performed to study the effects of fluid properties and flow conditions on bubble and slug lengths, liquid film hold-up and bubble velocities. As earlier described by Garstecki et al. (2006) and then by van Steijn et al. (2007), the bubble generation process can be partitioned into several steps and the bubble and slug lengths are a function of the gas and liquid flow rates and independent of fluid properties such as the viscosity and surface tension. This study shows however that a single scaling law for all gas–liquid flows generated in the T-junction is not always possible. The bubble and slug lengths are shown not to depend solely on the gas and liquid flow rates and suggest that the liquid properties (such as wettability) and velocities are also important under certain conditions. This work highlights the effects of the competition between inertial forces and capillarity on the leakage flow and thus on the bubble break-up frequency, which have been negligible in previous studies in the literature due to the low Reynolds numbers employed. Indeed, increasing the inertia of the fluid system results in increased leakage flow and consequently to a decreased frequency of bubble formation. Bubble and slug lengths are, therefore, increased. The results of numerical simulations were found to be in relatively good agreement with the experiments despite their 2D nature. They allow the dimensionless bubble lengths to be predicted relatively well and provide a good estimation of the liquid film thickness in the case of high aspect ratio microchannels, which is difficult to measure experimentally. Furthermore, the 2D simulations allow the stagnant film hypothesis used in modelling to be confirmed. 3D simulations are underway, however, these are very computationally expensive. They will allow a more accurate comparison with the experimental results since the effect of the lateral wall of the microchannel is suspected to contribute to the bubble dynamics. They will also provide more detailed information on the liquid film thickness around the bubbles.

Acknowledgments This work was financed by the French "Agence Nationale de la Recherche" in the framework of the project MIGALI no. ANR-09-BLAN-0381-01. We also acknowledge the support for this project from the CNRS research federation FERMaT, such as the CALMIP project for providing computational resources.

References

Akbar MK, Plummer DA, Ghiaasiaan SM (2003) On gas–liquid two-phase flow regimes in microchannels. Int J Multiph Flow 29:855–865

Aussillous P, Quéré D (2000) Quick deposition of a fluid on the wall of a tube. Phys Fluids 12(10):2367

Bonometti T, Magnaudet J (2007) An interface-capturing method for incompressible two-phase flows. Validation and application to bubble dynamics. Int J Multiph Flow 33:109–133

Brackbill J, Kothe DB, Zemach C (1992) A continuum method for modeling surface tension. J Comput Phys 100:335–354

Bretherton FP (1961) The motion of long bubbles in tubes. J Fluid Mech 10:166

de Lózar A, Juel A, Hazel AL (2008) The steady propagation of an air finger into a rectangular tube. J Fluid Mech 614:173–195

De Menech M, Garstecki P, Jousse F, Stone HA (2008) Transition from squeezing to dripping in a microfluidic T-shaped junction. J Fluid Mech 595:141–161

Dupont J-B, Legendre D (2010) Numerical simulation of static and sliding drop with contact angle hysteresis. J Comput Phys 229:2453–2478

Fouilland TS, Fletcher DF, Haynes BS (2010) Film and slug behaviour in intermittent slugannular microchannel flows. Chem Eng Sci 65:5344–5355

Francois MM, Cummins SJ, Dendy ED, Kothe DB, Sicilian JM, Williams MW (2006) A balanced-force algorithm for continuous and sharp interfacial surface tension models within a volume tracking framework. J Comput Phys 213:141–173

Garstecki P, Fuerstman MJ, Stone HA, Whitesides GM (2006) Formation of droplets and bubbles in a microfluidic T-junction—scaling and mechanism of break-up. Lab chip 6:437–446

Giavedoni MD, Saita FA (1997) The axisymmetric and plane cases of a gas phase steadily displacing a Newtonian liquid—a simultaneous solution of the governing equations. Phys Fluids 9(8):2428

Guillot P, Colin A (2005) Stability of parallel flows in a microchannel after a T junction. Phys Rev E 72:066301

Gupta A, Kumar R (2010) effect of geometry on droplet formation in the squeezing regime in a microfluidics T-junction. Microfluid Nanofluid 8:799–812

Gupta R, Fletcher DF, Haynes BS (2009) On the CFD modelling of Taylor flow in microchannels. Chem Eng Sci 64:2941–2950

Gupta R, Fletcher DF, Haynes BS (2010) CFD modelling of heat and mass transfer in the Taylor flow regime. Chem Eng Sci 65:2094–2107

Han Y, Shikazono N (2009a) Measurement of the liquid film thickness in micro tube slug flow. Int J Heat Fluid Fl 35:842–853

Han Y, Shikazono N (2009b) Measurement of the liquid film thickness in micro square channel. Int J Multiph Flow 30:896–903

Haverkamp V, Ehrfeld W, Gebauer K, Hessel V, Lowe H, Richter T, Wille C (1999) The potential of micromixers for contacting of disperse liquid phases. Fresen J Anal Chem 364:617–624

Hazel AL, Heil M (2002) The steady propagation of a semi infinite bubble into a tube of elliptical or rectangular cross-section. J Fluid Mech 470:91–114

Kreutzer MT, Kapteijn F, Moulijn JA, Heiszwolf JJ (2005a) Multiphase monolith reactors: chemical reaction engineering of segmented flow in microchannels. Chem Eng Sci 60:5895–5916

Kreutzer MT, Kapteijn F, Moulijn JA, Heiszwolf JJ (2005b) Inertial and interfacial effects on pressure drop of Taylor flow in capillaries. AIChE J 51:2428–2440

Lafaurie B, Nardone C, Scardovelli R, Zaleski S, Zanetti G (1994) Modelling merging and fragmentation in multiphase flow with SURFER. J Comput Phys 113:134–147

Leclerc A, Philippe R, Houzelot V, Schweich D, de Bellefon C (2010) Gas–liquid Taylor flow in square microchannels: New inlet geometries and interfacial area tuning. Chem Eng J 165:290–300

Leung SSY, Liu Y, Fletcher DF, Haynes BS (2010) Heat transfer in well-characterised Taylor flow. Chem Eng Sci. doi:10.1016/j.ces.2010.09.014

Liu D, Wang S (2008) Hydrodynamics of Taylor flow in noncircular capillaries. Chem Eng Process 47:2098–2106

Pohorecki R, Kula K (2008) A simple mechanism of bubble and slug formation in Taylor flow in microchannels. Chem Eng Res Des 86:997–1001

Qian D, Lawal A (2006) Numerical study on gas and liquid slugs for Taylor flow in a T-junction microchannel. Chem Eng Sci 61:7609–7625

Renardy Y, Renardy M (2002) PROST: a parabolic reconstruction of surface tension for the volume-of-fluid method. J Comput Phys 183:400–421

Sarrazin F, Bonometti T, Loubière K, Prat L, Gourdon C, Magnaudet J (2006) Experimental and numerical study of droplets hydrodynamics in microchannels. AIChE J 52:4061–4070

Scardovelli R, Zaleski S (1999) Direct numerical simulation of free-surface and interfacial flow. Annu Rev Fluid Mech 31:567–303

Sobieszuk P, Cyganski P, Pohorecki R (2008) Volumetric liquid side mass transfer coefficient in a gas–liquid microreactor. Chem Process Eng 29:651–661

van Steijn V, Kreutzer MT, Kleijn CR (2007) μ-PIV study of the formation of segmented flow in microfluidic T-junction. Chem Eng Sci 62:7505–7514

Taha T, Cui ZF (2006) CFD modelling of slug flow inside square capillaries. Chem Eng Sci 61:665–675

Taylor GI (1961) Deposition of a viscous fluid on the wall of a tube. J Fluid Mech 10:161–165

Triplett KA, Ghiaasiaan SM, Abdel-Khalik SI, Sadowsli DL (1999) Gas–liquid two-phase flow in microchannels. Part i: two-phase flow patterns. Int J Multiph Flow 25:377–394

Völkel N (2009) Design and characterization of gas–liquid microreactors, PhD Thesis, Institut National Polytechnique de Toulouse, France

Waelchli S, von Rohr PR (2006) Two-phase flow characteristics in gas–liquid microreactors. Int J Multiph Flow 32:791–806

Wong H, Radke CJ, Morris S (1995) The motion of long bubbles in polygonal capillaries Part 1:Thin films. J Fluid Mech 292:71–94

Yue J, Chen G, Yuan Q, Luo L, Gonthier Y (2007) Hydrodynamics and mass transfer characteristics in gas–liquid flow through a rectangular microchannel. Chem Eng Sci 62:2096–2108

Yue J, Luo L, Gonthier Y, Chen G, Yuan Q (2008) An experimental investigation of gas–liquid two-phase flow in single microchannel contactors. Chem Eng Sci 63:4189–4202

Yun J, Lei Q, Zhang S, Shen S, Yao K (2010) Slug flow characteristics of gas-miscible liquids in a rectangular microchannel with cross and T-shaped junctions. Chem Eng Sci 65:5256–5263